SYNTHESIS, CRYSTAL STRUCTURE AND MAGNETISM OF PEROVSKITE-BASED TRANSITION METAL OXIDES

SYNTHESIS, CRYSTAL STRUCTURE AND MAGNETISM OF PEROVSKITE-BASED TRANSITION METAL OXIDES

By

FARSHID RAMEZANIPOUR, B.Sc., M.Sc.

A Thesis

Submitted to the School of Graduate Studies

in Partial Fulfilment of the requirements

for the Degree

Doctor of Philosophy

McMaster University

DOCTOR OF PHILOSOPHY (2011) McMaster University

Department of Chemistry and Chemical Biology Hamilton. Ontario

TITLE: Synthesis, Crystal Structure and Magnetism of Perovskite-Based Transition Metal Oxides

AUTHOR: Farshid Ramezanipour, B.Sc. (Razi University), M.Sc. (Tarbiat Moallem University)

SUPERVISOR: Doctor John E. Greedan

NUMBER OF PAGES: xxvi, 256

Abstract

A series of layered perovskite-based compounds were synthesized and studied as follows.

$La_5Mo_{2.76(4)}V_{1.25(4)}O_{16}$ is a new pillared-perovskite synthesized by solid state chemistry method. It has layers of corner-sharing octahedra separated by dimers of edge-sharing octahedra, and is the first Mo-based pillared-perovskite whose magnetic structure was determined by neutron diffraction.

Ca_2FeMnO_5 is an oxygen-deficient-perovskite with a brownmillerite-type ordering of oxygen vacancies, resulting in layers of corner-sharing octahedra separated by chains of corner-sharing tetrahedra. The octahedral layer contains mostly (~87%) Mn, while the tetrahedral layer is mainly (~91%) occupied by Fe. Long-range G-type magnetic ordering is present, where the moment on each site is coupled antiferromagnetically relative to all nearest neighbors.

Ca_2FeCoO_5 has a brownmillerite superstructure with space group *Pcmb*, a rare space group for brownmillerites that requires doubling of one unit cell axis. Ca_2FeCoO_5 is the first brownmillerite to contain intra-layer cation ordering. It has a long-range G-type ordering, and is the first brownmillerite to show spin re-orientation as function of temperature.

Sr_2FeMnO_{5+y} was synthesized in both air (y~0.5) and argon (y~0), both of which resulted in vacancy-disordered cubic structures. The argon compound has a local brownmillerite structure, i.e. local ordering of vacancies. It has a superparamagnetic state below ~55K, with domains of short range (50Å) G-type ordering at 4K. For the air synthesized compound, y~0.5, long range G-type ordering is observed in ~4% of the sample.

$Sr_2Fe_{1.9}M_{0.1}O_{5+y}$ (M=Mn, Cr, Co; y= 0, 0.5) were synthesized in both air(y~0.5), and argon(y~0). All argon materials are brownmillerites with G-type magnetic ordering, but T_N's are significantly different. The air-synthesized Co-material has long range vacancy ordering and magnetic ordering, while the Mn and Cr-materials (air) lack such orderings and both show spin-glass-like transitions.

$Sr_2Fe_{1.5}Cr_{0.5}O_5$ has a vacancy-disordered cubic structure, but contains long range G-type magnetic ordering, unlike the other vacancy-disordered materials studied.

Acknowledgements

I would like to express my gratitude to people who made my time at McMaster a truly memorable experience.

First, I would like to thank my supervisor, Dr. John Greedan for all his help and support. Having the chance to learn from him was a unique opportunity that I am grateful for. His kindness made working in his group a pleasure, and his knowledge and expertise were exceptional resources that I could always rely on.

I would also like to thank the members of my research group, Shahab, Diego, Heather, Tomoko, Jonathan, Craig and Andrew, for their help, friendship, and the happy environment we had in the office. Thanks to Dr. Jacques Barbier and Dr. Yurij Mozharivskyj, my committee members, and Dr. Gillian Goward for participating in my comprehensive exam. Thanks to Dr. Hanna Dabkowska, Dr. Anton Dabkowski and all the members of our lunch group for their friendship.

I would also like to thank the staff of Chemistry Department and Brockhouse Institute for Materials Research, Dr. Jim Britten, Dr. Paul Dube, and Frank Gibbs. My friends at McMaster deserve my special thanks and gratitude. They made my time in Hamilton enjoyable and unforgettable. I am truly grateful for their friendship, and for all the happy memories they created for me.

Last but not least, I would like to thank my family for their love, support, and for believing in me and encouraging me every step of the way. I can never thank them enough for everything that they have done for me.

Table of Contents

Chapter 3: Synthesis, Crystal Structure and magnetic properties of a new pillared perovskite $La_5Mo_{2.75}V_{1.25}O_{16}$

Chapter 4: Crystal and Magnetic Structures of the Brownmillerite Compound $Ca_2Fe_{1.039(8)}Mn_{0.962(8)}O_5$

Chapter 5: Intra-layer Cation Ordering in a Brownmillerite Super-Structure: Synthesis, Crystal and Magnetic Structures of Ca_2FeCoO_5…………..……………109

List of Figures

Chapter 1: Introduction

Chapter 2: Experimental Techniques and Methods

Chapter 3: Synthesis, Crystal Structure and magnetic properties of a new pillared perovskite $La_5Mo_{2.75}V_{1.25}O_{16}$

Chapter 4: Crystal and Magnetic Structures of the Brownmillerite Compound $Ca_2Fe_{1.039(8)}Mn_{0.962(8)}O_5$

Chapter 5: Intra-layer Cation Ordering in a Brownmillerite Super-Structure: Synthesis, Crystal and Magnetic Structures of Ca_2FeCoO_5

Chapter 6: The local and average structures and magnetic properties of Sr_2FeMnO_{5+y}, y = 0.0, 0.5. Comparisons with Ca_2FeMnO_5 and the Effect of the A-site Cation.

Chapter 7: The effect of B site cation on crystal and magnetic structures of $Sr_2Fe_{1.9}M_{0.1}O_{5+y}$ (M=Mn, Cr, Co; y= 0, 0.5)

Chapter 8: A Vacancy-Disorder Oxygen-Deficient Perovskite with Long Range Magnetic Ordering: Local and Average Structures and Magnetic Properties of $Sr_2Fe_{1.5}Cr_{0.5}O_5$

List of Tables

Chapter 3: Synthesis, Crystal Structure and magnetic properties of a new pillared perovskite $La_5Mo_{2.75}V_{1.25}O_{16}$

Chapter 4: Crystal and Magnetic Structures of the Brownmillerite Compound $Ca_2Fe_{1.039(8)}Mn_{0.962(8)}O_5$

Chapter 5: Intra-layer Cation Ordering in a Brownmillerite Super-Structure: Synthesis, Crystal and Magnetic Structures of Ca_2FeCoO_5

Chapter 6: The local and average structures and magnetic properties of Sr_2FeMnO_{5+y}, y = 0.0, 0.5. Comparisons with Ca_2FeMnO_5 and the Effect of the A-site Cation.

Chapter 7: The effect of B site cation on crystal and magnetic structures of $Sr_2Fe_{1.9}M_{0.1}O_{5+y}$ (M=Mn, Cr, Co; y= 0, 0.5)

Chapter 8: A Vacancy-Disorder Oxygen-Deficient Perovskite with Long Range Magnetic Ordering: Local and Average Structures and Magnetic Properties of $Sr_2Fe_{1.5}Cr_{0.5}O_5$

Chapter 9: Conclusion

Chapter 1

Introduction

This chapter presents a short introduction on the theory of magnetism and a review of the concept of diffraction by introducing Bragg’s law, the reciprocal lattice and Ewald’s sphere. In addition, an introduction on the structure and magnetism of pillared perovskites and brownmillerites is provided.

1.1. Basics of Magnetism

Paramagnetism

Paramagnetism arises in materials containing atoms (or ions) with unpaired electrons where electron spins on different atoms do not interact with each other. Therefore, no net magnetic moment is observed in a paramagnet. However, there is a magnetic moment associated with each atom as a result of the orbital and spin angular momenta of electrons [1].

For N non-interacting atoms (N is Avogadro's number) one can derive the mean magnetic moment using statistical methods [2] to get:

$$\mu = \mathrm{N}\mathrm{g}_{\mathrm{s}}\mathrm{S}\mathrm{B}_{\mathrm{s}}(\eta)\mu_{\mathrm{B}} \quad (g_S = 2.0023 \approx 2) \qquad (1.1.1)$$

$$\mu = \mathrm{N}\mathrm{g}_{\mathrm{J}}\mathrm{J}\mathrm{B}_{\mathrm{J}}(\eta)\mu_{\mathrm{B}} \qquad (1.1.2)$$

Note that for d-elements the orbital angular momentum is frequently quenched, and so the magnetic moment can be expressed only in terms of spin angular momentum. Therefore, (1.1.1) describes d-elements, while (1.1.2) is for f-group elements.

N is Avogadro's number. g is Landé splitting factor, and has a value of ~2 for d-group elements, while for f-elements it is described by g_J=3/2 + [S(S+1) – L(L+1)]/2J(J+1). The function $\mathrm{B}_{\mathrm{J}}(\eta)$ is called Brillouin function, $\mathrm{B}_{\mathrm{J}}(\eta) = \frac{1}{\mathrm{J}}[\left(\mathrm{J}+\frac{1}{2}\right)\coth\left(\mathrm{J}+\frac{1}{2}\right)\eta - \frac{1}{2}\coth\frac{\eta}{2}]$ with argument, η, which is the ratio of magnetic energy to thermal energy, $\eta = \mathrm{g}\mathrm{H}\mu_{\mathrm{B}}/\mathrm{k}_{\mathrm{B}}\mathrm{T}$, where H is magnetic field, T is temperature and k_B is Boltzmann's constant. Therefore, it can be seen that magnetic moment is a function of η. At $\eta \ll 1$, which is the case of high temperature or low field, and by using the concept of susceptibility that is the ratio of the moment to the field and will be discussed in the next section, one can define a quantity called the effective magnetic moment, that is shown by

$$\mu_{\mathrm{eff}} = [4S(S+1)]^{1/2}\mu_B \tag{1.1.3}$$

or

$$\mu_{\mathrm{eff}} = \mathrm{g_J}[\mathrm{J}(\mathrm{J}+1)]^{1/2}\mu_B \tag{1.1.4}$$

S is the spin angular momentum quantum number, J is total angular momentum quantum number when the spin-orbit coupling is taken into account, and g_J is Landé splitting factor that was previously introduced.

When $\eta \gg 1$, which is the case of low temperature or high field, the magnetic moment is called saturation moment, μ_{sat}, and is given by

$$\mu_{\mathrm{sat}} = \mathrm{g_s S}\mu_B \tag{1.1.5}$$

Or

$$\mu_{\mathrm{sat}} = \mathrm{g_J J}\mu_B \tag{1.1.6}$$

These moments are per mole, so Avogadro’s number, N, cancels.

Therefore, at high temperature the effective moment, and at low temperature the saturation moment is valid.

Magnetic susceptibility

When materials are placed in a magnetic field, the total flux inside the matter, B, will be different from the flux of the applied magnetic field, H. This is shown by the following equation [3]:

$$B = H + 4\pi I \qquad (1.1.7)$$

where I is the induced flux or magnetization. This equation can be further simplified as

$$B/H = 1 + 4\pi I/H \qquad (1.1.8)$$

B/H is called permeability, and I/H is called susceptibility. Further modification of this equation can be performed to accommodate the molar susceptibility, χ_M.

$$B/H = 1 + 4\pi\,(d/M_m)\,\chi_M \qquad (1.1.9)$$

where d is density and M_m is the molar mass.

The induced magnetization in a paramagnetic material is positive, and therefore the total flux inside the material is greater than the applied flux, and the applied flux is attracted by the material. In a diamagnet however, the induced magnetization is negative, and the flux is repelled by the material.

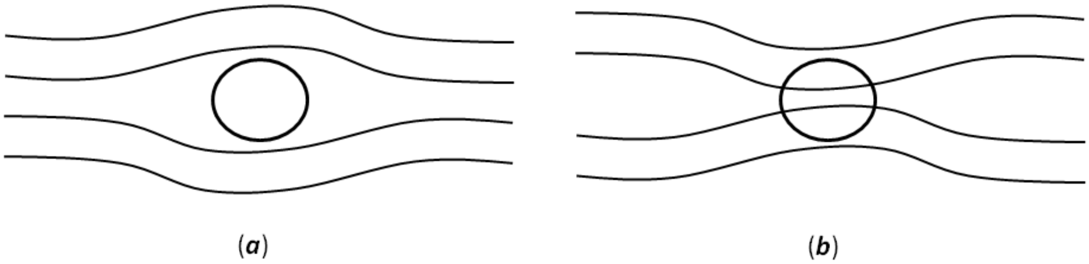

Figure 1.1.1. (a) a diamagnet in the magnetic field. The magnetic flux is repelled by the matter. (b) A paramagnetic material attracts magnetic flux.

The positive susceptibility induced in a paramagnet is generally temperature dependent, while the negative diamagnetic induced susceptibility is temperature independent. Note that diamagnetic susceptibility occurs in all materials due to the presence of paired electrons in core orbitals. However, its magnitude is about 100 times smaller than the paramagnetic susceptibility, so for many materials it can be practically neglected.

In a semi-classical description, the diamagnetic susceptibility arises from the precession (called Larmor's precession) of the orbital angular momentum around the axis parallel to the direction of the applied field. The magnitude of the diamagnetic susceptibility depends on the atomic number (i.e. number of electrons) and the atomic radius.

The paramagnetic susceptibility can be described based on the distribution of magnetic moments over the accessible magnetic states, according to the Boltzmann distribution. This description can be shown as the following equation called van Vleck equation [3].

$$\chi = \frac{N \sum_i \left(\frac{E_i^{(1)^2}}{kT} - 2E_i^{(2)} \right) \exp(-\frac{E_i^0}{kT})}{\sum_i \exp(-\frac{E_i^0}{kT})} \tag{1.1.10}$$

where E_i^0 is the unperturbed energy in the absence of the external field, and $E_i^{(1)}$ and $E_i^{(2)}$ are the first and second order Zeeman energies that show the perturbation of states due the presence of the field.

This equation can be modified to simpler forms depending on the condition. Here are different conditions that may occur:

(a) When there is a well defined ground state, $E_i^0 = 0$, which is degenerate, and no excited states are present, i.e. $E_i^{(2)} = 0$, then the van Vleck equation, is simplified to

$$\chi = \frac{N \sum_i \frac{E_i^{(1)^2}}{kT}}{n} = \frac{C}{T} \tag{1.1.11}$$

which is the Curie law for the high temperature case, where there is no interaction between the moments, as expected in an ideal paramagnet. This is the case for half filled shells $3d^5$ and $4f^7$.

(b) When there is a singlet ground state, $E_i^0 = 0$, and the excited states, $E_i^{(2)}$ separated from the ground state by >>kT, are present, then we get

$$\chi = \mathrm{N} \sum_i -2\mathrm{E}_i^{(2)} = \mathrm{N}\alpha \qquad (1.1.12)$$

As seen here the susceptibility becomes temperature independent. This applies to d^0 or low spin d^6 cases.

(c) When there is a degenerate ground state, and the excited states separated from the ground state by >>kT are present, the susceptibility will be a combination of the two cases above.

$$\chi = \frac{\mathrm{C}}{\mathrm{T}} + \mathrm{N}\alpha \qquad (1.1.13)$$

Often the magnetic moments on the atoms in paramagnetic systems are not ideally isolated from each other and there are interactions between them. To take into account these interactions, the above susceptibility expressions are modified to the following forms:

$$\chi = \frac{\mathrm{C}}{\mathrm{T}-\theta} \qquad (1.1.14)$$

and

$$\chi = \frac{\mathrm{C}}{\mathrm{T}-\theta} + \mathrm{N}\alpha \qquad (1.1.15)$$

θ is called Weiss temperature, and will be shown later to be related to the interactions between individual atomic magnetic moments, equation 1.1.20.

The Curie constant, C, is related to the effective magnetic moment in the following way:

$$8\mathrm{C} = \mu_{\mathrm{eff}}^{2} \qquad (1.1.16)$$

For the μ_{eff} of equation (1.1.3), this will give

$$\mathrm{C} = \frac{[(4\mathrm{S}(\mathrm{S}+1))^{1/2}]^{2}}{8} = \frac{\mathrm{S}(\mathrm{S}+1)}{2} \qquad (1.1.17)$$

Susceptibility, χ, and Curie constant, C, are calculated for individual atoms, but the values obtained for the atoms in a system can be directly added together, i.e. $\mathrm{C}_{\mathrm{total}} = \sum_{\mathrm{i}} \mathrm{C}_{\mathrm{i}}$ and $\chi_{\mathrm{total}} = \sum_{\mathrm{i}} \chi_{\mathrm{i}}$, but this is not the case for μ_{eff} of the individual atoms. The μ_{eff} values are additive in the following way: $\mu_{\mathrm{eff}_{\mathrm{total}}} = [\sum_{\mathrm{i}} \mu_{\mathrm{eff}_{\mathrm{i}}}{}^{2}]^{1/2}$

Note that μ_{eff} is the magnetic moment of an atom at high temperature and low field, and therefore, finding the Curie constant through magnetic moment measurement is only possible at high temperature and low field.

Interactions between magnetic moments in oxides

As discussed above, in an ideal paramagnet magnetic moments on different atoms do not interact with each other. However, interactions between moments are commonly observed in different materials. Here the discussion will focus on transition metal oxides where orbital angular momentum is quenched, and spin angular momentum is the major factor that determines the moment. Therefore, the interactions between magnetic moments can be discussed in terms of interactions between spins on different atoms. These interactions (or couplings) can result in particular alignments of spins, as opposed to random orientation in a paramagnet. Therefore, the well known ordered states occur: ferromagnetism where spins are aligned parallel and in the same direction, antiferromagnetism where spins are aligned parallel but point in opposite directions (anti-parallel), and ferrimagnetism where spins are anti-parallel but do not completely cancel each other. The latter can happen as a result of coupling between atoms with different spin moments. If the ordering of spins is restricted to a limited length scale, then short range ordering occurs. However, if the length scale of spin order is effectively infinite, long range ordering is obtained. The ordered systems can be achieved by cooling a paramagnet below a certain temperature called the critical temperature.

The interactions between magnetic moments can be described by a mechanism called superexchange [4-6]. This name is adopted due to the fact that magnetic atoms are usually separated by ligands (oxide ions) and the distances between them are usually larger than the sum of their ionic radii. In this mechanism, the ligand has a bridging effect that helps align the spins of the two magnetic atoms either parallel or anti-parallel relative to each other. This process has been described for cases where the metal–O–metal angles are 90° and 180° [4,7]. The mechanism assumes transfer of one electron from the ligand's orbital to each metal. Figure 1.1.2 illustrates this process for two metal ions with d^3 configuration and metal–O–metal angle of 180°. If the line connecting the nuclei is assumed to be along z, then there is σ-overlap between the p_z orbital of the ligand and d_{z^2} of the metal atoms. Note that the oxide ion is diamagnetic. Now, if an electron is transferred from p_z to d_{z^2}, according to Hund's rule the electron in d_{z^2} has to have the same spin orientation as the electrons in the t_{2g} orbitals. Similarly, the second electron from p_z can also be transferred to d_{z^2} of the other metal, and its spin has to be parallel to the electrons of t_{2g} orbitals. Noting that the spin orientation does not change during the transfer, the unpaired t_{2g} electrons on the second metal atom have to be anti-parallel to those on the first metal atom. Therefore, the coupling between the two metals will be antiferromagnetic.

A similar process can happen for the π-overlap between metals' t_{2g} orbitals and p_x or p_y of the ligand. However, these interactions are weaker than the σ-interactions. The case of 90° angle is more complicated, as it is not possible for the same p orbital of the ligand to overlap with both metal atoms. Therefore d_{z^2} orbital of one metal atom interacts with ligand's p_x orbital, and $d_{x^2-y^2}$orbital of the other metal atom interacts with ligand's p_y orbital.

Another mechanism proposed for exchange interactions is called double exchange [8,9], which is especially useful for describing interactions between cations with different oxidation states of the same element, such as Mn^{3+} and Mn^{4+}. This mechanism involves transfer of an electron from the less-oxidized cation to the ligand, and transfer of an electron from ligand to the more oxidized cation. Therefore, the overall process appears as an electron transfer from the less-oxidized to the more oxidized cation. For cases such as Mn^{3+} /Mn^{4+} the coupling is ferromagnetic, as required by Hund's rule.

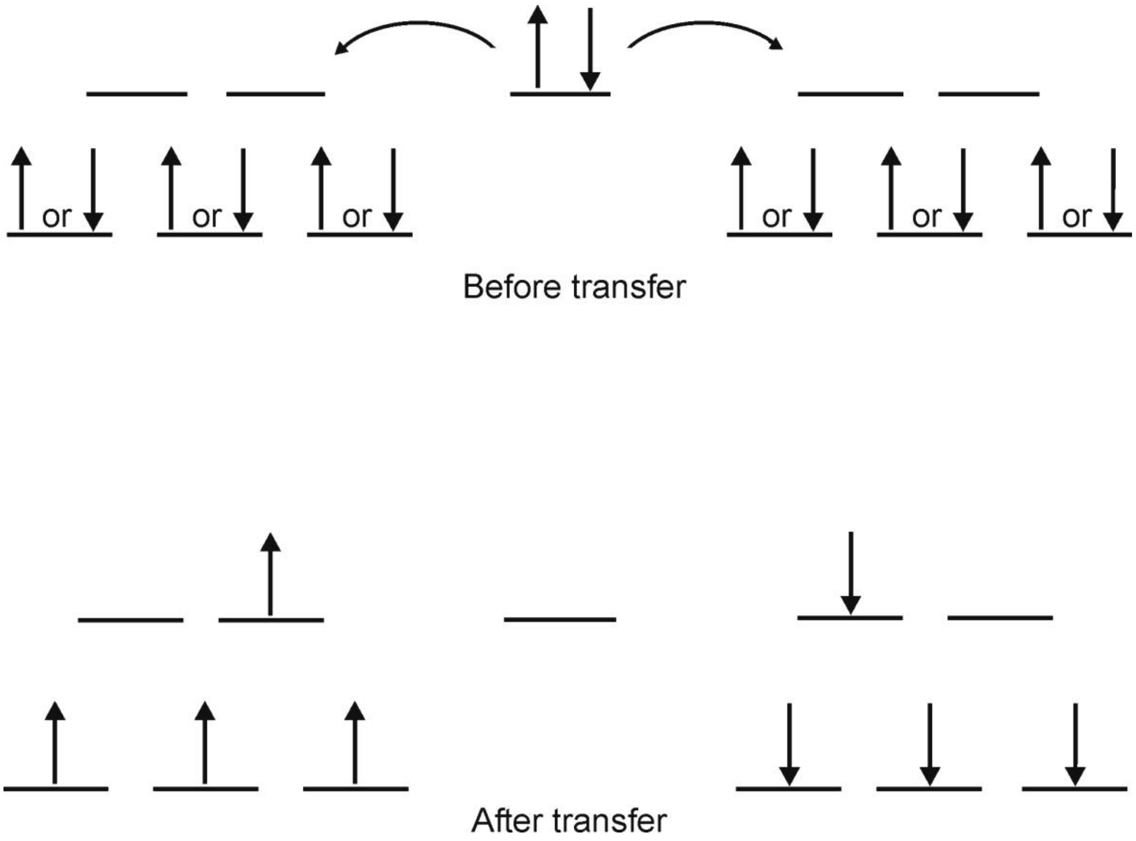

Figure 1.1.2. A schematic representation of superexchange process for $Cr^{3+}(d^3)$ –O–$Cr^{3+}(d^3)$, in linear arrangement.

Now, to give a quantitative description of spin interactions, the following Hamiltonian [10] can be used:

$$H = -2J_{ij} \sum_{ij} S_i S_j \tag{1.1.18}$$

where S_i and S_j are spin operators for the two interacting atoms, and J_{ij} is a scalar called exchange constant. Note that this Hamiltonian may sometimes appear without the negative sign. For the above sign convention (with the minus sign), $J<0$ will indicates antiferromagnetic and $J>0$ shows ferromagnetic interactions.

A perturbation theory can be used [6] to describe the exchange constant J_{ij} using an electron transfer integral e_{ij}:

$$J_{ij} = -2\frac{e_{ij}^2}{U} \tag{1.1.19}$$

U is the correlation energy that refers to the repulsion between electrons when an electron is transferred to a half-filled orbital.

The exchange constant, J, is also related to the Weiss temperature, θ, in the Curie-Weiss law, χ=C/T–θ. As stated before, θ is indicative of magnetic interactions that result in deviations from Curie law, χ=C/T. To show the relationship between θ and J, one can use mean-field (or molecular) theory [1,2], which suggests the presence of an internal field on each atom caused by the magnetic moments of the neighboring atoms, in addition to the externally applied field. Using this theory, one can show that

$$\theta = \frac{2S(S+1)}{3k_B}\sum_{n=1}^{N} Z_n J_n \tag{1.1.20}$$

where S is the total spin quantum number, k_B is Boltzmann's constant, Z_n is the number of *n*th nearest neighbors (1st nearest neighbors, etc.) and N is the number of sets of nearest neighbors that have $J_n \neq 0$. The above expression shows the significance of θ, as it is directly related to the weighted algebraic sum of all magnetic interactions for an atom, and the spins of the atom. $\theta < 0$ indicates antiferromagnetic and $\theta > 0$ shows ferromagnetic interactions.

To describe one or two dimensional magnetic interactions [10], an expanded form of (1-18) can be used

$$H = -2\sum_{ij}(J_{xx}S_{xi}S_{xj} + J_{yy}S_{yi}S_{yj} + J_{zz}S_{zi}S_{zj}) \qquad (1.1.21)$$

If J_{xx}~J_{yy}<< J_{zz}, the spin dimensionality is said to be one, and it is called the Ising model. If J_{zz}<<J_{xx}~J_{yy}, the spin dimensionality is two and it is called the XY model. Finally if J_{xx}~J_{yy}~J_{zz}, spin dimensionality is three, and it is called the Heisenberg model.

Note that all of the above spin dimensionalities, d, can result in long range magnetic ordering in a three dimensional crystal lattice. However, if the lattice (spatial) dimensionality, D, is one or two, mostly short range ordering occurs, except for the case of D=2 and d=1 [11].

1.2. Basics of Diffraction

Diffraction and Bragg's Law

One of the methods of obtaining information about the arrangement of atoms in a material is diffraction. This involves scattering of a beam of x-rays, neutrons or electrons by atoms that are organized in a periodic arrangement in the system, i.e. a crystal lattice. The common diffraction techniques include application of electron, x-ray or neutron beams. The latter two were used in structural studies of the materials in this thesis. A common feature for all diffraction methods is that observation of the diffracted beam is possible only when a certain criterion is satisfied. This condition is described by Bragg's law (equation 1.2.1) that uses the concept of imaginary parallel planes that are located at equal distances, d, from each other. These planes include atoms of the crystal lattice. There can be a number of sets of planes in each crystal system, running in different directions, and they are named according to their interception with the axes of the unit cell, the smallest repeated unit in the crystal system. For example in a simple cubic system, a set of planes labeled (2 0 0) are parallel to the *bc*-plane. They do not intercept with *b* and *c* axes, but divide the *a*-axis in 2. The labels are called *hkl*, Miller indices.

The interaction of the beam with the crystal system is described by its reflection by these planes. As seen in Figure 1.2.1, the lower incident beam travels a longer distance compared to the upper beam. Similarly the reflected lower beam will travel longer to exit the material. A constructive interference between the diffracted beams, to generate a diffraction peak, will be possible only if the total difference between the traveled distances is equal to $n\lambda$: AB+BC = $n\lambda$, where n is an integer, and λ is the wavelength. Note that AB = BC = $d\sin\theta$, and therefore:

$$2d\sin\theta = n\lambda \tag{1.2.1}$$

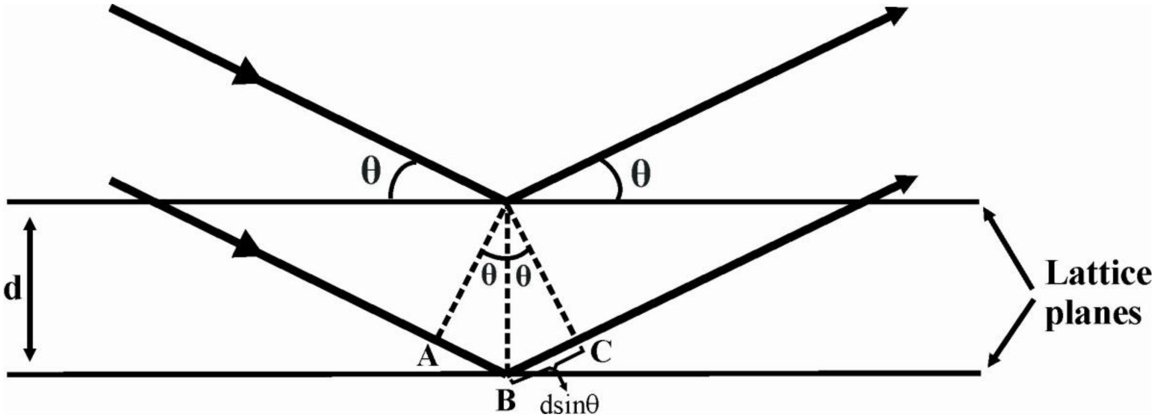

Figure 1.2.1. A graphical illustration of Bragg's law, $2d\sin\theta = n\lambda$.

This is the Bragg's law that sets the condition for diffraction peaks to be observed, as the diffracted beams that do not follow this law will interfere destructively. The diffraction data are commonly illustrated as a function of 2θ. One obvious consequence of Bragg's law is that the diffraction peak corresponding to the largest *d* spacing will appear at lowest 2θ.

Reciprocal Lattice

One approach to visualize the diffraction process, involves the concept of the reciprocal lattice [12]. One can define a^*, b^* and c^* as reciprocal lattice axes by formulae (1.2.2) to (1.2.4). Note that dot product of two vectors equals a scalar which is the product of the absolute values of the two vectors and the cosine of the angle between them.

On the contrary, the cross product of two vectors is a vector, whose magnitude is equal to the product of the absolute values of the two vectors and the sine of the angle between them. In other words the length of this vector is equal to the area of the parallelogram made by the two original vectors. The direction of this vector will be perpendicular to the plane of the original two vectors.

$$\overrightarrow{a^*} = \frac{1}{V}\,(\vec{b} \times \vec{c}) \qquad (1.2.2)$$

$$\overrightarrow{b^*} = \frac{1}{V}\,(\vec{a} \times \vec{c}) \qquad (1.2.3)$$

$$\overrightarrow{c^*} = \frac{1}{V}\,(\vec{a} \times \vec{b}) \qquad (1.2.4)$$

Note that if the lattice is orthogonal, then these equations simplify to $\overrightarrow{a^*}=1/\vec{a}$, $\overrightarrow{b^*}=1/\vec{b}$ and $\overrightarrow{c^*}=1/\vec{c}$.

Since a^* is perpendicular to the *bc* plane, while b^* is perpendicular to the *ac* plane, and c^* is perpendicular to the *ab* plane,

$$a^*.b = a^*.c = b^*.a = b^*.c = c^*.a = c^*.b = 0 \qquad (1.2.5)$$

and

$$a^*.a = b^*.b = c^*.c = 1 \qquad (1.2.6)$$

Similarly, one can introduce a vector d^*, which is perpendicular to the corresponding set of real space *hkl* planes, and its length is proportional to $1/d$.

$$|d^*_{hkl}| = \frac{1}{d_{hkl}} \qquad (1.2.7)$$

Therefore each set of crystallographic planes can be represented in reciprocal space by a d^* vector, or by a point at the end of that vector [12]. In Figure 1.2.2, this is represented in a two-dimensional lattice.

The reciprocal lattice has the same symmetry as the real space lattice.

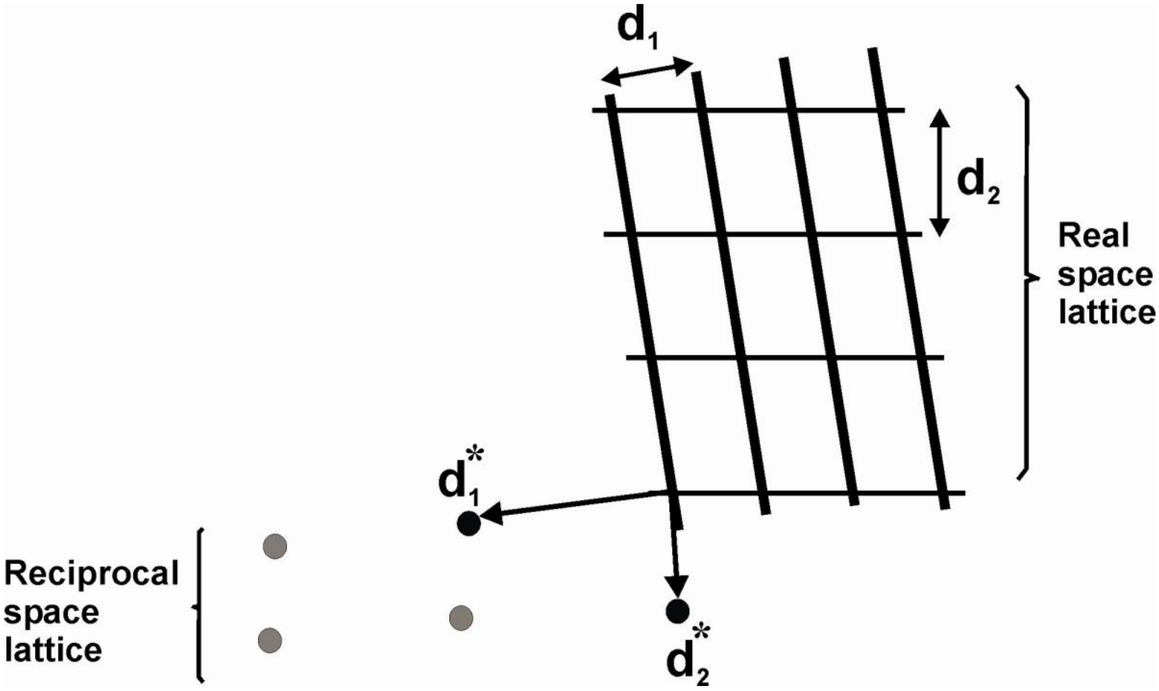

Figure 1.2.2. Schematic representation of the reciprocal lattice. Note that each set of planes in the real space lattice is represented by one point at the end of a d* vector. Two sets of planes d_1, d_2 and their corresponding reciprocal lattice pints are shown. The other points in the reciprocal lattice correspond to other sets of planes.

Ewald's Sphere

If one considers an incident beam with propagation vector $\vec{k}$ and wavelength λ, and also chooses the length of $\vec{k}$ to be 1/λ, upon an elastic scattering event, the scattered wave vector, $\vec{k'}$, will have the same length, i.e. $|k|=|k'|=1/\lambda$. The angle between $\vec{k}$ and $\vec{k'}$ is 2θ. Now, if one overlaps these two vectors with a reciprocal lattice, so that the end of k falls at the origin of the reciprocal lattice, then as shown by Ewald, diffraction can happen only if the end of $\overrightarrow{k'}$ coincides with a lattice point. This gives a diffraction peak corresponding to that lattice point that is in fact the end point of a *d** vector. Therefore, this will be diffraction corresponding to an *hkl* set of planes represented by that $\overrightarrow{d^*}$ vector. Considering that $\vec{k}$ and $\overrightarrow{k'}$ are equal, all possible directions of $\overrightarrow{k'}$, i.e. all possible incident angles, will result in a sphere in 3-dimension. The surface of the sphere will represent all possible endings of $\overrightarrow{k'}$ vector in different directions, as the end of $\vec{k}$ vector is fixed at the origin of the reciprocal lattice. Consequently, any lattice point that coincides with the surface of this sphere can give a diffraction peak.

This sphere is called the Ewald's sphere. In Figure 1.2.3, a two dimensional profile of this sphere is shown.

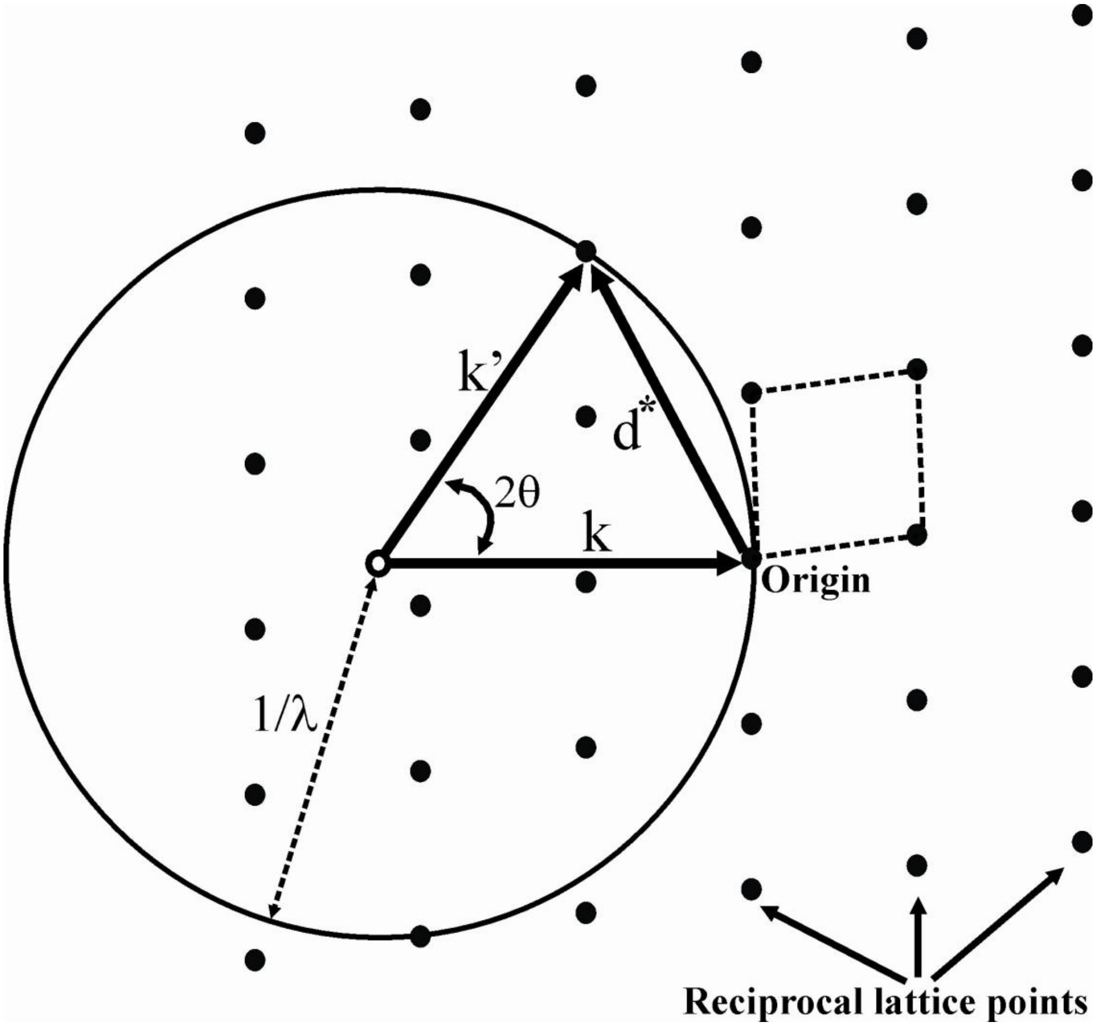

Figure 1.2.3. Construction of the Ewald's sphere (which appears as a circle in this two-dimensional representation).

Using simple geometry from Figure 1.2.3, one can now derive the Bragg's law. Note that

$$sin\theta = \frac{d^*/2}{\mathrm{k}} = \frac{d^*/2}{\mathrm{k}'} \qquad (1.2.8)$$

Recalling that $|d^*|=1/d$, and choosing $\mathrm{k}=\mathrm{k}'=1/\lambda$, one can conclude:

$$(1/\lambda)\sin\theta = (1/\lambda)\sin\theta = 1/2d \qquad (1.2.9)$$

that gives the Bragg's law: $2d\sin\theta = \lambda$

Note that in actual experiments the sample is rotated to ensure that a large number of reciprocal lattice points will coincide with the surface of Ewald's Sphere.

Ewald's Sphere in Powder Diffraction

The above discussion was for diffraction from a single crystal. The situation is somewhat different in diffraction from powder or polycrystalline materials, where a large number of crystals oriented randomly participate in the process. As a result, a large number of identical d^* vectors will exist that generate a circle on the surface of the Ewald's sphere, and perpendicular to the incident wave vector. Corresponding to these d^* vectors, there will be a large number of scattered wave vectors, k′, that make a cone-shape arrangement. If the number of diffracting crystals is infinite, then the intensity of the diffraction will be the same around the circumference of the cone base, or the ring formed on the detector. Therefore the final detected outcome will be a set of rings with different diameters (Figure 1.2.4), each corresponding to one d^* (and in fact to the corresponding *hkl* set of planes in real space). Assuming a uniform distribution of intensity around each ring, measuring only a narrow portion of the rings, shown by a rectangle in Figure 1.2.4, gives enough information about the diffraction.

In diffraction data, the intensity is usually presented as a function of the Bragg angle, 2θ, and occasionally *d*-spacing, or Q, which is the scattering wave vector where $Q = 4\pi\sin\theta/\lambda = 2\pi/d$.

Note that in the above discussions the reciprocal lattice points were assumed to be ideal zero-dimensional points, while in practice they are diffuse spheres, partly due to the wavelength variation. This means the Ewald's sphere has a thickness, and that's why diffraction peaks are never infinitely narrow [12].

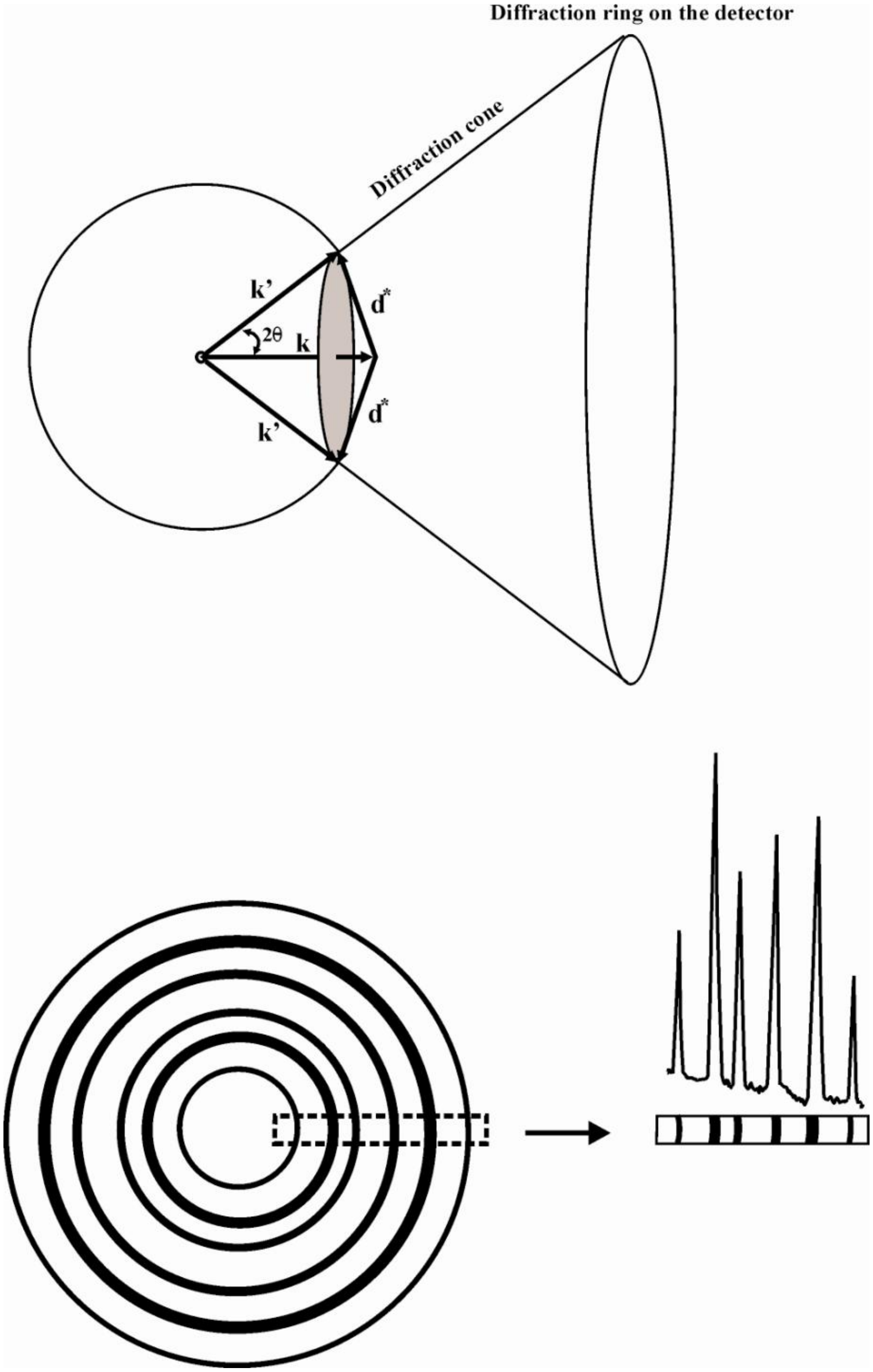

Figure 1.2.4. Diffraction by a powder sample. Assuming random orientation of crystals in a polycrystalline sample, the scattering process results in formation of rings on the detector.

1.3. Structure and magnetism of pillared perovskites and brownmillerites

The general formula for perovskites is ABO_3, where B cations are octahedrally coordinated by oxygens, and A is a large cation usually from the rare-earth or alkaline-earth group, residing within the interstitial spaces between the BO_6 octahedra. Each BO_6 octahedron shares all of its corners with other octahedra, forming a three dimensional network of corner sharing octahedra. There are different structure types derived from perovskites such as those discussed in this thesis, pillared perovskites, disordered-oxygen-deficient-perovskites and brownmillerites.

Pillared perovskites

Pillared perovskites have a general formula $A_5B_2MM'O_{16}$ (A=La; B=Mo^{4+}, Re^{5+}, Os^{5+} ; M = Mo^{5+}, Re^{5+}, Os^{5+}, Ta^{5+}, V^{4+}; M' = Mo^{4+}, Mg^{2+}, Mn^{2+}, Fe^{2+}, Co^{2+}, Ni^{2+}, V^{4+}) [13-19]. The B, M and M' cations are octahedrally coordinated. The crystal structure consists of layers of corner-sharing MO_6 and $M'O_6$ octahedra, so that each MO_6 has only $M'O_6$ neighbors and vice-versa (Figure 1.3.1). These layers are separated from each other by dimeric (pillaring) units of edge-sharing BO_6 octahedra. Each BO_6 octahedron also shares one corner with an $M'O_6$ octahedron. Therefore, MO_6 and $M'O_6$ octahedra are different in that MO_6 shares only four equatorial corners and not the apical corners, while $M'O_6$ has all of its corners shared.

While some perovskite related structure types have been extensively studied, there are only a small number of pillared perovskites known to date, partly due to the difficulties associated with the synthesis of these materials. $La_5Mo_4O_{16}$ [13, 14], synthesized using an electrolysis method, was the first material reported to have this structure type. Several years later $La_5Re_3MO_{16}$ (M=Mn, Mg, Fe, Co, Ni), $La_5Mo_{4-x}M_xO_{16}$ (M=Mn, Mg, Fe, Co and x~0.75) and $La_5Os_3MnO_{16}$ were reported [15 - 18]. The most recent member of this family [19] is $La_5Mo_{2.75}V_{1.25}O_{16}$ that will be discussed in this thesis.

Pillared perovskites exhibit interesting magnetic properties. The edge-sharing dimeric units incorporate short distances between the metal centers, and multiple metal-metal bonds seem to occur within these dimers, making them diamagnetic. While, the separations between the layers in these materials are ~10Å, the inter-layer magnetic interactions are present and long range three-dimensional magnetic ordering has been observed with antiparallel alignment of moments within the corner-sharing octahedral layers, and also between the layers [15, 17-24].

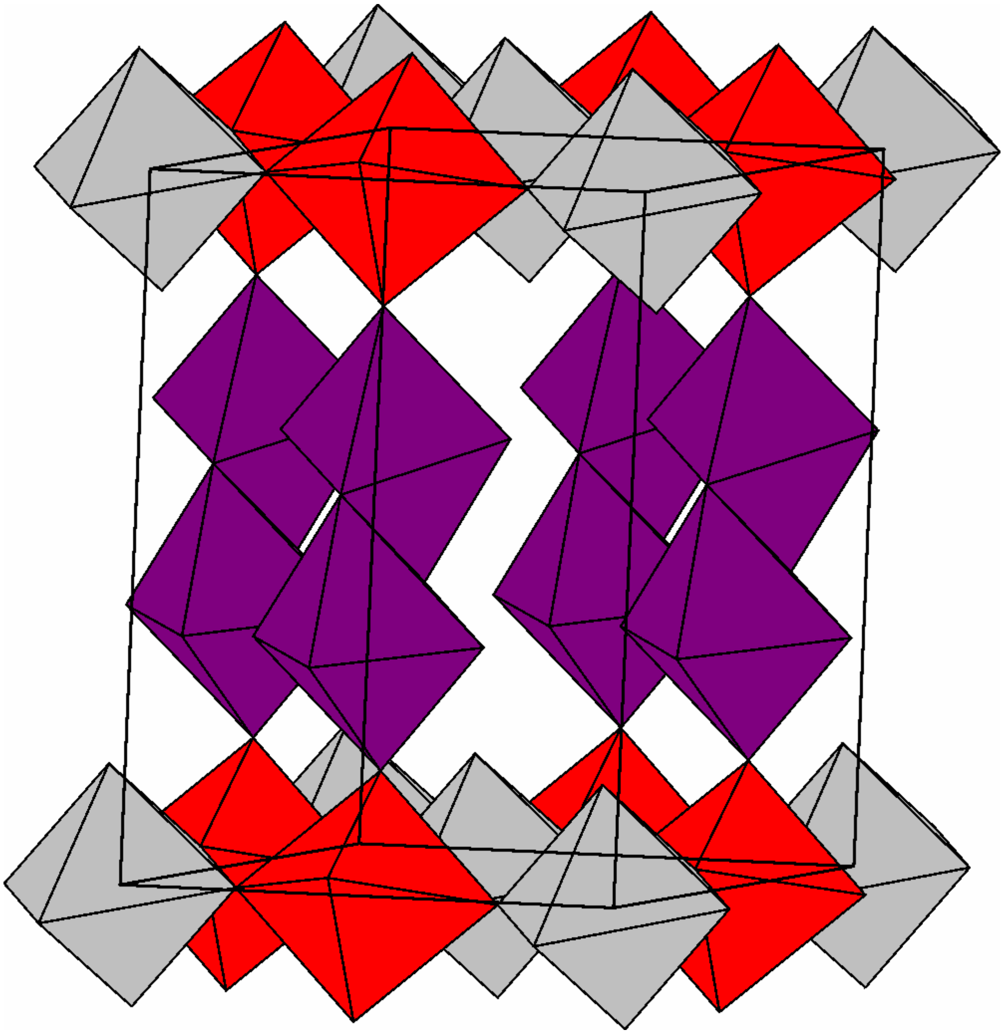

Figure 1.3.1. Pillared perovskite structure, $A_5B_2MM'O_{16}$. The layers of corner-sharing MO_6 (grey) and $M'O_6$ (red) octahedra are separated by dimeric units of edge-sharing BO_6 octahedra (purple). Note that the edge-sharing dimeric units (purple) are only attached to $M'O_6$ octahedra (red).

Oxygen-deficient-perovskite and brownmillerites

It is possible to synthesize materials from the perovskite family with smaller oxygen content, ABO_{3-y}. Therefore, some of the sites previously occupied by oxygens will be vacant. These oxygen vacancies may be distributed randomly throughout the structure to form a disordered perovskite structure, or they may order. One possible ordering is the distribution of oxygen vacancies in a way to form layers of octahedrally coordinated B-cations separated by chains of tetrahedrally coordinated B'-cations. This is called the brownmillerite structure (Figure 1.3.2). Within the octahedral layer, each octahedron shares four equatorial corners with other octahedra, while the two axial corners are shared with two tetrahedra above and below. The brownmillerite unit cell is nearly eight times larger than that of a simple perovskite and the cell parameters are related in the following way: $a_b \approx \sqrt{2}a_p, b_b \approx 4a_p, c_b \approx \sqrt{2}a_p$.

The space groups of brownmillerites are determined by the relative orientations of the tetrahedral chains [25-27]. These chains can have two possible orientations that are arbitrarily called right handed (R) and left handed (L). If all tetrahedral chains are oriented in the same way, the resulting space group will be *I2mb* (*Ibm2* and *Ima2* are the other settings of this space group, commonly used for brownmillerites). Note that the tetrahedral chains are located beside each other in layers sandwiched between the octahedral layers. If all chains within one layer have the same orientation, but opposite to the neighboring layer, the *Pnma* space group is obtained. There is also a rare type of chain ordering that involves alternating orientations of chains within each layer and between the layers. This type of ordering results in the *C2/c* or *Pcmb* (*Pbcm*) space groups, and has been observed only for $La_{1-x}A_xMnO_{2.5}$ (x=0.2 - 0.4 for A= Sr, Ba and x=0.2 - 0.3 for A=Ca,) [25]. Ca_2FeCoO_5, that will be discussed in this thesis, has this type of ordering as well [28]. Finally if the tetrahedral chains have random orientations, the space group will be *Imma* (*Icmm*). While different settings of these space groups have been used, the notations, *I2mb, Pnma, Pcmb,* and *Imma* refer to a setting with $b > c > a$. Attempts have been made to explain the occurrence of different space groups in terms of minimization of the chain dipole moments, resulting from deviation of the chains from linearity [25, 29, 30]. Therefore, the long-range orientations of tetrahedral chains (and hence the space groups) are suggested to depend on two parameters: the separation between the tetrahedral chains and the twisting angles within the chains.

The brownmillerite compounds containing magnetic ions usually undergo a transition to a long-range antiferromagnetic order of the G-type [31-41]. This ordering involves anti- parallel alignment of magnetic moments relative to all nearest neighbors (Figure 1.3.3). When both octahedral and tetrahedral sites contain magnetic ions, the octahedral sublattice alone usually contains antiferromagnetic intra-layer, but ferromagnetic inter-layer alignment of moments. The same situation applies to the tetrahedral sublattice [28, 39].

However, in some cases such as $Sr_2GaMnO_{5.0}$ [31], $SrCaMnGaO_{5+y}$ [32] and Ca_2MnAlO_5 [41], the magnetic ions are only located on one of the two sites. In these materials, Mn occupies the octahedral site, while Ga or Al resides on the tetrahedral site. Therefore, the magnetic moments are only present on the octahedral sites. These octahedral-moments have G-type antiferromagnetic orderings, i,e. intra- and inter-layer antiparallel alignment [32], in contrary to the octahedral-moments of materials that have magnetic ions on both octahedral and tetrahedral sites. This is remarkable because the separations between octahedral layers are ~8.10 Å, ~7.89Å and 7.48Å for $Sr_2GaMnO_{5.0}$ [31], $SrCaMnGaO_{5+y}$ [32] and Ca_2MnAlO_5 [41], respectively.

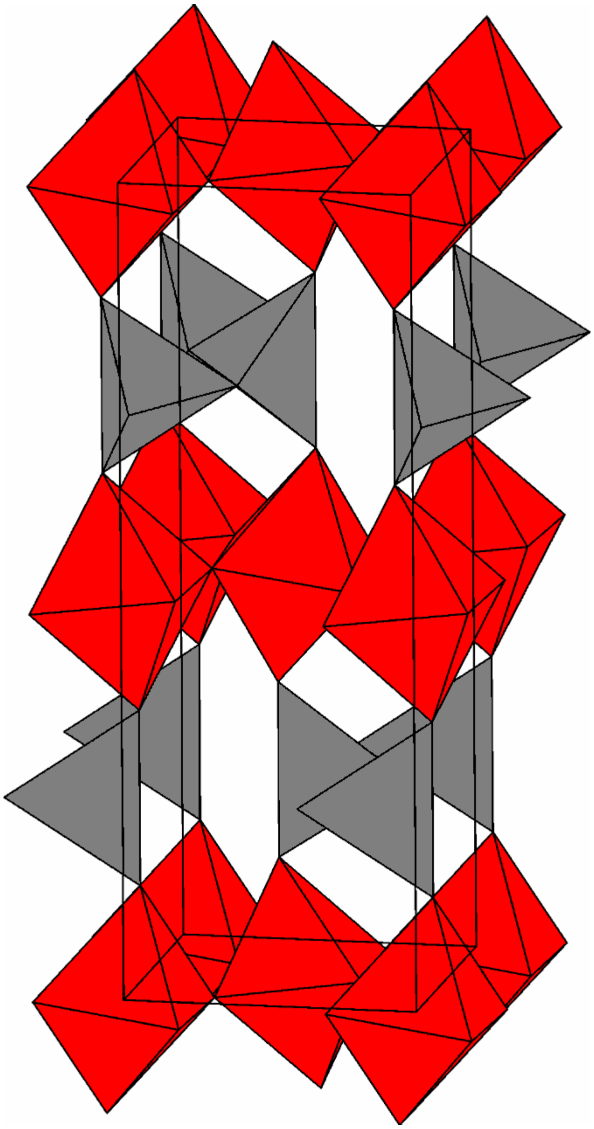

Figure 1.3.2. Brownmillerite structure. The layers of corner-sharing octahedra are separated by chains of corner-sharing tetrahedra.

In addition, the magnetic moment orientations for many brownmillerites, especially the Fe-based compounds, are along the shortest axis [33-38]. However, the Mn-based brownmillerites seem to prefer the longest axis, as observed in materials such as Sr_2GaMnO_5 [31], $SrCaMnGaO_{5+y}$ [32], Ca_2FeMnO_5 [39], Ca_2GaMnO_5 [40] and Ca_2MnAlO_5 [41].

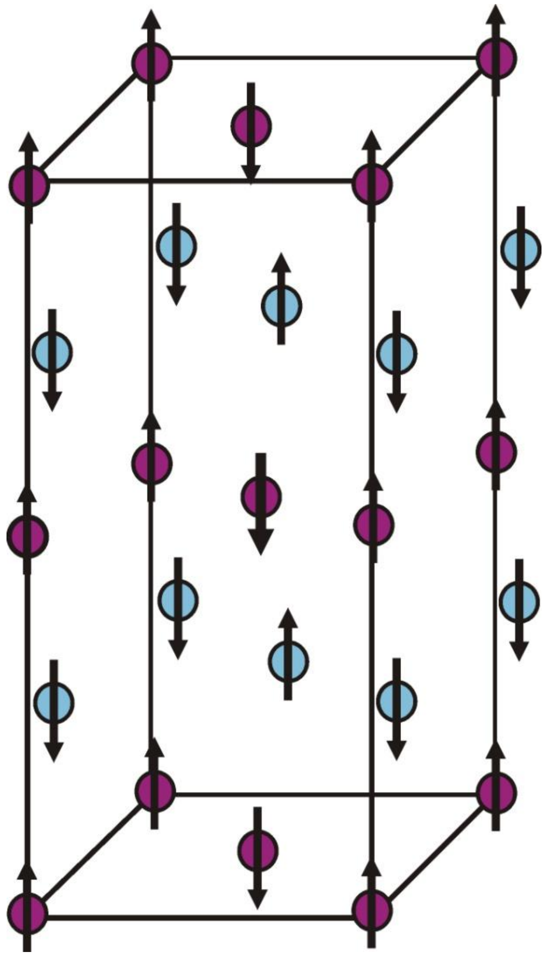

Figure 1.3.3. G-type magnetic structure. The moments on each site are oriented alti-parallel to all nearest neighbors.

References

[1] Smart, J. S. ‘Effective Field Theories of Magnetism’, Saunders, Philadelphia, PA, 1966

[2] Carlin, R. L., van Duyneveldt, A. J. ‘Magnetic Properties of TransitionMetal Compounds’, Springer-Verlag, NewYork, 1977.

[3] Mabbs, F. E., Machin, D. J. ‘Magnetism and Transition Metal Complexes’, Chapman & Hall, 1973.

[4] Goodenough, J. B. ‘Magnetism and the Chemical Bond’, Interscience, New York, 1963.

[5] Anderson, P. W. *Phys. Rev.* 79 (1950) 350.

[6] Anderson, P. W. *Phys. Rev.* 115 (1959) 2.

[7] Kanamori, J. *J. Phys. Chem. Solids* 10 (1959) 87.

[8] Zener, C. *Phys. Rev.* 81 (1951) 440.

[9] de Gennes, P. G. *Phys. Rev.* 118 (1960) 141.

[10] Greedan, J. E. ‘Magnetic Oxides’. Encyclopedia of Inorganic Chemistry. Wiley, 2006.

[11] Collins, M. F. ‘Magnetic Critical Scattering’, Oxford University Press, 1989.

[12] Pecharsky, V.; Zavalij, P. “Fundamentals of Powder Diffraction and Structural Characterization of Materials” Springer, New York, 2005.

[13] McCarroll, W. H.; Darling, C.; Jakubicki, G. *J. Solid State Chem. 48* (1983) 189.

[14] Ledesert, M.; Labbe, Ph.; McCarroll, W. H.; Leligny, H.; Raveau, B. *J. Solid State Chem. 105* (1993**)** 143.

[15] Wiebe, C.R.; Gourrier, A.; Langet, T.; Britten, J.F.; Greedan, J.E. *J. Solid State Chem. 151* (2000**)** 31.

[16] Ramanujachary, K.V.; Lofland, S.E.; McCarroll, W.H.; Emge, T.J.; Greenblatt, M. *J. Solid State Chem. 164* (2002) 70.

[17] Chi, L.; Green, A.E.C.; Hammond, R.; Wiebe, C.R.; Greedan, J.E. *J. Solid State Chem. 170* (2003) 165.

[18] Chi, L.; Swainson, I.P.; Greedan, J.E. *J. Solid State Chem. 177* (2004) 3086.

[19] Ramezanipour, F.; Derakhshan, S.; Greedan, J. E.; Cranswick, L.M.D. *J. Solid State Chem.* 181 (2008) 3366.

[20] Ramanujachary, K.V.; Greenblatt, M.; McCarroll, W.H.; Goodenough, J.B. *Mater. Res. Bull. 28* (1993) 1257.

[21] Green, A.E.C.; Wiebe, C.R.; Greedan, J.E. *Solid State Sci. 4* (2002) 305.

[22] Lofland, S.E.; Scabarozi, T.; Ramanujachary, K.V.; McCarroll, W.H. *J. Magn. Magn. Mater. 260* (2003) 184.

[23] Lofland, S.E.; Hattrick-Simpers, J.; Ramanujachary, K.V.; McCarroll, W.H. *J. Magn. Magn. Mater. 265* (**2**003) 113.

[24] Cuthbert, H.L.; Cranswick, L.; Greedan, J.E. *J. Solid State Chem. 179* (2006)1938.

[25] Parsons, T. G.; D'Hondt, H.; Hadermann, J.; Hayward, M. A. *Chem. Mater.* 21(2009) 5527.

[26] Greaves, C. ; Jacobson, A.J. ; Tofield, B.C. ; Fender, B.E.F. *Acta Crystallogr. B*31(1975) 641.

[27] Lambert, S. ; Leligny, H. ; Grebille, D. ; Pelloquin, D. ; Raveau, B. *Chem. Mater.* 14 (2002) 1818.

[28] Ramezanipour, F., Greedan, J. E., Grosvenor, A.P., Britten, J.F., Cranswick, L.M.D., Garlea, V.O. Chem. Mater. 22 (2010) 6008.

[29] Hadermann, J.; Abakumov, A. M.; D'Hondt, H.; Kalyuzhnaya, A. S.; Rozova, M. G.; Markina, M. M.; Mikheev, M. G.; Tristan, N.; Klingeler, R.; Büchnerd, B.; Antipov, E. V. *J. Mater. Chem.* 17 (2007) 692.

[30] Abakumov, A. M.; Kalyuzhnaya, A. S.; Rozova, M. G.; Antipov, E. V.; Hadermann, J.; Tendeloo, G. V. *Solid State Sci.* 7 (2005) 801.

[31] Sheptyakov, D.V.; Abakumov, A.M.; Antipov, E.V.; Balagurov, A.M.; Billinge, S.J.L.; Fischer, P.; Keller, L.; Lobanov, M.V.; Pavlyuk, B.Ph.; Pomjakushin, V.Yu.; Rozova, M.G. *Appl. Phys.* A 74 (2002) S1734

[32] Battle, P. D., Bell, A. M. T., Blundell, S. J., Coldea, A. I., Gallon, D. J., Pratt, F. L., Rosseinsky, M. J., Steer, C. A. J. *Solid State Chem.* 167 (2002) 188.

[33] Istomina, S.Y., Abdyushevab, S.V., Svenssonc, G., Antipov, E.V. *J. Solid State Chem.* 177 (2004) 4251.

[34] Takeda, T.; Yamaguchi, Y. ; Tomiyoshi, S. ; Fukase, M. ; Sugimoto, M. ; Watanabe, H. *J. Phys. Soc. Japan* 24 (1968) 446.

[35] Takeda, T. ; Yamaguchi, Y. ; Watanabe, H. ; Tomiyoshi, S. ; Yamamoto, H. *J. Phys. Soc. Japan* 26 (1969) 1320.

[36] Istomin, S. Ya. ; Abdyusheva, S. V. ; Svensson, G. ; Antipov, E. V. *J. Solid State Chem*. 177 (2004) 4251.

[37] Battle, P.D.; Bollen, S.K.; Gibb, T.C.; Matsuo, M. *J. Solid State Chem*. 90 (1991) 42.

[38] Battle, P. D.; Gibb, T. C.; Lightfoot, P. *J. Solid. State Chem.* 76 (1988) 334.

[39] Ramezanipour, F.; Cowie, B.; Derakhshan, S.; Greedan, J. E.; Cranswick, L.M.D. *J. Solid State Chem.* 182 (2009) 153.

[40] Pomjakushin, V. Yu. ; Balagurov, A. M. ; Elzhov, T. V. ; Sheptyakov, D. V. ; Fischer, P. ; Khomskii, D. I. ; Yushankhai, V. Yu. ; Abakumov, A. M. ; Rozova, M. G. ; Antipov, E. V. ; Lobanov, M. V. ; Billinge, S. J. L. *Phys. Rev. B* 66 (2002) 184412.

[41] Wright, A.J.; Palmer, H.M.; Anderson, P.A.; Greaves, C. *J. Mater. Chem.* 12 (2002) 978–982

Chapter 2

Experimental Techniques and Methods

This chapter describes the techniques and methods used for material characterizations. The topics include x-ray diffraction, constant wavelength and TOF neutron diffraction, Pair Distribution Function Analysis, and magnetization measurements.

2.1. X-ray diffraction

The hypothetical *hkl* lattice planes discussed in the previous chapter represent different arrangements of atoms. The diffraction results when radiation is scattered by atoms, and in case of x-rays, by electrons of each atom. Therefore, it is not surprising that the scattering power, called the scattering factor, f_o, of each atom depends on the number of electrons, or in other words, on the atomic number, Z. Atoms with larger atomic number scatter the x-ray beam better than light atoms. This represents one of the problems of x-ray diffraction, which is its low sensitivity to light atoms. The scattering factor f_o is also strongly dependent on sinθ/λ, and decreases exponentially upon increase in sinθ/λ. The scattering factor for different elements [1] can therefore be given by:

$$f_0^j(sin\theta/\lambda) = c_0^j + \sum_{i=1}^{4} a_i^j e^{(-b_i^j sin\theta/\lambda)} \tag{2.1.1}$$

The coefficients c_0, a_1 to a_4 and b_1 to b_4 are numbers unique to each atom. When $\theta = 0$, the scattering is called forward scattering, and is always constructive as it satisfies Bragg's condition. When forward scattering occurs, $\sin\theta/\lambda=0$ and the sum of the above 8 coefficients will be equal to number of reflecting electrons, i.e. atomic number, Z.

However, note that there is an additional parameter that affects the scattering factor, and that is the vibration of atoms, which increases as temperature increases. This results in changes in the electron cloud and the resulting scattering from that electron cloud. Consequently, a parameter called the displacement factor, or temperature factor, B, is defined as $B= 8\pi^2u^2$, where u is atomic displacement in Å, which results in the unit Å^2 for

B. Taking into account the effect of the displacement factor, one more modification will be made to the scattering factor [2], to give the final equation:

$$f = f_0 e^{(-\mathrm{B}\sin^2\theta/\lambda^2)} \tag{2.1.2}$$

The constructive interference of the beams reflected by atoms that correspond to a certain *hkl* set of planes will result in observation of a diffraction peak. Therefore each peak corresponds to a particular d spacing in the crystal. The intensity of each peak depends on the structure factor of the diffracting atoms as well as the positions of those atoms defined by three coordinates, *x*, *y* and *z* parallel to *h*,*k*, and *l*, respectively. A parameter called structure factor, F_{hkl}, is therefore defined [2] as

$$F_{hkl} = \sum_j f_j e^{[i2\pi(hx_j + ky_j + lz_j)]} \tag{2.1.3}$$

Note that the summation is performed over all *j* atoms in a unit cell. The intensity of a diffraction peak is proportional to the square of the structure factor.

$$I_{hkl} \alpha\, F_{hkl}^2 \tag{2.1.4}$$

2.2. Neutron Diffraction

Basics of Neutron Diffraction

Neutron diffraction (ND) is a bulk probe with several advantages over other diffraction techniques. One of the major benefits of ND is its sensitivity to light atoms, and the ability to distinguish elements with similar atomic numbers that are difficult to study with conventional x-ray diffraction instruments. In addition, ND provides information about magnetic structure, i.e. the relative arrangement of magnetic moments' orientations, in a material. The disadvantages of ND include the scarcity and low flux of its sources and the large quantity of sample needed for obtaining good-quality data.

There are two types of neutron sources available. One is the steady state source that produces neutrons through the fission process in a nuclear reactor, and the other is the pulsed or spallation source that generates neutrons by colliding pulses of accelerated charged particles such as protons into a heavy element target. The neutrons generated in both methods have a high velocity, and are slowed down by a moderator to be useful for ND experiments. This involves collision of neutrons with nuclei that have masses similar to that of the neutron to maximize the energy transfer. As a result, hydrogen or deuterium rich materials such as H_2O and D_2O are commonly used as moderators. Depending on the type and temperature of the moderator, a distribution of energy (wavelength) will be obtained for the neutrons, with a peak indicating the energy (wavelength) of majority of neutrons. This distribution, shown in Figure 2.2.1, is called Maxwellian.

The neutrons produced at spallation sources always have a low wavelength (high energy) tail before the peak distribution (Figure 2.2.1). Thus, in general they have higher flux at low wavelength region compared to the reactor source neutrons. Therefore, the study of small d-spacing region is better done using spallation sources. Due to the fact that the flux of neutrons generated in these sources is pulsed, they can be used for time of flight experiments that will be discussed later.

For steady state sources, a particular wavelength of neutrons for the diffraction experiment can be selected by a monochromator.

Considering that neutrons have no charge and have a high mass, they penetrate into the atoms without being diffracted by electrons. The scattering occurs through interaction of neutrons with the nucleus. The probability of interaction between neutrons and the nucleus is determined by the intensity of the neutron beam and a parameter called the cross section, σ. In practice, it can be defined as the effective area presented to the neutron beam by a particular nucleus, and has units of area, barn, where 1barn= 10^{-24}cm^2. However, note that this parameter is not actually related to the area or size of the nucleus.

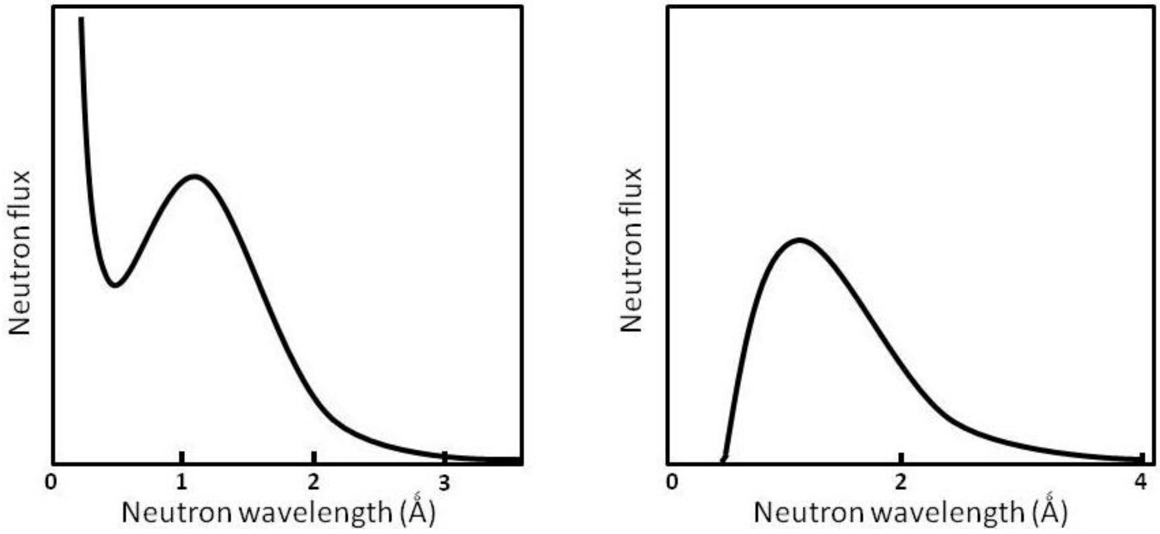

Figure 2.2.1. The distribution of Neutron wavelengths in a spallation source (left) and a reactor source (right).

The interaction between neutron and the nucleus can be in the form of absorption or scattering, and therefore the cross section consists of two components: the scattering cross section, σ_{sc}, and the absorption cross section, σ_{abs}. The scattering cross section [3] is given by:

$$\sigma_{sc} = 4\pi b^2 \tag{2.2.1}$$

where b is a parameter called the scattering length, which is analogous to the x-ray scattering factor, but has different properties due to the difference between scattering processes of neutrons and x-rays. The scattering of neutrons can be regarded as instantaneous capture and re-emission of the neutron by the nucleus. Therefore, the neutron scattering power is different from the x-ray scattering power in that b is related to the nuclear forces and there is no theory to predict its value, and therefore it has to be determined experimentally for different nuclei. Also, unlike the x-ray scattering factor, there is no angle dependence for b, and therefore in a neutron diffraction pattern, the intensities of structural peaks do not vanish at large 2θ angle. Also, b depends on the type of nucleus, and therefore, different isotopes of the same element will have different b values. Note that b can be described in terms of a real and an imaginary component, where the imaginary component corresponds to the absorption of neutrons. But the latter is significant only for a few nuclei. For majority of nuclei the imaginary part is insignificant.

Another interesting property of *b*, is that it can be negative for some nuclei, which implies a 180° phase change upon scattering. This can happen because in a scattering event, when the neutron is momentarily captured by the nucleus, there will be two possible couplings between the spin of the neutron, ±1/2, and the spin of the nucleus, I, as follows: I+1/2 and I–1/2

The first coupling is represented by b^+ and the second by b^-. These two couplings will be weighted by two weighing parameters, g^+ and g^-, respectively [3]:

$$g^+ = \frac{(\mathrm{I}+1)}{(2\mathrm{I}+1)} \tag{2.2.2}$$

$$g^- = \frac{\mathrm{I}}{(2\mathrm{I}+1)} \tag{2.2.3}$$

The total value of *b* for a given nucleus will be

$$b = g^+b^+ + g^-b^- \tag{2.2.4}$$

Therefore the sign of *b* depends on the spin of the nucleus, I.

In some cases such as ^{51}V, the two components cancel each other so that $b \approx 0$. This means almost no interaction with the neutron beam, which is why the sample containers for neutron diffraction experiments are made of ^{51}V. There are also cases such as ^{55}Mn that have negative scattering lengths.

Neutron Diffraction from many nuclei

First the scattering wave vector of neutron, Q, needs to be introduced (Figure 2.2.2). It is defined as Q = k – ḱ, where k and ḱ are the incident and scattered beam wave vectors, respectively. Q is related to the scattering angle θ, by $Q = 4\pi\sin\theta/\lambda$. The neutron diffraction patterns are sometimes expressed in terms of intensity versus Q.

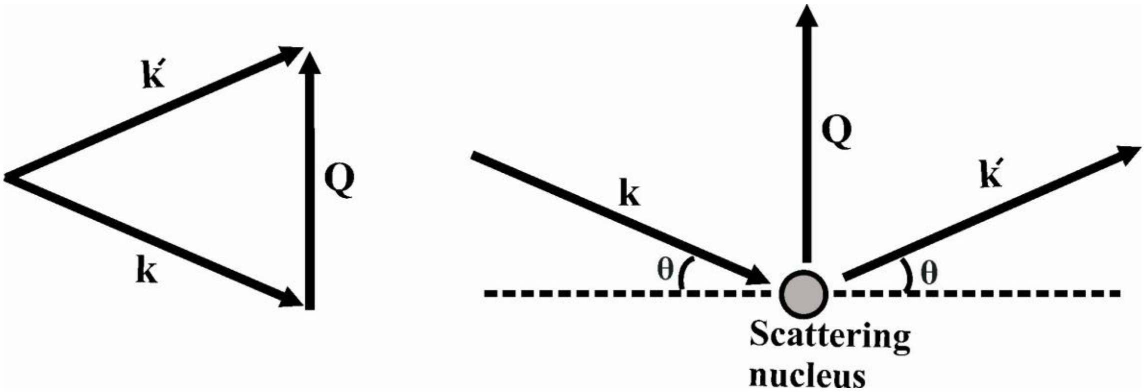

Figure 2.2.2. Schematic representation of the scattering vector, Q = k – ḱ, derived from the incident beam vector k, and scattered beam vector, ḱ.

The previous discussion on scattering cross section focused on scattering from a single nucleus. In the case of diffraction by many nuclei, the scattering lengths of different nuclei participating in the diffraction are different from each other, due to the variety of isotopes and spin states. The scattering cross section will therefore have two components [3]. One component describes the scattering as if all participating nuclei had the same *b*, which is the weighted, elemental average of their *b* values, $\langle b \rangle^2$. This called the coherent scattering cross section:

$$\sigma_{coh} = 4\pi\langle b \rangle^2 \qquad (2.2.5)$$

The coherent cross section will have a Q-dependence, and therefore is the useful part in most diffraction experiments.

The other component describes the deviations of individual scattering lengths from the average, and is called the incoherent cross section:

$$\sigma_{incoh} = 4\pi(\langle b^2\rangle - \langle b\rangle^2) \tag{2.2.6}$$

The incoherent cross section is independent of Q, and therefore results in a constant background throughout the diffraction pattern. The enormous incoherent background of ^1H is the reason why neutron studies of organic materials in many cases are done on deuterated samples.

By focusing on the coherent scattering, which is the useful part in most neutron diffraction experiments, one can obtain a structure factor similar to the x-ray diffraction case. The final equation [3] is the following:

$$F_{hkl} = \sum_j b_j e^{[i2\pi(hx_j + ky_j + lz_j)]} \tag{2.2.7}$$

Therefore, for neutrons b replaces the x-ray structure factor, f. Also note that there is a reduction in scattering due to the effect of temperature [3], as with x-rays, which is neglected in the above formula.

Basics of Magnetic Neutron diffraction

Due to the spin associated with neutrons, they have a magnetic moment that can interact with the magnetic moments of the atoms in the material of study. As a result, just similar to the scattering by nuclei, there will be a scattering of neutrons by the magnetic moments of atoms. The amplitude of this scattering can be expressed [4] by

$$a_m = p\, f\, \mu_\perp \tag{2.2.8}$$

The three components p, f and $\mu_\perp$ are described as follows.

(a) p is a constant with a numerical value $p = 0.2696\times10^{-12}$cm, which is obtained from

$$p = \frac{\gamma}{2}\left(\frac{e^2}{mc^2}\right) \tag{2.2.9}$$

where γ is the magnetic moment of neutron that has the value -1.913 μ_N (μ_N is nuclear magneton). The other parameters, e, m and c are the electron charge, electron mass and the speed of light, respectively, so that the term in parentheses becomes equal to 0.282×10^{-12} cm, which is the classical electron radius [4].

(b) f is the magnetic form factor, which is similar to the x-ray scattering factor and has a strong dependence on the scattering angle. It decreases rapidly with increasing scattering angle. As a result, magnetic scattering peaks are observed only at low 2θ, and diminish at high angle.

(c) $\mu_\perp$ is the component of atomic magnetic moment which is within the scattering plane, and perpendicular to the scattering vector, ε, in Figure 2.2.3.

Scattering of Neutrons by a Paramagnet

The magnetic scattering amplitude shown above is the counterpart of b in nuclear scattering [3]. One can then use this amplitude to introduce differential magnetic scattering cross section per unit solid angle [5]. For randomly oriented magnetic moments in a paramagnet, this is expressed as

$$\mathrm{d}\sigma_{\mathrm{M}} = p^2 f^2 \langle \mu_{\perp}^2 \rangle \tag{2.2.10}$$

$\langle \mu_{\perp}^2 \rangle$ is the mean value of the in-plane component of magnetic moment.

Note that for transition elements, where the magnetic moment can be expressed only in terms of the spin moment, $\langle \mu_{\perp}^2 \rangle = \frac{2}{3} \mathrm{g}^2\, \mathrm{S}(\mathrm{S}+1)$, where g=2, and S is spin quantum number, resulting in

$$\mathrm{d}\sigma_{\mathrm{M}} = \frac{8}{3} p^2 f^2 S(S+1) \tag{2.2.11}$$

On the other hand, for f-group elements where there is contribution from both spin and orbital magnetic moments, $\langle \mu_{\perp}^2 \rangle = \frac{2}{3} \mathrm{g}_{\mathrm{J}}^2\, \mathrm{J}(\mathrm{J}+1)$, where J is the total angular momentum and g_{J} is Landé splitting factor described in section 1.1. This gives

$$\mathrm{d}\sigma_{\mathrm{M}} = \frac{2}{3} p^2 f^2 \mathrm{g}_{\mathrm{J}}^2\, \mathrm{J}(\mathrm{J}+1) \tag{2.2.12}$$

Scattering of Neutrons by a magnetically ordered system

The scattering by magnetic moments that are ordered in long range is described by a differential cross section similar to the paramagnetic case given by equation (2.2.10), but the values for $\langle \mu_\perp^2 \rangle$ will be different.

For transition elements $\langle \mu_\perp^2 \rangle = q^2g^2S^2 = 4q^2S^2$ and for f-elements $\langle \mu_\perp^2 \rangle = q^2g_J^2J^2$, where q is called "magnetic interaction vector" (Figure 2.2.3), and is defined as

$$q = \varepsilon(\varepsilon.K) - K \tag{2.2.13}$$

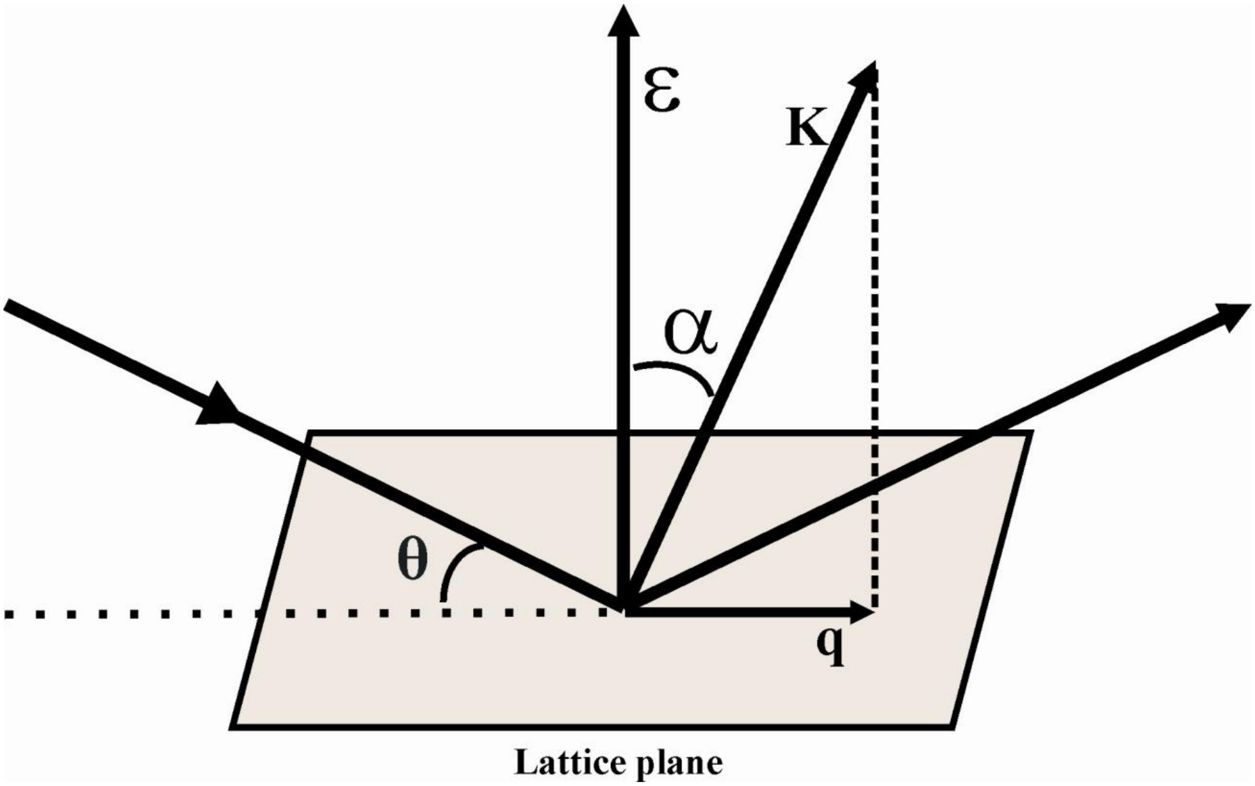

Figure 2.2.3. Schematic representation of the vectors that determine the magnetic interaction vector, q, which is given by q= ε(ε.K)–K = sinα. Here, ε is the scattering vector and K is a unit vector in the direction of magnetic moment. Then, q will be the projection of K on the lattice plane, with a length equal to sinα. Therefore, q is perpendicular to ε, and is in the same plane as ε and K.

As shown in Figure 2.2.3, ε is the scattering vector (that was previously called Q in Figure 2.2.2), and K indicates a unit vector in the direction of magnetic moment. Thus, q will be perpendicular to ε, which means it will be in the lattice plane, and in the same plane as ε and K [3]. In fact, q is the projection of K on the lattice plane and has the magnitude

$$q = \sin\alpha \tag{2.2.14}$$

where α is the angle between ε and K.

Therefore, the differential cross sections will be expressed as

$$d\sigma_M = 4p^2 f^2 q^2 S^2 \tag{2.2.15}$$

and

$$d\sigma_M = p^2 f^2 q^2 g_J^2 J^2 \tag{2.2.16}$$

Due to the presence of q, the orientation of magnetic moments will become important in scattering, and that's why it is possible to determine this orientation by neutron diffraction experiments.

Similar to the nuclear scattering, the magnetic structure factor is defined as:

$$F_{hkl} = \sum_j a_{\mathrm{m}} e^{[i2\pi(hx_j+ky_j+lz_j)]} \tag{2.2.17}$$

Note that magnetic scattering amplitude a_{m} appears in place of nuclear scattering length, *b*.

For unpolarized neutron diffraction experiments, the intensities of the nuclear and magnetic scatterings are additive. Since intensity is proportional to the square of structure factor, then

$$F_{total}^2 = F_{nuclear}^2 + q^2 F_{magnetic}^2 \tag{2.2.18}$$

According to the definition of q, q=sinα, when the magnetic moments are parallel to the scattering planes, the value for q^2 becomes unity. Also, if the moments are perpendicular to the scattering planes, the $q^2=0$ [3].

In neutron diffraction, two overlapping patterns are obtained: one corresponding to the magnetic cell and the other to the nuclear cell. The magnetic peaks are identified by the strong temperature dependence of their intensity, since the increase of temperature lowers the degree of ordering of magnetic moments. The magnetic peak intensities are also a function of the scattering angle, and diminish at high angle. In addition they are stronger for materials with larger atomic magnetic moments.

If the nuclear and magnetic cells are the same, then one expects to see the diffraction peaks of the two cells at the same 2θ angle, unless the symmetry of the magnetic cell is lower, which is sometimes the case for antiferromagnets. For a ferromagnetically ordered material, the two cells are always the same and the magnetic scattering strengthens the nuclear scattering peaks. In case of antiferromagnetic compounds, the magnetic cell can be larger than the nuclear cell. In that case the difference between the two cells is described by the so called magnetic propagation vector, k. For example if the *a* axis of the magnetic cell is two times larger than that of the nuclear cell, then k=(½, 0, 0), and if all three axes are doubled, then k=(½, ½, ½). Note that the ratio between the magnetic and nuclear cell axes does not have to be an integer.

2.3. Time of Flight (TOF) Neutron Diffraction

In this technique a neutron beam with a range of wavelengths is used. In other words the beam is not monochromated. It uses a pulsed neutron source, which is usually a spallation source where neutrons are generated by colliding accelerated protons into a target, up to 60 times per second. However, it is possible to generate pulses by chopping a steady current of neutrons produced in a reactor [6, 7]. Time of flight method takes advantage of the inverse relationship between the wavelength and velocity of neutron. Therefore, the shorter the wavelength, the shorter the time needed to reach the detector. This uses de Broglie relation:

$$\lambda = \frac{h}{mv} = \frac{ht}{mL} \qquad (2.3.1)$$

Where λ is the wavelength, m is the mass of neutron, v is the velocity of neutron, h is Plank's constant, t is the time of flight and L is the distance travelled by neutron. Equating this with Bragg's law gives

$$\lambda = 2d sin\theta = \frac{ht}{mL} \rightarrow \quad d = \frac{ht}{2mL sin\theta} \tag{2.3.2}$$

Therefore, by recording the time it takes for a neutron to reach the detector, one can calculate its wavelength, or the *d*-spacing of the set of planes by which it is diffracted [6, 7]. Note that unlike monochromated methods, here each detector, which is fixed in place, collects a complete diffraction pattern upon occurrence of each neutron pulse. This is because different wavelength neutrons corresponding to different *d*-spacings reach the detector at different times. The resolution of the data is related to the uncertainty in the *d*-spacing, δd, which is given by the following general equation for both constant wavelength and TOF neutron beams [7].

$$(\delta d/d)^2 = (\delta\lambda/\lambda)^2 + (\cot\theta\ \delta\theta)^2 \tag{2.3.3}$$

where θ is scattering angle. Note that in TOF experiments the wavelength, λ, is directly proportional to time of flight, t, and is inversely proportional to the path length, L, as shown in equation 2.3.1. Therefore the wavelength component, $(\delta\lambda/\lambda)^2$, consists of two parameters $(\delta t/t)^2$ and $(\delta L/L)^2$ [6, 7]. Consequently, lowering the uncertainty in *d* can be accomplished by long flight distance, L, which also results in long t, as well as placing the detectors at high angle [6]. The latter means that back scattering, where the angle is large (2θ >90º), results in the sharpest peaks [7]. Also note that increase in the length of the flight path results in lowering the flux [7]. The uncertainty in time of flight, t, is caused by the duration of the pulse and the fact that neutrons penetrate the moderator. Also, the uncertainty in the flight path depends on the thickness of the moderator [7], as well as thickness of the neutron detector [6].

Considering that the TOF instruments usually don't have moving part, the detectors are installed at different 2θ angles, Figure 2.3.1. A detector at a lower angle (lower bank) records large d-spacings, while a high-angle (high bank) detector collects small d-spacings. Of course there will be some overlap between the *d*-regions covered by these detectors. As discussed above, for low-angle detectors the resolution is lower, but this does not cause difficulty in data analysis, as there is a lower peak density at larger *d*-region [6].

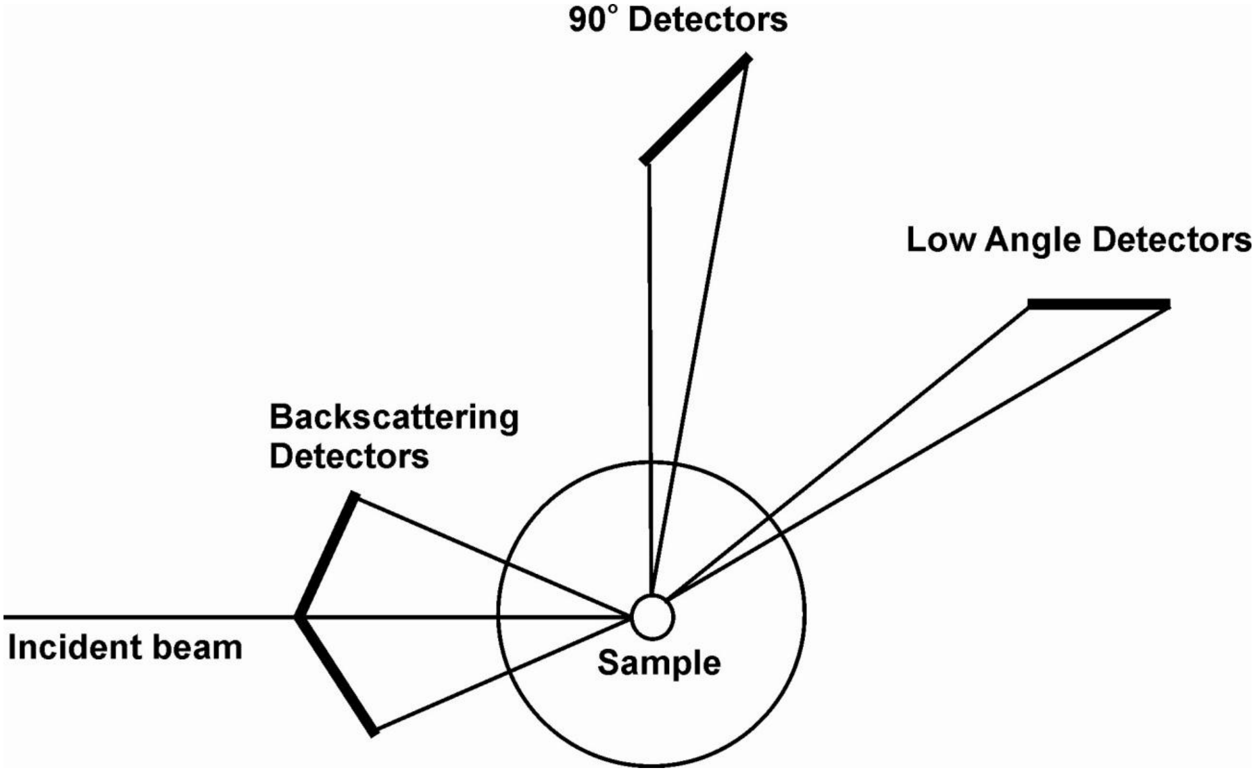

Figure 2.3.1. Schematic representation of the time of flight instrument set up.

2.4. Total Scattering and Pair Distribution Function Analysis

The commonly used methods of scattering rely on the assumption of periodicity of atomic arrangement in the crystalline system extended to an infinite range. However, in reality most crystals have defects and there exist local arrangements of atoms with features different from the average structure. In powder diffraction it is sometimes possible to observe the effects of these local atomic arrangements in the form of diffuse peaks. However, usual data analyses and fitting methods deal with sharp Bragg peaks and diffuse features are ignored or folded into the background. The distribution of defects in some materials is random, while in some compounds there is local ordering of defects. However, due to the absence of long-range defect periodicity, the powder diffraction pattern shows similar Bragg Peaks for both types of compounds.

In some cases the local structure has a great impact on the property of the material, and therefore, being able to study the local atomic arrangement can provide valuable information. For this purpose, the “total scattering” approach has proved to be of great help. The idea here is to treat both Bragg peaks and diffuse scattering equally in a powder diffraction study [8]. In other words we no longer rely only on sharp Bragg reflections. The data collection procedure is similar to that of the regular measurement. However, a large number of corrections are made to ensure the reliability of data for the detailed studies to follow. The intensity, $I(Q)$, is expressed as function of Q, the momentum transfer upon diffraction: $Q = 4\pi\sin\theta/\lambda$. However, the normalized version of the intensity, called S(Q), is usually used. This is obtained through dividing intensity by the number of scattering atoms and the average scattering power per atom. An additional modification is also made if there is more than one type of scatterer present. The result is a powder pattern which is corrected for experimental errors and normalized. S(Q) is called “total scattering structure function”. It is possible to perform total scattering measurements using laboratory x-ray sources but the Q ranges are much smaller than those obtained in synchrotron or in spallation neutron sources, where a high flux of high-energy neutrons is available. The back scattering measurements using Mo K_α tube can have maximum $Q=16Å^{-1}$ [8], while with neutron spallation sources one can routinely obtain data with Q above $50Å^{-1}$. Sometimes it’s even possible to acquire data with Q_{max} as high as $100Å^{-1}$ [9], though most of the time $50Å^{-1}$ is high enough to provide sufficient information [8]. As mentioned before, the powder data are divided by the average scattering power, which is b_{ave}^2 for neutron and $f(Q)_{ave}^2$ for x-ray. While the neutron coherent scattering length, b, is independent of Q, there is a Q-dependence for the x-ray scattering factor, f(Q), resulting in very low intensities at high Q. To deal with this issue, for x-ray, the high Q data are divided by a small number to be intensified. Therefore, in addition to taking into account a large range of Q, there is a weight added to the high Q data. In principle, one can use the corrected and normalized data, S(Q), for general Rietveld Refinement. However, usually the raw data is used for this purpose, as the corrections made by Rietveld parameters are similar to those made during generation of S(Q).

Now, one can perform a Fourier transform and convert the reciprocal space S(Q) to a special type of real space data, G(r), which is called atomic Pair-Distribution-Function (PDF). This represents the probability of the occurrence of different inter-atomic distances, *r*, in the material. The PDF data is plotted as intensity versus *r*, and each peak represents an inter-atomic distance. It is possible to obtain PDF data for distances up to thousands of angstrom [8], though the data beyond ~50Å usually does not provide new structural information [9]. Note that in some lower resolution instruments, the data at high Q will have a very low intensity [9]. Recall that diffuse scattering here is treated equal to the Bragg scattering, which implies the inclusion of inter-atomic distances corresponding to the local, non-periodic features of the structure. A structural model can be fit to the observed PDF data. The program PDFGUI is a fitting program that can be used for this purpose.

Much care should be taken when fitting PDF data, as the data has to be first truncated to a particular Q_{max}. The improper choice of Q_{max} can introduce unreal features into the G(r) pattern due to an effect called “termination ripple” [9].

Another feature is that the structural model is valid only for the range of *r* used for that particular fitting [9]. This opens up the possibility of fitting different regions of *r*, independently. Sometimes a model can better describe shorter inter-atomic distances, while different model gives a better match for longer range of *r*.

2.5. Bulk Magnetic measurements

As discussed before, for magnetic materials a quantity commonly used is susceptibility, which is obtained by first measuring the magnetization of the sample and then dividing it by the field applied during the measurement.

Since magnetic susceptibility, χ, is a function of temperature, T, it is common to measure χ over a range of temperature. The application of a magnetic field is necessary to be able to measure susceptibility. Conventionally, two χ versus T measurements are performed: (a) Zero Field Cooled (ZFC) measurement, which is cooling the sample in the absence of a field and then measuring susceptibility in the applied field as temperature increases. (b) Field Cooled (FC) measurement, which is cooling the sample in the presence of the field and then measuring the susceptibility in the same field as temperature increases. If plotted on the same χ versus T graph, the data obtained from these two measurements may overlap or diverge from each other. The divergence can indicate the formation of magnetic domains induced by the applied field. For a paramagnet the χ versus T plot appears as a curve smoothly increasing by the decrease of T. Any deviation from this behavior is indicative of the presence of a magnetically ordered state. Therefore, the susceptibility data can be used to determine the magnetic transition temperatures.

Another common type of magnetic measurements is measuring magnetization of a material as a function of the applied filed, H, at constant temperature. The magnetization is recorded while H increases, followed by a measurement while H decreases. For a paramagnet, the magnetization versus H graph is linear (as long as the saturation at high field and low T is not reached) and the data collected by both increase and decrease of H will overlap. However, if there is any uncompensated magnetic moment in the system, then the data obtained upon increase and decrease of H will diverge. This divergence is called hysteresis. At high enough fields, one may see a plateau, where the magnetization does not increase by the field anymore. This is the maximum magnetization for the material, called saturation magnetization that was discussed in section 1.1.

A commonly used instrument for magnetic measurements is the Superconducting Quantum Interference Device (SQUID) magnetometer (Figure 2.5.1). This instrument works by detecting changes in the magnetic flux as a result of the magnetization of the sample. The geometry of this magnetometer is such that the sample is surrounded by three superconducting detection coils. The magnetization of the sample results in changes in the applied magnetic flux, and these changes induce a current in the detection coils.

The capability to measure small magnetic moments comes from the fact that the coils are connected to a Superconducting Quantum Interference Device that uses the concept of electron tunneling in a Josephson junction, which consists of two layers of superconducting materials separated by a thin layer of an insulator through which the electron tunneling occurs [10,11].

The sample is placed in a gelatin capsule for the data collections from 2K to 300K, and in a quarts tube for 300K-700K experiments. For the measurements above room temperature, a furnace is installed on the instrument. The magnetic field up to 5.5T can be achieved in the system.

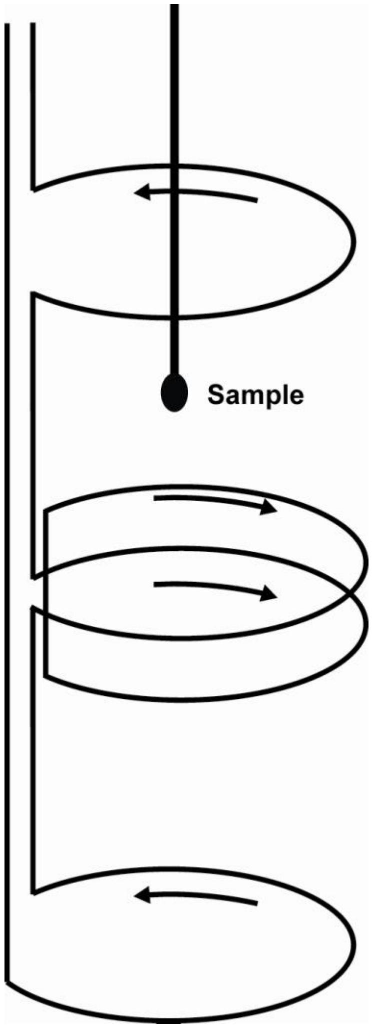

Figure 2.5.1. A schematic representation of the detection coils in the SQUID magnetometer. The arrows show the directions of coil winding.

References

[1] Pecharsky, V.; Zavalij, P. “Fundamentals of Powder Diffraction and Structural Characterization of Materials” Springer, New York, 2005

[2] Stout, G.H.; Jensen, L.H. “X-ray Structure Determination-A Practical Guide” 2nd edition, Wiley & Sons Inc., New York, 1989

[3] Bacon, G.E. “Neutron Diffraction” Clarendon Press, Oxford, UK, 1955

[4] Harrison, R.J. “Neutron Diffraction of Magnetic Materials” in “Neutron Scattering in Earth Sciences” The Mineralogical Society of America, Chantilly, VA, 2006

[5] Rossat-Mignod, J. “Magnetic Structures” in “Methods of Experimental Physics, Volume 23, Part C: Neutron Scattering” Academic Press Inc., Orlando, 1987

[6] Cockcroft, J.K.; Fitch, A.N. “Experimental Setups” in “Powder Diffraction - Theory and Practice” The Royal Society of Chemistry, Cambridge, UK, 2008

[7] Vogel, C.V.; Priesmeyer, H.-G. “Neutron Production, Neutron Facilities and Neutron Instruments” in “Neutron Scattering in Earth Sciences” The Mineralogical Society of America, Chantilly, VA, 2006

[8] Billinge, S. “Local Structure from Total Scattering and Atomic Pair Distribution Function (PDF) Analysis” in “Powder Diffraction - Theory and Practice” The Royal Society of Chemistry, Cambridge, UK, 2008

[9] Proffen, Th. “Analysis of Disordered Materials Using Total Scattering and the Atomic Pair Distribution Function” in “Neutron Scattering in Earth Sciences” The Mineralogical Society of America, Chantilly, VA, 2006

[10] Cullity, B. D.; Graham, C. D. “Introduction to Magnetic Materials” 2nd edition, Wiley-IEEE Press, Hoboken, NJ, 2009

[11] Clarke, J.; Braginski, A. I. “The SQUID Handbook, 2 : Applications of SQUIDs and SQUID Systems” WILEY-VCH Verlag GmbH & Co. KGaA, Weinheim, Germany, 2006

Chapter 3

Synthesis, Crystal Structure and magnetic properties of a new pillared perovskite $La_5Mo_{2.75}V_{1.25}O_{16}$

This chapter encompasses the manuscript "Synthesis, Crystal Structure and magnetic properties of a new pillared perovskite $La_5Mo_{2.75}V_{1.25}O_{16}$" published in "Journal of Solid State Chemistry", volume 181 (2008), pages 3366-3373.

The formula $La_5Mo_{2.76(4)}V_{1.25(4)}O_{16}$, given in the text, is better represented as $La_5Mo_{2.75(4)}V_{1.25(4)}O_{16}$.

The candidate performed the synthesis of this material, bulk magnetization, crystal and magnetic structure studies, and preparation of the manuscript.

Reprinted with permission from "Ramezanipour, F., Derakhshan, S., Greedan, J. E., Cranswick, L.M.D. (2008) Journal of Solid State Chemistry. 181: 3366-3373". Copyright 2008 Elsevier.

Synthesis, Crystal Structure and magnetic properties of a new pillared perovskite $La_5Mo_{2.75}V_{1.25}O_{16}$

Farshid Ramezanipour[†,‡], Shahab Derakhshan[†,‡], John E. Greedan[†,‡*], Lachlan M. D. Cranswick[§]

[†]Department of Chemistry, McMaster University, Hamilton, Ontario, Canada, L8S 4M1

[‡]Brockhouse Institute for Materials Research, McMaster University, Hamilton, Ontario Canada, L8S 4M1

[§]Canadian Neutron Beam Centre, National Research Council, Chalk River Laboratories, Chalk River, Ontario, Canada, K0J 1J0

* Corresponding author.

Abstract.

A new pillared perovskite compound $La_5Mo_{2.76(4)}V_{1.25(4)}O_{16}$, has been synthesized by solid-state reaction and its crystal structure has been characterized using powder X-ray and neutron diffraction. The magnetic properties of this compound have been investigated using SQUID magnetometry, and the magnetic structure has been studied using neutron diffraction data. A theoretical calculation of relative strengths of spin interactions among different magnetic ions and through different pathways has been performed using extended Hückel, spin dimer analysis. The crystal structure of this material contains perovskite-type layers that are connected through edge-sharing dimeric units of octahedra. The structure is described in space group $C2/m$ with unit cell parameters a=7.931(2)Å, b=7.913(2)Å, c=10.346(5)Å and β=95.096(5)°. The material shows both short-range ferrimagnetic correlations from ∼200 to 110K and long-range antiferromagnetic order below T_c∼100K. The magnetic structure was investigated by neutron diffraction and is described by k=(0 0 ½) as for other pillared perovskites. It consists of a ferrimagnetic arrangement of Mo and V within the layers that are coupled antiferromagnetically between layers. This is the first magnetic structure determination for any Mo-based pillared perovskite.

Key Words: Pillared perovskites, Short-range and long-range magnetic order, Crystal and magnetic structure, Neutron diffraction.

Introduction

Materials with perovskite-related structures have been attracting a great deal of interest over the past decades. Observation of interesting physical properties such as superconductivity, metal–insulator transitions and colossal magnetoresistance in perovskite-type structures with possible applications in magnetic memory devices and in detection of magnetic fields has inspired a large number of studies [1–7] . Starting with the synthesis of $La_5Mo_4O_{16}$ in 1983 [8] via fused salt electrolysis and the report of its crystal structure 10 years later [9] a new family of perovskite-related materials was introduced (Fig. 3.1), consisting of a quasi-two-dimensional structure with perovskite-type layers separated by dimeric units of edge-sharing octahedra (hatched grey). Note that there are two types of octahedra in a corner-sharing layer: the $M(1)O_6$octahedron (grey) shares only four equatorial corners with the other octahedra, and its apical corners are not shared. The second octahedron, $M(2)O_6$ (black), shares all six corners: the two apical corners are shared with the pillaring units located on the top and below, and the four equatorial corners are shared with the other octahedra within the perovskite-type layer. The two types of octahedra are arranged so that $M(1)O_6$ has only $M(2)O_6$ neighbors and vice versa. For several years this material was the unique example of this structure type, until two groups of compounds with the formulae $La_5Re_3MO_{16}$ (M=Mn, Mg, Fe, Co, Ni) and $La_5Mo_{4-x}M_xO_{16}$ (M=Mn, Mg, Fe, Co and x~0.75) were reported [10–12] , followed by another compound, $La_5Os_3MnO_{16}$ [13] . In these cases Re^{5+} and Os^{5+} substitute for Mo^{4+} in both the dimers and the perovskite layers on the $M1$ site and divalent 3*d* transition metal ions occupy the $M2$ site. These materials exhibit interesting magnetic properties. Short metal–metal distances within the dimeric units provide evidence for multiple metal–metal bonding. Due to the long separation (~10Å) of the perovskite layers by the pillaring, diamagnetic, dimeric units, one may expect to see a two-dimensional magnetic correlations in these materials, with only weak interaction between the layers. However, detailed magnetic studies of these compounds showed long-range magnetic order at temperatures up to 193K [10,12–18] . Neutron diffraction studies of $La_5Re_3MnO_{16}$ for example showed an antiferromagnetic coupling of ferrimagnetic layers (Re ↓ Mn ↑) resulting in a three-dimensional magnetic structure below 162K [15] .

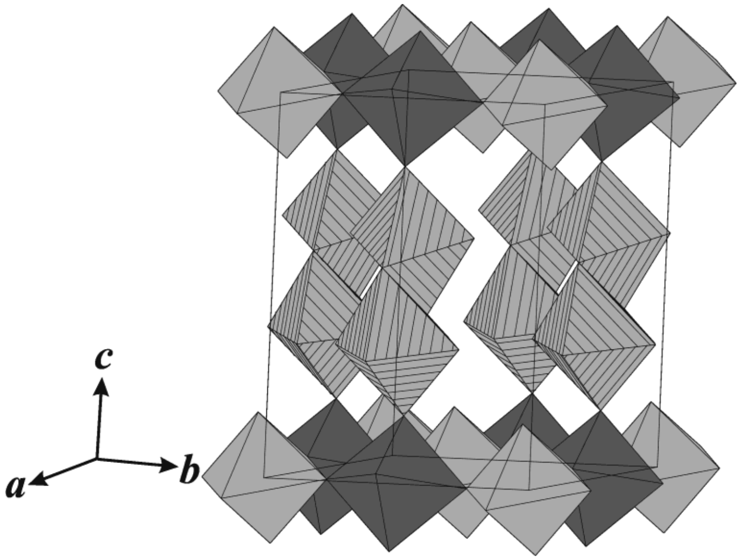

Figure 3.1. Crystal structure of a pillared perovskite. The octahedral environments of distinct atomic positions are shown with different shadings. The perovskite layers contain two octahedral sites, M1 (grey) and M2 (black), which are pillared through corner sharing at M2 by edge-sharing dimeric units shown in grey with hatching.

It is of interest to extend the crystal chemistry of this new perovskite-related family to include other 3*d* series transition elements, especially the so-called "early" 3*d* elements. Major synthetic difficulties are associated with these materials, especially the original molybdenum-based series. For example $La_5Mo_4O_{16}$ has been prepared only by molten salt electrolysis. Some members of the $La_5Mo_{4-x}M_xO_{16}$ series can be synthesized by standard solid-state methods but generally not as single-phase products [11] . Here the synthesis, crystal structure and magnetic properties of a new molybdenum-based pillared perovskite containing V^{4+} with the formula $La_5Mo_{2.76(4)}V_{1.25(4)}O_{16}$ is reported using standard solid-state methods. Sufficient material was produced in this manner to permit a neutron diffraction study of the magnetic structure for the first time for any Mo-based pillared perovskite.

Experimental Section

Synthesis. A large variety of different synthetic conditions were examined, and a compound, which later proved to be $La_5Mo_{2.76(4)}V_{1.25(4)}O_{16}$ was finally prepared using La_2O_3(99.99% Alfa Aesar), MoO_2 (99.9% CERAC), V_2O_5 (99.6% Aldrich) and V_2O_3 (prepared in the lab by reduction of VO_2 99.5% CERAC) as starting materials. La_2O_3 was pre-fired at 1000°C over night before being used in the experiment. Stoichiometric amounts of the reactant powders were weighed, ground together, pressed into a pellet, wrapped in a platinum sheet and sealed in a silica tube under the vacuum ($\sim 10^{-3}$Pa). The reaction was completed in 24h at a temperature of 950°C.

Initially, a Mo:V ratio of 3:1 (in the form of MoO_2 and V_2O_5) was used in the expectation that the low melting point of V_2O_5 would facilitate the solid-state reaction at relatively low temperatures and that the redox couple, $Mo^{4+}/V^{5+}=Mo^{5+}/V^{4+}$ might be operative. The molar ratio of La_2O_3:MoO_2:V_2O_5 used for the experiment was 2.5:3:0.5. However, a large amount of a side product, identified as $La_{2.4}Mo_{1.6}O_8$ [19] with a disordered fluorite structure and Mo oxidation state of +5.5 always appeared along with a majority phase with the pillared perovskite structure. Thus, additional vanadium oxide in the form of V_2O_3 was added to reduce molybdenum to the desired oxidation states (4+ and 5+), and to form the target V-containing material instead of a purely Mo-containing phase. Different trial amounts of excess V, in form of V_2O_3 (and by keeping the above-mentioned ratio for the other reactants), were added and finally 50% excess by mole of vanadium resulted in the desired pillared perovskite compound along with a small amount of an unidentified side product. Structural analysis of the obtained pillared perovskite compound, to be discussed later, showed the actual formula to be $La_5Mo_{2.76(4)}V_{1.25(4)}O_{16}$. Therefore, another experiment was tried using a Mo:V ratio of 2.76(4):1.25(4), that still resulted in formation of a large amount of the side product $La_{2.4}Mo_{1.6}O_8$ [19] along with the pillared perovskite compound. Accordingly, the aforementioned procedure with excess of V (V_2O_3) seems to be the best reaction condition.

X–ray and Neutron diffraction. X-ray powder diffraction data was obtained using a PANalytical X'Pert Pro MPD diffractometer with a linear X'Celerator detector. Cu$K\alpha_1$ radiation (λ=1.54056Å) in the 2θ range of 10–110° with a 2θ step interval of 0.0084° was used for data collection. Powder neutron diffraction measurements were performed on the C2 diffractometer at the Canadian Neutron Beam Centre at Chalk River, Ontario. The data were collected at three different temperatures, 3.8, 110.2 and 300K. Two different wavelengths were used at 3.8 and 300K with the same step size of 0.100°. The wavelength 1.33037Å was used to collect data within the 2θ range of 35–115°, and the wavelength 2.37150Å was applied to obtain data in the 2θ range of 5–85°. The number of Bragg reflections and profile points contained in the short wavelength dataset was 689/673 and 69/582 for the long wavelength dataset.

Magnetic property measurements. Magnetic data were collected on a Quantum Design MPMS SQUID magnetometer. The zero-field cooled and field cooled (ZFC/FC) magnetic susceptibility from 5 to 300K and isothermal magnetization data from 0 to 5.5T were obtained on a powder sample in a gelatin capsule. Diamagnetic corrections of

20×10^{-6} (La^{3+}), 17×10^{-6} (Mo^{4+}), 12×10^{-6} (Mo^{5+}), 7×10^{-6} (V^{4+}) and 12×10^{-6}emu/mol (O^{2-}) were made to the susceptibility data [20] .

Theoretical calculations; Spin dimer analyses. A computational estimation of relative strengths of spin interactions among different magnetic ions and through different pathways was obtained using extended Hückel, spin dimer analysis [21] . The strengths of spin interaction manifested in the exchange constant J are related to the hopping energies among different magnetic sites, Δe, as well as the electron correlation energy, U, resulting from accommodation of two electrons within the same orbital. These quantities are related through the formula

$$J = -2\frac{(\Delta e)^2}{U} \quad (1)$$

When comparing J values of different interaction pathways, the correlation energy U is constant and therefore the difference in the Δe value determines the significance of a particular spin interaction relative to the other possible pathways.

In these computations different interaction pathways among two $M1$ sites (Mo-rich sites), two $M2$ sites (V-rich sites), as well as an $M1$ and an $M2$ site within a perovskite-type layer were examined, and the values of the intersite hopping energy, Δe, were acquired by employing the CAESAR package [22]. Fig. 3.2 shows a schematic representation of four different spin interactions within a perovskite-type layer. Also the values of valence shell ionization potential H_{ii} , and the ζ_i and ζ_i' coefficients of double zeta Slater-type orbitals applied in the calculations [23,24] are tabulated in Table 3.1 .

Table 3.1. The values for the ζ_i coefficients and valence shell ionization potentials H_{ii} of the STO's employed for the spin dimer calculations

Atom	Orbital	H_{ii} (ev)	ζ_i	C	ζ'_i	C'
O	2s	-32.3000	2.688	0.7076	1.675	0.3745
O	2p	-14.8000	3.694	0.3322	1.659	0.7448
Mo	4s	-8.3400	1.955	1.0000		
Mo	4p	-5.2400	1.360	1.0000		
Mo	4d	-10.5000	3.954	0.4930	2.047	0.6458
V	3s	-8.8100	1.6970	1.00000		
V	3p	-5.5200	1.2600	1.00000		
V	3d	-11.0000	5.0520	0.37380	2.173	0.7456

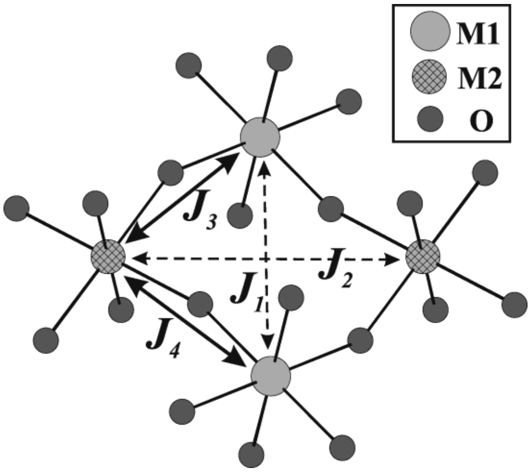

Figure 3.2. Spin interactions between magnetic ions within a corner-sharing layer. The solid and dashed arrows represent strong and weak spin interactions, respectively.

Results and discussion

Crystal structure. The crystal structure of $La_5Mo_{2.76(4)}V_{1.25(4)}O_{16}$ was characterized using both X-ray and neutron diffraction data. Data were contaminated by a small amount of an unidentified side product whose peaks were excluded from the diffraction pattern for the final refinement. The Rietveld refinement was performed using the FullProf program [25], employing WinPLOTR [26]. The non-standard space group $C-1$ has been previously reported for pillared perovskite compounds [10–13], based on Re or Os, although the space group of the original member of this family, $La_5Mo_4O_{16}$, was reported to be $C2/m$ [9]. In fact, the refined cell constants of the Re and Os materials are metrically triclinic while those for $La_5Mo_4O_{16}$ are metrically monoclinic. On the other hand, cell constants for the substituted molybdenum phase, $La_5Mo_{3.31}Co_{0.69}O_{15.8}$, are also metrically monoclinic but the single-crystal X-ray data were refined in $C-1$ due to poor averaging of equivalent reflections in $C2/m$. Lacking single-crystal X-ray data it is impossible to make a definitive choice here. Thus, the X-ray and neutron diffraction data were refined in both space groups. The refinement in $C-1$ resulted in unit cell parameters that were metrically very close to those of a monoclinic cell with α=89.989(17)° and γ=90.065(16)°. A full refinement in $C-1$, using 70 parameters, gave a somewhat better set of agreement indices than with $C2/m$, using 59 parameters, but the derived interatomic distances were not significantly different between the two cases. Thus, we report here only the results for $C2/m$.

An initial refinement was performed on X-ray diffraction data to obtain unit cell parameters and atomic positions for the metal sites to be used for the refinement of the neutron diffraction pattern. These results are shown in Fig. 3.3 (top) where the impurity reflections are indicated. While the identity of the phase or phases involved could not be determined, the relative intensities suggest an impurity level of ~5–10%. The sensitivity of neutron diffraction to oxygen was a key factor that provided accurate atomic positions, as well as acceptable displacement factors for the oxygen atoms. The large difference between the scattering lengths of Mo and V is another useful feature, as V is nearly invisible to neutrons with a scattering length of −0.3824(12)fm compared to 6.715(20)fm for Mo. Fig. 3.3 (bottom) shows the observed, calculated and difference profiles for the long wavelength neutron data (λ=2.37150Å), as well as the short wavelength neutron data (λ=1.33037Å).

The initial refinement was based on a 1:1 ratio of Mo:V in the two special positions, *M*1 and *M*2, within a perovskite layer, with Mo positioned at *M*1. The abnormal behavior of the displacement factors of these metal sites in both X-ray and neutron data signaled the possibility of some mixing between Mo and V. This hypothesis was then verified by the refinement of the site occupancies that indicated mixing predominantly on the *M*1 site. Further refinement of site occupancies to reach convergence revealed the ratio of Mo:V at the *M*1 site to be 0.76(4):0.25(4). There was at most a few percent of Mo on the *M*2 site but this was not refined and was taken as fully occupied by V. Essentially the same results were obtained from refinement of the X-ray diffraction data.

A summary of the final refinement results obtained from simultaneous refinement of short and long wavelength neutron data is given in Table 3.2.

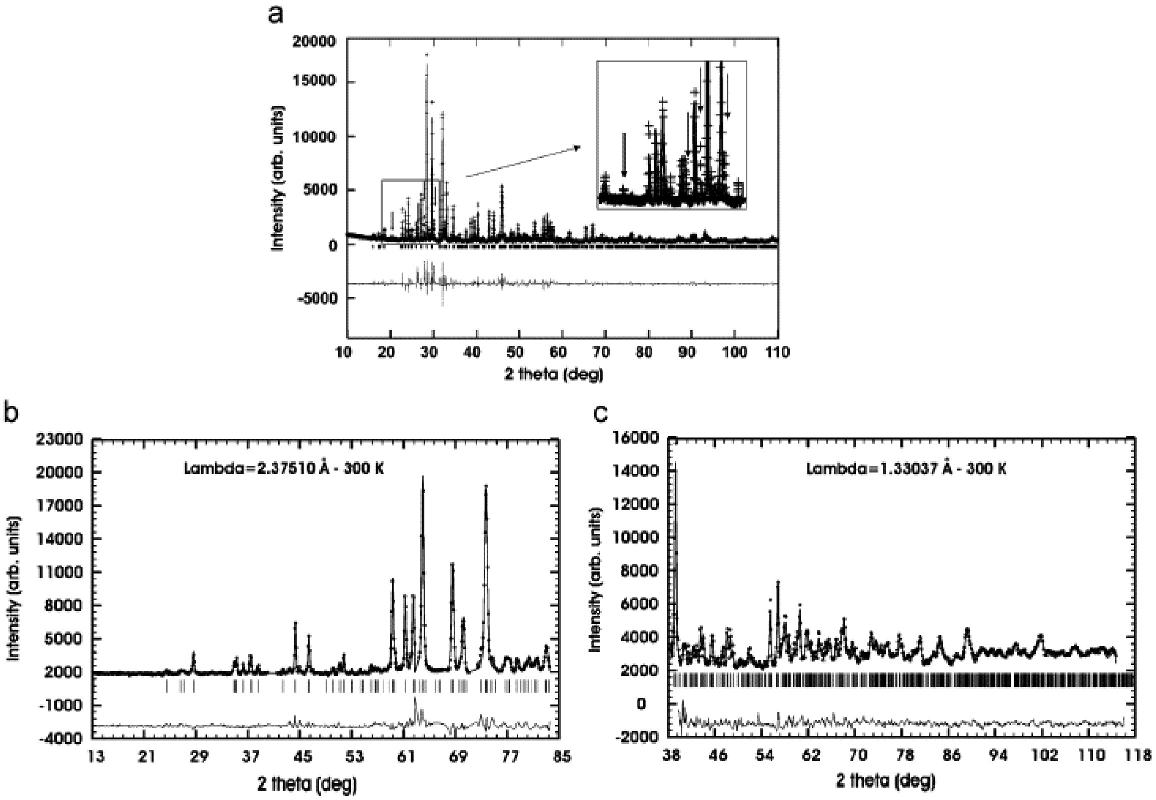

Figure 3.3. (a) Rietveld refinement of powder X-ray diffraction data with λ=1.54056Å at room temperature. The main impurity peaks are shown by arrows in the inset that magnifies the X-ray pattern in 2θ range of 18–31.5°. (b) Rietveld refinement of neutron diffraction data with λ=2.37150 and 1.33037Å. The impurity peaks are omitted for final refinement. The black dots are the data, the solid line the model, the vertical tic marks locate Bragg peak positions and the lower line is the difference plot.

Table 3.2. The final refinement results for $La_5Mo_{2.76(4)}V_{1.25(4)}O_{16}$ neutron diffraction data at 300 K.

Space group	*C* 2/m	
Lattice parameters	*a* = 7.931(2) Å	
	b = 7.913(2) Å	
	c = 10.346(5) Å	
	β = 95.096(5)°	
Z	2	
Agreement factors	R_p (1.33037 Å) = 0.038	R_p (2.37150 Å) = 0.048
	R_{wp} (1.33037 Å) = 0.051	R_{wp} (2.37150 Å) = 0.066
	R_B (1.33037 Å) = 0.063	R_B (2.37150 Å) = 0.098

Table 3.3. The atomic coordinates, site occupancies and displacement factors for $La_5Mo_{2.76(4)}V_{1.25(4)}O_{16}$ at 300 K.

Atom	*x*	*y*	*z*	Occupancy	B_{iso}(Å^2)
La1	0.2755(12)	0.2483(11)	0.1987(9)	1	0.65(20)
La2	0.0	0.0	0.5	1	1.2(4)
Mo1	0.567(2)	0.0	0.3974(15)	1	0.9(3)
Mo2	0	0	0	0.76(4)	1.1(6)
V2	0	0	0	0.25(4)	1.1(6)
V1	0	0.5	0	1	0.5
O1	0.0385(15)	0.2656(15)	0.3616(10)	1	0.1(2)
O2	0.287(3)	0.5	0.329(2)	1	0.8(4)
O3	0.315(3)	0.0	0.434(2)	1	1.0(3)
O4	0.465(2)	0.0	0.1818(16)	1	0.1(4)
O5	0.068(2)	0.0	0.1748(17)	1	0.3(4)
O6	0.044(3)	0.255(4)	0.004(3)	0.5	1.3(6)
O7	0.249(3)	0.959(3)	0.961(2)	0.5	0.6(5)

Table 3.3 shows a list of the atomic positions, site occupancies and the thermal displacement factors.

It is of course of great interest to assign oxidation states to the metal ions in the various sites in the pillared perovskite structure. For the Mo-based series it is reasonable to place $Mo^{4+}(4d^{2})$ ions in the dimeric edge-sharing octahedra that connect layers of corner-sharing octahedra. The Mo–Mo distance within the dimers, Mo1–Mo1, is very short, 2.46(2)Å, in this case, and consistent with a Mo–Mo double bond. This value falls within the range found for corresponding intra-dimer distances in $La_5Mo_4O_{16}$, 2.406(1)Å and $La_5Mo_{3.31}Co_{.69}O_{15.8}$, 2.4920(5)Å [9,11] . The constraints imposed by the edge sharing of two octahedra as well as the corner sharing between Mo_2O_{10} units and perovskite-type layers account for the significant distortion in these pillaring units. Bond distances range from Mo–O1=1.901(12)Å to Mo1–O4=2.30(2)Å and the O–Mo–O angles vary from 87.1(17)° to 102.6(12)°.

Table 3.4. Selected bond lengths (Å) and angles (deg) for $La_5Mo_{2.76(4)}V_{1.25(4)}O_{16}$ at 300K.

Mo1–O1	1.901(12) x 2
Mo1–O2	1.94(3)
Mo1–O3	1.90(3)
Mo1–O3	2.07(3)
Mo1–O4	2.30(2)
Mo1–Mo1	2.46(2)
Mo2(V2)–O5	1.841(17) × 2
Mo2(V2)–O6	2.05(3) × 2
Mo2(V2)–O7	2.08(2) × 2
V1 –O4	1.925(17) × 2
V1 –O6	1.97(3) × 2
V1 –O7	2.02(2) × 2
O1–Mo1–O1	154.7(11)
O1–Mo1–O2	91.4(13) × 2
O1–Mo1–O3	102.6(12)
O2–Mo1–O3	87.1(17)

Now, concerning the two sites within the perovskite layers, M1 at (000) and M2 at (0.5 0 0), the formal charges must sum to +9 if full occupancy of the La and O sites is assumed. There are 0.75 Mo ions and 1.25 V ions distributed over these sites. If these are solely Mo^{5+} and V^{4+}, the charge sum is +8.75 which implies either some admixture of Mo^{6+} or V^{5+} or an O^{2-} deficiency. The average M1–O distance is 1.99(2)Å and that for M2–O is 1.97(2)Å, which are not significantly different. This is in accord with the very similar radii of Mo^{5+} (0.61Å) and V^{4+} (0.58Å) and the intersite mixing. The occupation of the M1 site refined to ~0.75 Mo and ~0.25 V and with O^{2-}(1.38Å) the expected M1–O distance is 1.98Å, which is in reasonable agreement with the observed. Full occupation of M2 by V^{4+} leads to an expected distance of 1.96Å. Note that an O^{2-} deficiency of only 0.78% would provide charge balance. Such was claimed for $La_5Mo_{3.31}Co_{0.69}O_{15.8}$ from refinement of X-ray single-crystal data. Attempts to investigate this possibility by refinement of the occupation rates of the oxygen sites were inconclusive. The bond valence sum calculations [27,28] give 5.0 for Mo2, 3.6 for V1, and 3.6 for V2, which are close to the expected values of 5 and 4 for Mo and V, respectively, in the perovskite layer. However, it may be problematic to apply this approach to sites for which metal–metal bonding is important as with the Mo1 here. This may explain the large BVS value of 4.7 obtained for Mo1. Given the very short Mo1–Mo1 distance found here and in all other Mo-based pillared perovskites, the only reasonable oxidation state assignment for this site is +4. Core level spectroscopic measurements are planned to probe the distribution of metal oxidation states in this material. As well, note that the M1–O octahedron shows a pronounced psuedo-tetragonal compression (Table 3.4). The Mo2–O5 distance is only 1.841(17)Å, compared to the other two distances at 2.05(3) and 2.08(2)Å. The O5 atom is not bonded to the pillaring dimeric group. A similar distortion is also seen in $La_5Mo_4O_{16}$ and $La_5Mo_{3.31}Co_{0.69}O_{15.8}$ and one of a slightly smaller magnitude exits at the Re layer site in the $La_5Re_3MO_{16}$ series. Finally, given the very small differences in radii and formal charge between Mo^{5+} and V^{4+}, the strong preference of Mo^{5+} for the M1 site is remarkable.

Magnetic properties. Magnetic susceptibility data in the range of 2–300K, are shown in Fig. 3.4. The data are dominated by a fairly sharp maximum at ∼110K and a ZFC/FC divergence is seen below the maximum. These data are similar to those obtained for many other pillared perovskite materials. Attempts to fit the high temperature data to the Curie–Weiss function were not successful as the parameters obtained depended strongly on the fitting range. It is concluded that the Curie–Weiss regime is not reached for this material below 300K. Useful information can be obtained from a plot of χT vs. T for the ZFC data shown in Fig. 3.5. The horizontal line marks the calculated spin-only Curie constant, 0.75 emu/mol-K, for two S = ½ ions, appropriate for both Mo^{5+} and V^{4+}, per formula unit. As can be seen, the data approach this value as T approaches 300K. The χT product exceeds the spin only, paramagnetic, value below about 175K and reaches a maximum value at 110K. This is taken as evidence for short-range ferrimagnetic correlations within the perovskite planes. Note also the shoulder near 150K which might signal short-range intra-planar AF correlations. The sharp drop in χT below the maximum normally signals long-range AF coupling of ferrimagnetic layers.

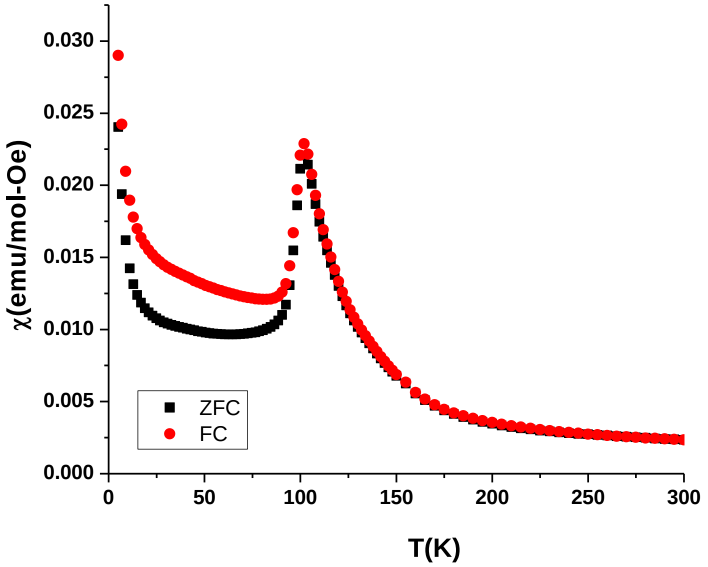

Figure 3.4. ZFC and FC molar susceptibility data as a function of temperature. Note the sharp maximum near 110 K.

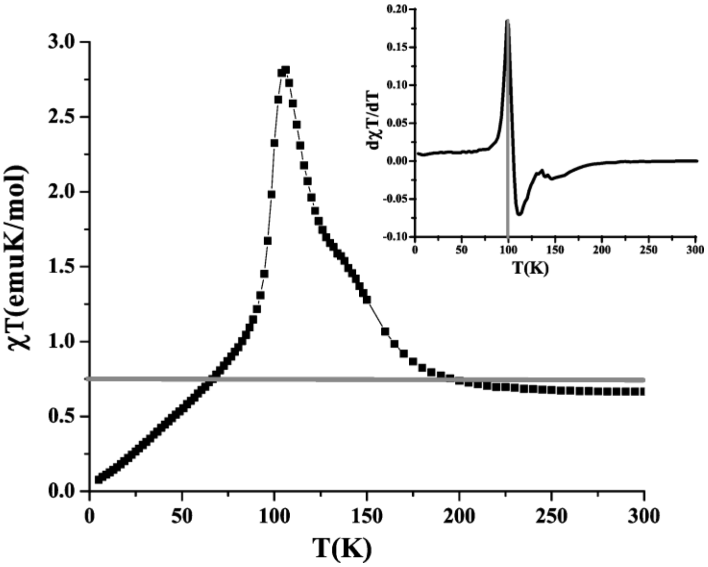

Figure 3.5. χT as a function of temperature. The horizental line shows the calculated spin-only Curie constant. The inset shows the Fisher heat capacity [29] in which the transition temperature is marked by a vertical line.

The critical temperature can be estimated from a plot of the so-called Fisher heat capacity, $d(\chi T)/dT$ vs. T shown in the inset which gives T_c=100K [29].

Isothermal magnetization data were also obtained (Fig. 3.6). The data at 5K show a linear increase of magnetization up to ~1.7T and then a rapid increase to reach $0.343\mu_B$ at 5.5T. However, saturation is not achieved at this field. A hysteresis is present at 5K and a remnant magnetization of $0.2\mu_B$ is observed. The data at 100K follow a similar trend by a gradual upturn to 0.4T followed by a rapid rise in magnetization. A clear hysteresis can also be observed at 100K. The data at higher temperatures of 150 and 300K are linear consistent with a typical paramagnetic system. The observation of a sharp increase in magnetization at low fields is a feature observed in layered materials with relatively weak inter-layer antiferromagnetic interactions. This behavior can be explained by a metamagnetic-like transition in which application of a magnetic field flips the antiferromagnetic spin alignment between the layers. In this powder sample the metamagnetic critical field can be estimated as ~1.7T from the beginning of an upturn in the 5K data, although single-crystal data would be needed to determine this value more precisely. The hysteresis observed in the isothermal magnetization data is an indication of a ferromagnetic component that can be attributed to the residual moment in the perovskite layers due to the ferrimagnetic order and possibly spin canting. In this material both the $M1$ and $M2$ sites are occupied by S = ½ ions, so the net moment will be small and will depend on differences in g-factors and on the exact distribution of ions over the two sites, an issue which has been discussed earlier. Note that a net moment of the magnitude seen here is perhaps best understood if one site is diluted by a diamagnetic component. Both the critical field for the metamagnetic transition and the saturation moment can be compared with corresponding values for $La_5Mo_4O_{16}$ which were obtained on single crystals [16] . For this material, at 5K the saturation moment is ~$0.38\mu_B$ and the metamagnetic critical field appears to be ~1T or 10^4Oe, both values being similar to those found for $La_5Mo_{2.75}V_{1.25}O_{16}$.

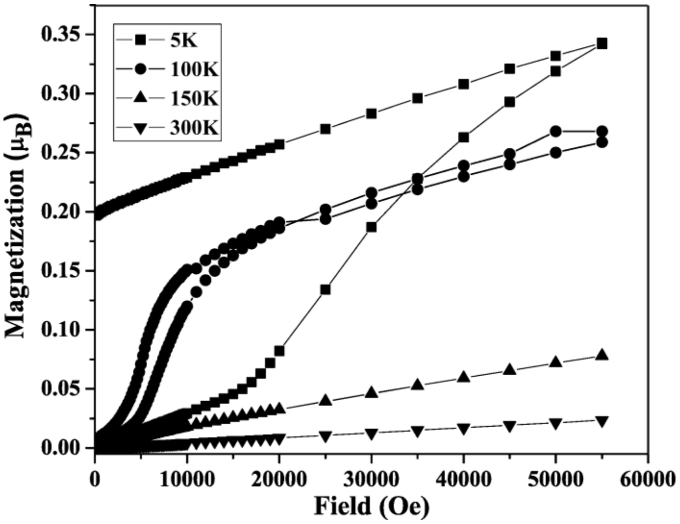

Figure 3.6. The isothermal magnetization vs. applied field behavior. A hysteresis persists up to 100 K, and disappears at 150 K. Note the metamagnetic transitions for 100 and 5 K.

The availability of a relatively large sample permitted neutron diffraction studies which allow a study of the magnetic structure of this material and for the first time for any Mo-based pillared perovskite. Given that the magnetic ions involved have $S=1/2$ with small local magnetic moments and that the system is magnetically very dilute (two magnetic ions out of 25) the intensity of the magnetic peaks is expected to be very weak. Nonetheless, it was possible to identify two magnetic reflections from a comparison of data at 300 and 3.8K (Fig. 3.7), at 24.99(1)° and 25.77(3)° which can be indexed as (−1

−1 ½)/(−1 1 ½), and (1 −1 ½)/(1 1 ½), respectively, consistent with the case of the Re-based materials [12,15,18] . A structure peak (1 1 0)/(1 −1 0) is also indexed. Due to the low intensity of the magnetic peaks and also overlap of the 24.99(1)° peak with a peak from the side product, a refinement of magnetic structure was not possible. However, the data are sufficient to propose a model magnetic structure by simulation and comparison of relative intensities. From the indices the ordering wave vector is **k** = (0 0 ½) which requires an inter-layer AF ordering. The intra-layer order may be ferro(F) or AF(ferrimagnetic). Simulations showed that only the AF intra-layer model resulted in intensities at the observed magnetic reflections. This is consistent with the results of a spin dimer calculation of the intra-planar exchange interactions which will be discussed in the next section.

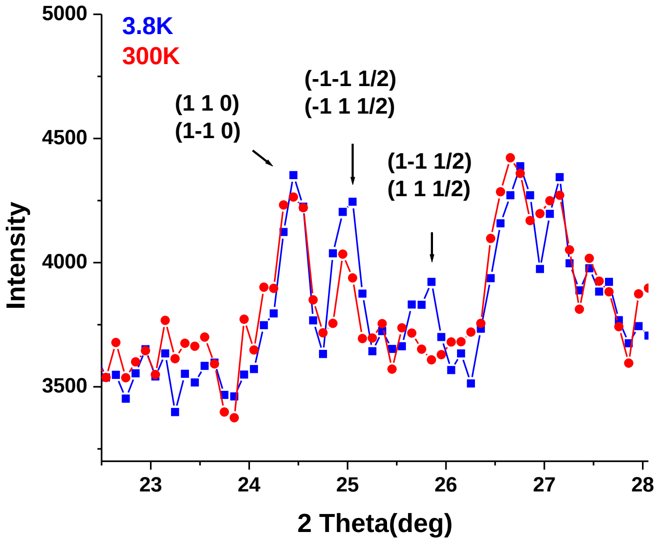

Figure 3.7. Comparison of neutron diffraction data at 300 and 3.8 K. Magnetic reflections are indexed along with a pure crystal structure reflection.

Table 3.5. Observed intensities of magnetic and non-magnetic reflections for $La_5Mo_{2.76(4)}V_{1.25(4)}O_{16}$.

	3.8 K	3.8 K	300 K	300 K
(hkl)	Peak Pos. (deg)	Int.	Peak Pos. (deg)	Int.
(1 1 0)/(1 -1 0)	24.45(1)	267(22)	24.44(1)	267(30)
(-1 1 1/2)/(-1 -1 1/2)	24.99(1)	236(28)	24.99(1)	88(22)
(1 1 1/2)/(1 -1 1/2)	25.76(3)	140(37)	-	-

Table 3.6. Comparison of observed and calculated relative intensities for $La_5Mo_{2.76(4)}V_{1.25(4)}O_{16}$ assuming a model with $1\mu_B$ each on the M1 and M2 intra-planar sites and a moment direction parallel to the *c*-axis.

(*h k l*)	3.8 K		3.8 K	
	Int. (Calc.)	Int. (Rel.)	Int. (obs.)	Int. (Rel.)
(1 1 0)	202			
(1 -1 0)	16			
Total	218	1	267(22)	1
(-1 -1 1/2)	68		236(28)	
(-1 1 1/2)	68		-88(22)	
Total	136	0.62	148(22)	0.55(11)
(1 1 1/2)	63			
(1 -1 1/2)	63			
Total	126	0.58	140(37)	0.52(11)

Thus, the magnetic structure is one in which the moments on *M*1 and *M*2 show AF coupling within the layers, and AF coupling between the layers as well (Fig. 3.8) as has been found for the Re- and Os-based pillared perovskites. An estimate of the ordered moments can be obtained from fitting the magnetic and non-magnetic (1 1 0)/(1 −1 0) reflection to Gaussians and comparison with calculated values from simulations. The spin direction is taken as parallel to the *c*-axis as no (0 0 ½) reflection was observed. Moments of $1\mu_B$ each were placed at the *M*1 and *M*2 sites and the magnetic intensities were calculated. The results are shown in Tables 3.5 and 3.6. The agreement is seen to be reasonable. Given the large uncertainties associated with the data, further efforts to refine to the model were considered unwarranted.

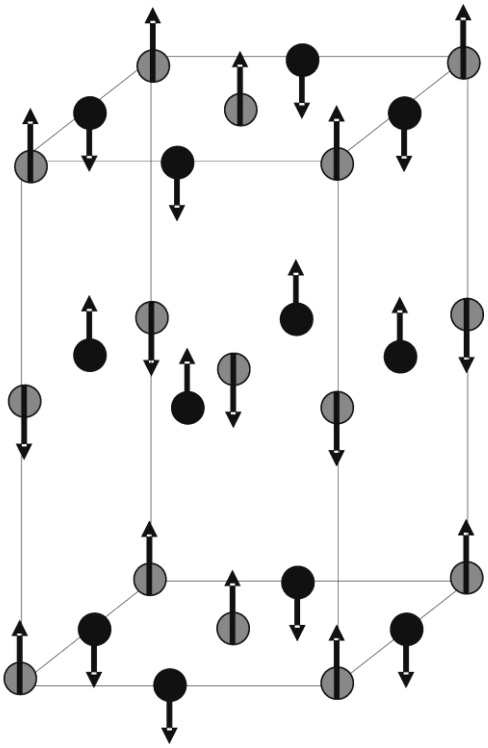

Figure 3.8. The magnetic structure of $La_5Mo_{2.76(4)}V_{1.25(4)}O_{16}$. The grey and black circles represent *M*1 and *M*2 sites, respectively. The diamagnetic dimer sites are not shown. The long axis is the magnetic *c*-axis which equals $2c_{\text{chem}}$.

Tight binding, magnetic dimer model. The relative strengths of different possible spin interactions within the layers of this material were calculated. Fig. 3.2 illustrates these interaction pathways labled as J_1–J_4, the metal/metal distances for which are given in Table 3.5. In this material the d^1 ions Mo^{5+} and V^{4+} are responsible for the spin exchange interactions. From the results of Table 3.4, a psuedo-tetragonal compression is associated with both sites. This results in lifting the degeneracy of the t_{2g} orbitals by depressing the d_{xy} state compared to the d_{xz} and d_{yz} orbitals. The orbitals involved in the exchange are determined by the degree of the splitting. Two extreme cases can be considered. For a large splitting the single unpaired electron will reside exclusively in d_{xy} which is well separated from the other states. Consequently, only one orbital of each magnetic ion is involved in the spin exchange, and therefore there is only one interaction in each pathway for which Δe should be calculated. However, if the separation between these states is not significant, the occupation probability of d_{xz} and d_{yz} electron will be high, and these two orbitals will participate in spin interactions as well. At the other extreme, the probability that d_{xy} , d_{xz} and d_{yz} participate in the spin exchange will be the same, and the Δe resulting from each state should be taken into account. Therefore the intersite hopping energy will be given by the general formula

$$\left\langle (\Delta e)^2 \right\rangle \approx \frac{1}{N^2}\sum_{\mu=1}^{\mathrm{N}}(\Delta e_{\mu\mu})^2 \quad (2)$$

where N is the number of orbitals and μ indicates each particular orbital participating in the interactions. Finally the obtained value for $\langle (\Delta e)^2 \rangle$ will be used to determine the strengths of different interaction pathways according to

$$J = -2\frac{\left\langle (\Delta e)^2 \right\rangle}{U} \quad (3)$$

A further assumption is that the inter-electron repulsion, U, will not be appreciably different for the two d^1 ions involved, Mo^{5+} and V^{4+}. While this is not strictly true, we note that this assumption will result in errors of at most a factor of two or so. Calculations were done for both extreme cases for the four pathways identified in Fig. 3.2, the interatomic distances for which are listed in Table 3.7. The calculated Δ*e* values are listed in Table 3.8 and reveal that J_3 and J_4, corresponding to the two possible *M*1–*M*2 nearest-neighbor interactions along the 〈100〉 and 〈010〉 directions, are the strongest interactions by $\sim 10^4$ over J_1 and J_2, which correspond to next nearest neighbor *M*1–*M*1 and *M*2–*M*2 interactions, respectively. The result is qualitatively the same for both extreme cases and by extension, any intermediate case. This is consistent with the magnetic structure found for this material that was discussed earlier, as large Δ*e* values obtained by the extended Hückel, method indicate antiferromagnetic interaction of spins between the nearest neighbor *M*1 and *M*2 sites.

Table 3.7. Metal/Metal distances for spin interaction within a perovskite-type layer.

Exchange pathway	Distance (Å)
M1–M1 (J_1)	5.596
M2–M2 (J_2)	5.596
M1–M2 (1) (J_3)	3.953
M1–M2 (2) (J_4)	3.960

Table 3.8. Spin dimer analysis for the various exchange pathways identified in Fig. 3.2 for $La_5Mo_{2.76(4)}V_{1.25(4)}O_{16}$ assuming single occupation of d_{xy} and equal occupation of d_{xy},d_{xz} and d_{yz} orbitals.

Pathway	Δe^2(meV)^2 (d_{xy})	Rel.	Δe^2(meV)^2 (d_{xy},d_{xz},d_{yz})	Rel.
J_1	1224	8.9×10^{-4}	1231	2.1×10^{-4}
J_2	616	4.5×10^{-4}	616	1.05×10^{-4}
J_3	1.33×10^6	0.97	5.83×10^6	0.98
J_4	1.37×10^6	1	5.96×10^6	1

Conclusions

A new pillared perovskite compound containing an “early 3*d* transition element, $La_5Mo_{2.76(4)}V_{1.25(4)}O_{16}$, was synthesized by solid-state reaction, thus extending the crystal chemistry of this series. A structure refinement in *C*2/*m* using both X-ray and neutron diffraction data showed that within the perovskite layers, the *M*1 site has a mixed occupancy of Mo and V in the ratio Mo/V=0.75/0.25, while the *M*2 is almost completely occupied by V. It is argued that the *M*1 site contains Mo^{5+} and V^{4+} while the *M*2 site is predominantly V^{4+}. A very short Mo–Mo distance of 2.46(2)Å is found in the dimeric edge-sharing units, indicating a Mo–Mo double bond between two $Mo^{4+}(4d^2)$ ions as seen in the related materials, $La_5Mo_4O_{16}$ and $La_5Mo_{3.31}Co_{.69}O_{15.8}$. Thus, the Mo1 sites do not contribute to the paramagnetic susceptibility. The bulk magnetic properties of this compound are similar to those of other pillared perovskites. Short-range intra-planar correlations set in below ~250K, indeed, a pure Curie–Weiss regime is not found up to 300K. The dominant short-range order is ferrimagnetic, causing an increase of the χT product with decreasing temperature to well above the spin only value for two S = 1/2 ions. Long-range order sets in below 100K. Isothermal field sweeps give evidence for a metamagnetic critical field of ~1.7T at 5K. The magnetic structure of this material was determined from neutron diffraction data for the first time for any Mo-based pillared perovskite. The ordering wave vector is **k** = (0 0 ½) and ferrimagnetically ordered layers of moments of ~$1\mu_B$ each on the *M*1 and *M*2 sites are coupled antiferromagnetically between the layers. A theoretical study of spin interactions within the perovskite-type layers using extended Hückel, spin dimer analysis is consistent with the observed ferrimagnetic intra-planar spin correlations.

Acknowledgements.

We acknowledge support for this work from the Natural Sciences and Engineering Research Council of Canada through a Discovery Grant to J.E.G. and MRS grants to the Canadian Neutron Beam Centre and the Brockhouse Institute for Materials Research. Mr. Subrata Shaw carried out early work on the synthesis of this material.

References

[1] K.-I. Kobayashi, T. Kimura, H. Sawada, K. Terakura, Y. Tokura, Nature 395 (1998) 677.

[2] A.P. Ramirez, J. Phys.: Condens. Matter 9 (1997) 8171.

[3] T.H. Kim, M. Uehara, S.W. Cheong, S. Lee, Appl. Phys. Lett. 74 (1999) 1737.

[4] G.D. Tang, X.M. Liu, Z.Z. Li, D.L. Hou, X. Zhao, L.H. Liu, W.H. Qi, Y. Yu, R.C. Yu, C.Q. Jinphys, Stat. Sol. (a) 203 (2006) 2522.

[5] M.A. Basith, Sk. Manjura Hoque, Md. Shahparan, M.A. Hakim, M. Huq, Physica B 395 (2007) 126.

[6] M. Imada, A. Fujimori, Y. Tokura, Rev. Mod. Phys. 70 (1998) 1039.

[7] L.O.-S. Martin, J.P. Chapman, L. Lezama, J.S. Marcos, J. Rodrı´guez-Ferna´ ndez, M.I. Arriortua, T. Rojo, Eur. J. Inorg. Chem. (2006) 1362–1370.

[8] W.H. McCarroll, C. Darling, G. Jakubicki, J. Solid State Chem. 48 (1983) 189.

[9] M. Ledesert, Ph. Labbe, W.H. McCarroll, H. Leligny, B. Raveau, J. Solid State Chem. 105 (1993) 143.

[10] C.R. Wiebe, A. Gourrier, T. Langet, J.F. Britten, J.E. Greedan, J. Solid State Chem. 151 (2000) 31.

[11] K.V. Ramanujachary, S.E. Lofland, W.H. McCarroll, T.J. Emge, M. Greenblatt, J. Solid State Chem. 164 (2002) 70.

[12] L. Chi, A.E.C. Green, R. Hammond, C.R. Wiebe, J.E. Greedan, J. Solid State Chem. 170 (2003) 165.

[13] L. Chi, I.P. Swainson, J.E. Greedan, J. Solid State Chem. 177 (2004) 3086.

[14] K.V. Ramanujachary, M. Greenblatt, W.H. McCarroll, J.B. Goodenough, Mater. Res. Bull. 28 (1993) 1257.

[15] A.E.C. Green, C.R. Wiebe, J.E. Greedan, Solid State Sci. 4 (2002) 305.

[16] S.E. Lofland, T. Scabarozi, K.V. Ramanujachary, W.H. McCarroll, J. Magn. Magn. Mater. 260 (2003) 184.

[17] S.E. Lofland, J. Hattrick-Simpers, K.V. Ramanujachary,W.H. McCarroll, J. Magn. Magn. Mater. 265 (2003) 113.

[18] H.L. Cuthbert, L. Cranswick, J.E. Greedan, J. Solid State Chem. 179 (2006) 1938.

[19] P.H. Hubert, P. Michel, C. Vincent, C. R. Acad. Sci. Ser. IIc 269 (1969) 1287.

[20] P.W. Selwood, Magnetochemistry, second ed., Interscience Publishers, Inc., New York, 1996.

[21] M.H. Whangbo, H.J. Koo, D.J. Dai, J. Solid State Chem. 176 (2003) 417.

[22] J. Ren, W. Liang, M.H. Whangbo, Crystal and Electronic Structure Analysis Using CAESAR, /http://www.primeC.comS, 2005.

[23] E. Clementi, C. Roetti, At. Data Nucl. Data Tables 14 (1974) 177.

[24] A.D. McLean, R.S. Mclean, At. Data Nucl. Data Tables 26 (1981) 197.

[25] T. Roisnel, J. Rodriguez-Carvajal, FULLPROF ver 1.9c: Rietveld, Profile Matching & Integrated Intensity Refinement of X-ray and/or Neutron Data, Laboratoire Le´on Brillouin, Saclay, France, 2001.

[26] T. Roisnel, J. Rodrìguez-Carvajal, WinPLOTR: a Windows tool for powder diffraction patterns analysis, In: R. Delhez, E.J. Mittenmeijer (Eds.), Proceedings of the Seventh European Powder Diffraction Conference (EPDIC 7), Mater. Sci. Forum (2000) 118–123.

[27] I.D. Brown, D. Altermatt, Acta Crystallogr. B 41 (1985) 244.

[28] VALENCE program, /http://www.ccp14.ac.uk/ccp/web-mirrors/i_d_brown/S.

[29] M.E. Fisher, Philos. Mag. 7 (1962) 1731.

Chapter 4

Crystal and Magnetic Structures of the Brownmillerite Compound $Ca_2Fe_{1.039(8)}Mn_{0.962(8)}O_5$

This chapter encompasses the manuscript "Crystal and Magnetic Structures of the Brownmillerite Compound $Ca_2Fe_{1.039(8)}Mn_{0.962(8)}O_5$" published in "Journal of Solid State Chemistry", volume 182 (2009), pages 153-159.

The formula $Ca_2Fe_{1.039(8)}Mn_{0.962(8)}O_5$, given in the text, is better represented as $Ca_2Fe_{1.039(8)}Mn_{0.961(8)}O_5$.

The candidate performed the synthesis of this material, bulk magnetization, crystal and magnetic structure studies, and preparation of the manuscript.

Reprinted with permission from "Ramezanipour, F., Cowie, B., Derakhshan, S., Greedan, J. E., Cranswick, L.M.D. (2009) Journal of Solid State Chemistry. 182: 153-159".

Crystal and Magnetic Structures of the Brownmillerite Compound $Ca_2Fe_{1.039(8)}Mn_{0.962(8)}O_5$

Farshid Ramezanipour[†,‡], Bradley Cowie[†,‡], Shahab Derakhshan[†,‡], John E. Greedan[†,‡*], Lachlan M. D. Cranswick[§]

[†]Department of Chemistry, McMaster University, Hamilton, Ontario, Canada L8S 4M1

[‡]Brockhouse Institute for Materials Research, McMaster University, Hamilton, Ontario, Canada L8S 4M1

[§]Canadian Neutron Beam Centre, National Research Council, Chalk River Laboratories, Chalk River, Ontario, Canada K0J 1J0

* Corresponding author at: Department of Chemistry, McMaster University, Hamilton, Ontario, Canada L8S 4M1. Fax: +1905 5212773.
E-mail address: greedan@mcmaster.ca (J.E. Greedan)

Abstract. The crystal and magnetic structures of the brownmillerite material, $Ca_2Fe_{1.039(8)}Mn_{0.962(8)}O_5$ were investigated using powder X-ray and neutron diffraction methods, the latter from 3.8 to 700K. The compound crystallizes in *Pnma* space group with unit cell parameters of *a*=5.3055(5)Å, *b*=15.322(2)Å, *c*=5.4587(6)Å at 300K. The neutron diffraction study revealed the occupancies of Fe^{3+} and Mn^{3+} ions in both octahedral and tetrahedral sites and showed some intersite mixing and a small, ~4%, Fe excess. While bulk magnetization data were inconclusive, variable temperature neutron diffraction measurements showed the magnetic transition temperature to be 407(2)K below which a long range antiferromagnetic ordering of spins occurs with ordering wave vector *k*=(000). The spins of each ion are coupled antiferromagnetically with the nearest neighbors within the same layer and coupled antiparallel to the closest ions from the neighboring layer. This combination of intra- and inter-layer antiparallel arrangement of spins forms a G-type magnetic structure. The ordered moments on the octahedral and tetrahedral sites at 3.8K are 3.64(16) and 4.23(16)μ_B, respectively.

Key Words: Ca_2FeMnO_5, Brownmillerite, Long range magnetic order, Crystal and magnetic structure, Neutron diffraction.

Introduction

There has been considerable interest in materials with oxygen-deficient perovskite-related structures in recent years. Fuel cells and dense membranes for the partial oxidation of hydrocarbons are some of the areas of possible applications for these materials [1]. Brownmillerites are a family of oxygen-deficient compounds that form when a series of vacancies are introduced into the perovskite structure in an ordered manner. The result of the presence of these ordered arrays of vacancies is a structure involving alternating layers of octahedra and tetrahedra. The general formula for brownmillerites is $A_2MM'O_5$, where M and M' are octahedral and tetrahedral site cations, respectively, and A is a large cation residing in the spaces between the layers. The crystal structure involves both octahedral and tetrahedral layers alternating along the *b*-axis (Fig. 4.1). The octahedra share four equatorial corners with other octahedra within the layers. These layers are separated by chains of tetrahedra that run parallel to the *a*–*c* plane. The chains of tetrahedra are connected to the apical corners of octahedra from the layers above and below. Three space groups have been reported for brownmillerite materials, *Pnma*, *Ibm*2 and *Imma* and their variants [2–6]. The distinction arises due to the relative orientations of the tetrahedral chains as discussed by Greaves et al. [7] and Lambert et al. [8]. If the chains have the same orientation, one has the non-centric space group *Ibm*2, while if the chain orientations are opposite but ordered, *Pnma* is the choice and if the chains are disordered, *Imma* results. It has also been argued that materials which seem to be described in *Imma* actually contain ordered but modulated chains of the two orientations [8]. As well, the space group can change with composition and temperature. This has been documented for the brownmillerite series $Ca_2Fe_{2-x}Al_xO_5$ [9,10].

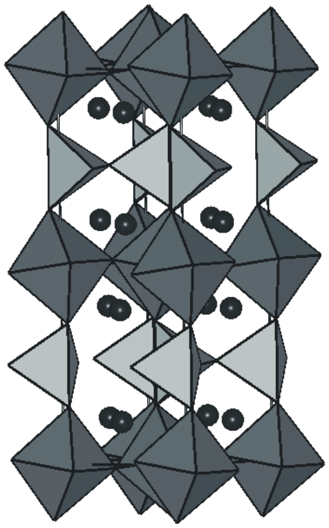

Figure 4.1. Crystal structure of a brownmillerite. The corner-sharing octahedral layers (dark gray) are connected together through chains of corner-sharing tetrahedra (light gray). The counter ions are black spheres.

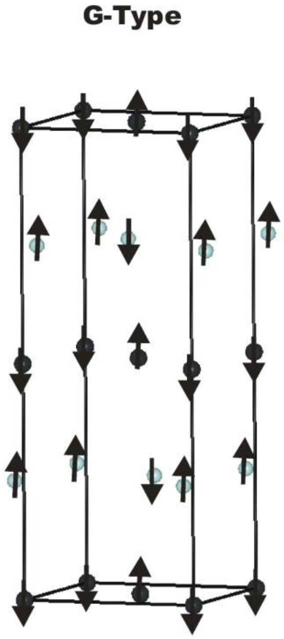

Figure 4.2. The G–type magnetic structure of $Ca_2Fe_2O_5$. The octahedral and tetrahedral sites are shown by different colors. Each site couples antiferromagnetically with all nearest neighbors within the same layer and in the adjacent layers.

The magnetic properties of brownmillerites have been of interest, and detailed magnetic structure determinations for some brownmillerite systems have been performed. $Ca_2Fe_2O_5$ for example has been studied extensively during the past decades [11–13]. This material has a G-type antiferromagnetic structure, in which the spin on each atom is aligned antiparallel to all nearest neighbor spins (Fig. 4.2). This compound also shows a weak ferromagnetic component that has been attributed to the spin canting [11], where the angles between antiparallel spins are slightly different from 180°. The magnetic structure of Sr_2GaMnO_5 [14,15] has also been found to involve antiferromagnetic coupling of Mn spins both within the planes and between the planes. This is an interesting case as the Mn^{3+} ions in two octahedral layers are separated by a non-magnetic Ga-containing tetrahedral layer. The distance between the Mn^{3+} ions on two neighboring layers is twice as long as the intra-layer distance. In addition, some small ferromagnetic domains within the antiferromagnetic system were suggested due to an anomaly in the magnetization versus temperature behavior [16]. A similar magnetic structure was found in the brownmillerite Ca_2MnAlO_5 [15]. A ferromagnetic component was also suggested for this system due to a divergence in the zero field and field cooled susceptibility data. This was considered as an indication of spin canting [15].

There is surprisingly little reported about the brownmillerite compound Ca_2FeMnO_5. Its crystal structure was studied using powder X-ray diffraction several years ago [17]. The unit cell constants are listed in Table 4.1 in square brackets. In a very recent work using Mössbauer spectroscopy a G-type magnetic structure has been proposed with the preferred spin direction along the *b*-axis [18]. The critical temperature was not reported. Also, unfortunately, the authors of [18] did not report the lattice constants of their sample and thus, the extent of oxidation is not known. In this paper the crystal and magnetic structures of this compound are studied using X-ray and neutron diffraction. Application of neutron diffraction provided information about the iron and manganese contents, and site occupancies of these ions in the crystal structure, to give the formula $Ca_2Fe_{1.039(8)}Mn_{0.962(8)}O_5$. As well, neutron diffraction provided a definitive determination of the magnetic structure, values for the ordered moments and also the critical temperature for magnetic ordering, as bulk magnetization data were ambiguous.

Experimental Section

Synthesis. $Ca_2Fe_{1.039(8)}Mn_{0.962(8)}O_5$ was synthesized using $CaCO_3$ (99.99% Alfa Aesar), Fe_2O_3 (99.998% Alfa Aesar), and MnO (99.99% Alfa Aesar) as starting materials. The preparation was performed in two steps. Initially, the stoichiometric amounts of powders of the above reagents were weighed, ground together, pressed into a pellet and fired for 24h at 1250°C in air. The second step was performed by regrinding and heating the sample at 1250°C under argon atmosphere for 48h.

X-ray and neutron diffraction. A PANalytical X′Pert Pro MPD diffractometer with a linear X′Celerator detector was used for the X-ray powder diffraction study. The data were collected in a 2θ range of 5–90° with a 2θ step interval of 0.0084° using Cu$K\alpha_1$ radiation (λ=1.54056Å). Powder neutron diffraction measurements were performed on the C2 diffractometer at the Canadian Neutron Beam Centre at Chalk River, Ontario. The data were collected at 39 different temperatures starting from the base temperature, 3.8-700K. A wavelength of 2.37150Å, was used to obtain data within a 2θ range of 3.4-84.5° with a step size of 0.100°. The fine collimation data were also obtained at 300 and 550K, using a wavelength of 1.33037Å with a 2θ step interval of 0.050° in a 2θ range of 34.9-115°.

Magnetic property measurements. A quantum design MPMS SQUID magnetometer was used to obtain the magnetic data. The zero-field cooled and field cooled (ZFC/FC) magnetic susceptibility data were collected from 5 to 300K on a powder sample in a gelatin capsule. The data were also collected from 300 to 700K by heating and cooling in a furnace using a quartz sample holder, with an applied field of

1000Oe. The isothermal magnetization data from 0 to 5.5T were also obtained at three different temperatures. Diamagnetic corrections of 8×10^{-6} emu/mol (Ca^{2+}), 10×10^{-6} emu/mol (Fe^{3+}), 10×10^{-6} emu/mol (Mn^{3+}) and 12×10^{-6} emu/mol (O^{2-}) were made to the susceptibility data [19].

Results and discussion

Crystal structure. The crystal structure of $Ca_2Fe_{1.039(8)}Mn_{0.962(8)}O_5$ was determined by powder X-ray and neutron diffraction. The Rietveld refinement was performed using the GSAS program [20], employing the EXPGUI interface [21]. The space group *Pnma* has been previously reported for brownmillerites including Ca_2FeMnO_5 [17]. The presence of reflections such as (131) and (151), which violate I-centering indicate that this is the correct choice. Table 4.1 gives the final refinement results.

Table 4.1. The final refinement results for $Ca_2Fe_{1.039(8)}Mn_{0.962(8)}O_5$. Refinements at three different temperatures were performed on neutron data (λ=2.37150 Å). Fine collimation data (λ=1.33037Å) were also obtained and refined at 550 and 300 K. In addition, a refinement of X-ray data was performed at 300 K using Kα$_1$ (λ=1.54056 Å). The last column shows parameters from Nakahara et al. at ~300K [17].

Space group	*Pnma*			
Z	4			
Lattice parameters	3.8 K	300 K	550 K	Ref. [17]
a (Å)	5.2985(4)	5.3055(5)	5.3251(1)	5.338
b (Å)	15.286(1)	15.322(1)	15.3865(3)	14.834
c (Å)	5.4530(5)	5.4587(5)	5.4787(1)	5.515
V (Å^3)	441.67(7)	443.74(7)	448.89(1)	436.69
R_{wp} (%)	5.95(λ=2.37150 Å)	4.62(λ=1.33037Å) 2.28 (X-ray, Kα$_1$)	4.38 (λ=1.33037 Å) 4.05 (λ=2.37150 Å)	
Magnetic moments (μ_B)				
Mn	3.6(2)	2.7(1)		
Fe	4.2(2)	3.3(1)		
R_{mag} (%)	5.40	8.61		

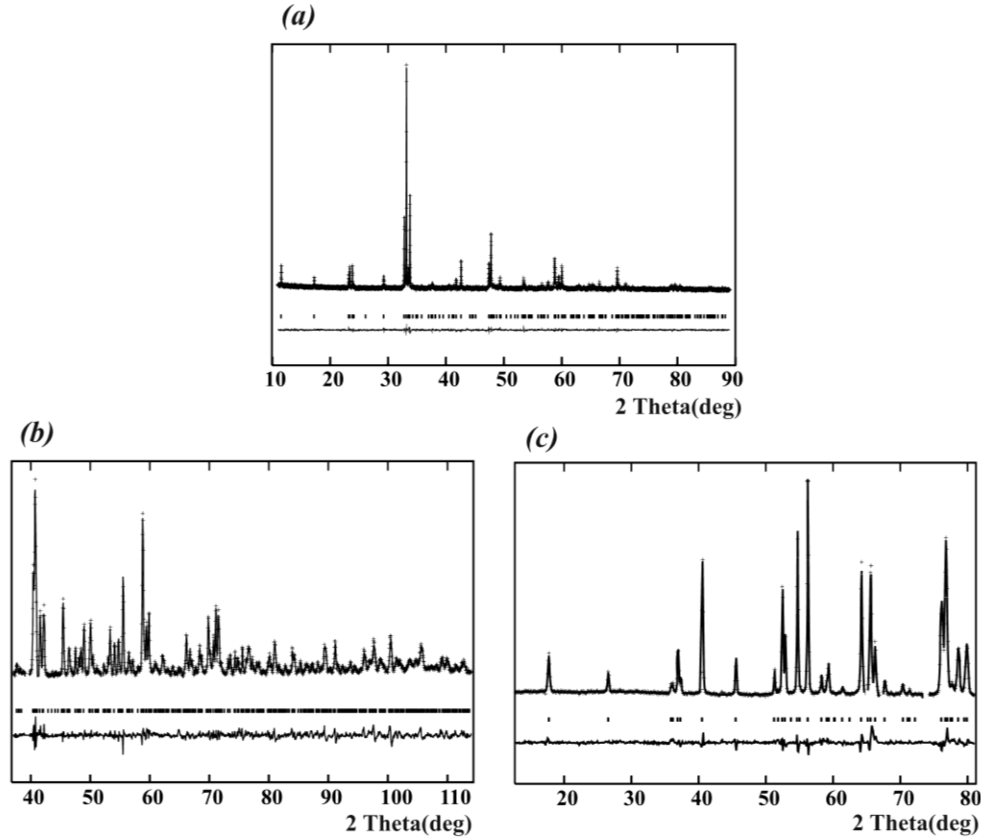

Figure 4.3. Rietveld refinements of (a) powder X-ray diffraction data with λ = 1.54056 Å, (b) fine collimation neutron diffraction data with λ = 1.33037 Å, (at 550 K) and (c) neutron data with λ = 2.37150 Å (at 550 K). The black dots are the experimental data, the solid line the model, the vertical tic marks locate Bragg peak positions and the lower line is the difference plot.

The refinement was first performed on the powder X-ray diffraction data to obtain the cell parameters and metal positions to be used as input for refinement of the neutron data. Neutron diffraction has significant advantages here, as unlike for X-ray diffraction, there exists a strong contrast between Mn and Fe due to a very large difference between their scattering lengths: 9.45(2)fm for Fe and −3.75(2)fm for Mn. There were three very weak peaks in the neutron data indicating a very small amount of a side product that could not be identified due to its low concentration and possible peak overlaps. These peaks were excluded for the final refinement. Fig. 4.3 shows the observed, calculated and difference profiles for X-ray data, long wavelength neutron data (λ=2.37150Å) and fine collimation short wavelength neutron data (λ=1.33037Å) at 550K, above the magnetic ordering temperature.

Initially, a fully ordered model with only Mn on the octahedral (O_h) site and Fe on the tetrahedral (T_d) site was refined as suggested in [17] . This resulted in a very large displacement factor, U_{iso}=0.150(8)Å^2 at the O_h site, more than 10 times the value of any other site displacement factor, R_{wp}=0.0664 and χ^2=2.50. Two other models were tried: (1) Fe was added to the O_h site and (2) Fe and Mn were distributed over both sites. The results for (1) gave 14.8% excess Fe on the O_h site with U_{iso}=0.006(4)Å^2, R_{wp}=0.0588 and χ^2=2.21. Model (2) gave for the contents of the O_h site, 86.8% Mn and 13.2% Fe, and for the T_d site, 90.6% Fe and 9.4% Mn with U_{iso} (O_h)=0.020(5)Å^2, U_{iso}(T_d)=0.0115(11), R_{wp}=0.0557 and χ^2 = 2.10. Model (2) results in a slight excess of Fe, 4% overall. It is difficult to choose between (1) and (2) based only on the refinement results. Model (2) is closer to a 1:1 ratio for Fe and Mn as used in the synthetic mixture and there is no evidence for additional phases at the level of ~15% which would be demanded for Model (1). Thus, Table 4.2 gives a list of the atomic positions, site occupancies and the thermal displacement factors based on (2). Also a list of selected bond lengths and angles is given in Table 4.3.

Table 4.2. The atomic coordinates, site occupancies and displacement factors for $Ca_2Fe_{1.039(8)}Mn_{0.962(8)}O_5$ at 550 K

Atom	*x*	*y*	*z*	Occupancy	U_{iso} (Å^2)
Ca1	–0.012(1)	0.1101(2)	0.4802(8)	1.0	0.015(1)
Fe1	0.9484(7)	0.25	0.9353(6)	0.907(6)	0.012(1)
Mn1	0.0	0.0	0.0	0.868(5)	0.020(5)
Fe2	0.0	0.0	0.0	0.132(5)	0.020(5)
Mn2	0.9484(7)	0.25	0.9353(6)	0.094(6)	0.012(1)
O1	0.257(1)	–0.0125(2)	0.2388(6)	1.0	0.016(1)
O2	0.0210(7)	0.1424(2)	0.0653(6)	1.0	0.020(1)
O3	0.089(1)	0.25	0.6156(9)	1.0	0.024(2)

Table 4.3. Selected bond lengths (Å) and angles (°) for $Ca_2Fe_{1.039(8)}Mn_{0.962(8)}O_5$ at 550 and 300K […]

Mn1(Fe2) – O1	1.903(5) × 2 [1.901(6)]
Mn1(Fe2) – O1	1.939(5) × 2 [1.929(6)]
Mn1(Fe2) – O2	2.223(3) × 2 [2.206(5)]
Fe1(Mn2) – O2	1.844(3) × 2 [1.845(5)]
Fe1(Mn2) – O3	1.905(5) [1.905(8)]
Fe1(Mn2) – O3	1.935(5) [1.923(9)]
O1 – Mn1(Fe2) – O1	92.15(2) × 2 [92.2(4)]
O1 – Mn1(Fe2) – O1	87.85(2) × 2 [87.8(4)]
Mn1(Fe2) – O1 – Mn1(Fe2)	167.8(2) [167.2(2)]
O2 – Fe1(Mn2) – O2	127.8(3) [127.8(4)]
O2 – Fe1(Mn2) – O3	105.8(2) × 2 [105.4(5)]
O2 – Fe1(Mn2) – O3	105.3(2) × 2 [105.7(5)]
O3 – Fe1(Mn2) – O3	104.8(2) [104.9(6)]
Fe1(Mn2) – O3 – Fe1(Mn2)	121.4(3) [121.5(5)]

Table 4.4. Distortion indices for various Ca-based brownmillerites of Fe^{3+} and Mn^{3+}.

Compound	Distortion index (see text)	Reference
Ca_2AlFeO_5	1.096	[5]
Ca_2GaFeO_5	1.084	[22]
$Ca_2Fe_2O_5$	1.084 (1.078)	[3,23]
Ca_2FeMnO_5	1.157	This work
Ca_2AlMnO_5	1.185	[24]
Ca_2GaMnO_5	1.172	[24]

In the octahedral layers the bonds parallel to the layers (equatorial bonds) are significantly shorter than those out of the planes (axial bonds). While it is tempting to attribute this to a static Jahn–Teller distortion, as the octahedral site mainly contains Mn^{3+}, in fact similar elongations are observed in most brownmillerites, even those for which the octahedral site contains only Fe^{3+}, a non-Jahn–Teller ion. In Table 4.4 the distortion indices (defined as the ratio of the axial bond length to the average equatorial bond length) are listed for Ca-based brownmillerites containing both Fe^{3+} and Mn^{3+} on the octahedral site. The index is significantly greater for the Mn^{3+} materials, indicating a role for a static Jahn–Teller component. The octahedra in $Ca_2Fe_{1.039(8)}Mn_{0.962(8)}O_5$ are distorted and octahedral angles show deviations of ~2° from the ideal angle of 90°. This is similar to the average deviation of bond angles in $Ca_2Fe_2O_5$, although the bond angles are distributed over a wider range in that compound [3].

In contrast to the octahedral layers, in the tetrahedral layers of $Ca_2Fe_{1.039(8)}Mn_{0.962(8)}O_5$ the bonds parallel to the layers (connected to the oxygens which are shared between two tetrahedra) are longer than the bonds out of the plane (connected to the oxygens shared between a tetrahedron and an octahedron). The tetrahedra are also distorted and deviations from the ideal angles of more than 4° are observed. The iron-only compound, $Ca_2Fe_2O_5$ shows a compression of the tetrahedra along the *b*-axis as well [3]. The distortion of the tetrahedra in that compound is less than that of $Ca_2Fe_{1.039(8)}Mn_{0.962(8)}O_5$.

The metal–oxygen bond distances obtained for $Ca_2Fe_{1.039(8)}Mn_{0.962(8)}O_5$ are consistent with tetrahedral Fe–O and octahedral Mn–O bond distances found in brownmillerites [3,15] .

Bond valence calculations [25] give 3.164 for Mn and 2.885 for Fe which are in good agreement with the expected bond valence, 3, for both ions.

The unit cell parameters, especially the *b*-axis, for $Ca_2Fe_{1.039(8)}Mn_{0.962(8)}O_5$ differ markedly from those obtained previously [17] , and the cell volume here is 1.4% larger. This indicates that the oxygen content of the sample in [17] is significantly greater than the sample here. Attempts to measure the oxygen content using reductive thermal gravimetry by heating the sample in a pure hydrogen gas stream at 900°C resulted in a mixture of reduction products and the result was inconclusive. However, the study of $Ca_2GaMnO_{5+\delta}$ is relevant where a correlation was established between the unit cell volume and δ [26]. This calibration can be used to estimate δ in $Ca_2FeMnO_{5+\delta}$ for the sample in [17] which is ~0.2, a substantial level of oxidation.

Magnetic properties.

The zero field cooled/field cooled (ZFC/FC) magnetic susceptibility data at a temperature range of 5–300K are shown in Fig. 4.4 a. The remarkable features in this diagram are a sudden increase in susceptibility at 125K and the ZFC/FC divergence. The origin of these features is unclear. Susceptibility data were also collected in the range of 300–700K (Fig. 4.4 b). These data show a broad feature at 470K, as well as a divergence between the data obtained from heating and cooling. However, these features can only correspond to short range ordering and no sharp transition was observed. Therefore, the magnetic transition temperature could not be found using the SQUID magnetometry data. Consequently, neutron diffraction was employed to study the magnetic properties as will be discussed later. A possible contamination of the sample by even small quantities of a magnetic side product can dominate the susceptibility data, and can also be partially responsible for some features such as ZFC/FC divergences.

The isothermal magnetization data were also collected at various temperatures (Fig. 4.5). A very weak hysteresis is present at 5, 50 and 310K but the data at 500K are linear and show no hysteresis, consistent with a typical paramagnetic system. Results for $Ca_2Fe_2O_5$ at 300K, where spin canting is known to be present, are included for comparison indicating that there is little evidence for significant sublattice canting in $Ca_2Fe_{1.039(8)}Mn_{0.962(8)}O_5$.

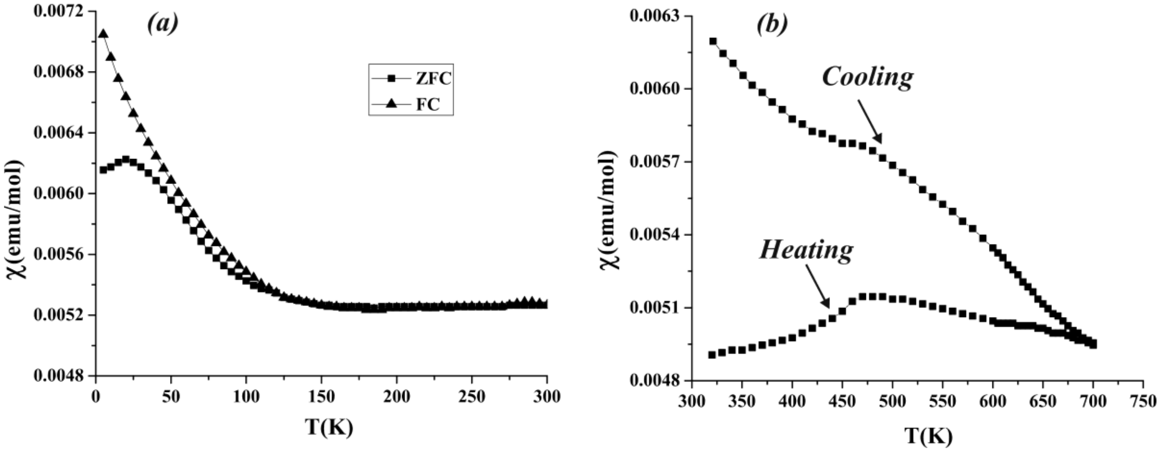

Figure 4.4. (a) ZFC and FC molar susceptibility data within the temperature range of 5–300K. Note the sudden upturn below 125 K. (b) The susceptibility data collected in furnace by heating and cooling in the field. The same feature is observed in both heating and cooling data at about 470 K.

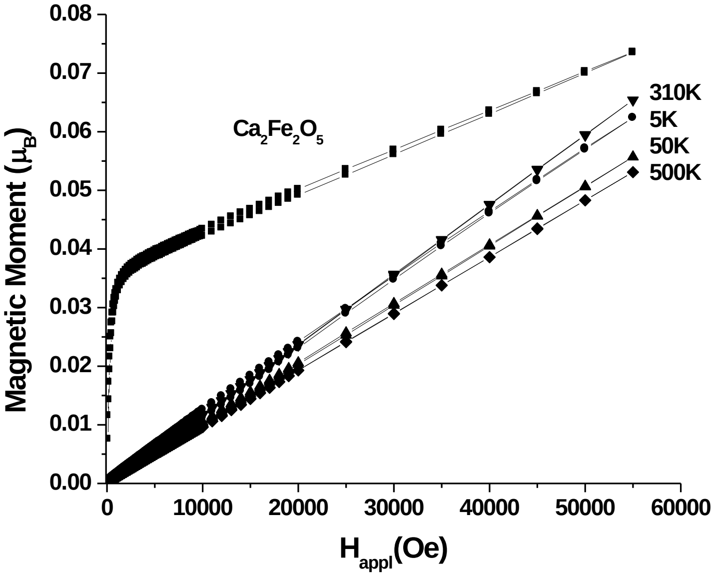

Figure 4.5. Isothermal magnetization versus applied field behavior for Ca_2MnFeO_5 at various temperatures. Very weak hysteresis is observed at 5, 50 and 310 K. The 500 K data show a typical paramagnetic behavior. Results for $Ca_2Fe_2O_5$ at 300K are shown for comparison.

Neutron Diffraction

Data were collected from 3.8 to 700K, spanning the range of the susceptibility data. Fig. 4.6 shows data at 3.8K where a number of magnetic reflections can be identified. The most significant of these (which are more intense than any structural reflections) appear at 30.99° and 31.60° and are indexed as (021)/(0−21) and (120)/(1−20), respectively. The other magnetic peaks are at 27.40° indexed as (110)/(1−10), 37.51° indexed as (−1−11)/(−111)/(1−11)/(111), 61.74° indexed as (−1−22)/(−122)/(1−22)/(122) and 62.83° indexed as (−2−21)/(−221)/(2−21)/(221). There is also a small peak at 38.2° that disappears at 149.5K and is possibly related to the side product.

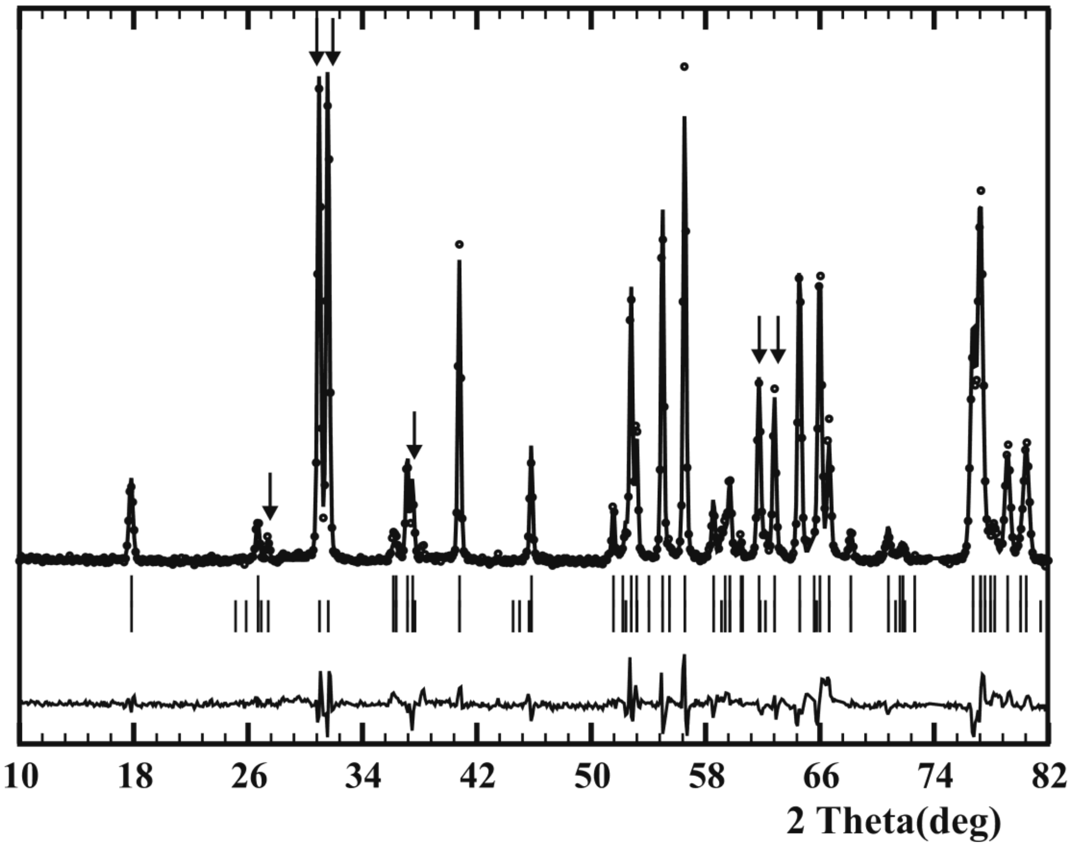

Figure 4.6. The refinement result for the magnetic structure of $Ca_2Fe_{1.039(8)}Mn_{0.962(8)}O_5$ at 3.8K. The most significant magnetic peaks are marked by arrows. The black dots are the experimental data; the solid line the model; two rows of the vertical tic marks locate Bragg peak positions for the crystal (top) and magnetic (bottom) structures and the lower line is the difference plot. The magnetic structure is confirmed as G-type (see Fig. 4.2) with the preferred moment direction along *b*. R_{mag}=0.054 and the ordered moments on the octahedral and tetrahedral sites are 3.64(16) and 4.22(16)μ_B, respectively.

The magnetic structure of $Ca_2Fe_{1.039(8)}Mn_{0.962(8)}O_5$ was determined by refining the neutron diffraction data using the FullProf program [27], employing WinPLOTR [28]. A G-type magnetic structure model, Fig. 4.2, was verified. Fig. 4.6 shows the refinement results, R_{mag}=0.054, for the magnetic structure. The spins on each site are oriented along the *b*-direction. The magnetic structure determined by neutron diffraction confirms that proposed from the Mössbauer study but of course provides much more detail [18].

By following the temperature dependence of the magnetic peak intensities, the critical temperature for long range order can be determined. The magnetic reflections disappear between 405 and 410K. Plotting the refined magnetic moments of the *M* (mostly Mn^{3+}) and *M′* (mostly Fe^{3+}) sites as a function of temperature indicates T_c=407(2)K (Fig. 4.7). The ordered moments on the *M* and *M′* sites at 3.8K are 3.64(16) and 4.22(16)μ_B, respectively, which agree reasonably with the spin only values, 2*S*, for Mn^{3+}(*S*=2) and Fe^{3+}(*S*=5/2), given some level of intersite mixing.

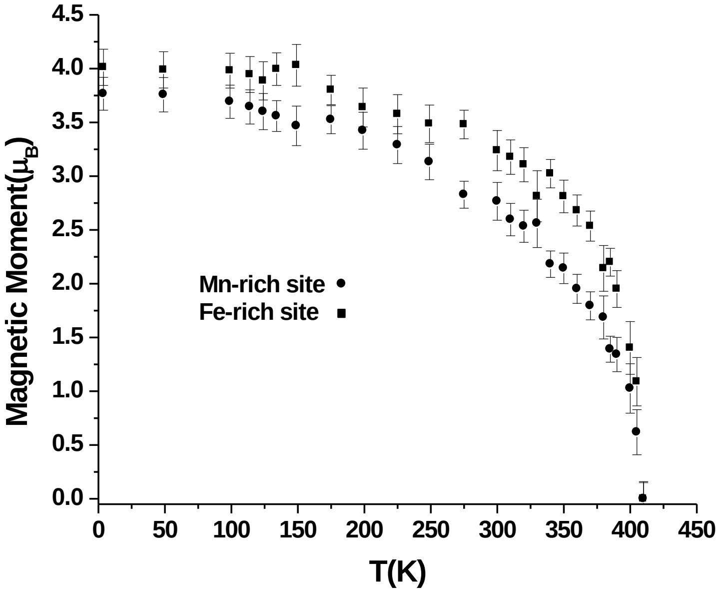

Figure 4.7. Magnetic moments of Mn and Fe sites as functions of temperature. Note that the moments approach zero at about 407K, indicating the magnetic transition temperature.

Above the transition temperature no long range ordering exists. However the presence of diffuse magnetic scattering at temperatures as high as 440K (Fig. 4.8) is an indication of the presence of short range magnetic correlations which could explain in part the bulk susceptibility data which show no feature at T_c. Nonetheless, the bulk susceptibility is still difficult to understand and clearly provides little useful information regarding the true magnetic properties of this material. The presence of a small concentration of $Ca_2Fe_2O_5$ which would be difficult to detect due to peak overlap with Ca_2MnFeO_5 and which has T_c=725K and a weak ferromagnetic moment is a possible explanation of the bulk data.

The magnetic structure of $Ca_2Fe_{1.039(8)}Mn_{0.962(8)}O_5$ can be explained based on the principles of the superexchange mechanism. In this case the superexchange interactions will involve contributions from both t_{2g} and e_g orbitals [29]. Antiferromagnetic coupling of spins between two d^4, and two d^5 ions is expected as both σ and π superexchange pathways predict an antiparallel coupling of the two ions [30]. However the interaction between a d^4 and a d^5 ion in an ideal case (180°) can be ferromagnetic as the σ pathway of the superexchange will couple the two ions ferromagnetically [30]. However, crystal structural factors in $Ca_2Fe_{1.039(8)}Mn_{0.962(8)}O_5$ can diminish the ferromagnetic interactions. The distortion of superexchange pathways from linear is an important factor that needs to be taken into account. The M–O–M and M'–O–M' angles show large deviations from 180° (Table 4.3). It should be noted that even though some mixing of ions exists, the majority of octahedral sites are still occupied by Mn and the majority of tetrahedral sites are occupied by Fe, and therefore the Mn–Fe interactions are mostly inter-layer interactions. The inter-layer superexchange angle M–O–M' is 144.35°, a significant distortion from linearity. These distortions are direct results of the layered structure of brownmillerites. Unlike the perovskite structure that involves corner sharing of only octahedra, the brownmillerite structure needs to accommodate the corner sharing of both octahedra and tetrahedra and that imposes a large amount of twisting to the bond angles. The geometric features of tetrahedra do not allow the formation of linear bond angles while corner sharing with other tetrahedra and octahedra exists.

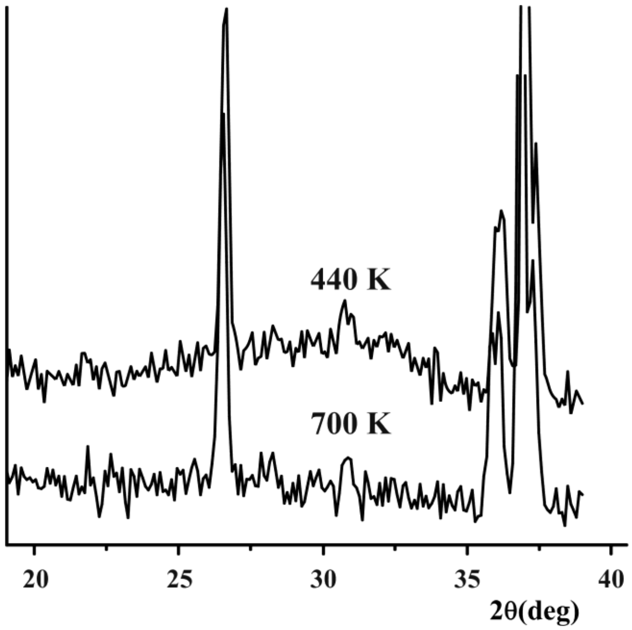

Figure 4.8. Diffuse magnetic scattering at 440 K, compared to the data at 700 K. A noticeable hump appears at 440 K within 27–35° region, but is absent at 700 K.

Summary and conclusions

The crystal and magnetic structures of the brownmillerite compound $Ca_2Fe_{1.039(8)}Mn_{0.962(8)}O_5$ were determined. Neutron diffraction showed small levels of mixing of Mn and Fe in both octahedral and tetrahedral sites and an overall ~4% Fe excess. The compound shows a long range antiferromagnetic ordering below the transition temperature, 407(2)K. The magnetic structure of this compound involves both intra- and inter-layer antiferromagnetic coupling of nearest neighbor spins forming a G-type magnetic structure. The ordered moments at 3.8K are 3.64(16) and 4.22(16)μ_B for the octahedral and tetrahedral sites, respectively. The possible intra-layer Fe^{3+}–Mn^{3+} ferromagnetic coupling predicted by the superexchange mechanism is not evident due perhaps to the large deviations from linearity of superexchange pathways as a result of the structural constraints of a brownmillerite system.

Acknowlegements

We thank the Natural Sciences and Engineering Research Council of Canada for a Discovery Grant to J.E.G. and Major Resource Access Grants to the Canadian Neutron Beam Centre and the Brockhouse Institute for Materials Research.

References

[1] J. Malveiro, T. Ramos, L.P. Ferreira, J.C. Waerenborgh, M.R. Nunes, M. Godinho, M.D. Carvalho, J. Solid State Chem. 180 (2007) 1863–1874.

[2] E.F. Bertaut, P. Blum, A. Sagnieres, Acta Crystallogr. 12 (1959) 149–159 (PNMA).

[3] J. Berggren, Acta Chem. Scand. 25 (1971) 3616–3624.

[4] D.K. Smith, Acta Crystallogr. 15 (1962) 1146–1152 (IMMA).

[5] A.A. Colville, S. Geller, Acta Crystallogr. B 27 (1971) 2311–2315 (IBM2).

[6] F. Lindberg, S.Y. Istomin, P. Berastegui, G. Svensson, S.M. Kazakov, E.V. Antipov, J. Solid State Chem. 173 (2003) 395–406.

[7] C. Greaves, A.J. Jacobson, B.C. Tofield, B.E.F. Fender, Acta Crystallogr. B 31 (1975) 641–646.

[8] S. Lambert, H. Leligny, D. Grebille, D. Pelloquin, B. Raveau, Chem. Mater. 14 (2002) 1818–1826.

[9] K. Fukuda, H. Ando, J. Am. Ceram. Soc. 85 (2002) 1300–1302.

[10] G.J. Redhammer, G. Tippelt, G. Roth, G. Amthauer, Am. Mineral. 89 (2004) 405–420.

[11] T. Hirone, J. Appl. Phys. 36 (1965) 988–992.

[12] T. Takeda, Y. Yamaguchi, S. Tomiyoshi, M. Fukase, M. Sugimoto, H. Watanabe, J. Phys. Soc. Jpn. 24 (1968) 446–452.

[13] P. Berasteguil, S.G. Eriksson, S. Hull, Mater. Res. Bull. 34 (1999) 303–314.

[14] D.V. Sheptyakov, A.M. Abakumov, E.V. Antipov, A.M. Balagurov, S.J.L. Billinge, P. Fischer, L. Keller, M.V. Lobanov, B.Ph. Pavlyuk, V.Yu. Pomjakushin, M.G. Rozova, Appl. Phys. A 74 (2002) S1734–S1736.

[15] A.J. Wright, H.M. Palmer, P.A. Anderson, C. Greaves, J. Mater. Chem. 12 (2002) 978–982.

[16] A.J. Wright, H.M. Palmer, P.A. Anderson, C. Greaves, J. Mater. Chem. 11 (2001) 1324–1326.

[17] Y. Nakahara, S. Kato, M. Sugai, Y. Ohshima, K. Makino, Mater. Lett. 30 (1997) 163–167.

[18] A.I. Rykov, K. Nomura, Y. Ueda, A.N. Vasiliev, J. Magn. Magn. Mater. 320 (2008) 950–956.

[19] P.W. Selwood, Magnetochemistry, second ed., Interscience Publishers, Inc., New York, 1996.

[20] A.C. Larson, R.B. Von Dreele, General Structure Analysis System (GSAS), Los Alamos National Laboratory Report LAUR, 1994, pp. 86–748.

[21] B.H. Toby, J. Appl. Crystallogr. 34 (2001) 210–213.

[22] R. Arpe, Hk. Müller-Buschbaum, R.V. Schenck, Z. Anorg. Allg. Chem. 410 (1974) 97–103.

[23] P. Berastegui, S.-G. Eriksson, S. Hull, Mater. Res. Bull. 34 (1999) 303–314.

[24] A.M. Abakumov, M.G. Rozova, E.V. Antipov, Russ. Chem. Rev. 73 (2004) 847–860.

[25] I.D. Brown, D. Altermatt, Acta Crystallogr. B 41 (1985) 244–247.

[26] A.M. Abakumov, M.G. Rozova, B.Ph. Pavlyuk, M.V. Lobanov, E.V. Antipov, O.I. Lebedev, G. van Tendeloo, D.V. Sheptyakov, A.M. Balagurov, F. Bouree, J. Solid State Chem. 158 (2001) 100.

[27] T. Roisnel, J. Rodriguez-Carvajal, FULLPROF ver 1.9c: Rietveld, Profile Matching & Integrated Intensity Refinement of X-ray and/or Neutron Data, Laboratoire Léon Brillouin, Saclay, France, 2001.

[28] T. Roisnel, J. Rodrı´guez-Carvajal, WinPLOTR: a Windows tool for powder diffraction patterns analysis, in: R. Delhez, E.J. Mittenmeijer (Eds.), Proceedings of the Seventh European Powder Diffraction Conference (EPDIC 7), Materials Science Forum, 2000, pp. 118–123.

[29] R.L. Martin, in: H.J. Emeleus (Ed.), New Pathways in Inorganic Chemistry, Cambridge University Press, Cambridge, 1968.

[30] J.B. Goodenough, Magnetism and the Chemical Bond, Interscience, New York, 1963.

Chapter 5

Intra-layer Cation Ordering in a Brownmillerite Super-Structure: Synthesis, Crystal and Magnetic Structures of Ca_2FeCoO_5

This chapter encompasses the manuscript "Intra-layer Cation Ordering in a Brownmillerite Super-Structure: Synthesis, Crystal and Magnetic Structures of Ca_2FeCoO_5" published in "Chemistry of Materials", volume 22 (2010), pages 6008–6020: http://dx.doi.org/10.1021/cm1023025

It includes the synthesis, crystal and magnetic structure studies of the first brownmillerite material with intra-layer cation ordering and temperature dependent spin re-orientation.

The candidate performed the synthesis of this material, bulk magnetization, crystal and magnetic structure studies, and preparation of the manuscript.

Reprinted with permission from "Ramezanipour, F., Greedan, J. E., Grosvenor, A.P., Britten, J.F., Cranswick, L.M.D., Garlea, V.O. (2010) Chemistry of Materials. 22: 6008–6020". Copyright 2010 American Chemical Society.

Intra-layer Cation Ordering in a Brownmillerite Super-Structure: Synthesis, Crystal and Magnetic Structures of Ca_2FeCoO_5

Farshid Ramezanipour[1,2], John E. Greedan*[1,2], Andrew P. Grosvenor[3], James F. Britten[1,2], Lachlan M.D. Cranswick[4], V. Ovidiu Garlea[5]

[1]Department of Chemistry, McMaster University, Hamilton, Ontario, Canada, L8S 4M1

[2]Brockhouse Institute for Materials Research, McMaster University, Hamilton, Ontario, Canada L8S 4M1

[3]Department of Chemistry, University of Saskatchewan, Saskatoon, Saskatchewan, Canada S7N 5C9

[4]Canadian Neutron Beam Centre, National Research Council, Chalk River Laboratories, Chalk River, Ontario, Canada K0J 1J0

[5]Neutron Scattering Sciences Division, Oak Ridge National Laboratory, Oak Ridge, Tennessee 37831, United States

* Corresponding author at: Department of Chemistry, McMaster University, Hamilton, Ontario, Canada L8S 4M1.

E-mail address: greedan@mcmaster.ca

Key Words: Ca_2FeCoO_5, brownmillerite, intra-layer cation ordering, spin re-orientation, crystal and magnetic structure, neutron diffraction.

Abstract

The synthesis, crystal, and magnetic structures and the bulk magnetic properties of Ca_2FeCoO_5, a brownmillerite type oxide, are presented. The crystal structure, solved and refined from single crystal X-ray and powder neutron diffraction data, is described in *Pbcm* with cell parameters, a = 5.3652(3) Å, b = 11.0995(5) Å, c = 14.7982(7) Å. Thus, one axis, b in this setting, is doubled in comparison with the standard brownmillerite structure description giving rise to two sets of octahedral and tetrahedral sites. Aided by the strong scattering contrast between Fe and Co for neutrons, a nearly perfect intralayer cation site ordering, not observed for any brownmillerite before, is detected in the tetrahedral layers. There is a lesser degree of cation site ordering in the octahedral sites. Overall, the Fe/Co site ordering is of the NaCl type both within and between the tetrahedral and octahedral layers. There are also both intra- and interlayer ordering of tetrahedral chain orientations. The left- and right-handed orientations alternate within each tetrahedral layer as well as between the closest tetrahedral layers. The occurrence of the rare *Pbcm* space group in Ca_2FeCoO_5 is not consistent with a recently proposed structure-field map for brownmillerite oxides. The magnetic structure is G-type antiferromagnetic, with preferred orientation of magnetic moments parallel to the longest axis between 3.8 K to 100 K which switches to the shortest axis between 225 K and 550 K. The neutron diffraction data indicate different site specific ordering temperatures at about 450(5) K and 555(5) K. The refined ordered moments at 3.8 K are somewhat smaller than expected for Fe^{3+} and Co^{3+}(high spin) but are similar to those found in

Sr_2FeCoO_5. There is evidence for spin canting from isothermal magnetization data that shows well pronounced hystereses and remnant magnetizations at 5 K and 200 K.

Introduction

Oxides with perovskite type structures exhibit a wide range of physical properties, making them strong candidates for both fundamental studies and technological applications. Colossal magnetoresistance, metal−insulator transitions, and superconductivity are just some of the interesting properties observed in these materials.[1-7] An understanding of the parameters that govern and control the structure and physical properties of these compounds can help to design materials with the properties desired for a particular application.

The formula of perovskite is ABO_3, where BO_6 octahedra condense to form a three-dimensional network of corner sharing octahedra with the A cations residing in the interstitial spaces. A number of perovskite based superstructures exist due to crystallographic ordering of for example cations on the A or B sites, $AA'B_2O_6$ or $A_2BB'O_6$, which have been studied extensively.[8-11] As well, superstructures exist in oxygen deficient perovskites with formula $A_2BB'O_5$, due to ordering of oxide vacancies. One of the most common superstructures of this type is that of brownmillerite, in which layers of corner sharing BO_6 octahedra are separated by chains of corner sharing $B'O_4$ tetrahedra.

The cell parameters of a brownmillerite are related to the perovskite structure in the following way: $a_b \approx \sqrt{2}a_p$, $b_b \approx 4a_p$, $c_b \approx \sqrt{2}a_p$. The most common space groups for typical brownmillerites are *Pnma*, *I*2*mb*, and *Imma*. These space groups refer to an unit cell setting where $b > c > a$. Various authors have chosen different settings of the unit cell leading to a variety of equivalent but somewhat confusing space group settings. Table 5.1 shows these common space groups and their different settings. The space groups of brownmillerite compounds are determined by the relative orientation of tetrahedral chains.[12-14] They can adopt two orientations that are mirror images of each other and are assigned arbitrary labels of left handed (L) and right handed (R). If all tetrahedral chains have the same orientation throughout the structure, the space group *I*2*mb* is obtained. If the long-range orientation is the same within a layer but opposite to the neighboring layer, *Pnma* results. There is also a much less common arrangement, previously observed only in $La_{1-x}A_xMnO_{2.5}$ ($x = 0.2-0.4$ for A = Sr, Ba and $x = 0.2-0.3$ for A = Ca)[12] consisting of both intra- and interlayer ordering of R and L chains which can result in the *C2/c* or *Pcmb* (*Pbcm*) space groups. Lastly, if chain orientations are long-range disordered, space group *Imma* occurs. In addition, a modulated distribution of tetrahedral chains has been suggested for $Ca_2Co_{2-x}Al_xO_5$, using the formalism of (3+1)-dimensional crystallography.[14] Also, local alternation of R and L chains within a layer has been studied for $Sr_2MnGaO_{4.97}$.[15] The intra- and interlayer chain configurations for *I2mb, Pnma*, and *Pcmb* are shown in Figure 5.1.

Table 5.1. Common brownmillerite space groups and their different settings

Compound	$b > c > a$	$b > a > c$	$c > b > a$	$a > b > c$
$Ca_2Fe_2O_5$ [16]	*Pnma*^{a} [#62]	*Pcmn*		
Sr_2GaMnO_5 [45]	*I2mb* [#46]	*Ibm*2		*Ima*2^a
Sr_2FeCoO_5 [29], $Sr_2Fe_2O_5$ [18]	*Imma*^{a} [#74]	*Icmm*		
$La_{2-x}Sr(Ca)_xMn_2O_5$(x=0.7,0.8)[12]	*Pcmb* [#57]		*Pbcm*^{a}	

^{a} Denotes standard setting International Tables

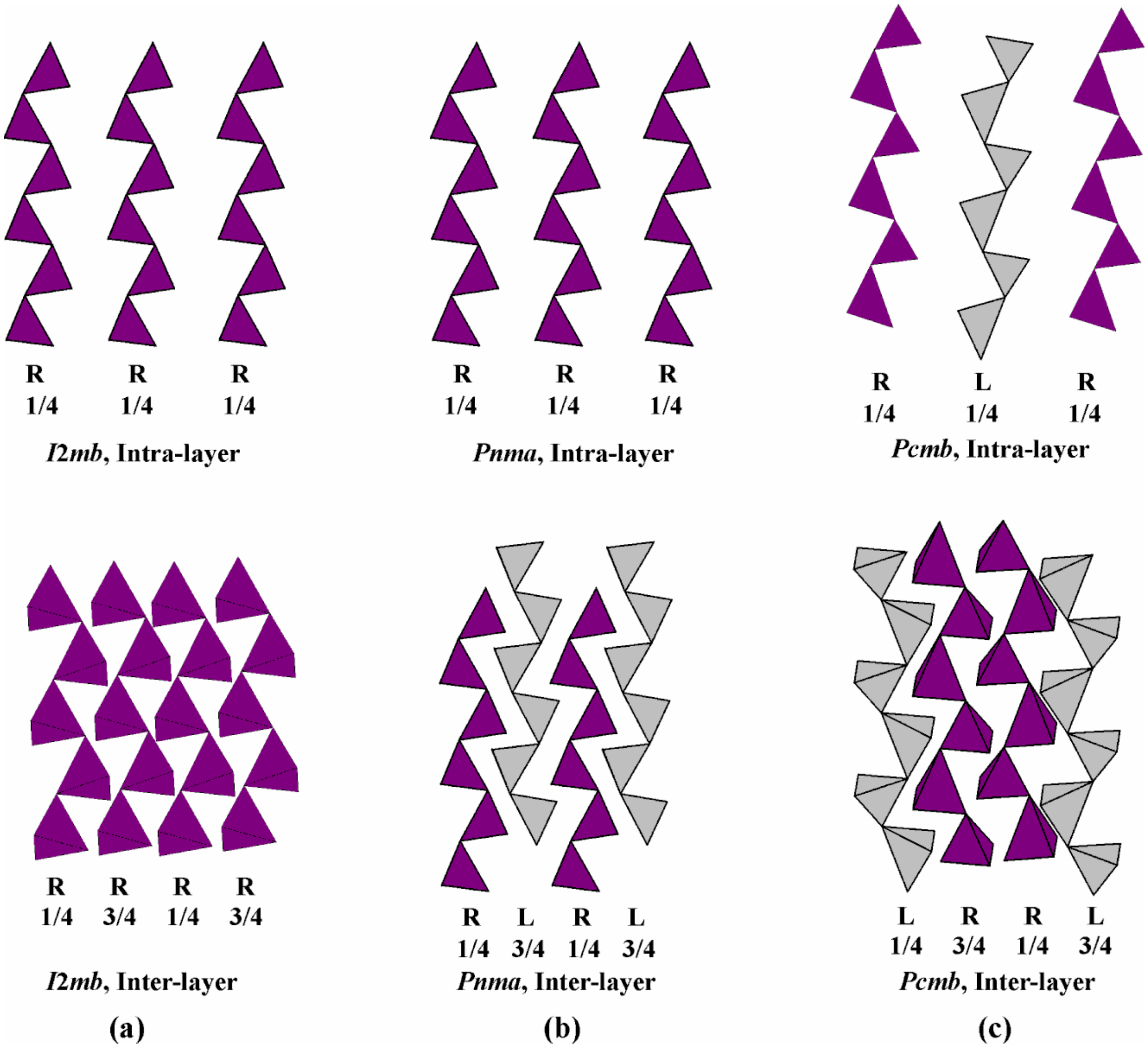

Figure 5.1. Schematic illustration of relative orientations of tetrahedral chains in brownmillerites. The common arrangements are shown in (a) and (b), while that for *Pcmb*, is shown in (c). The top figure in each shows the chain orientations in one tetrahedral layer, at $y = 1/4$, with the *a*-axis vertical and the *c*-axis horizontal. The bottom figure shows a view roughly along the *b*-axis for two layers at $y = 1/4$ and 3/4. In *I*2*mb*, (a), the chains have the same orientation within a layer and between the layers. In *Pnma*, (b), the chains have the same orientation within a layer but opposite orientation relative to the neighboring layer. In *Pcmb*, (c), the chains have opposite orientations relative to the neighboring chains within the same layer and in the adjacent layer.

A number of oxygen deficient perovskites with Fe or Co on the B-site have been studied previously. $Ca_2Fe_2O_5$ is one of the well-known brownmillerite compounds which crystallizes in *Pnma*.[16] $Sr_2Fe_2O_5$ also has a brownmillerite structure, with two reported space groups *Ibm*2 (*I*2*mb*) [17] and *Imma* although it has been shown that the latter is correct.[13, 18] Both Ca and Sr compounds can be synthesized using standard solid state methods. The long-range ordering of oxygen vacancies in both of these materials is accompanied by long-range antiferromagnetic ordering of spins.[17, 18, 19-21]

$Ca_2Co_2O_5$, with Co on the B-site, has been synthesized by different methods including thermal decomposition of solid-solution precursors, molten salt methods, and the citrate sol−gel process.[22-24] These methods were chosen to avoid problems associated with solid state synthesis of this compound, due to higher decarbonation temperature of the raw materials compared to the phase formation temperature.[23, 24] The structure of this compound is not known in detail, but it is proposed to incorporate alternating square pyramidal and octahedral layers. Thermoelectric properties of this material have been of interest.[23-26] Recently, thin films of $Ca_2Co_2O_5$ deposited on a $NdGaO_3$ substrate by pulsed laser deposition were prepared.[27] Based on an electron microscopy study, the structure of the thin film was suggested to be brownmillerite type, with long-range ordering of O-vacancies and alternating octahedral and tetrahedral layers.[27] The Sr analogue, $Sr_2Co_2O_5$, has been studied as well. The crystal structure of this compound has been described as brownmillerite, *Ima*2 (*I*2*mb*), at room temperature.[28] However, it undergoes several structural phase transitions between room temperature and 1200 °C.[28]

It is also possible to mix both Fe and Co on the B/B′ sites. An *Icmm* brownmillerite structure has been assigned for Sr_2FeCoO_5 that was synthesized more than two decades ago.[29] Also, there have been reports of the formation of Ca_2FeCoO_5 as a result of thermal decomposition of carbonate or hydroxide precursors with unit cell dimensions a = 5.372 Å, b = 14.779 Å, and c = 11.123 Å and space group $P2_12_12_1$. Note the doubling of the *c*-axis.[22, 30]

In this paper, preparation of single crystals of Ca_2FeCoO_5 is reported. The availability of single crystals enabled solution of the structure by single crystal X-ray diffraction. Powder neutron diffraction data showed intralayer ordering of Fe and Co atoms between the tetrahedral sites which was not detected by X-rays. The bulk magnetic properties were studied from 5 K to 700 K. Neutron diffraction measurements were performed at several temperatures, from 3.8 K to 565 K, to determine the magnetic structure and show a temperature dependent spin reorientation.

Experimental Section

Synthesis. Accurately weighed $CaCO_3$ (99.99% Alfa Aesar), Fe_2O_3 (99.99% Alfa Aesar), and CoO (99.5% Cerac), with 4:1:2 molar ratio, were mixed and ground to fine powder. Pellets were made and sintered at 1100 °C in air for 24 h. The heating and cooling rates for this step and all subsequent refirings were 100 °C/hour. The sample (usually 1 to 2 g) was then reground and refired at 1200 °C in air for 48 h. After a final regrinding, the sample was sintered at 1250 °C in air for 48 h. Single crystals of Ca_2FeCoO_5 resulted from this procedure which proved to be suitable for single crystal X-ray diffraction studies. In all steps an alumina crucible covered by a platinum sheet was used as sample container.

X-ray and Neutron diffraction.

Single crystal X-ray diffraction data were obtained on a Bruker Mo Smart APEX2 diffractometer with a wavelength of 0.7107 Å and θ range of 2.76° to 45.34°. Limiting indices were $-10 < h < 10$, $-22 < k < 15$, and $-29 < l < 23$.

A PANalytical X'Pert Pro MPD diffractometer with a linear X'Celerator detector was used to obtain the powder X-ray diffraction data. The data were collected with a 2θ step interval of 0.0084° using $CuK\alpha_1$ radiation ($\lambda = 1.54056$ Å).

Powder neutron diffraction measurements below 300 K were performed on the C2 diffractometer at the Canadian Neutron Beam Centre at Chalk River, Ontario. The data were collected at ten different temperatures from 3.8 K to 300 K. A wavelength of 2.373 Å with 2θ step size of 0.100° was used to collect data within the 2θ range of 4.4° to 83.6° and a wavelength of 1.331 Å with the same 2θ step size for the data from 34.9° to 114.6°. Neutron powder diffraction data above 300 K were collected using the HB2A diffractometer, at the High Flux Isotope Reactor at ORNL. Measurements were performed using an incident neutron wavelength of 2.41 Å, selected from the (113) plane of a vertically focusing Ge monochromator. A pyrolytic graphite (PG) filter was used to remove the higher order contamination of the beam. We used a 12′ Soller slit collimator in front of the monochromator and 21′ in front of the sample. The scattered neutrons were detected by an array of 44 equally spaced (~ 2.7°) ^{3}He detectors, each proceeded by a 6′ mylar foil collimator. For the data collection, the detector array was scanned to cover the total 2θ range of 8° to 130°, in steps of 0.05°. More details about the HB2A instrument and data collection strategies can be found in ref 31. Powder samples weighing about 3 g were placed in vanadium cans (8 mm i.d. by 5 cm) and loaded in a Janis top-loading CCR capable of achieving temperatures up to 700 K.

Magnetic property measurements. A Quantum Design MPMS SQUID Magnetometer was used to perform bulk magnetic measurements. The zero-field cooled and field cooled (ZFC/FC) magnetic susceptibility and isothermal magnetization data were obtained in the temperature range of 5 to 300 K on a powder sample in a gelatin capsule. The susceptibility data from 300 K to 700 K were obtained while heating the sample in a furnace using a quartz sample holder. Isothermal magnetization data from 0 to 5.5 T were also obtained at 5 K, 200 K, and 300 K.

Results and discussion

Crystal structure

Initially, a polycrystalline sample of Ca_2FeCoO_5 was studied using XRD data. The program GSAS [32] using EXPGUI interface [33] was used for refinement of the powder X-ray diffraction data. Refinements were attempted using the common space groups for brownmillerites, including *Pnma*, *Ibm*2, and *Imma* assuming the standard brownmillerite cell dimensions. However, in all cases there were extra peaks that could not be fitted to the models, indicating the possibility of a superlattice.

Table 5.2. X-ray single crystal results for Ca_2FeCoO_5 at 293 K[a]

Space group	*Pbcm*
Lattice parameters	*a* = 5.36750(10)Å *b* = 11.1072(3)Å *c* = 14.7787(3)Å V = 881.08(3) Å^3
Z	8
Agreement factors	*R(all data)* = 0.0668 *wR* = 0.0910

Atom	*x*	*y*	*z*	Occupancy	U_{iso} (Å^2)
Ca1	-0.01196(7)	0.76115(6)	0.39239(4)	1	0.00978(10)
Ca2	-0.48847(7)	0.51099(6)	0.60752(4)	1	0.00967(10)
Fe1	0.44810(8)	0.71773(3)	0.2500	1	0.00661(7)
Fe2	-0.05003(8)	0.53219(3)	0.2500	1	0.00659(7)
Co1	-0.50320(5)	0.7500	0.5000	1	0.00754(11)
Co2	0.0000	1.000	0.5000	1	0.00657(11)
O1	0.0937(3)	0.68961(17)	0.2500	1	0.0088(3)
O2	0.5961(3)	0.56069(17)	0.2500	1	0.0090(3)
O3	-0.2538(3)	0.6240(2)	0.48463(9)	1	0.00883(18)
O4	-0.7545(3)	0.6260(2)	0.48888(9)	1	0.00978(19)
O5	0.0207(3)	0.4672(2)	0.36023(15)	1	0.0120(4)
O6	0.5125(3)	0.7823(3)	0.36033(17)	1	0.0135(4)

[a] Note that Fe and Co could not be distinguished by X-rays, but the following arrangement, with Fe on the tetrahedral sites and Co on the octahedral sites gave a slightly better agreement factor. For powder neutron diffraction results see Tables 5.3 and 5.4.

After synthesizing single crystals of Ca_2FeCoO_5, an X-ray single crystal study was performed. The X-ray reflections could be indexed on a cell, *a* = 5.36750(10), *b* = 11.1072(3), *c* = 14.7787(3), that is, a supercell, two times the volume of that for a typical brownmillerite. Systematic absences were consistent with space group *Pbcm*. The program WinGX was used for solution and refinement of the single crystal structure.[34] The structure was initially solved in *P*1, and then symmetry was added so that all reflections could be explained using the highest symmetry. Table 5.2 shows the X-ray single crystal measurement results. These results confirm the larger cell reported in ref

26, but the correct space group, *Pbcm*, is now determined. Of course due to the very weak scattering contrast between Fe and Co using conventional X-rays, it was not possible to determine site preferences with confidence. It was found that a model with Fe on the tetrahedral sites and Co on the octahedral sites gave slightly smaller agreement indices and more satisfactory atomic displacement parameters as reported in Table 5.2. It should be noted that this space group, *Pbcm*, and unit cell, with one shorter axis doubled, is very rare among brownmillerite oxides, having been reported only quite recently for the materials $La_{2-x}Sr_xMn_2O_5$ and $La_{2-x}Ca_xMn_2O_5$ for $x = 0.70$ and 0.80.[12]

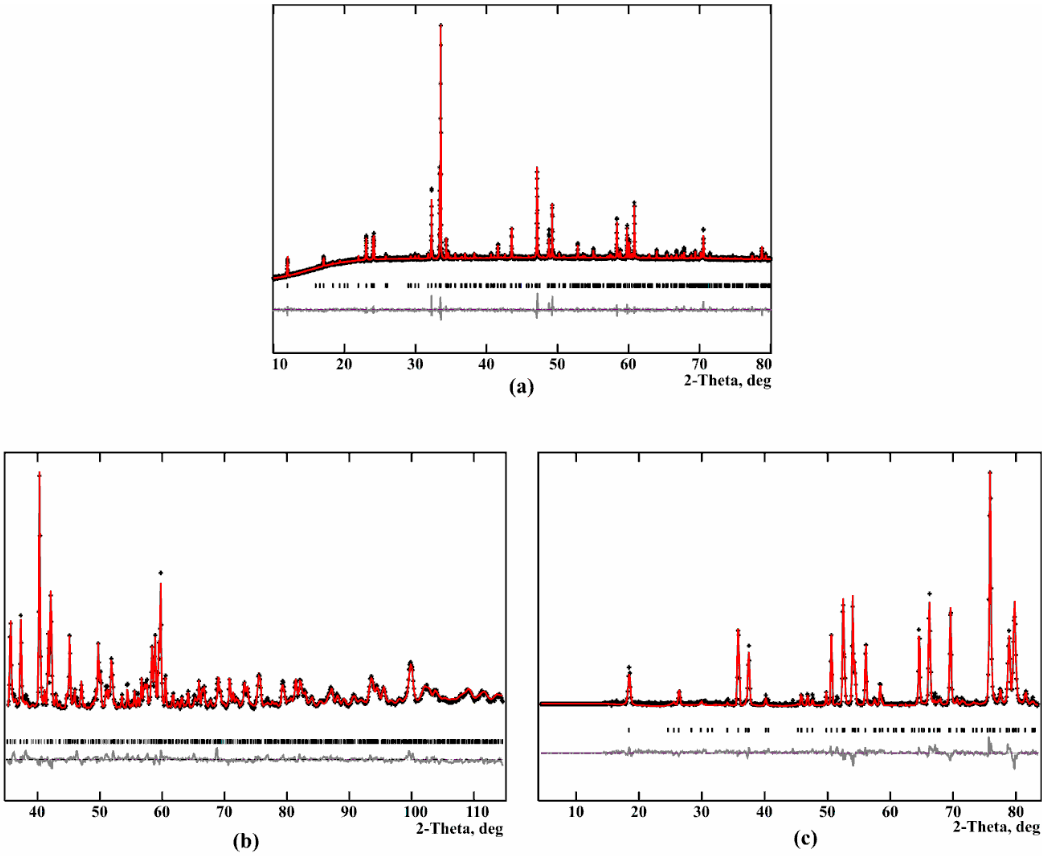

Figure 5.2. (a) X-ray powder diffraction refinement profile for Ca_2FeCoO_5, $\lambda = 1.54056$ Å, (b) neutron powder diffraction data $\lambda = 1.33037$ Å, and (c) neutron data $\lambda = 2.37150$ Å, at 300 K. The model is given in Table 5.4. For $\lambda = 2.37150$ Å data, the magnetic peaks were removed for structure refinement.

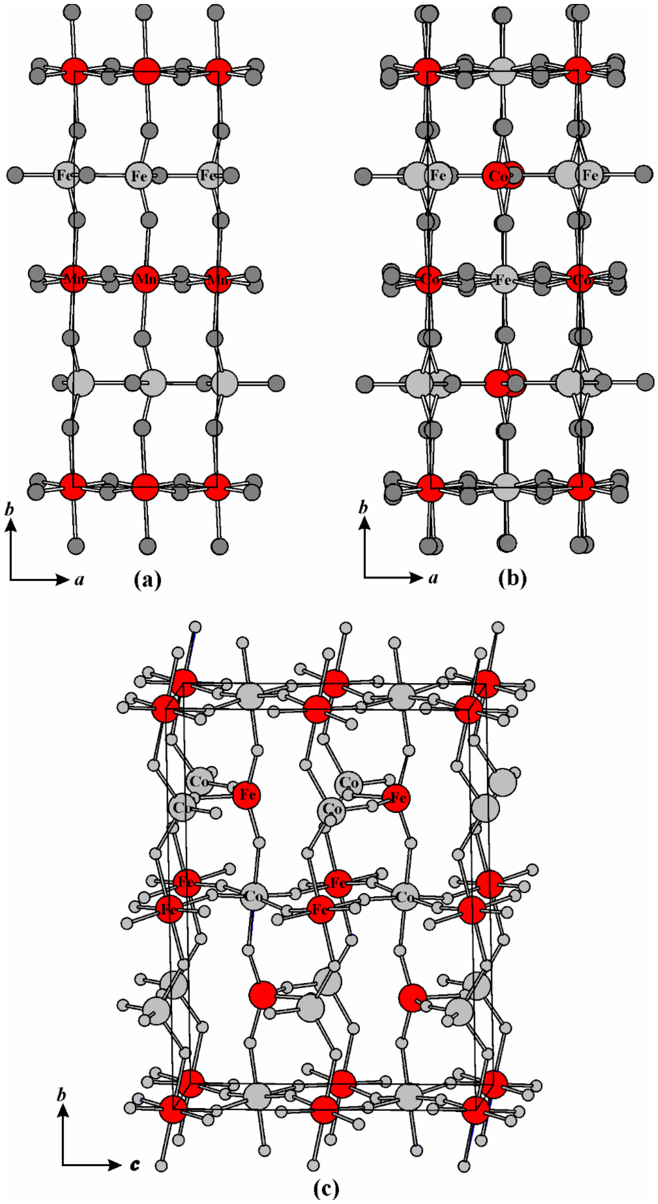

Figure 5.3. A comparison between (a) a regular brownmillerite structure Ca_2FeMnO_5 (*Pnma*)[35] and (b and c) the super structure of Ca_2FeCoO_5 (*Pcmb* setting is shown here, so that *a* and *b* are the shortest and longest axes in all three figures). In (a), there is only one octahedral B site, mostly occupied by Mn, and one tetrahedral B′ site, mostly occupied by Fe. Viewed along the *c* axis, all tetrahedral site cations are eclipsed. In (b), there are two octahedral sites, one occupied mostly by Fe and the other mostly by Co, and two tetrahedral sites, one fully occupied by Fe and the other by Co. The two distinct tetrahedral sites are especially evident in this figure. Also note that tetrahedral site cations are not eclipsed by the cations immediately behind them. In (c) the presence of both intra- and interlayer cation orderings, i.e., an overall NaCl type cation ordering is shown.

In a typical brownmillerite structure there are unique octahedral B and tetrahedral B′ sites arranged in layers parallel to the long axis. For cases with different B and B′ ions, interlayer site ordering is observed, for example Mn^{3+} and Cr^{3+} show a strong preference for the octahedral site in Ca_2FeMnO_5 [35] and $Ca_2Fe_{1.5}Cr_{0.5}O_5$.[36] Ca_2FeCoO_5, however, has two inequivalent octahedral and tetrahedral sites (Figure 5.3). This structure type can thus accommodate both intra- and interlayer cation site ordering.

To answer questions concerning the details of the crystal structure, such as site preferences for Fe and Co, a powder neutron diffraction study was performed. There is good neutron scattering length contrast between Co (b = 2.49fm) and Fe (b = 9.45fm), while these two are virtually indistinguishable using conventional X-rays.

To determine the distribution of cations over tetrahedral and octahedral sites, different models were tested. The initial refinement was performed with Fe on both of the tetrahedral sites and Co on both octahedral sites which is the best result from the X-ray single crystal work, as mentioned. This resulted in very large agreement indices, with χ^2 values >30 for the short wavelength data. The intensity of the (002) reflection was particularly underdetermined by this model. Detailed inspection of the refinement results showed very large thermal displacement factors, about 20 times larger than normal, for one of the tetrahedral sites, indicating that this site should be occupied fully or mostly by Co. There were also relatively large negative and positive displacement factors for the octahedral sites, indicating mixing of Fe and Co on these sites. Finally, a model with site ordering by Fe and Co over the two tetrahedral sites and mixing of Fe and Co on the octahedral sites was found to be the right model. The refinement profiles are shown in

Figure 5.2b,c for the two wavelengths. For the $\lambda = 2.37150$ Å data set, the magnetic peaks, readily identified as those with a strong temperature dependence, were removed for structural refinement. The major magnetic peaks appeared at 31.0° and 31.7° with no structural overlap, along with smaller peaks at 60.6°, 60.9°, 62.2°, and 63.5°. The refinement results for Ca_2FeCoO_5 are given in Table 5.3. The unit cell parameters are compared to two typical brownmillerite compounds, with similar compositions. Table 5.4 lists atomic coordinates and site occupancies for Ca_2FeCoO_5. Each atomic position for a typical brownmillerite splits into two sites due to the Ca_2FeCoO_5 super structure. The oxygen occupancies were refined, and no significant variation from full occupancy was observed. Therefore, it was decided to fix the oxygen occupancies at 1. Cation occupations at each site were constrained to 1 as well but not to the overall nominal bulk composition. We note a ~6.5% difference in overall cation composition between the Rietveld refinement results, $Ca_2Fe_{1.065}Co_{0.935}O_5$, and the nominal bulk sample composition, Ca_2FeCoO_5. It is not clear that this difference is significant given the limitations of Rietveld refinement of complex structures from powder data. What is clear is that the tetrahedral sites show nearly perfect Fe/Co site ordering, while the octahedral sites show lesser but still significant ordering levels.

Ca_2FeCoO_5 is the first example of a brownmillerite oxide showing intralayer ordering of cations. In addition, there is an interlayer ordering between octahedral and tetrahedral layers, so that an Fe-site in a tetrahedral layer is connected to Co-rich sites in the octahedral layers below and above. Similarly, a Co-site in a tetrahedral layer has Fe-rich sites as nearest neighbors in the adjacent octahedral layers. The overall pattern is that of NaCl (rock salt) ordering. This is illustrated in Figure 5.3c.

Tetrahedral site occupancies in Ca_2FeCoO_5 should be compared to those of Ca_2FeMnO_5 that has only one tetrahedral site, mostly occupied by Fe, with a 90%:10% ratio of Fe:Mn. This can be expected due to the difference between site preferences of Fe^{3+} and Mn^{3+}, with Mn^{3+} favoring the octahedral site. The two octahedral positions in Ca_2FeCoO_5 are jointly occupied by Fe and Co, with significantly more Fe content on one site and more Co content on the other, leading to a partial but substantial site ordering.

Table 5.3. Powder refinement results for Ca_2FeCoO_5 at 300 K[a]

	Ca_2FeCoO_5 (300K)	Ca_2FeMnO_5 (550K)	Sr_2FeCoO_5 (300K)
Space group	*Pbcm*	*Pnma*	*Icmm*
Lattice parameters	a = 5.3652(3) Å	a = 5.3251(1) Å	a = 5.6243(2) Å
	b = 11.0995(5)Å	b = 15.3865(3) Å	b = 15.6515(5) Å
	c = 14.7982(7)Å	c = 5.4787(1) Å	c = 5.5017(2) Å
	V = 881.3(1)$Å^3$	V = 448.89(1) $Å^3$	V = 484.31 $Å^3$
Z	8	4	4
Agreement factors	R_p (X–ray, λ=1.54056 Å) = 0.0139		
	R_{wp} (X–ray, λ=1.54056 Å) = 0.0262		
	R_p (neutron, λ=1.33037 Å) = 0.0447		
	R_{wp} (neutron, λ=1.33037 Å) = 0.0571		
	R_p (neutron, λ=2.37150 Å) = 0.0441		
	R_{wp} (neutron, λ=2.37150 Å) = 0.0573		

[a] The neutron refinements for the data with two wavelengths were done simultaneously. The X-ray refinement was done separately. The cell parameters for Ca_2FeMnO_5 [35] and Sr_2FeCoO_5 [29] are also shown for comparison.

Table 5.4. Atomic coordinates, site occupancies, and displacement factors for Ca_2FeCoO_5 from refinement of neutron diffraction data at 300 K.

Ca_2FeCoO_5					
Atom	*x*	*y*	*z*	Occupancy	U_{iso} (Å^2)
Ca1	-0.015(3)	0.759(1)	0.390 (2)	1.0	0.018(7)
Ca2	-0.486(3)	0.512(1)	0.606 (2)	1.0	0.013(5)
Fe1	-0.046(2)	0.533(1)	0.25	1.0	0.032(4)
Co1	0.426(7)	0.715(4)	0.25	1.0	0.002(8)
Co2	-0.496(3)	0.75	0.5	0.16(6)	0.027(7)
Fe2	-0.496(3)	0.75	0.5	0.84(6)	0.027(7)
Co3	0	0	0	0.71(5)	0.01(1)
Fe3	0	0	0	0.29(5)	0.01(1)
O1	0.099(4)	0.694(2)	0.25	1.0	0.031(6)
O2	0.591(4)	0.566(2)	0.25	1.0	0.021(5)
O3	-0.251(5)	0.622(2)	0.4830(6)	1.0	0.018(3)
O4	-0.755(4)	0.627(2)	0.4884(6)	1.0	0.016(3)
O5	0.020(2)	0.468(2)	0.362(1)	1.0	0.020(4)
O6	0.510(3)	0.782(2)	0.359(1)	1.0	0.018(4)

From previous K-edge XANES studies the cation oxidation states are Fe^{3+}/Co^{3+}.[37] Given the nearly even distribution of cations over the octahedral and tetrahedral layers, Co^{3+} must be high spin or at least intermediate spin as low spin Co^{3+} has a very strong octahedral site preference. The cation valences are also confirmed using bond valence sum (BVS) calculations.[38, 39] For Fe1 and Co1 on the tetrahedral sites, the values are 2.88 and 2.846, respectively. For the octahedral sites, due to the mixed occupancies, an average value of BV parameters for Fe and Co was used, taking into account the percentages of each cation on each site. The BVS values obtained for the octahedral positions were 3.04 and 2.80 for Fe2(Co2) and Co3(Fe3) sites, respectively.

Table 5.5 shows selected bond distances and angles for Ca_2FeCoO_5. The two tetrahedral sites, Fe1 and Co1, have similar bond lengths and angles. Both FeO_4 and CoO_4 tetrahedra are highly distorted. In both cases the two bonds in the *a*-*b* plane are significantly longer than the bonds out of the plane. The extent of distortion of the tetrahedra is similar to that observed in the closely related compounds Ca_2FeMnO_5[35] and Sr_2FeCoO_5.[29] The tetrahedral bond angles in Ca_2FeCoO_5 show deviations from the ideal angle (109.5°). The largest deviations are observed for the angles that only involve O5 and O6 oxygen atoms. This is expected, as the bridging role of these oxygens between the tetrahedra and octahedra requires the occurrence of fairly irregular angles. Considering the similarity of bond distances and valences of Fe and Co in tetrahedral layer, their ordering is remarkable and puzzling.

The two octahedral sites in Ca_2FeCoO_5 show similar bond lengths, with elongation of the two out of plane bonds for both sites. For each octahedral site there are three pairs of equivalent bonds. For the Co3(Fe3) site, the octahedral site on the origin, all equivalent bonds are oriented opposite to each other, making 180° angles. This is due to the -1 point symmetry at the origin. However, for the other octahedral site, Fe2(Co2), where the point symmetry is only 2, the equivalent bonds within the *a*-*b* plane are oriented adjacent to each other, and the equivalent out of plane pair are opposite to each other with O−Fe−O angles deviating from linearity. The elongation of out-of-plane bonds for the octahedral sites occurs in regular brownmillerite compounds as well.[29, 35] Such elongation seems to be required by this structure type in order to accommodate the linkage between octahedral and tetrahedral layers. Compression of tetrahedral out-of-plane bonds can accompany the elongation of octahedra. Also deviation from ideal angles for tetrahedral site bonds is much more pronounced compared to that of an octahedral site.

Table 5.5. Selected bond lengths (Å) and angles (^{o}) for Ca_2FeCoO_5 at 293 K, taken from single crystal x-ray diffraction data while the site occupations are from the neutron data

Ca_2FeCoO_5 at 293K	
Tetrahedral sites	
Fe1-O1	1.9112(19)
Fe1-O2	1.9258(19)
Fe1-O5	1.822(2) × 2
Co1- O1	1.9276(18)
Co1-O2	1.9165(19)
Co1-O6	1.815(2) × 2
O1-Fe1- O2	104.34(9)
O1-Fe1- O5	106.18(8) × 2
O2-Fe1- O5	105.70(6) × 2
O5-Fe1- O5	126.80(15)
O1-Co1- O2	105.16(9)
O1-Co1- O6	104.60(6) × 2
O2-Co1- O6	106.30(8) × 2
O6-Co1- O6	127.96(17)
Fe1 – O1 – Co1	123.13(10)
Fe1 – O2 – Co1	123.95(10)
Octahedral sites	
Fe2(Co2)-O3	1.950(2) × 2
Fe2(Co2)-O4	1.935(2) × 2
Fe2(Co2)-O6	2.097(2) × 2
Co3(Fe3)-O3	1.951(2) × 2
Co3(Fe3)-O4	1.929(2) × 2
Co3(Fe3)-O5	2.100(2) × 2
O3-Fe2(Co2)-O3	93.28(12)
O4-Fe2(Co2)-O4	91.60(12)
O3-Fe2(Co2)-O4	87.59(11) × 2
O3-Fe2(Co2)-O4	178.06(5) × 2
O3-Fe2(Co2)-O6	87.95(7) × 2
O3-Fe2(Co2)-O6	88.87(7) × 2
O4-Fe2(Co2)-O6	89.43(7) × 2
O4-Fe2(Co2)-O6	93.80(7) × 2
O6-Fe2(Co2)-O6	175.38(8)
O3-Co3(Fe3)-O3	180.000(1)
O4-Co3(Fe3)-O4	180.00(8)
O3-Co3(Fe3)-O4	87.41(11) × 2
O3-Co3(Fe3)-O4	92.59(12) × 2
O3-Co3(Fe3)-O5	92.58(7) × 2
O3-Co3(Fe3)-O5	87.42(7) × 2
O4-Co3(Fe3)-O5	90.35(7) × 2
O4-Co3(Fe3)-O5	89.65(7) × 2
O5-Co3(Fe3)-O5	180.000(1)
Fe2(Co2)-O3-Co3(Fe3)	166.59(7)
Fe2(Co2)-O4-Co3(Fe3)	170.18(8)

Schematic comparisons between the structure of a typical brownmillerite and the super structure of Ca_2FeCoO_5 are shown in Figures 5.3 and 5.4. The two distinct tetrahedral sites of Ca_2FeCoO_5 are particularly evident in Figure 5.3b. Viewed along the same direction, the tetrahedral site cations are completely eclipsed in a regular brownmillerite, while they have a significant shift relative to each other in Ca_2FeCoO_5. The shift of the octahedral cations is less pronounced. This is also evident from the atomic coordinates of octahedral and tetrahedral cations shown in Table 5.4.

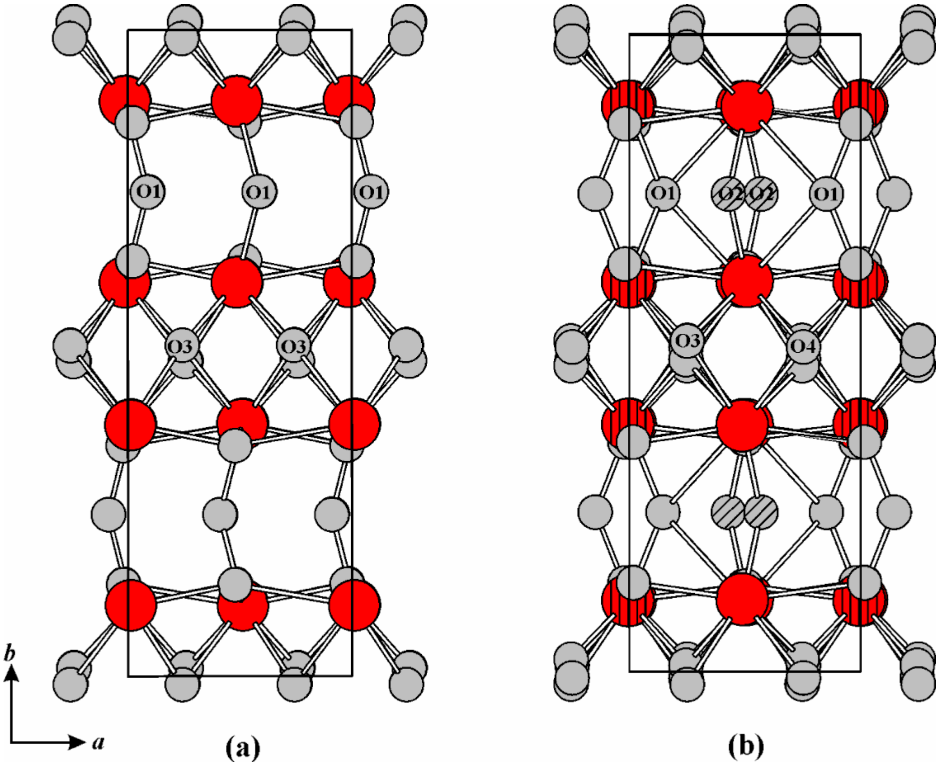

(a) (b)

Figure 5.4. The Ca–O sublattices of (a) a regular brown millerite structure Ca_2FeMnO_5 (*Pnma*) [35] and (b) the super structure of Ca_2FeCoO_5 (*Pcmb* setting is shown here, so that *a* and *b* are the shortest and longest axes in both parts (a) and (b) of the figure). In (a) Ca cations (large red circles) are arranged in layers that have only one type of oxygen on each side (O1 on one side and O3 on the other side). In (b) two oxygen positions are present on each side of a Ca-layer. The pronounced distinction between O1 and O2 is especially evident in this figure. There are two types of Ca positions. Ca1 is vertically hatched to be distinguished from Ca2.

The splitting of oxygens can also be seen in Figures 5.3 and 5.4. The oxygen atoms bridging the tetrahedral and octahedral layers are all of the same type and eclipse fully for a regular brownmillerite, while there are two different types of bridging oxygens, O5 and O6 for Ca_2FeCoO_5. However, the most pronounced case of two distinct oxygens that would be on the same site in a regular brownmillerite is seen for O1 and O2, as evident from Figure 5.4. This figure shows that the major difference between the Ca−O sublattices of a typical brownmillerite and Ca_2FeCoO_5 arises from the splitting of the O1 site, in a regular brownmillerite, into two sites labeled O1 and O2 in Ca_2FeCoO_5. Close inspection of the structure reveals that O1 and O2 are the oxygens bonded only to the tetrahedral cations with no connection to the octahedral ions. In fact, it appears that the symmetry of the octahedral layer does not deviate significantly from that of a regular brownmillerite, while the symmetry of the tetrahedral chains is the major factor that encourages formation of a super structure (Figure 5.3). As illustrated previously in Figure 5.1 the relative orientation of the tetrahedral chains determines the space group symmetry of materials in brownmillerite family.

There have been a number of attempts to correlate brownmillerite space group symmetry to observable parameters, in particular the interlayer separation and degree of twisting of the tetrahedral chains.[12, 40, 41] The degree of chain twisting is a measure of the chain dipole moment, and the minimization of these moments is postulated to be responsible for the different chain configurations and thus the space groups. In ref 12, the most comprehensive and systematic study of brownmillerites to date, a structure field map was proposed based on these two parameters. The rare *Pcmb* (*Pbcm*) space group characterized by simultaneous intra- and interlayer ordering of chains is confined to the region where the tetrahedral layer separation exceeds ~8Å, and the distortion of tetrahedral chains from linearity exceeds ~62º. However, for Ca_2FeCoO_5 the interchain separation is 7.41 Å and the average tetrahedral chain distortion angle is 56.5° which places this material within the *Pnma* region. The origin of this discrepancy is unclear at present but some observations may point the way to a resolution. Note that the *Pcmb* (*Pbcm*) region of the structure map relies on data from materials of composition $La_{1-x}A_xMnO_{2.5}$, containing the cations Mn^{3+} which is Jahn−Teller (JT) active and occupies the octahedral sites, and Mn^{2+} which resides on the tetrahedral sites. While all octahedral site cations in BM oxides exhibit a local tetragonal elongation along the *b* (longest axis), this effect is enhanced significantly for JT active ions as discussed for Ca_2FeMnO_5.[35] As well, Mn^{2+} (IV) has a very large effective radius, 0.66 Å compared to Fe^{3+}(IV) of 0.49 Å.[42] Both effects would act to enhance the *b*-axis length and, thus, the interchain separation. Indeed, the long axis dimensions reported for these materials lie in the range of 16−17 Å which is remarkable given the rather small radius of the A-site ions, ~ 1.2 Å for the combination $La_{0.6}Sr_{0.4}$ for CN = 8. In comparison the *b*-axis dimension for $Ba_2In_2O_5$ is 16.7 Å, [43] where both Ba^{2+}(CN=8), 1.42 Å, and In^{3+}(CN = 6), 0.80 Å, (CN=4), 0.62 Å have much larger radii than most of the ions involved here. Thus, the materials in which the rare *Pcmb* (*Pbcm*) space group and its unique chain configuration have been seen previously to this work may exhibit anomalously large *b*-axis lengths (and thus interchain separations) due to the presence of the strong JT ion Mn^{3+} and the large tetrahedral ion Mn^{2+}. Nonetheless, that Ca_2FeCoO_5 crystallizes in *Pcmb* (*Pbcm*) is still puzzling. It is not impossible that the Fe/Co tetrahedral site ordering plays a role. Note that tetrahedral Co^{3+} has the JT active configuration $e^3t_2^3$ which could drive a site preference. However, the bond distances for the two tetrahedral sites are similar, and also tetrahedral site ordering does not occur in Sr_2FeCoO_5,[29] which exhibits the random chain space group, *Imma*, suggesting that the A cation may play a subtle role.

Magnetic structure

Neutron diffraction was used to determine the magnetic structure of this compound. The FullProf program, [44] employing WinPLOTR [45], was used to refine the neutron diffraction data. Figure 5.5 shows the refinement profile for crystal and magnetic structures of Ca_2FeCoO_5 at 3.8 K. The principal magnetic reflections, indexed as (022) and (102) on the chemical cell and marked with arrows, are diagnostic of the so-called G-type structure which is always found for brownmillerites with magnetic ions on both octahedral and tetrahedral sites.

Table 5.6. Refined magnetic moments for Ca_2FeCoO_5 [a]

Temperature Moments' orientation	3.8K *b*-axis	50K *b*-axis	100K *b*-axis	225K *a*-axis	250K *a*-axis	275K *a*-axis	300K *a*-axis
Fe1(Td)	3.1(2)	3.2(3)	3.1(2)	2.7(5)	2.4(6)	2.0(4)	2.4(4)
Co1(Td)	2.8(2)	2.7(2)	2.7(2)	2.9(5)	2.8(6)	2.9(4)	2.4(3)
Fe2(Co2)(Oct)	3.6(3)	3.5(3)	3.7(2)	3.1(5)	2.7(6)	2.1(4)	2.8(4)
Co3(Fe3)(Oct)	2.3(2)	2.3(3)	2.1(2)	2.2(5)	2.2(7)	2.6(4)	1.9(4)
R_{mag} (%)	10.4	11.7	13.0	12.6	12.5	13.9	13.1

[a] Below 100 K, the preferred magnetic moment orientation is *b* (longest axis), while above 225 K, it is *a* (shortest axis). Due to the availability of high quality data with two wavelengths (1.331 Å and 2.373 Å) at 3.8 K and 300 K, the atomic positions used to refine the 50 K and 100 K moments were taken from the 3.8 K data refinement and the atomic positions used to refine the 225 K, 250 K, and 275 K moments were taken from 300 K data refinement.

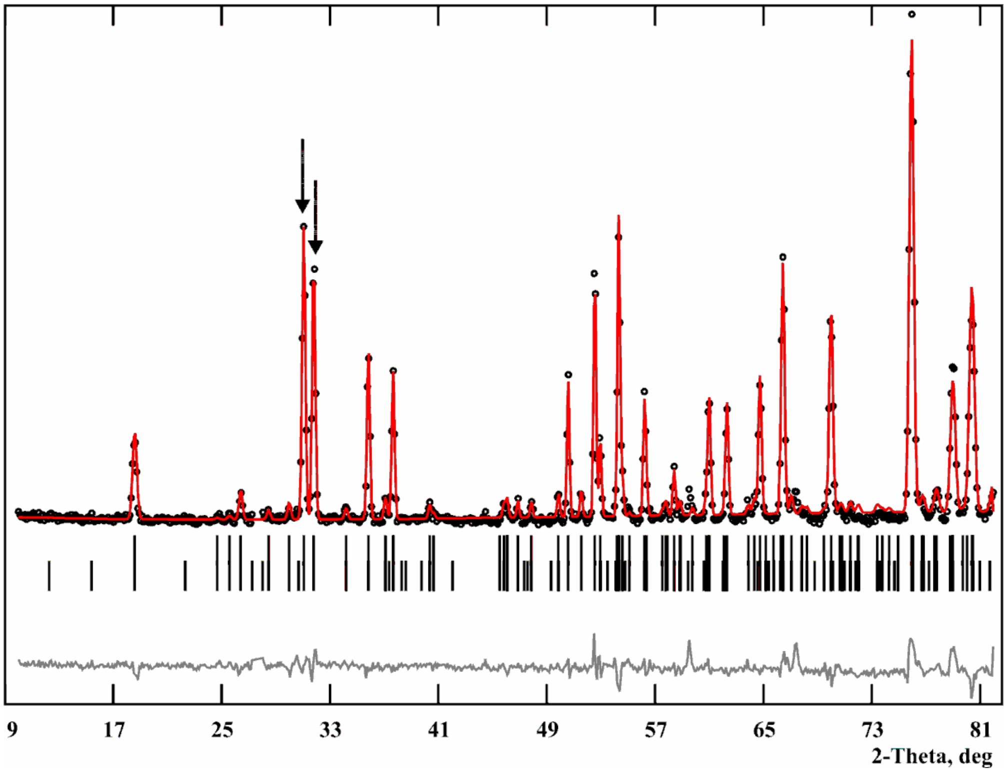

Figure 5.5. Crystal and magnetic structure refinement profile of neutron powder diffraction data for Ca_2FeCoO_5, $\lambda = 2.37150$ Å, at 3.8 K. The black circles are the experimental data; the solid line is the model; two rows of the vertical bars show Bragg peak positions for the crystal (top) and magnetic (bottom) structures, and the lower line is the difference plot. The two major magnetic peaks are shown by arrows. The magnetic structure was found to be G-type with the preferred moment orientation along the longest axis (*b* in *Pcmb* setting) at 3.8 K.

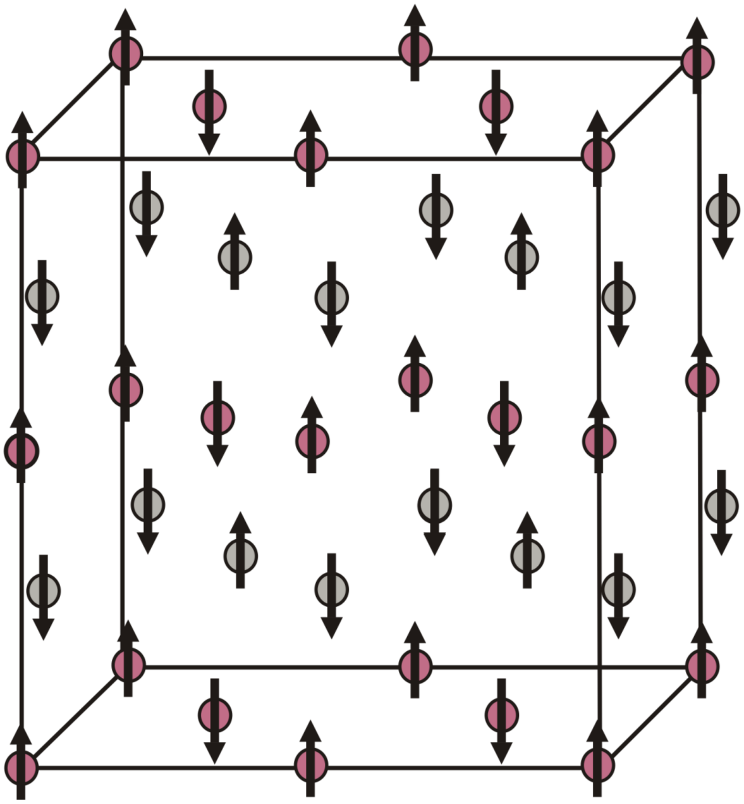

Figure 5.6. The G-type magnetic structure of Ca_2FeCoO_5 at 3.8 K (cell setting *b* > *c* > *a*, chemical space group *Pcmb*). The octahedral and tetrahedral cations are shown in red and grey, respectively. The magnetic moment on each site is aligned antiferromagnetically relative to all nearest neighbors within the same layer and in the adjacent layers. Note that the octahedral and tetrahedral site components, taken separately, are actually C-type. Thus, an alternative description would be as two interpenetrating C-type magnetic structures.

The G-type structure is shown in Figure 5.6 where the spins on each site are oriented antiparallel to those of all nearest neighbor sites within the same layer as well as in adjacent layers. The use of this nomenclature for brownmillerites, which was developed originally for perovskites - which have only octahedral sites - can lead to ambiguities, so some brief remarks are in order. Note from Figure 5.6 that the spin configuration for the octahedral sites (or the tetrahedral sites) taken alone is actually what is called C-type in perovskites. This is why the indices of the strongest magnetic reflections are (022) and (102) which are those expected for a perovskite C-type.[46] Nonetheless, when the two sites are taken together, all nearest neighbor moments are indeed antiparallel which is the situation for a G-type magnetic structure and such nomenclature has been adopted for brownmillerites. Regarding the orientation of magnetic moments, the intensity ratio of the (022)/(102) doublet is also diagnostic. Simulations show that for moment orientation along the longest axis (*b* in this case) the (022)/(102) intensity ratio is 1.2. For orientation along the shortest axis (*a*-axis in this case and in most settings for the brownmillerite cell) the ratio is 2.9. For orientation along the third axis the intensity ratio is 0.4. In Figure 5.7a,b are plotted the temperature dependences of the individual intensities and the ratio. Note the highly unusual behavior with temperature of the individual reflection intensities (5.7a) and the results of 5.7b which indicate clearly a spin reorientation from along the *b*-axis between 3.8 K and 100 K to along the *a*-axis by about 200 K which remains unchanged to 502 K, although the errors are larger in the data for $T > 300$ K. Most Fe-based brownmillerites show a preferred moment direction along the shortest (a) axis such as $Ca_2Fe_2O_5$,[47] $Sr_2Fe_2O_5$,[48] $Ca_2Fe_{1.5}Cr_{0.5}O_5$ [36], and Sr_2FeCoO_5,[29] although for the latter the magnetic structure is known only at room temperature. Only Ca_2FeMnO_5 shows a preferred moment direction along the longest axis (*b*) at all temperatures. It is worth noting that the Mn^{3+}-based brownmillerites Ca_2GaMnO_5 and Sr_2GaMnO_5 [46] also have a preferred *b*-axis at all temperatures, indicating a strong anisotropy associated with the Mn^{3+} ion. $Ca_2Co_{1.6}Ga_{0.4}O_5$ with Co^{3+} on both octahedral and tetrahedral sites takes the *a*-

axis at 298 K.[49] Clearly, more work is needed to understand the systematics of magnetic anisotropy in brownmillerites.

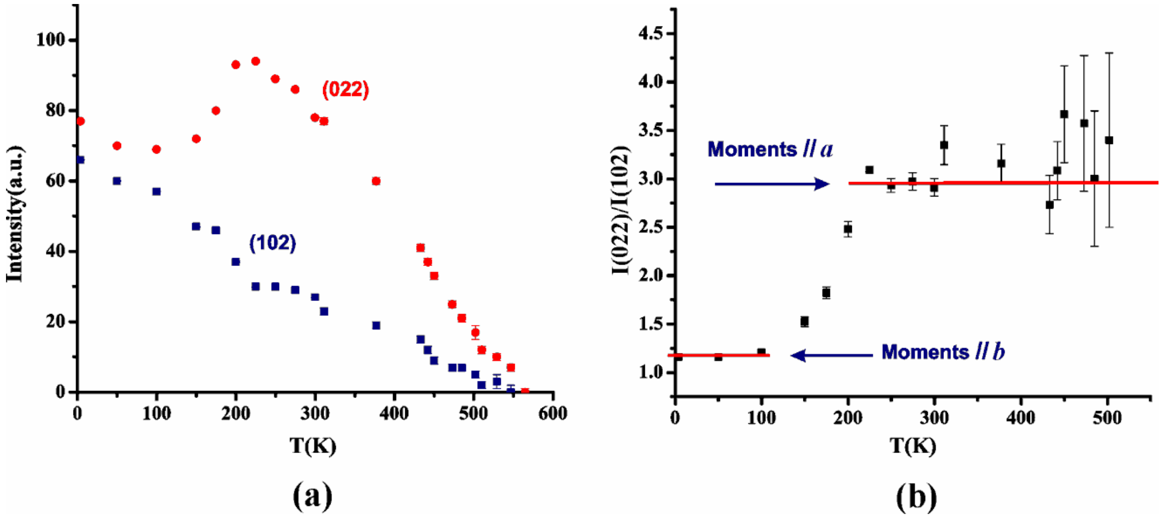

Figure 5.7. (a) Temperature dependence of two major magnetic reflections for Ca_2FeCoO_5 (*Pcmb*) at 31.06° indexed as (0 2 2) and 31.80° indexed as (1 0 2). The unusual changes in relative intensities below 300 K are due to spin reorientation as a function of temperature. Note the presence of plateau near 450 K and 500 K. (b) The ratio of (0 2 2)/(1 0 2) peak intensities as function of temperature. For ratios close to 1, below 100 K, the moments are parallel the longest axis, *b*-axis, and for ratios close to 3, above 225 K, the moments point along the shortest axis, *a*-axis in *Pcmb* setting.

The preferred directions deduced from Figure 5.7b were confirmed by magnetic structure refinements which converged only when the moment directions for all four sites were taken as indicated. The refined magnetic moments for all four crystallographic sites for the two regions up to 300 K are listed in Table 5.6. Note that the uncertainties of the moments are rather large. In fact comparing these values to those obtained for the simpler Ca_2FeMnO_5 material from the same diffractometer over the same Q-range, the uncertainties range from twice (at low temperature) to three or four times (at high temperature).[35] This is likely due to the fact that the number of magnetic reflections is actually the same for both materials, while the number of magnetic sites has doubled. The same effect appears for the chemical structure refinement where the uncertainties in atomic positions for Ca_2FeCoO_5 are significantly larger than those for $CaFeMnO_5$. Again, the data span the same Q-range, but the model contains twice as many atoms for the doubled cell material. Thus, the least-squares landscape for Ca_2FeCoO_5 appears to consist of many shallow minima.

Given this problem it is not surprising that the refined moment magnitudes were found to be remarkably sensitive to the refinement strategy. For the data taken at the C2 diffractometer encompassing the temperature range 3.8 K to 300 K, full data sets (both wavelengths) were available only for the two terminal temperatures while for all others only the long wavelength data exist. It was, thus, not possible to refine atomic positions and moments simultaneously at all temperatures. The best results (in terms of R_{mag}) were obtained when the atomic positions found at 3.8 K from the neutron data were used to refine the magnetic moments at 3.8 K, 50 K, and 100 K, and those found from the 300 K refinement were used for the 225 K, 250 K, 275 K, and 300 K, and these are the values listed in Table 5.6. In all cases an overall displacement parameter, B_{ov}, was refined. The obtained magnetic moments are generally smaller than what is expected for Fe^{3+} (d^5, S = 5/2) and high spin Co^{3+} (d^4, S = 2). Low magnetic moments comparable to those reported here have been observed previously for Sr_2FeCoO_5.[29] Further speculation regarding the origin of these apparent discrepancies is unwarranted at this time. The use of core level spectroscopies to determine the spin state of the Co ions for example may prove helpful.

Refinements using the data taken above 300 K at HFIR led to moment values which were extremely sensitive to the choice of atomic positions and which did not correspond to the values obtained from the refinement of the C2 low temperature data. For example refinement of the atomic positions and moments at 311 K gave values for the Fe moments on both the O_h and T_d sites which were more than one Bohr magneton smaller and for the Co moments more than one Bohr magneton greater than those found for the C2 data at 300 K. Upon substituting the atomic positions for 300 K (which are not significantly different in terms of the statistical uncertainty), the moment values were reversed between the Fe and Co sites! This problem is likely due to the more restricted Q-range and the somewhat lower signal-to-noise ratio of the HFIR data which compounds the rather highly underdetermined nature of the problem as discussed previously. Nonetheless, there are clear indications from the high temperature data of Figure 5.7a that not all four magnetic sites order at the same temperature. The temperature dependence below 200 K of the two strongest magnetic reflections, (022) and (102), is of course dominated by the effects of the spin reorientation. Even above 300 K there are anomalies. Consider the temperature dependence of the (102) reflection which shows order parameter like behavior with an approximate critical temperature of ~ 450K followed by a plateau to 529 K. In fact the (102) intensity is not observable at 547 K. A similar but less pronounced effect occurs for the (022) reflection near 450 K which is followed by a plateau between 510 K and 547 K. At the maximum temperature, 565 K, the (022) peak is not distinguishable from background, although the counting statistics are poor. This complex behavior should be investigated in more detail with better counting statistics and a finer temperature grid, but the indication of multiple ordering temperatures seems clear.

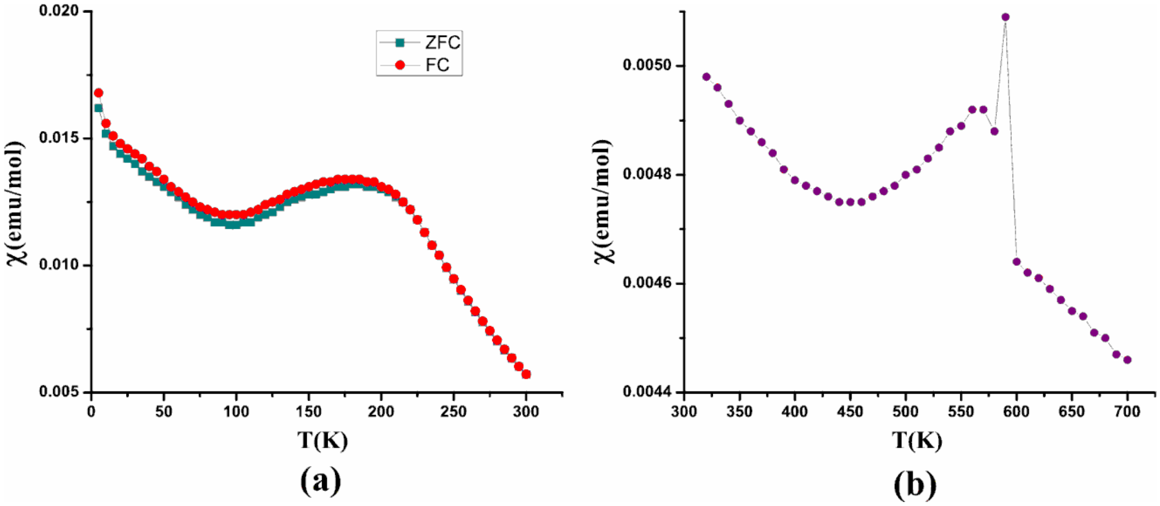

Figure 5.8. (a) ZFC and FC molar susceptibility data within the temperature range 5−300 K. Note the minimum at ~100K and the maximum at ~ 200K indicative of the spin reorientation found in the neutron data. Also, a ZFC/FC divergence sets in below 200 K, indicating spin canting. (b) Magnetic susceptibility data upon heating the sample from 300 K−700 K. The unusual spike above ~580K is reproducible. Note the minimum at ~ 450K which corresponds to the lower ordering temperature from the neutron study and the broad maximum at ~ 570K, close to the maximum ordering temperature from the neutron data.

The bulk magnetic susceptibility data, Figure 5.8a,b, reflect the effects seen by neutrons. The susceptibility minimum at 100 K and the maximum at 200 K are consistent with the observed spin reorientation. An additional feature is the ZFC/FC divergence below 200 K and the hysteresis which indicates some degree of spin canting. This is confirmed by isothermal magnetization data, Figure 5.9, that shows hysteresis at 5 K and 200 K. The remnant magnetization is especially well-defined at 200 K. As well, the high temperature susceptibility data show a minimum near 450 K which corresponds to one of the apparent ordering temperatures from the high temperature neutron data. There is a broad maximum at ~ 570K, and a reproducible spike at 585 K, close to the maximum magnetic transition from neutron data.

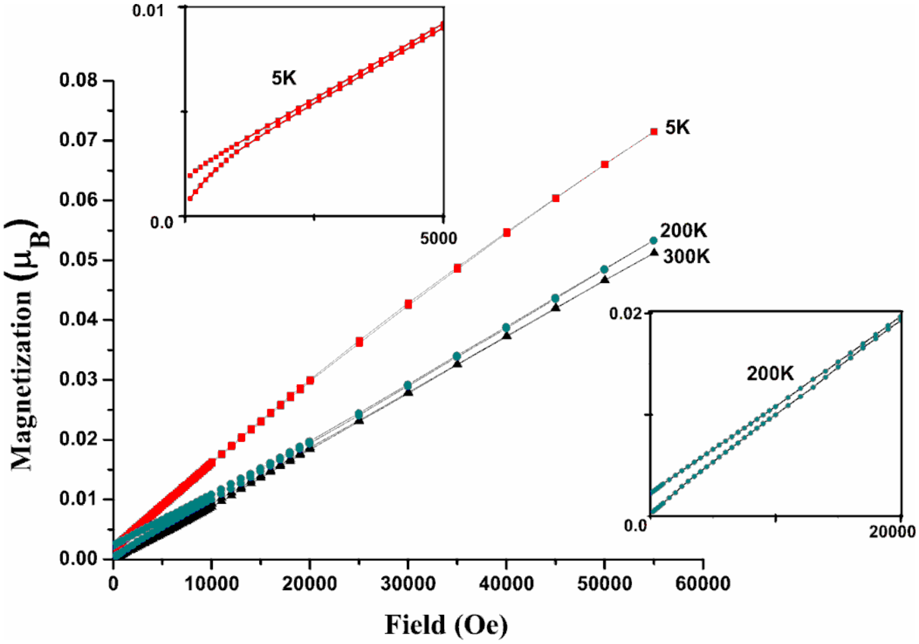

Figure 5.9. Isothermal magnetization versus applied field for Ca_2FeCoO_5 at various temperatures. Hystereses are observed at 5 K and 200 K, magnified in the insets. The remnant magnetization is especially well pronounced at 200 K.

Summary and Conclusions.

The mixed B-site brownmillerite, Ca_2FeCoO_5, was synthesized using standard solid state chemistry methods from which single crystals could be recovered. A number of new phenomena, not seen previously in brownmillerite oxide materials, were observed. It is one of the rare brownmillerite oxides to crystallize in *Pbcm* (*Pcmb*) requiring a supercell with doubling of one of the short axes and with an unique intra- and interlayer ordering of the tetrahedral chains. As well, there are two sets of octahedral and tetrahedral sites. Aided by the strong scattering contrast between Co and Fe for neutrons, an unprecedented intralayer Co/Fe site ordering was seen on the tetrahedral sites. A lesser but still pronounced level of site ordering occurs in the octahedral layers as well leading to an overall NaCl type Fe/Co ordering.

The magnetic structure of this compound was determined to be G-type antiferromagnetic, with both intra- and interlayer antiparallel alignment of spins. A reorientation of magnetic moments, unique to this material, from along the longest axis below 100 K to along the shortest axis above 200 K was observed. The ordered moments for Fe^{3+} and Co^{3+} are significantly smaller than expected for the high spin ions but are similar to those observed in Sr_2FeCoO_5. The high temperature neutron data indicate at least two distinct critical temperatures for long-range magnetic order at ~ 450K and ~ 555K, suggesting that pairs of the four magnetic sites behave differently. The current data are not sufficiently accurate to assign specific sites to the apparent critical temperatures. Bulk magnetic properties largely reflect the observations from neutron diffraction in terms of the spin reorientation and two ordering temperatures but also indicate spin canting below 200 K.

Acknowledgements.

J.E.G. acknowledges the support of the Natural Sciences and Engineering Research Council (NSERC) of Canada through a Discovery Grant. The Canadian Neutron Beam Centre is also supported by NSERC by a Major Facilities Access grant.

The work at the High Flux Isotope Reactor, Oak Ridge National Laboratory (ORNL), was sponsored by the Scientific User Facilities Division, Office of Basic Energy Sciences, U.S. Department of Energy (U.S. DOE). ORNL is operated by UT Battelle, LLC for the U.S. DOE under Contract No. DEAC05-00OR22725.

Supporting Information: A CIF file containing the details of X-ray single crystal experiment. This material is available free of charge via the Internet at http://pubs.acs.org.

References

[1] Kobayashi, K.-I.; Kimura, T.; Sawada, H.; Terakura, K.; Tokura, Y. *Nature* **1998,** 395, 677.

[2] Ramirez, A.P. *J. Phys.: Condens. Matter Phys.* **1997**, 9, 8171.

[3] Kim, T.H.; Uehara, M.; Cheong, S.W.; Lee, S. *Appl. Phys. Lett.* **1999,** 74, 1737.

[4] Tang, G.D.; Liu, X.M.; Li, Z.Z.; Hou, D.L.; Zhao, X.; Liu, L.H.; Qi, W.H.; Yu, Y.; Yu, R.C.; Jinphys, C.Q. *Stat. Sol. (a)* **2006,** 203, 2522.

[5] Basith, M.A.; Manjura Hoque, Sk.; Shahparan, Md.; Hakim, M.A.; Huq, M. *Physica B* **2007,** 395, 126.

[6] Imada, M.; Fujimori, A.; Tokura, Y. *Rev. Mod. Phys.* **1998,** 70, 1039.

[7] Martin, L.O.-S.; Chapman, J.P.; Lezama, L.; Marcos, J.S.; Rodríguez-Fernández, J.; Arriortua, M.I.; Rojo, T. *Eur. J. Inorg. Chem.* **2006**, 1362.

[8] Anderson, M. T.; Greenwood, K. B.; Taylor, G. A.; Poeppelmeier, K. R.; *Prog. Solid State Chem.* **1993**, 22, 197.

[9] Howard, C. J.; Kennedy, B. J.; Woodward, P. M. *Acta Crystallogr.* **2003**, B59, 463.

[10] Karen, P.; Woodward, P. M. *J. Mater. Chem.* **1999**, 9, 789.

[11] Chapman, J. P.; Attfield, J. P.; Molgg, M.; Friend, C. M.; Beales, T. P. *Angew. Chem. Int. Ed.* **1996**, 35, 2482.

[12] Parsons, T. G.; D'Hondt, H.; Hadermann, J.; Hayward, M. A. *Chem. Mater.* **2009**, 21, 5527.

[13] Greaves, C. ; Jacobson, A.J. ; Tofield, B.C. ; Fender, B.E.F. *Acta Crystallogr. B* **1975,** 31, 641.

[14] Lambert, S. ; Leligny, H. ; Grebille, D. ; Pelloquin, D. ; Raveau, B. *Chem. Mater.* **2002,** 14, 1818.

[15] Abakumov, A. M. ; Rozova, M. G. ; Pavlyuk, B. Ph. ; Lobanov, M. V. ; Antipov, E. V. ; Lebedev, O. I. ; Van Tendeloo, G. ; Ignatchik, O. L. ; Ovtchenkov, E. A. ; Koksharov, Yu. A. ; Vasil'ev, A. N. *J. Solid State Chem*. **2001,** 160, 353.

[16] Berggren, J. *Acta Chem. Scand.* **1971,** 25, 3616.

[17] Schmidt, M.; Campbell, S. J. *J. Solid State Chem.* **2001,** 156, 292.

[18] D'Hondt, H.; Abakumov, A. M.; Hadermann, J.; Kalyuzhnaya, A. S.; Rozova, M. G.; Antipov, E. V.; Tendeloo, G. V. *Chem. Mater*. **2008**, 20, 7188.

[19] Hirone, T. *J. Appl. Phys.* **1965,** 36, 988.

[20] Takeda, T.; Yamaguchi, Y.; Tomiyoshi, S.; Fukase, M.; Sugimoto, M.; Watanabe, H. *J. Phys. Soc. Jpn.* **1968,** 24, 446.

[21] Berasteguil, P.; Eriksson, S.G.; Hull, S. *Mater. Res. Bull.* **1999,** 34, 303.

[22] Vidyasagar, K.; Gopalakrishnan, J.; Rao, C. N. R. *Inorg. Chem.* **1984.** 23, 1206.

[23] Pei, J. ; Chen, G. ; Li, X. ; Li, Y.X. ; Zhou, N. *Mater. Lett.* **2009,** 63, 1459.

[24] Liu, P.S.; Chen, G. ; Pei, J. ; Cui, Y.; Lu, D.Q. ; Zhou, N. ; Xian, H.Z. *Physica B* **2008,** 403, 1808.

[25] Li, S.; Funahashi, R.; Matsubara, I. ; Ueno, K.; Sodeoka, S.; Yamada, H. *J. Mater. Sci. Lett.* **2000,** 19, 1339.

[26] Zhang, Y.; Zhang, J.; Lu, Q. *J. Alloys Compd.* **2005,** 399, 64.

[27] Boullay, P. ; Dorcet, V. ; Pérez, O. ; Grygiel, C. ; Prellier, W. ; Mercey, B. ; Hervieu, M. *Phys. Rev. B.* **2009,** 79, 184108.

[28] de la Calle, C. ; Aguadero, A.; Alonso, J.A.; Fernández-Díaz, M.T. *Solid State Sci.* **2008,** 10, 1924.

[29] Battle, P. D.; Gibb, T. C.; Lightfoot, P. *J. Solid. State Chem.* **1988,** 76, 334.

[30] Gu, Z.J. ; Xiang, X.; Li, F.; Liu, S.B.; Evans, D.G. *J. Phys. Chem. Solids* **2008,** 69, 1056.

[31] Garlea, V. O. ; Chakoumakos, B. C. ; Moore, S. A. ; Taylor, G. B. ; Chae, T. ; Maples, R. G.; Riedel, R. A. ; Lynn, G. W. ; Selby, D. L. *Applied Physics A* **2010,** 99, 531.

[32] Larson, A.C. ; Von Dreele, R.B. General Structure Analysis System (GSAS), Los Alamos National Laboratory Report LAUR, **1994**, pp. 86–748.

[33] Toby, B.H. *J. Appl. Crystallogr.* **2001,** 34, 210.

[34] Farrugia, L. J. *J. Appl. Cryst*. **1999**, 32, 837.

[35] Ramezanipour, F. ; Cowie, B. ; Derakhshan, S. ; Greedan, J. E. ; Cranswick, L. M. D. *J. Solid State Chem.* **2009,** 182, 153.

[36] Battle, P.D.; Bollen, S.K.; Gibb, T.C.; Matsuo, M. *J. Solid State Chem*. **1991,** 90, 42.

[37] Grosvenor, A.P.; Greedan, J. E. *J. Phys. Chem. C* **2009,** 113, 11366.

[38] Brown, I.D.; Altermatt, D. *Acta Crystallogr. B* **1985,** 41, 244.

[39] VALENCE program, /http://www.ccp14.ac.uk/ccp/web-mirrors/i_d_brown/S.

[40] Hadermann, J.; Abakumov, A. M.; D'Hondt, H.; Kalyuzhnaya, A. S.; Rozova, M. G.; Markina, M. M.; Mikheev, M. G.; Tristan, N.; Klingeler, R.; Büchnerd, B.; Antipov, E. V. *J. Mater. Chem.* **2007**, 17, 692.

[41] Abakumov, A. M.; Kalyuzhnaya, A. S.; Rozova, M. G.; Antipov, E. V.; Hadermann, J.; Tendeloo, G. V. *Solid State Sci.* **2005**, 7, 801.

[42] Shannon, R.D. *Acta. Cryst. A* **1976,** 32, 751.

[43] Gregory, D.H.; Weller, M.T. *J. Solid State Chem.* **1993,** 107, 134.

[44] Roisnel, T.; Rodriguez-Carvajal, J. FULLPROF ver 1.9c: Rietveld, Profile Matching & Integrated Intensity Refinement of X-ray and/or Neutron Data, Laboratoire Léon Brillouin, Saclay, France, **2001**.

[45] Roisnel, T.; Rodríguez-Carvajal, J. WinPLOTR: a Windows tool for powder diffraction patterns analysis, in: R. Delhez, E.J. Mittenmeijer (Eds.), Proceedings of the Seventh European Powder Diffraction Conference (EPDIC 7), Materials Science Forum, **2000**, pp. 118–123.

[46] Pomjakushin, V. Yu. ; Balagurov, A. M. ; Elzhov, T. V. ; Sheptyakov, D. V. ; Fischer, P. ; Khomskii, D. I. ; Yushankhai, V. Yu. ; Abakumov, A. M. ; Rozova, M. G. ; Antipov, E. V. ; Lobanov, M. V. ; Billinge, S. J. L. *Phys. Rev. B* **2002,** 66, 184412.

[47] Takeda, T. ; Yamaguchi, Y. ; Tomiyoshi, S. ; Fukase, M. ; Sugimoto, M. ; Watanabe, H. *J. Phys. Soc. Japan* **1968,** 24, 446.

[48] Takeda, T. ; Yamaguchi, Y. ; Watanabe, H. ; Tomiyoshi, S. ; Yamamoto, H. *J. Phys. Soc. Japan* **1969,** 26, 1320.

[49] Istomin, S. Ya. ; Abdyusheva, S. V. ; Svensson, G. ; Antipov, E. V. *J. Solid State Chem*. **2004**, 177, 4251.

Additional Note:

After obtaining neutron beam time at CNBC, in February 2011, new high temperature data were collected on the C2 instrument that has a higher efficiency than HB2A. These data showed that T_N for Ca_2FeCoO_5 is ~ 595K.

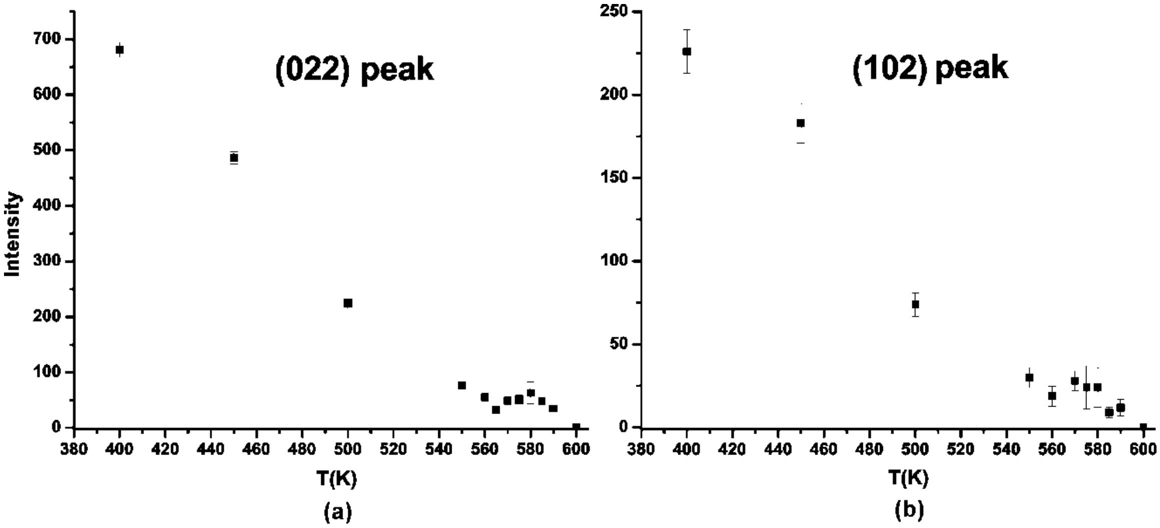

Additional Figure. The main magnetic peak intensities as a function of temperature.

Chapter 6

Local and Average Structures and Magnetic Properties of Sr_2FeMnO_{5+y}, y = 0.0, 0.5. Comparisons with Ca_2FeMnO_5 and the Effect of the A-Site Cation

This chapter encompasses the manuscript "Local and Average Structures and Magnetic Properties of Sr_2FeMnO_{5+y}, y = 0.0, 0.5. Comparisons with Ca_2FeMnO_5 and the Effect of the A-Site Cation" published in "Inorganic Chemistry", volume 50 (2011), pages 7779–7791: http://dx.doi.org/10.1021/ic200919m

The candidate performed the syntheses of the materials, bulk magnetization studies, local and average crystal structure determination from x-ray and neutron diffraction, and preparation of the manuscript.

Local and Average Structures and Magnetic Properties of Sr_2FeMnO_{5+y}, y = 0.0, 0.5. Comparisons with Ca_2FeMnO_5 and the Effect of the A-Site Cation

Farshid Ramezanipour,[†,‡] John E. Greedan,[*,†,‡] Joan Siewenie,[§] Th. Proffen,[§] Dominic H. Ryan,[‖] Andrew P. Grosvenor,[⊥] and Ronald L. Donaberger[#]

[†]Department of Chemistry and [‡]Brockhouse Institute for Materials Research, McMaster University, 1280 Main Street West, Hamilton, Ontario L8S 4M, Canada

[§]Lujan Neutron Scattering Center, Los Alamos National Laboratory, Los Alamos, New Mexico 87545, United States

[‖]Physics Department and Centre for the Physics of Materials, McGill University, 3600 University Street, Montreal, Quebec H3A 2T8, Canada

[⊥]Department of Chemistry, University of Saskatchewan, Saskatoon, Saskatchewan S7N 5C9, Canada

[#]Canadian Neutron Beam Centre, Chalk River, Ontario K0J 1J0, Canada

Corresponding Author: *E-mail: greedan@mcmaster.ca

Abstract

Sr_2FeMnO_{5+y} was synthesized under two different conditions, in air and in argon, both of which resulted in a cubic, *Pm-3m*, structure with no long-range ordering of oxygen vacancies. The unit cell constants were found to be a_0 = 3.89328(1) Å for argon (y = 0.0) and a_0 = 3.83075(3) Å for air (y = 0.5). In contrast, Ca_2FeMnO_5 retains long-range

brownmillerite oxygen vacancy ordering for either air or argon synthesis. Remarkably, $Sr_2FeMnO_{5.0}$ oxidizes spontaneously in air at room temperature. A neutron pair distribution function (NPDF) study of $Sr_2FeMnO_{5.0}$(Ar) showed evidence for local, brownmillerite-like ordering of oxygen vacancies for short distances up to 5 Å. Mössbauer spectroscopy results indicate more than one Fe site for Sr_2FeMnO_{5+y}(Ar and air), consistent with the noncubic local structure found by NPDF analysis. The isomer shifts and quadrupole splittings in both air- and argon-synthesized materials are consistent with the 3+ oxidation state for Fe in sites with coordination number four or five. This is confirmed by an L-edge XANES study. Mn is almost entirely in the 3+ state for $Sr_2FeMnO_{5.0}$(Ar), whereas Mn^{4+} is predominantly present for $Sr_2FeMnO_{5.5}$(air). Magnetic susceptibility data show zero-field-cooled/field-cooled (ZFC/FC) divergences near 50 K for the Ar sample and 25 K for the air sample, whereas Ca_2FeMnO_5 is long-range G-type antiferromagnetically ordered at 407(2) K. Hyperfine magnetic splitting, observed in temperature-dependent Mössbauer measurements, indicates short-range magnetic correlations that persist up to 150 K for $Sr_2FeMnO_{5.0}$(Ar) and 100 K for $Sr_2FeMnO_{5.5}$(air), well above the ZFC/FC divergence temperatures. Neutron diffraction data confirm the absence of long-range magnetic ordering at room temperature and 4 K for $Sr_2FeMnO_{5.0}$(Ar) but indicate the presence of domains with short-range G-type order at 4 K with an average dimension of ~50 Å ($y = 0$); thus, this material is actually a superparamagnet rather than a true spin glass. In sharp contrast, corresponding data for $Sr_2FeMnO_{5.5}$(air) show mainly a very weak magnetic Bragg peak, indicating that ~4% of the sample has G-type antiferromagnetic ordering at 4 K.

Introduction

Oxygen-deficient perovskites can have a variety of structures depending on different factors including the degree of anion deficiency and the composition. In this article, the focus is on oxygen-deficient perovskites with the formula $A_2BB'O_{5+x}$. The oxygen vacancies can order to form the brownmillerite structure in which the B cations are octahedrally coordinated, forming corner-sharing layers, and the B′ cations are tetrahedrally coordinated, forming corner-sharing chains. (Figure 6.1). This long-range vacancy-ordering results in a supercell that generally has dimensions with respect to the cubic perovskite cell constant, a_p, of $a_{br} \approx 2^{1/2}a_p$, $b_{br} \approx 4a_p$, and $c_{br} \approx 2^{1/2}a_p$. A number of different space group symmetries are observed, depending on subtle differences in the ordering of the tetrahedral chains within the unit cell. The chains can show either a right-handed (R) or left-handed (L) orientation and the correlation between the intra- and interlayer chain orientations and the resulting space groups are summarized in Table 6.1. As shown in this table, if all chains have the same orientation in all layers, the space group will be *I*2*mb*. The same chain orientation within each layer but opposite in the adjacent layer results in space group *Pnma*. Alternating R and L orientations within each layer and between the layers gives rise to space groups *Pcmb* and *C*2/*c*. Finally, if the ordering of chains is absent, the space group will be *Imma*. Although many oxygen-deficient perovskites of composition $A_2BB'O_{5+x}$ adopt the brownmillerite structure, there are exceptions, noted below, especially when Jahn-Teller ions such as Mn^{3+} are involved.

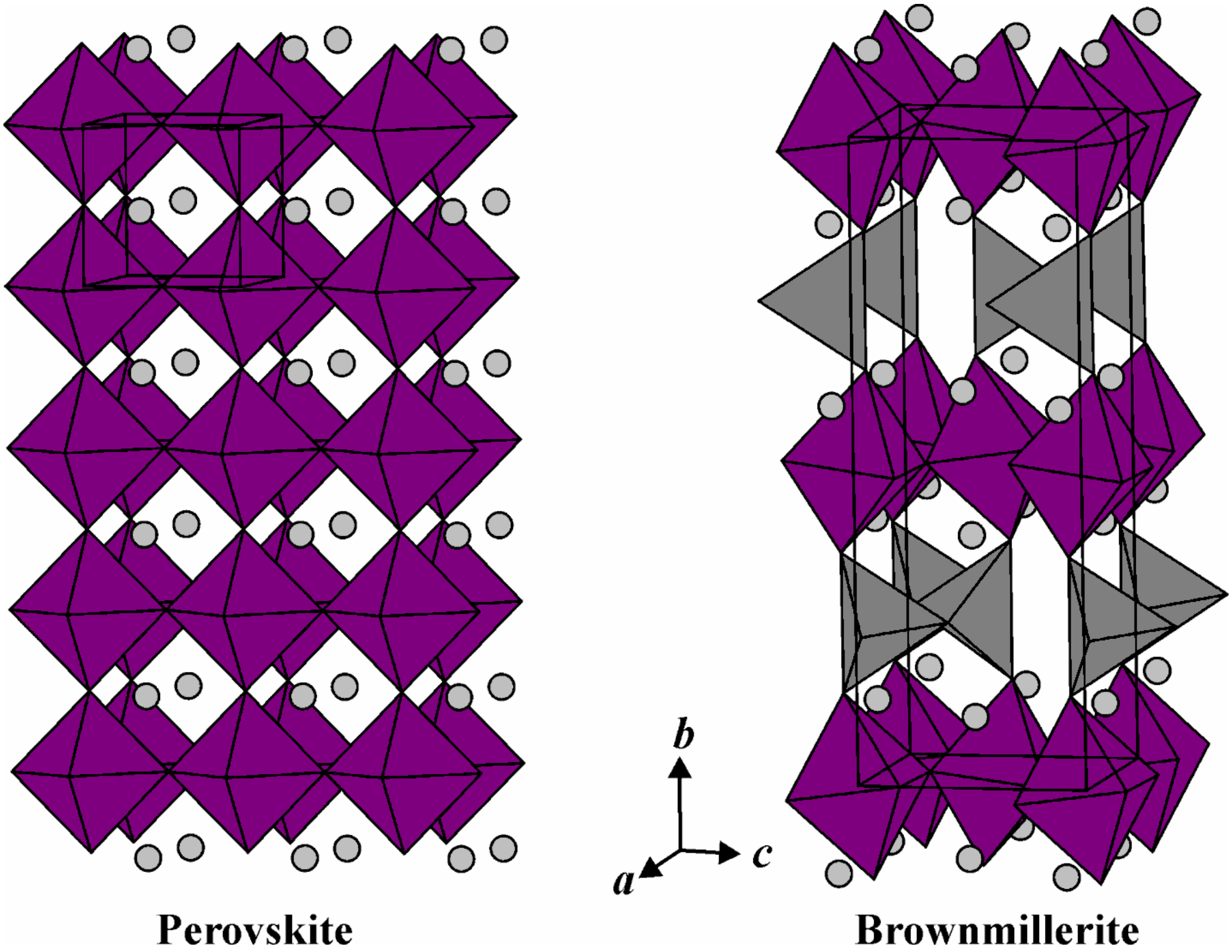

Figure 6.1. A comparison between the disordered perovskite and brownmillerite structures. The disordered perovskite structure consists of a network of corner sharing octahedra with oxygen vacancies randomly occupying the corner sites (left), while in a brownmillerite (right) the oxygen vacancies order to form layers of octahedra separated by chains of tetrahedra. The resulting brownmillerite superstructure is described by a unit cell of dimensions $a_{br} \sim 2^{1/2}a_p$, $b_{br} \sim 4a_p$, $c_{br} \sim 2^{1/2}a_p$ but a number of space group symmetries are observed. (See text)

Table 6.1. Correlations between the intra- and inter-layer tetrahedral (T) chain orientations and the resulting space groups for brownmillerites[a]

Ordering within one T-layer	Ordering in the neighboring T-layer	Space Group
L-L-L	L-L-L	*I2mb*
R-R-R	R-R-R	
L-L-L	R-R-R	*Pnma*
R-R-R	L-L-L	
L-R-L	R-L-R	*Pcmb*, *C*2/*c*[b]
R-L-R	L-R-L	
None	None	*Imma*

[a]L and R denote left and right handed chains, respectively. [b]For *Pbcm* and *C*2/*c*, $c_{\mathrm{br}} \sim 2\times2^{1/2}a_{\mathrm{p}}$ and there are two distinct tetrahedral sites per layer.

Oxygen-deficient perovskites containing Fe and Mn as B/B′ site ions and Ca and Sr as A-site cations have previously been reported. The iron-containing brownmillerite compounds $Ca_2Fe_2O_5$ and $Sr_2Fe_2O_5$ have been synthesized and studied.[1-3] These two materials exhibit one example of the effect of the A-site cation on the structure; $Ca_2Fe_2O_5$ crystallizes in the *Pnma* space group,[1] whereas $Sr_2Fe_2O_5$ belongs to the *Icmm* (*Imma*) space group.[2,3] The role of the larger Sr cation here is to disorder the chain orientations with respect to the Ca-based compound.

Both of these materials show long-range antiferromagnetic (AF) ordering with $T_c > 700$ K.[4-7] In addition, materials with the formula $Sr_2Fe_2O_{5+x}$, $0 < x < 1$,[8,9] show further oxide vacancy ordering and crystallize in the *Cmmm* (x = 0.5) and *I*4/*mmm* (x = 0.75) space groups.[9] A highly oxidized, disordered structure, *Pm*-3*m*, with x ≈ 1, can also be obtained by firing the sample in pure oxygen.[9] However, the oxidized samples can be reduced to $Sr_2Fe_2O_5$ by annealing in inert gas.[10] Now, with Mn on the B/B′ sites, both $Ca_2Mn_2O_5$ and $Sr_2Mn_2O_5$ have been synthesized. These materials do not adopt the brownmillerite structure, but instead, the B-site cations occupy a unique site with square-pyramidal geometry.[11-13] Although both of these materials are orthorhombic, the effect of the A-site cation can again be seen in the space group symmetry. $Ca_2Mn_2O_5$ crystallizes in space group *Pnma*, whereas for $Sr_2Mn_2O_5$, the space group is *Pbam*. It is noteworthy that, in the above cases, the change in A-site cation results in a change in space group, whereas the general structural type remains the same. Both $Ca_2Fe_2O_5$ and $Sr_2Fe_2O_5$ are brownmillerites and contain alternating layers of octahedra and tetrahedra. Also, in both $Ca_2Mn_2O_5$ and $Sr_2Mn_2O_5$, the geometry around all Mn sites is square-pyramidal. In this article, however, we show that the effect of the A-site cation is more significant when both Fe and Mn are present in the same $A_2BB'O_{5+x}$ compound. The synthesis, crystal structure, local structure, and magnetic properties of $Sr_2FeMnO_{5.0}$ and $Sr_2FeMnO_{5.5}$, prepared in argon and air atmospheres, respectively, are described and compared with the previously studied material, Ca_2FeMnO_5.[14] Sr_2FeMnO_{5+y} has been reported, prepared in an air atmosphere, to be cubic with a cell constant $a = 3.852$ Å, but no further details are available.[15]

Experimental Section

Synthesis. Sr_2FeMnO_{5+y} and Ca_2FeMnO_{5+y} were synthesized using stoichiometric amounts of $SrCO_3$ (99.9% Sigma Aldrich), $CaCO_3$ (99.9% Sigma Aldrich), Fe_2O_3 (99.998% Alfa Aesar), and Mn_2O_3 (99.9% Cerac) that were mixed and pressed into pellets. The pellets were annealed at 1250 ºC in an argon atmosphere for a total time of ~100 h and were then slowly cooled to room temperature. Several intermediate grindings were performed. The heating and cooling rates were both 100 ºC/h. The syntheses were also carried out in an air atmosphere using the same heating and cooling protocol to determine the effect of synthesis conditions on structure and physical properties.

X-ray and Neutron Diffraction. X-ray powder diffraction data were obtained using a PANalytical X'Pert Pro MPD diffractometer with a linear X'Celerator detector with CuKα_1 radiation (λ = 1.54056 Å) and a 2θ step interval of 0.0084º at room temperature. Room-temperature time-of-flight neutron-scattering data were collected on the instrument NPDF at the M. J. Lujan Jr. Center for Neutron Scattering at the Los Alamos Neutron Science Center.[16] Constant wavelength neutron data were obtained at the Canadian Neutron Beam Centre on the C2 diffractometer with wavelengths λ = 1.33 and 2.37 Å at room temperature and 4 K.

Thermal Gravimetric Analysis (TGA). TGA experiments were performed on a Netzsch STA-409 TGA-DTA (thermal gravimetric analyzer-differential thermal analyzer) instrument by heating the air synthesized samples in argon at a rate of 5 ºC/min, to 1225 ºC, and measuring the weight losses.

Magnetic Property Measurements. Bulk magnetic measurements were performed using a Quantum Design MPMS SQUID magnetometer. The zero-field-cooled/field-cooled (ZFC/FC) magnetic susceptibility data, as well as isothermal magnetization data, were obtained on a powder sample in a gelatin capsule in the temperature range of 5-300 K. A quartz sample holder was used for the susceptibility measurement from 320 to 700 K.

Mössbauer Spectroscopy. ^{57}Fe Mössbauer spectra were obtained in transmission mode on a conventional constant-acceleration spectrometer using a 50 mCi ^{57}CoRh source. The spectrometer was calibrated using α-Fe foil at room temperature, and all isomer shifts were measured relative to the centroid of the calibration spectrum. Temperatures down to 5 K were obtained using a vibration-isolated closed-cylcle fridge with the sample in helium exchange gas. Typical stabilities were better than 0.01 K during the measurements. The spectra were fitted using a conventional nonlinear least-squares minimization routine to a sum of equal-width Lorentzian line shapes. Several distinct models were used. The basic approach was to use a sum of paramagnetic quadrupole doublets or magnetic sextets with line positions determined from a first-order perturbation calculation; however, in some cases, a Gaussian distribution of quadrupole splittings with a correlated isomer shift distribution was employed, and some of the magnetic patterns were fitted using a model-free distribution of hyperfine fields based on Window's method.[17]

X-ray Absorption Near-Edge Spectroscopy (XANES). To determine the Fe and Mn oxidation states and local coordination environments in the materials investigated here, Fe and Mn L-edge XANES spectra were collected at the Canadian Light Source using the spherical grating monochromator (SGM) undulator beamline, 11ID-1.[18] The flux was ~1011 photons/s at 1900 eV and increased to ~4×10^{12} photons/s at 250 eV. The resolution was better than 0.3 eV at photon energies below 1500 eV, and the instrumental precision was better than ±0.1 eV. Powdered samples were mounted on carbon tape and measured in vacuo. Total electron yield (TEY) and X-ray fluorescence yield (FLY) spectra were collected simultaneously. TEY spectra are presented for the Fe and Mn L-edges. Spectra were collected from ~30 eV below the absorption edge to ~50 eV above the edge to get a suitable background for normalization. All spectra were collected with a 0.1 eV step size through the absorption edge. The Fe L-edge spectra were calibrated against Fe metal powder with the maximum in the first derivative of the L_3-edge set to 706.8 eV, and the Mn L-edge spectra were calibrated against Mn metal powder with the maximum in the first derivative of the L_3-edge set to 638.7 eV.[19] The spectra were analyzed using the Athena software program.[20]

Results and discussion

Crystal Structure of the Sample Synthesized in Argon, $Sr_2FeMnO_{5.0}$.

The crystal structure of $Sr_2FeMnO_{5.0}$(Ar) was characterized by X-ray and neutron diffraction. Rietveld refinements were carried out with the GSAS program suite[21] using the EXPGUI interface.[22] The initial refinement was performed on the X-ray data using a *Pm-3m* model. The refinement profile is shown in Figure 6.2a. Although an excellent fit was obtained, the exact Fe and Mn contents, as well as oxygen site occupancy (which, in an ideal case, should be 5/6), remained to be determined by neutron diffraction. For materials containing Fe and Mn, neutron diffraction is an excellent probe because of the large difference between scattering lengths of these elements: 9.45(2) fm for Fe and –3.75(2) fm for Mn. The refined cell parameters and metal atom positions obtained from refinement of the X-ray data were used for refinement of the neutron diffraction data. The results are reported in Tables 6.2 and 6.3 and Figure 6.2b.

Table 6.2. Refinement results with x–ray (300K), TOF (300K) and constant-wavelength neutron diffraction data (290K) for $Sr_2FeMnO_{5.0}$ synthesized in argon atmosphere

Space group	*Pm-3m*
Lattice parameters	a = 3.89328(1) Å V = 59.0130(10) $Å^3$
Z	1
Agreement factors	R_p (X–ray, λ=1.54056 Å) = 0.0265 R_{wp} (X–ray, λ=1.54056 Å) = 0.0348 R_p (TOF, four banks) = 0.0172 R_{wp} (TOF, four banks) = 0.0263 R_p (Neutron, λ= 1.32858 Å) = 0.0370 R_{wp} (Neutron, λ= 1.32858 Å) = 0.0481 R_p (Neutron, λ= 2.36950 Å) = 0.0410 R_{wp} (Neutron, λ= 2.36950 Å) = 0.0538

Table 6.3. The atomic coordinates, site occupancies and displacement factors for $Sr_2FeMnO_{5.0}$ (Ar) obtained from powder neutron diffraction data

	x	*y*	*z*	Occupancy	U_{iso} ($Å^2$)
			TOF, at 300K		
Sr	0.5	0.5	0.5	1.0	0.0148(2)
Fe	0	0	0	0.522(3)	0.0340(7)
Mn	0	0	0	0.478(3)	0.0340(7)
O	0.5	0	0	0.833(5)	0.0283(2)
	λ= 1.32858 and λ= 2.36950, at 290K, simultaneous refinement				
Sr	0.5	0.5	0.5	1.0	0.024(2)
Fe	0	0	0	0.475(9)	0.028(3)
Mn	0	0	0	0.525(9)	0.028(3)
O	0.5	0	0	0.78(2)	0.0311(8)

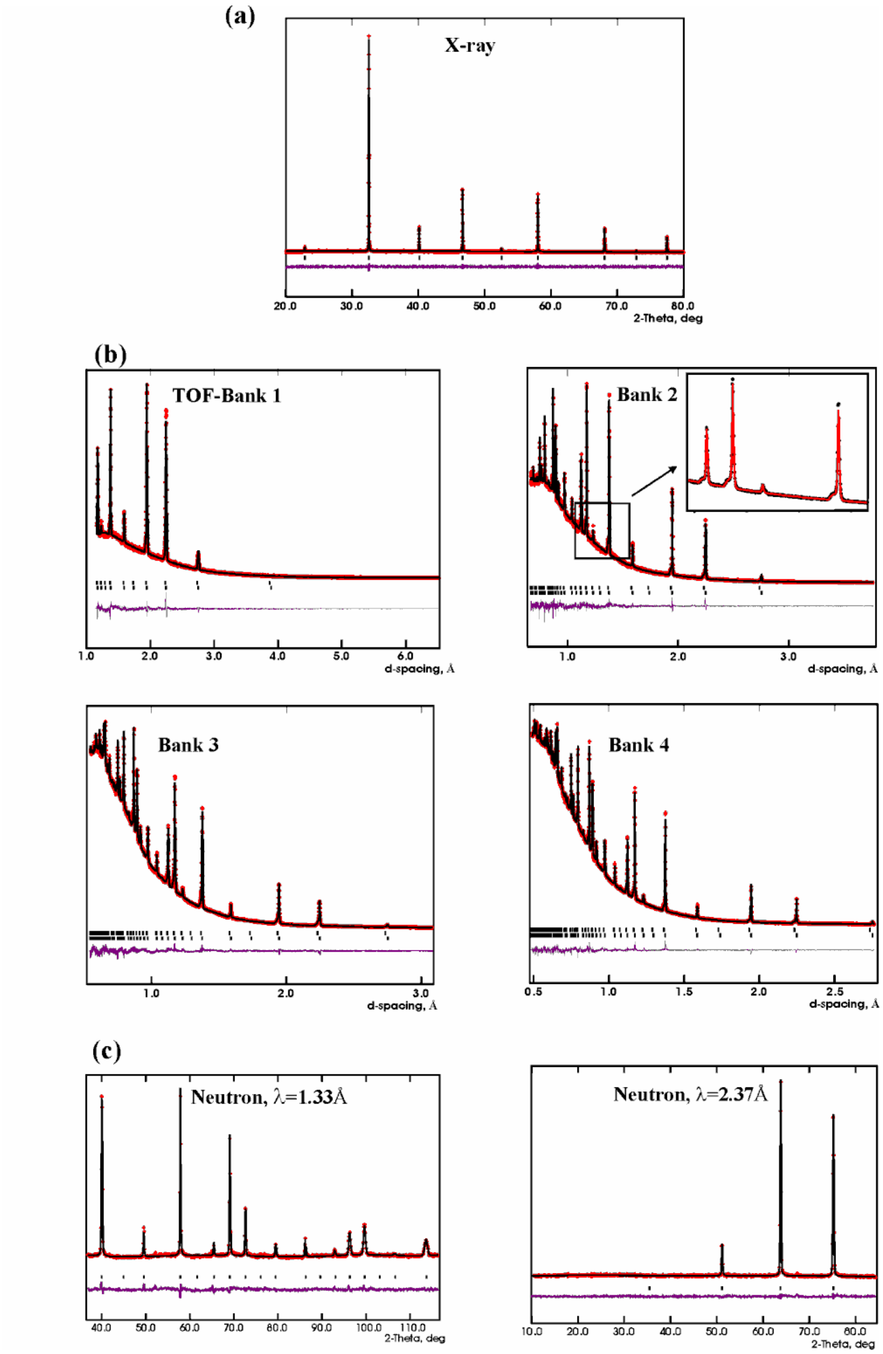

Figure 6.2. Rietveld refinement profiles for $Sr_2FeMnO_{5.0}$ (Ar) obtained from **(a)** powder X-ray diffraction data with λ = 1.54056 Å; **(b)** Time of Flight neuron diffraction data collected at detector angle of 46° (bank 1), 90° (bank 2), 119° (bank 3), 148° (bank 4), and **(c)** constant wavelength neutron with two different wavelengths. The stars are the experimental data, the solid line the model, the vertical tic marks locate Bragg peak positions, and the lower line is the difference plot.

The oxygen site occupancy from TOF data was refined to 0.833(5), which is exactly the value expected for stoichiometric $Sr_2FeMnO_{5.0}$, indicating the absence of excess oxygen. The refinement with the constant-wavelength neutron diffraction gives a smaller occupation for oxygen. The larger Q range covered by TOF data might be the reason for obtaining a more reasonable O occupancy compared to the constant-wavelength neutron diffraction. Concerning Fe and Mn site occupancies, although the values obtained from TOF and constant-wavelength neutron data are not the same, they both give values very close to the ideal, that is, within ~4% of 0.50.

Note also the much larger unit cell constant, a = 3.89328(1) Å, compared with the previously reported value, a = 3.852 Å, for a sample prepared in air.[15] The Fe(Mn)–O bond length, 1.94539(2) Å, is very close to the average Fe–O and Mn–O distances in $A_2Fe_2O_5$ and $A_2Mn_2O_5$ (A = Ca, Sr), respectively.[1,3,12,13] However, the Sr–O bond in $Sr_2FeMnO_{5.0}$, 2.75120(2) Å, is slightly longer than the average of the lengths observed in $Sr_2Fe_2O_5$ and $Sr_2Mn_2O_5$.[3,13]

Careful inspection of the neutron diffraction data revealed shoulders appearing on almost every major peak, shifted systematically to smaller d spacings; see the inset in Figure 6.2b. This signaled the presence of a slight amount of another cubic phase with similar composition but smaller cell parameters, which was confirmed by a two-phase Rietveld refinement. The cell parameter for the minority phase is 3.86228(8) Å, as opposed to 3.89328(1) Å for the majority component. The oxygen site occupancy in this second cubic phase was found to be 0.91(3), consistent with ~10% more oxygen compared to the main phase, which is expected, given the smaller cell constant. Although the amount of the second phase was small, the appearance of two phases in the neutron data was puzzling, because there was no indication of a second phase in the high-resolution X-ray data of Figure 6.2a. As the X-ray data were obtained within a few hours after synthesis whereas the neutron diffraction data were obtained a few weeks later, it was hypothesized that gradual air oxidation of $Sr_2FeMnO_{5.0}$ occurs at room temperature. This was later verified by an X-ray examination of a $Sr_2FeMnO_{5.0}$ sample within 1 h after preparation, as well as a few weeks later. In the next section, we show that a change in the synthesis route such that all of the preparation steps are performed in air (rather than argon) results in a highly oxidized sample with an even smaller cell parameter that still retains the cubic structure. Nevertheless, spontaneous oxidation of $Sr_2FeMnO_{5.0}$ at room temperature is a remarkable phenomenon.

A comparison between the crystal structures of $Sr_2FeMnO_{5.0}$ and our previously studied Ca analogue,[14] Ca_2FeMnO_5, is noteworthy. When the two materials are synthesized under argon, the latter crystallizes in the orthorhombic system, space group *Pnma*, with the vacancy-ordered brownmillerite structure. Mn^{3+} preferentially occupies the octahedral sites, with only a few percent of site mixing. A strong octahedral site preference of Mn^{3+} has been demonstrated for Ca_2GaMnO_5 and Sr_2GaMnO_5 as well.[23-25] Both polyhedra are highly distorted. For the octahedra, the four bonds in the *a*-*c* plane with an average distance of 1.92 Å are significantly shorter than the two bonds out of the plane, 2.22 Å, whereas for the tetrahedra, the four bond lengths range from 1.84 to 1.94 Å. Nonetheless, the average Fe(Mn)–O bond length, 1.97 Å, is similar to that observed in cubic $Sr_2FeMnO_{5.0}$, 1.94539(2) Å.

It is remarkable that substitution of the larger A-site cation, Sr, for Ca destroys the long-range ordering of oxygen vacancies in brownmillerite Ca_2FeMnO_5. Note that this does not occur when only Fe or Mn resides on the B/B′ sites, as both $Ca_2Fe_2O_5$ and $Sr_2Fe_2O_5$ are brownmillerites[1-3] and both $Ca_2Mn_2O_5$ and $Sr_2Mn_2O_5$ show the same square-pyramidal geometry for all B/B′ sites.[12,13]

There does not appear to be a simple, straightforward explanation for the remarkable absence of tetrahedral chains in the long-range sense, which is equivalent to the destruction of oxide vacancy order, in proceeding from Ca_2FeMnO_5 to Sr_2FeMnO_5. As has been noted, vacancy ordering is preserved between $Ca_2Fe_2O_5$ (*Pnma*) and $Sr_2Fe_2O_5$ (*Imma*), albeit in a less ordered manner in the Sr-containing phase.[1-3] Another relevant comparison is between Ca_2GaMnO_5 (*I*2*mb*) and Sr_2GaMnO_5 (*Imma*) in which vacancy ordering is retained but attenuated upon substitution of Sr for Ca.[23-25] Only for the B-site combination Fe/Mn does this substitution result in complete destruction of long-range vacancy order. Ga^{3+} and Fe^{3+} are nearly identical in ionic radius, and thus, it is difficult to ascribe an obvious role for the Jahn-Teller ion, Mn^{3+}, and its strong octahedral site preference, which has been noted for Ca_2FeMnO_5, Ca_2GaMnO_5, and Sr_2GaMnO_5. Sr_2FeMnO_5 was prepared under the same conditions in which the ideal brownmillerite composition is obtained for Ca_2FeMnO_5, Ca_2GaMnO_5, and Sr_2GaMnO_5,[14,25] which is under flowing inert gas, and the oxygen content determined by neutron diffraction from spallation source data is exactly correct. Oxidized phases of $Sr_2Fe_2O_{5+y}$ and Sr_2GaMnO_{5+y} with $y \approx 0.5$ and greater show intermediate structures with well-ordered oxide vacancies,[9,25] which are not observed here. We should note that most of the structural information obtained so far on Ca_2FeMnO_5 and Sr_2FeMnO_5 is from either neutron or X-ray diffraction and refers to the average structure. Our NPDF and Mössbauer results show that the local structure is more ordered. In the future, we hope to investigate this material using a more local diffraction probe, namely, electron diffraction (ED). Previous ED studies of apparently ordered BM phases, including $Sr_2Fe_2O_5$, Ca_2GaMnO_5, Sr_2GaMnO_5, Ca_2CoAlO_5, and others, revealed a complex microstructure involving intergrowths of small domains.[2,25,26]

Crystal Structures of Samples Synthesized in Air.

For the purpose of comparison, both Ca_2FeMnO_{5+y} and Sr_2FeMnO_{5+y} were synthesized.

Air-Synthesized Sr_2FeMnO_{5+y}. A cubic structure, *Pm*-3*m*, was found, as for the argon product, but with a smaller cell parameter, 3.83075(3) Å, which is even smaller than the previously cited literature value of $a = 3.852$ Å.[15] The refinement profiles for this compound are shown in Figure 6.3a-c. Unlike the argon product, the material synthesized in air does not show any gradual, spontaneous oxidation in air. Constant-wavelength neutron diffraction studies indicate an oxygen site occupancy of 0.926(10), which gives y = 0.56(6), consistent with the results of the TGA experiments described in the following section. The Fe and Mn site occupancies were determined to be 0.482(4) and 0.518(4), respectively, close to the ideal value of 0.50. Table 6.4 summarizes the refinement results for this compound. The Fe(Mn)–O bond length is 1.91981(4) Å, shorter than that observed in the argon material, 1.94539(2) Å, indicating a greater degree of cation oxidation. The contraction of the unit cell also results in shorter Sr–O bonds in the air-synthesized compound, 2.71502(4) Å as opposed to 2.75137(6) Å for the argon material.

Air-Synthesized Ca_2FeMnO_{5+y}. This material[15] was synthesized for the purpose of comparison. Although there are small differences between our powder pattern and that of ref 15, the occurrence of a brownmillerite phase is clearly evident in both patterns. Figure 6.3d shows the X-ray refinement profile for this compound in the *Pnma* space group.

Table 6.4. Refinement results from powder x-ray (300K) and neutron diffraction data (290K) for $Sr_2FeMnO_{5.5}$ synthesized in air.

Space group	*Pm-3m*
Lattice parameters	a = 3.83075(3) Å V = 56.215(1) $Å^3$
Z	1
Agreement factors	R_p (X–ray, λ=1.54056 Å) = 0.0389 R_{wp} (X–ray, λ=1.54056 Å) = 0.0510 R_p (Neutron, λ= 1.32858 Å) = 0.0402 R_{wp} (Neutron, λ= 1.32858 Å) = 0.0589 R_p (Neutron, λ= 2.36950 Å) = 0.0235 R_{wp} (Neutron, λ= 2.36950 Å) = 0.0339

Neutron results, λ=1.32858Å and λ=2.36950Å, simultaneous refinement at 290K:

	x	y	z	Occupancy	U_{iso} ($Å^2$)
Sr	0.5	0.5	0.5	1	0.0137(9)
Fe	0	0	0	0.482(4)	0.0030(13)
Mn	0	0	0	0.518(4)	0.0030(13)
O	0.5	0	0	0.926(10)	0.0146(5)

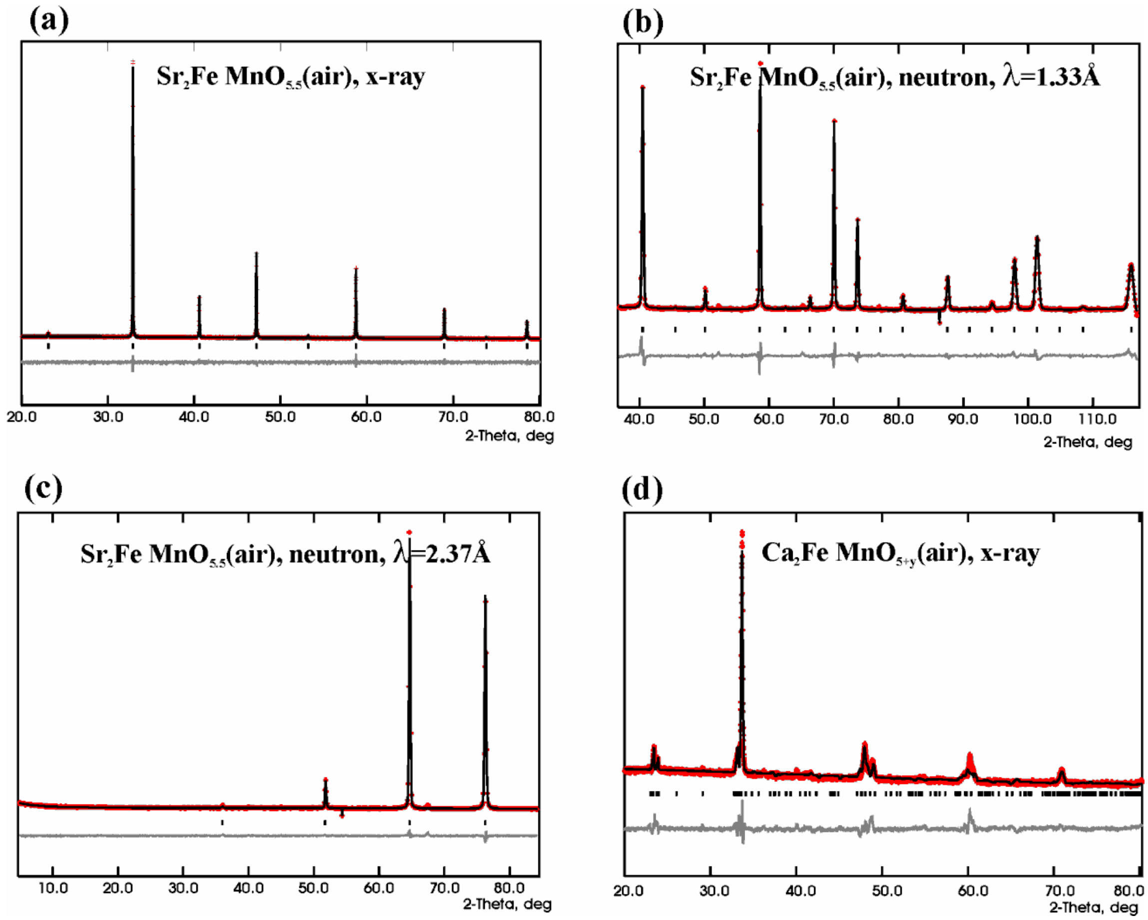

Figure 6.3. Rietveld refinement profiles for powder diffraction data. **(a-c)** Results for $Sr_2FeMnO_{5.5}$ (air). X-ray data (λ=1.54056Å) were obtained at 300K and neutron data at 290K. Panel **d** shows the powder X-ray profile for Ca_2FeMnO_{5+y} (air), and is given for the purpose of comparison, to show that, for the Ca-materials, the synthesis in air results in a brownmillerite structure, similar to the synthesis in Ar.

Experiments on both Sr and Ca compounds showed that the air oxidation is reversible upon subsequent refiring in argon under the same temperature conditions. The degree of oxidation was determined by thermogravimetric analyses. Based on these measurements, a 1.97% weight loss occurs when a Ca_2FeMnO_{5+y}(air) is fired in argon. This corresponds to $y = 0.34$ for the Ca compound. The weight loss for Sr_2FeMnO_{5+y}(air) fired in argon is 2.19(6)%, which gives $y = 0.51(1)$.

Local Structure of Argon-Synthesized $Sr_2FeMnO_{5.0}$.

Although the average structure obtained from refinement of neutron powder diffraction data is clearly cubic, the large atomic displacement parameters indicate that the local structure is likely to be much more complex. To examine the local structure, a neutron pair distribution function analysis was carried out. Figure 6.4 shows the S(Q) data obtained at 300 K extended to $Q_{max} = 30$ Å^{-1}. From the inset, it is clear that the background is highly modulated, indicating considerable short-range order. As these modulations are not seen in the X-ray diffraction data, their origin must be associated with short-range order of oxygen ions. In Figure 6.5a, the pairwise distribution function, G(r), derived from S(Q) by Fourier transform upon truncation at Q = 30 Å^{-1}, is shown out to 20 Å. The program PDFGUI[27] was used to perform refinements with the G(r) data to model the local structure.

These data were fit initially with the cubic model, with oxygen vacancy disorder, from 1.5 to 20 Å, as shown, and the agreement is seen to be poor at short r. If the fit is done within the ranges of 1.5 – 5 Å and 10 – 20 Å separately (Figure 6.5b,c), the agreement factors, R_w, are 19.7% and 12.3%, respectively, emphasizing that the disordered cubic structure is suitable only for the longer distances as the system begins to resemble the average structure. Examination of the short-r data shows the existence of shoulders on many peaks, which are not modeled by the average cubic structure but which correspond to bond distances of a vacancy-ordered brownmillerite structure (Figure 6.5d). Comparison of the positions of these shoulders with interatomic distances for the brownmillerite $Sr_2Fe_2O_5$[2,3] indicates an excellent match. Note that, for a cubic model, there is only one Fe(Mn)–O distance at ~1.945 Å, whereas a brownmillerite model involves a range of distances from1.857 to 2.203 Å. Some of these distances are shown in Figure 6.5d by dashed vertical lines in red. A similar situation applies to the Sr–O distances.

Therefore, a refinement with a brownmillerite model, *Ibm*2, was performed for the data-range from 1.5 to 5 Å (Figure 6.5e). This model incorporates ordering of oxygen vacancies that results in distinct octahedral (O) and tetrahedral (T) sites. Following the results for Ca_2FeMnO_5, a full cation site ordering was assumed with Fe on the T site and Mn on the O site.[14] The refinement results for short r (to r = 5 Å) showed a significantly better agreement with the brownmillerite model, R_w = 13.9%, compared to that for the disordered cubic model, R_w = 19.7%. Therefore, the NPDF results suggest that, unlike the average structure, the local structure resembles an oxygen-ordered brownmillerite-type system with Fe mostly in a T site.

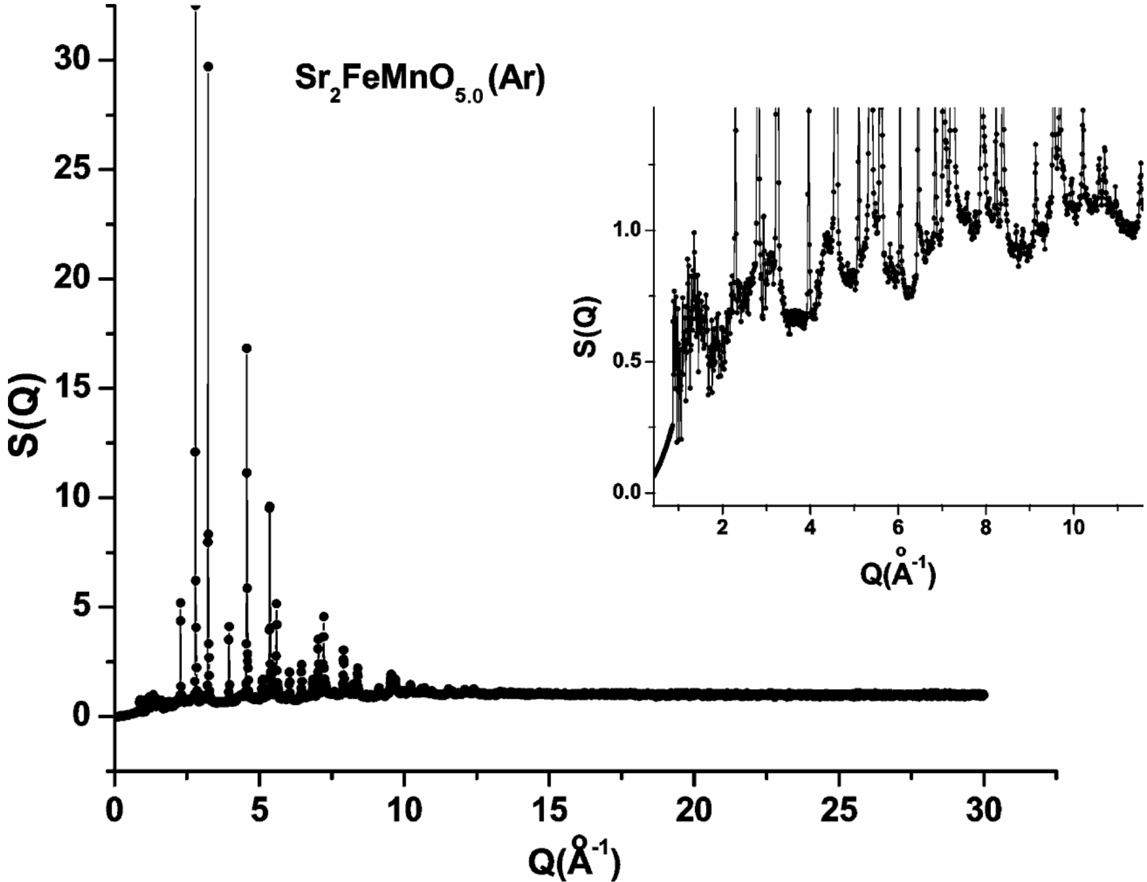

Figure 6.4. S(Q) extended to Q_{max} = 30 Å^{-1} at 300K for Sr$_2$FeMnO$_{5.0}$ synthesized in argon. The inset shows a strongly modulated background at low Q, indicative of short-range ordering of oxygen vacancies. These modulations do not appear in the X-ray data in the same Q-range.

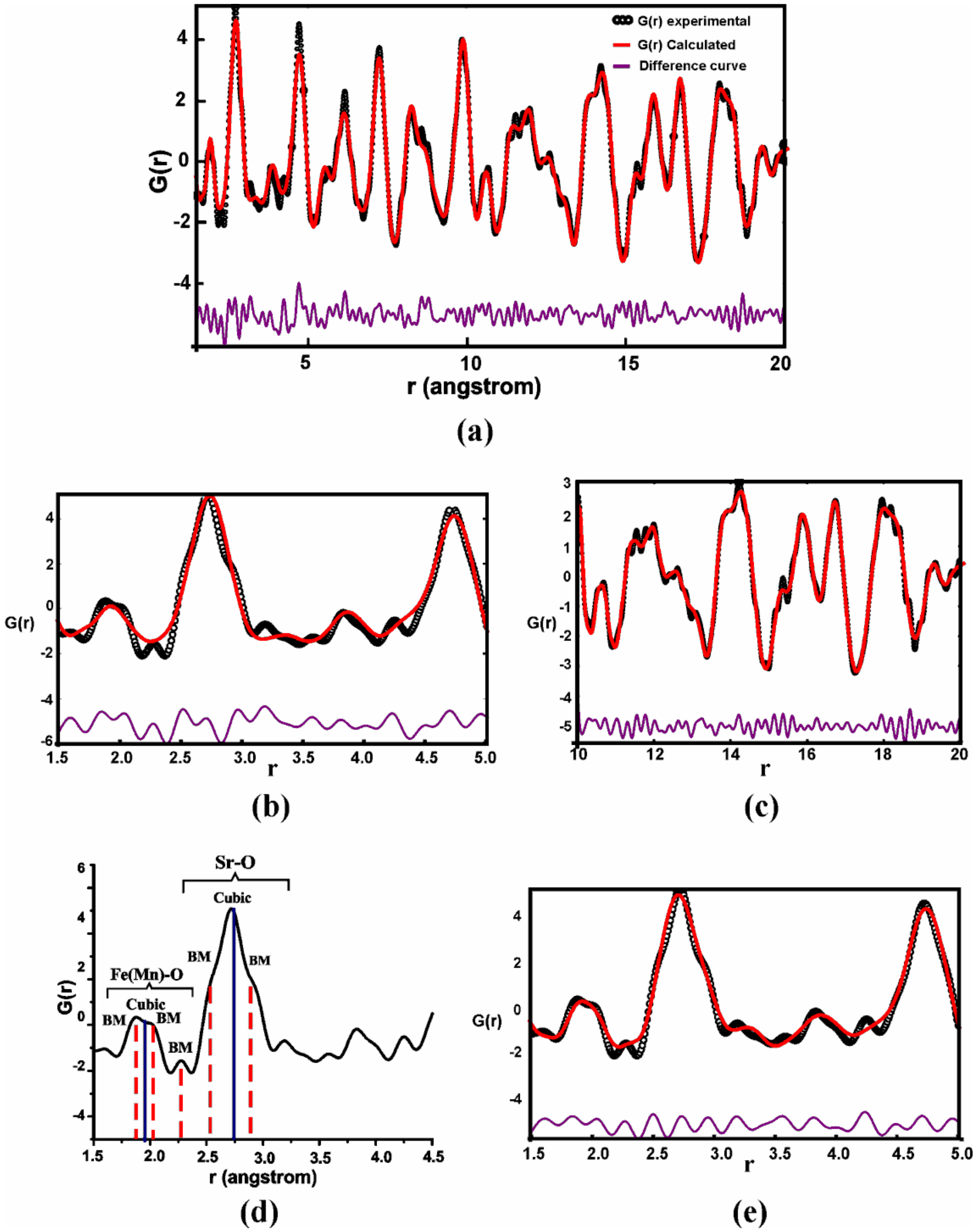

Figure 6.5. **(a)** G(r) for $Sr_2FeMnO_{5.0}$ (Ar), obtained by a Fourier transform of the S(Q) truncated at Q = 30 $Å^{-1}$. A cubic model, *Pm*-3*m*, with disordered oxygen vacancies was used for the fit out to r = 20 Å, R_w=16.2%. **(b)** G(r) fit with a *Pm*-3*m* model for short r, 1.5Å – 5Å, R_w=19.7%. **(c)** G(r) fit with a *Pm*-3*m* model for long r, 10 – 20 Å, R_w= 12.3%. **(d)** Short-range G(r) compared with interatomic distances corresponding to both a cubic *Pm-3m* model (vertical purple lines) and a brownmillerite (BM) *Ibm*2 model (dashed red lines). Note that the features observed in the G(r) correspond well to those expected for brownmillerite ordering. **(e)** G(r) fit with a brownmillerite *Ibm*2 model for short r, 1.5 – 5Å , R_w=13.9%.

Mössbauer Spectroscopy at Room Temperature

Mössbauer spectroscopy experiments were performed on both argon-synthesized and air-synthesized samples of Sr_2FeMnO_{5+y}, as this technique provides complementary information on the local structure. The results at room temperature are shown in Figure 6.6 and are summarized in Table 6.5. In neither case was it possible to find a unique fit. The room-temperature spectrum for $Sr_2FeMnO_{5.0}$(Ar; y = 0.0) presents as a severely asymmetric doublet that can be fitted using either three discrete sites or a Gaussian distribution of quadrupole splitting (QS) with strongly correlated isomer shifts (IS) (to reproduce the asymmetry). The latter model yields a relatively poor fit ($\chi^2 \approx 12$) and is unable to fully account for the shape of the low-velocity part of the spectrum in Figure 6.6. Therefore, the three-site fit, shown as the solid line in Figure 6.6 and summarized in Table 6.5, is favored, but caution about the absence of clearly resolved components makes this analysis qualitative in nature. The presence of multiple sites, with different isomer shifts and quadrupole splittings, is qualitatively consistent with the NPDF results, which indicate that the system is not locally cubic. Of the three sites found in the discrete model, all have IS and QS values that are consistent with Fe^{3+} in a site with coordination number less than 6. For comparison, the IS/QS values (in mm/s) for the ordered brownmillerite, $Sr_2Fe_2O_5$, are 0.649/0.411 for the octahedral (O) site and 0.361/0.854 for the tetrahedral site (T).[28] These results are also consistent with general trends shown by a wide range of Fe-based oxides and provide strong evidence that iron is present in the Fe^{3+} state in an environment that is likely tetrahedral.[29] Given the strong O site preference of

Mn^{3+} found in Ca_2FeMnO_5, Fe^{3+} is expected to be found in T sites in disordered Sr_2FeMnO_5.[14]

Table 6.5. Summary of fitting results for room-temperature Mössbauer spectra for Sr_2FeMnO_{5+y}.

$Sr_2FeMnO_{5.5}$(air) y ≈ 0.5 The spectrum can be fitted using two, equal-area doublets, leading to two statistically equivalent models (χ^2 = 1.39)			
	I.S. (mm/s)	Q.S. (mm/s)	
	Model 1		
Site 1	0.205(3)	0.805(6)	
Site 2	0.134(3)	0.160(8)	
	Model 2		
Site 1	–0.007(3)	0.411(5)	
Site 2	0.316(3)	0.554(6)	
$Sr_2FeMnO_{5.0}$(Ar) y ≈ 0 Spectrum best fitted using three quadrupole doublets, a three site model, χ^2 =1.5			
	I.S. (mm/s)	Q.S. (mm/s)	relative area (%)
Site 1	0.182(3)	1.60(8)	41
Site 2	0.286(4)	1.15(1)	34
Site 3	0.352(5)	0.67(1)	25

The room-temperature spectrum of $Sr_2FeMnO_{5.5}$(air; y = 0.5) is composed of two overlapping quadrupole doublets with essentially equal areas. This situation inevitably leads to two statistically equivalent models that cannot be distinguished on the basis of χ^2 alone, and the degeneracy can be lifted only by either ruling out one model on the basis of the fitted parameters or preparing a doped sample in which the 1:1 area ratio is changed. The parameters for the two models are given in Table 6.5. The most relevant site-ordered compound for comparison here is $Sr_4Fe_4O_{11}$ with the same oxygen content, which has two Fe sites of equal multiplicity, one square-pyramidal (SP) and one O, with respective IS/QS values of 0.136/0.146 and 0.572/0.434.[29] For both models (Table 6.5), the fitted parameters, especially the IS values, are inconsistent with O site occupation but support a low-coordination-number environment, possibly SP. The very low IS value of –0.007(3) mm/s found in model 2 might indicate Fe^{4+}, but this assignment is not definitive, and it might provide a basis for favoring model 1, as it yields more conventional isomer shifts. The presence of Fe^{4+} can be checked by XANES.

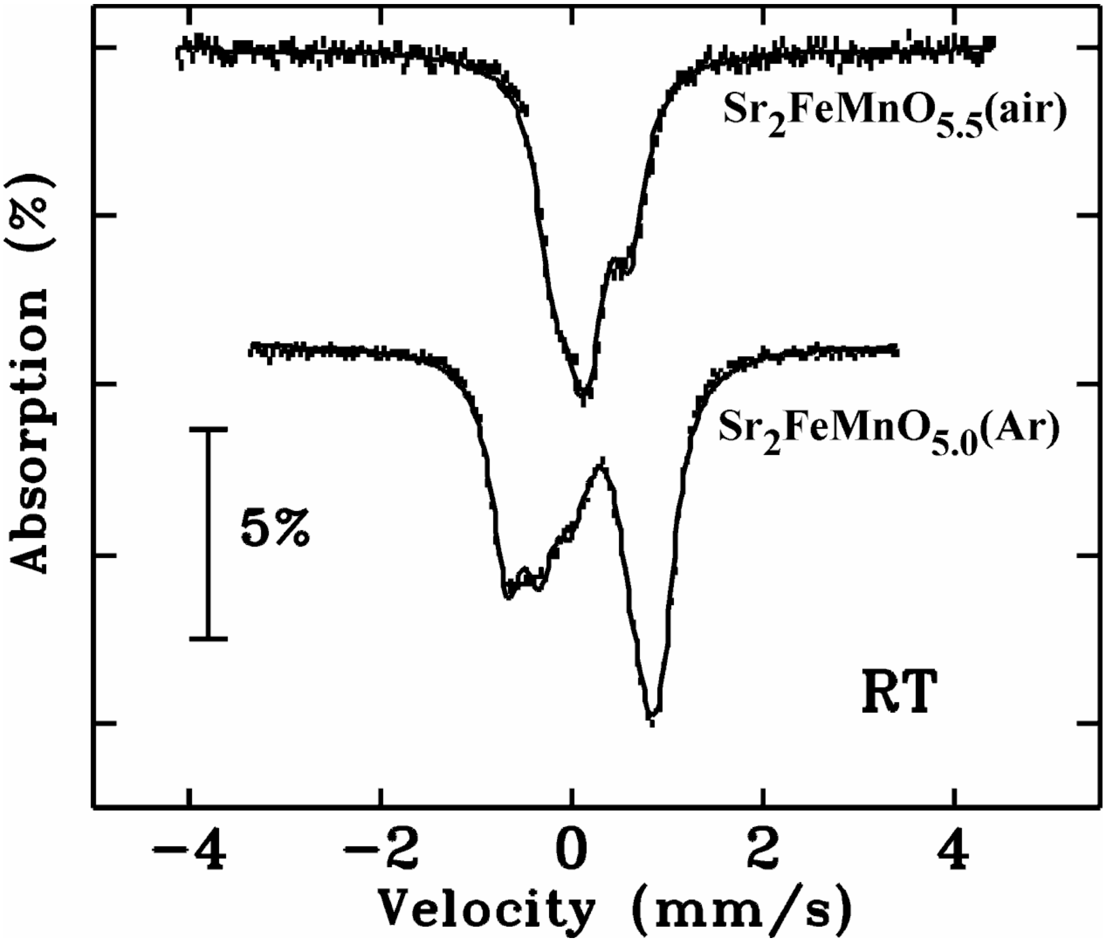

Figure 6.6. Room temperature Mössbauer spectra for (top) $Sr_2FeMnO_{5.5}$ (air) and (bottom) $Sr_2FeMnO_{5.0}$ (Ar). The parameters used to fit the spectra are summarized in Table 6.5.

In summary, the Mössbauer results support the NPDF analysis in part while indicating a more complex local picture with multiple Fe sites in low-coordination-number environments, T or SP.

XANES

To verify the oxidation states and local coordination environments of Fe and Mn, Fe and Mn L-edge X-ray absorption near-edge spectroscopy (XANES) was performed, with Fe_2O_3 and Ca_2FeMnO_5[14,30] as references. (Note that the cation combination in Ca_2FeMnO_5 is Fe^{3+}/Mn^{3+}.) These spectra result primarily from a dipolar excitation of 2p electrons to unoccupied 3d states and, as such, provide information on the local coordination environment through examination of the crystal-field-split 3d states.[31] Changes to the screening of the nuclear charge by varying the occupancy of the 3d states lead to shifts in absorption energy, allowing for an examination of metal charge.

For $Sr_2FeMnO_{5.0}$(Ar), by comparison to Fe_2O_3 and Ca_2FeMnO_5, the absorption energy of the Fe L_3-edge spectrum is consistent with Fe^{3+} (Figure 6.7a). The spectral line shape shows two peaks, representing crystal-field-split 3d states that are consistent in energy and intensity with Fe atoms primarily occupying a tetrahedral site. The slight increase in intensity of the low-energy peak relative to that from Fe in Ca_2FeMnO_5 implies that some Fe atoms in $Sr_2FeMnO_{5.0}$(Ar) might occupy octahedral sites. The corresponding Mn L_3-edge spectrum is presented in Figure 6.7b and indicates that most Mn atoms have a 3+ charge. The high-energy shoulder (see arrow) suggests some presence of Mn^{4+}, which was later found to be due to oxidation of the sample during handling. For $Sr_2FeMnO_{5.5}$(air), the XANES L_3-edge data indicate that Fe is in the 3+ state (Figure 6.8a), which is located mostly in tetrahedral sites but with some occupancy of octahedral sites (i.e., the line shape is between those of Fe_2O_3 and Ca_2FeMnO_5). There is no indication of Fe^{4+} in these spectra, which is an argument against model 2 for the Mössbauer data. The Mn L_3-edge spectrum (Figure 6.8b) is dominated by Mn^{4+}, but some Mn^{3+} is also present.

For both materials, the L-edge data discussed above are consistent with the NPDF and room-temperature Mössbauer studies, which indicated that Fe mostly resides in a tetrahedral site. Comparing spectra for the reduced and oxidized forms, it seems clear that oxidation involves mainly conversion of Mn^{3+} to Mn^{4+} and not Fe^{3+} to Fe^{4+}.

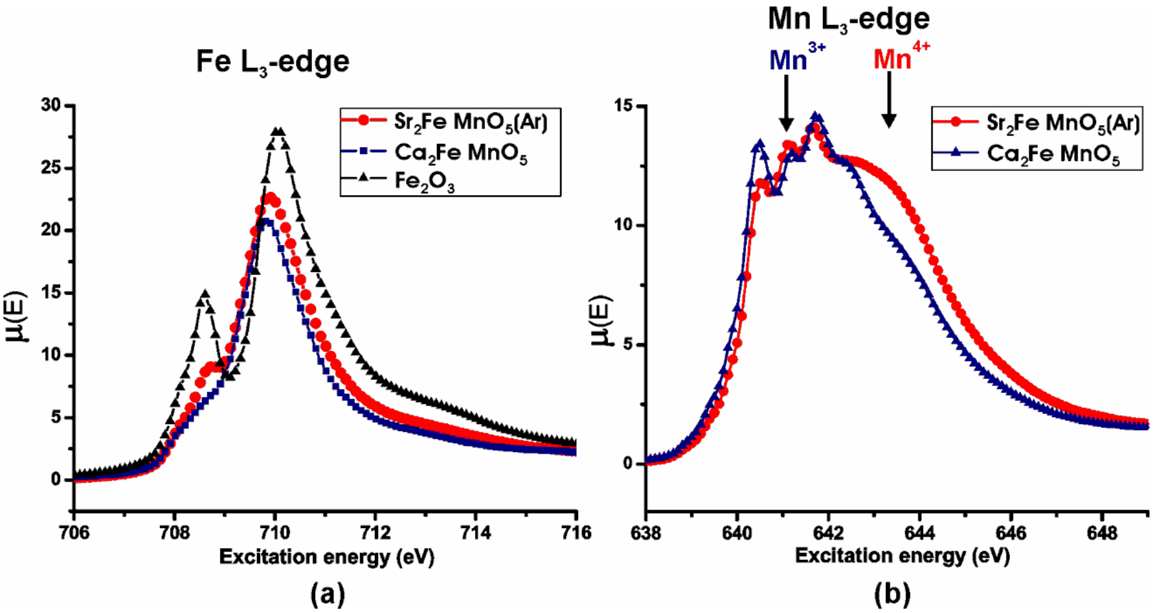

Figure 6.7. XANES spectra for $Sr_2FeMnO_{5.0}$(Ar), compared to those of Fe_2O_3 and Ca_2FeMnO_5. **(a)** Fe is in the 3+ state, closely resembling the spectrum for Ca_2FeMnO_5. **(b)** Mn is primarily in 3+ state. Some Mn^{4+} appears in the spectrum as a result of oxidation of sample during handling in air.

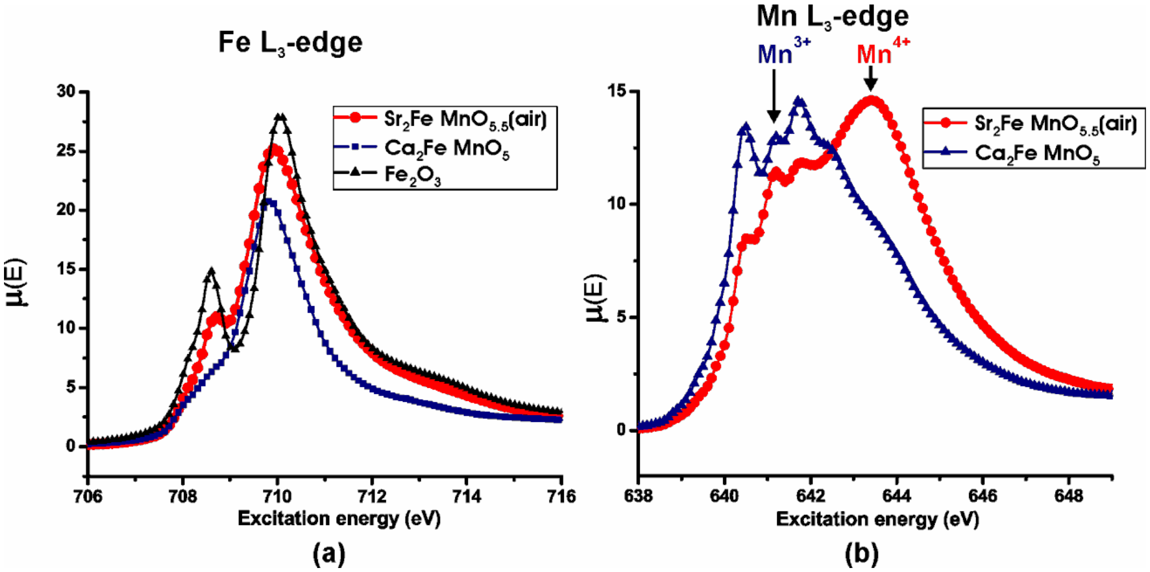

Figure 6.8. XANES spectra for $Sr_2FeMnO_{5.5}$ (air), compared to those of Fe_2O_3 and Ca_2FeMnO_5. **(a)** Fe is in the 3+ state, similar to the argon compound. **(b)** Mn is primarily in the 4+ state, with some Mn^{3+} present.

Magnetic Properties

The magnetic susceptibility data for $Sr_2FeMnO_{5.5}$(air) (Figure 6.9a) show a zero-field-cooled (ZFC)/field-cooled (FC) data divergence below ~25 K, behavior normally taken as indicative of spin freezing rather than long-range order. The broad maximum observed at ~120 K might indicate short-range magnetic ordering. From the inverse susceptibility data (Figure 6.9b,c), it is clear that Curie-Weiss behavior is found only above 320 K (Figure 6.9c). Parameters extracted from a fit between 320 and 700 K (Figure 6.9d) give a Curie constant of 6.07(3) emu.K/mol, close to the spin-only value for the Fe^{3+}/Mn^{4+} combination (6.25 emu.K/mol), determined by XANES. The magnetization data (Figure 6.9e) at 5 K show a pronounced hysteresis with a remnant magnetization of ~0.0214 μ_B, indicating the presence of uncompensated moments. These moments are absent at 100 K, where no hysteresis is present in the magnetization data.

The magnetic susceptibility as a function of temperature for $Sr_2FeMnO_{5.0}$(Ar) from 5 to 300 K is shown in Figure 6.10a. A ZFC/FC divergence similar to the one observed in the air sample is observed but with a much higher apparent T_f value, ~50 K. The 5-300 K inverse susceptibility is plotted in Figure 6.10b. Even though the plot might appear to reach a linear regime from 250 to 300 K, the high-temperature susceptibility measurements from 300 to 700 K (Figure 6.10c,d) show that the paramagnetic regime is not achieved even up to 700 K. Isothermal magnetization data (Figure 6.10e) show a clear hysteresis at 5 K. However, the hysteresis and the remnant magnetization are much smaller than those observed for the air-synthesized compound. Nevertheless, the hysteresis disappears at 100 K, similar to the observation for the air-synthesized material.

The Mössbauer spectra taken at low temperature show magnetic hyperfine splittings for both argon- and air-synthesized materials (Figure 6.11a-c). For $Sr_2FeMnO_{5.0}$(Ar), the magnetic patterns are broad, largely featureless sextets, indicating that Fe atoms in this system are subject to a very wide range of magnetic environments. The susceptibility anomaly is at about 50 K; however, it is clear from Figure 6.11a that a magnetic splitting is present for $Sr_2FeMnO_{5.0}$(Ar) at 3 times this temperature. However, closer inspection of the spectra reveals a marked change in appearance below 60 K, as the six hyperfine split lines become distinct. The form of the spectra led to the use of a distribution model to fit them,[17] and the results of this analysis are shown in Figure 6.11b. The changes upon cooling through $T_f \approx 50$ K are clear: The average hyperfine field ($<B_{hf}>$) increases sharply, and there is a marked drop in the width of the hyperfine field distribution. This likely reflects a change from short-ranged, possibly dynamic, spin correlations above T_f to more organized magnetic ordering below it. The average field of ~50 T at the lowest temperatures is typical of ordered Fe^{3+} compounds. For $Sr_2FeMnO_{5.5}$(air), the spectra presented in Figure 6.11c show that the magnetic splitting again appears well above the ~25 K event seen in the susceptibility. However, as with the $Sr_2FeMnO_{5.0}$(Ar) sample, there is a marked sharpening of the pattern below the apparent spin-freezing temperature derived from susceptibility. At 4.6 K, the spectrum is both sharper and more complex than that seen for the sample prepared in argon. Although only two equal-area iron sites could be resolved at room temperature, at least four magnetic components are needed to fit the spectrum at 4.6 K. Approximately 50% of the total area is present in two relatively sharp high-field components (50 and 47 T) that can be seen in the form of the two outer lines in Figure 6.11c. The remaining iron contributes to several much broader components with average hyperfine fields ranging from 25 to 30 T. The greatly reduced field and very broad distribution suggests that approximately half of the iron moments in the $Sr_2FeMnO_{5.5}$(air) sample are not fully ordered, even by 5 K, and that they might still be undergoing fluctuations on the Mössbauer time scale (~10^{-7}s).

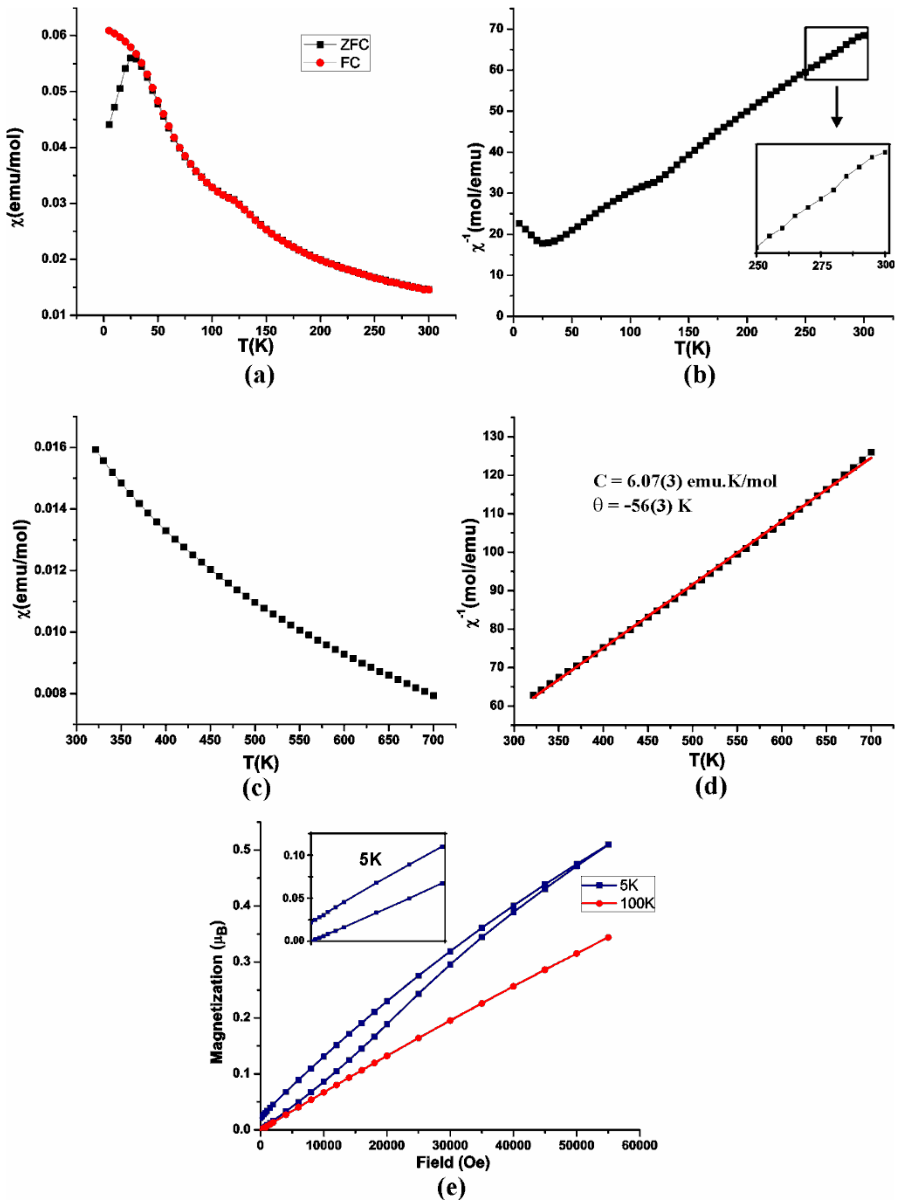

Figure 6.9. **(a)** ZFC and FC molar susceptibility data for $Sr_2FeMnO_{5.5}$ synthesized in air within the temperature range of 5 - 300 K. Note the ZFC–FC divergence at ~25 K. **(b)** Inverse susceptibility data. The inset shows clearly that a Curie-Weiss regime is not achieved up to 300 K. **(c)** High temperature magnetic susceptibility data obtained while heating the sample from 320 to 700K. **(d)** Inverse susceptibility data at high temperature fitted to the Currie-Weiss law. The red solid line shows the fit. The Curie constant C = 6.07(3) emu.K/mol is close to the spin only value for Fe^{3+}/Mn^{4+} combination (6.25 emu.K/mol), consistent with the XANES results. **(e)** Isothermal magnetization data at 5 and 100 K. Note the significant hysteresis observed at 5 K, with a remnant magnetization of ~0.0214 μ_B, magnified in the inset.

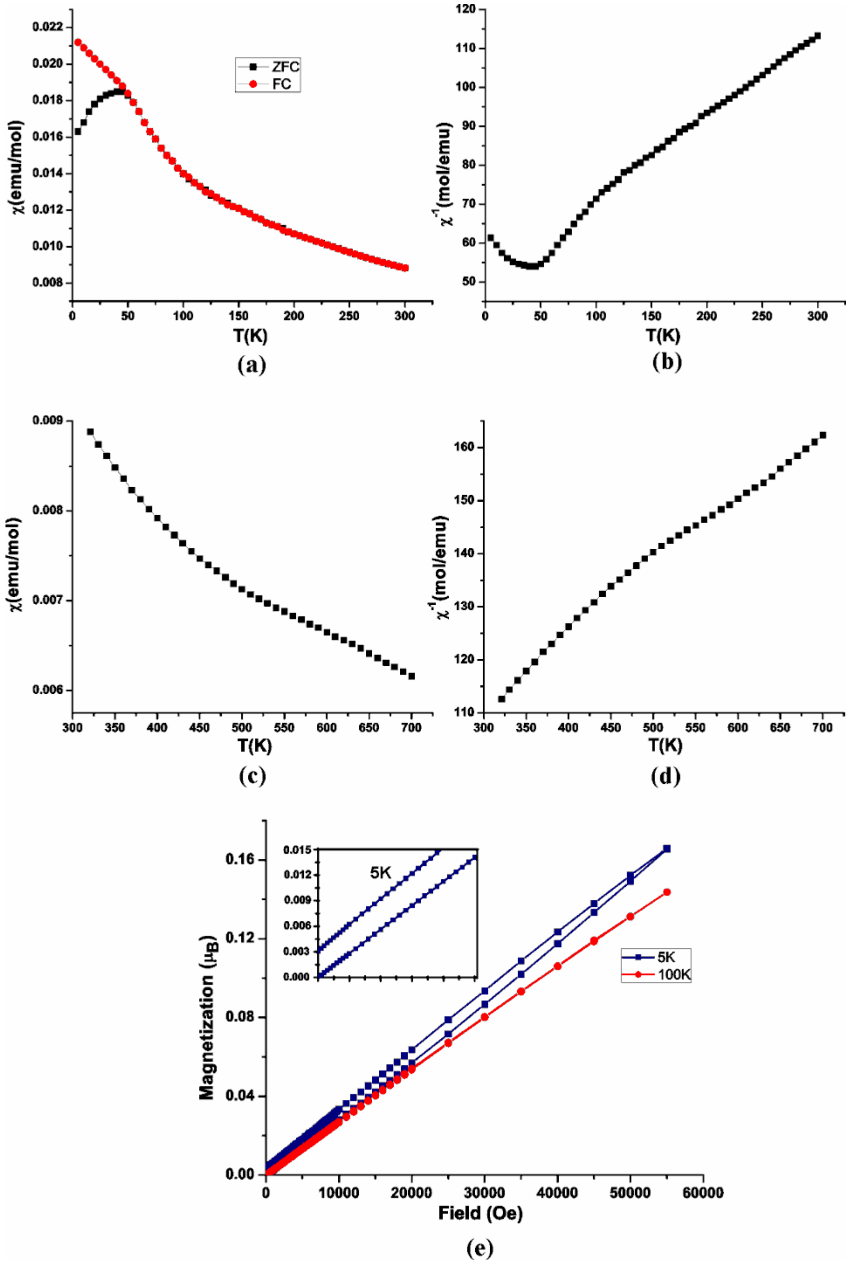

Figure 6.10. **(a)** ZFC and FC molar susceptibility data for $Sr_2FeMnO_{5.0}$ synthesized in argon within the temperature range of 5–300 K. Note the ZFC-FC divergence at ~50K. **(b)** Inverse susceptibility data from 5 to 300 K. **(c)** Susceptibility data collected while heating the sample from 320 to 700 K. **(d)** Inverse susceptibility from 320 to 700 K. Note that Curie-Weiss behavior is not seen up to 700K. **(e)** Isothermal magnetization data at 5 and 100 K. Note the hysteresis observed at 5 K, with a remnant magnetization of ~0.0031μ_B, magnified in the inset.

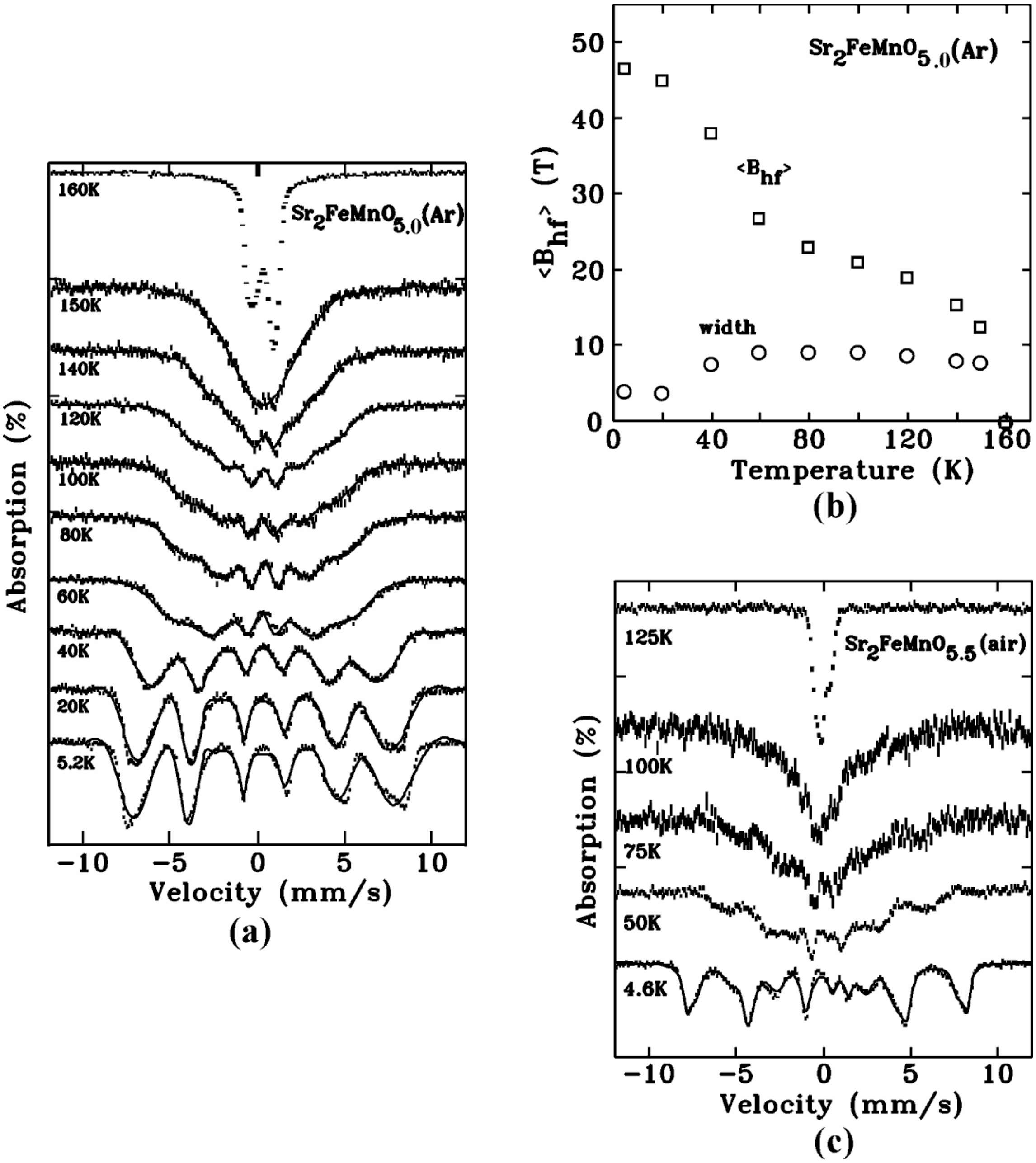

Figure 6.11. **(a)** Temperature-dependent Mössbauer spectra for $Sr_2FeMnO_{5.0}$ synthesized in argon with solid lines showing the distribution fits described in the text. **(b)** Average hyperfine field, $<B_{hf}>$, and the width of the distribution derived from the fits for $Sr_2FeMnO_{5.0}$ showing the marked break in behavior below T ≈ 50K. **(c)** Temperature-dependent Mössbauer spectra for $Sr_2FeMnO_{5.5}$ synthesized in air. Note that the short-range magnetic interactions, evident from the hyperfine splittings, persist up to ~150K for $Sr_2FeMnO_{5.0}$ (Ar) and to ~100K for $Sr_2FeMnO_{5.5}$ (air).

Finally, neutron diffraction data at 4 and 290 K provide more details regarding the low-temperature spin correlations in these materials. In Figure 6.12, for $Sr_2FeMnO_{5.0}$(Ar), two weak reflections at 30.90º and 60.95º are evident at 4 K, which can be indexed as (1/2 1/2 1/2) and (3/2 1/2 1/2) on the chemical cell, respectively, consistent with a G-type magnetic structure. However, the peaks are very weak, broad, and Lorentzian in shape rather than Gaussian, which indicates short-range spin correlations. To estimate the correlation length, the more intense peak at 30.90º ($Q = 1.41$ Å^{-1}) was fit to a Lorentzian line shape and analyzed using the Ornstein-Zernike model,[32] $I(Q) = A/[(Q - Q_0)^2 + \kappa^2]$, where $Q = (4\pi\sin\theta)/\lambda$, A is an amplitude, Q_0 is the peak center, and $\kappa = 1/\xi$ with ξ being the correlation length (Figure 6.13). The resulting values are $Q_0 = 1.408(7)$ Å^{-1} and $\xi =$ 50(1) Å, the latter involving a small correction for the resolution function of the diffractometer, indicating that these G-type spin correlations persist to more than 12 unit-cell-axis lengths. Thus, whereas the bulk susceptibility data suggest spin freezing, the actual magnetic ground state appears to consist of short-range domains of local G-type order. This is consistent with the Mössbauer spectra, which show indications below 60 K of a fairly well-ordered state. Very likely, an uncompensated moment is associated with each domain due to either surface spins or perhaps a local spin canting (the local structure is not cubic) giving rise to an unusual type of superparamagnet. Thus, the ZFC/FC divergence in the susceptibility data is understood as a blocking rather than a spin freezing temperature. This proposal is supported by the data of Figure 6.10e, which show hysteresis below but not above the apparent blocking temperature.

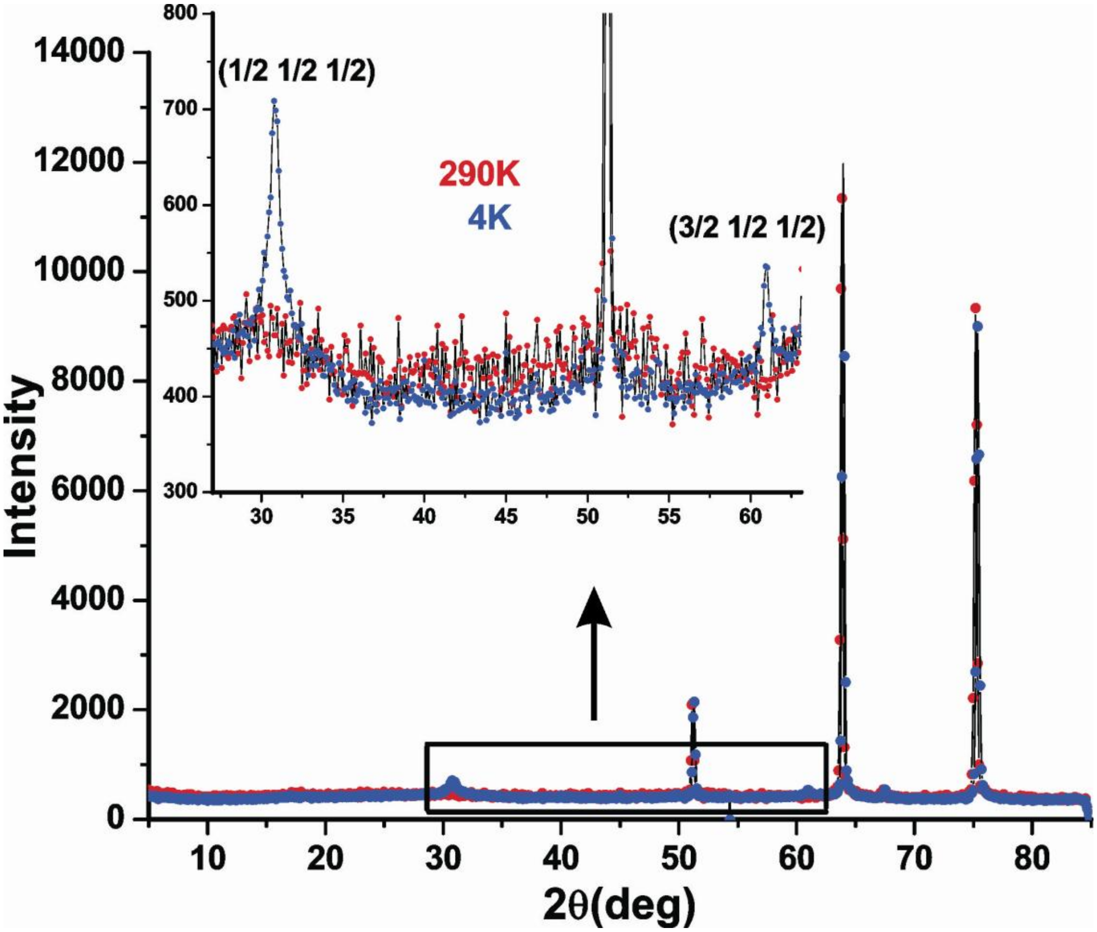

Figure 6.12. Neutron diffraction data for $Sr_2FeMnO_{5.0}$ (Ar) at 4 K (blue online) compared with data at 290 K (red online) showing the presence of broad magnetic features at ~31° and 61° that can be indexed as (1/2 1/2 1/2) and (3/2 1/2 1/2) on the primitive cubic cell, indicative of short-range G-type magnetic order (inset).

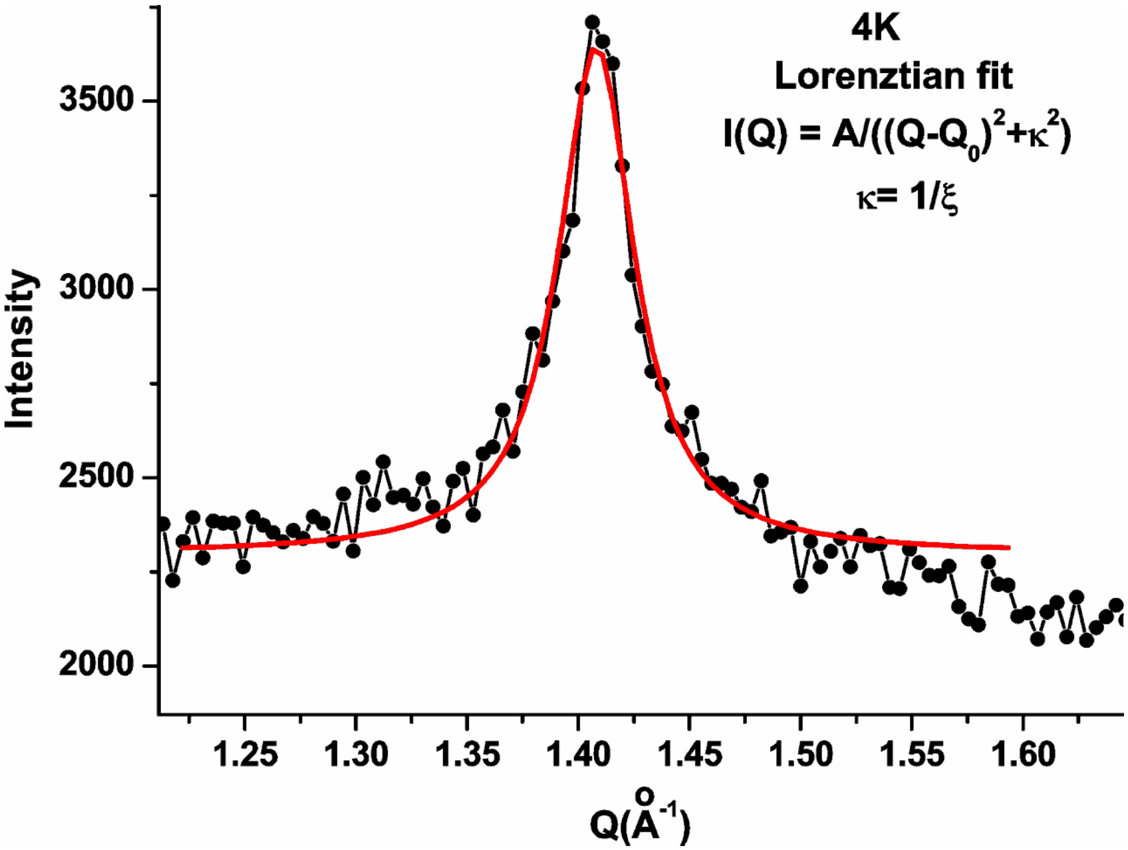

Figure 6.13. Fit of the (1/2 1/2 1/2) magnetic reflection of $Sr_2FeMnO_{5.0}$ (Ar) at 4 K to an Ornstein-Zernicke Lorentzian. The fitted values are Q_0 = 1.408(7) $Å^{-1}$ and κ = 0.0207(1) $Å^{-1}$. The resulting correlation length is ξ, = 50(1) Å after convolution with the resolution function.

For $Sr_2FeMnO_{5.5}$(air) the results are quite different, as seen in Figure 6.14. Only one very weak reflection is observed, which can be indexed as (1/2 1/2 1/2) for a G-type magnetic structure. Surprisingly, this peak is well-fitted by a Gaussian with a width identical within error to the neighboring (100) structure reflection, which indicates that at least some fraction of the sample volume is long-range-ordered. An estimate of the ordered fraction was obtained by comparison of the observed ratio of the (1/2 1/2 1/2)/(100) reflections with that calculated assuming reasonable ordered moments on Fe and Mn. The result is ~4% volume fraction. This result is also in accord with the Mössbauer observations, which indicated that a large fraction of the Fe moments were not long-range-ordered.

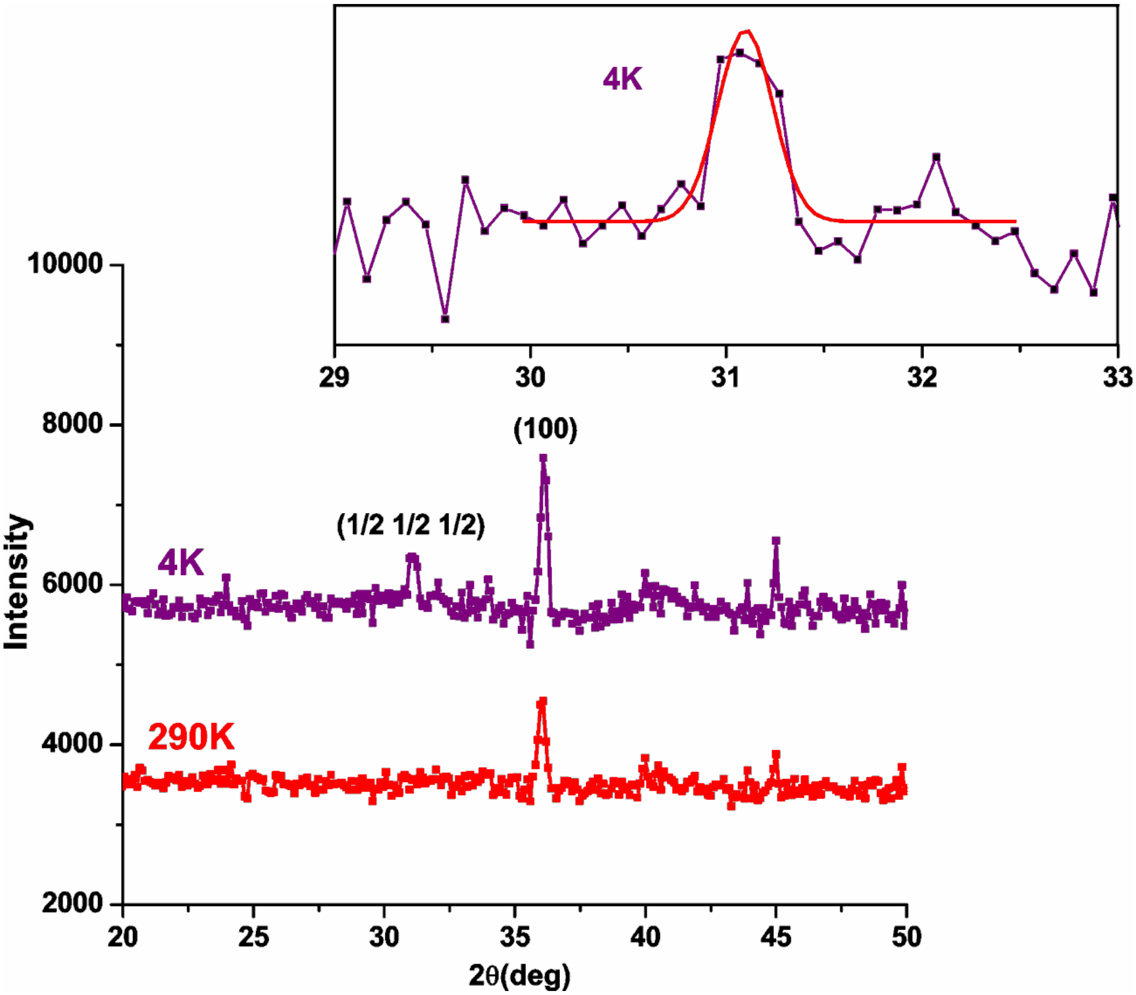

Figure 6.14. Comparison of the low-angle neutron diffraction patterns for $Sr_2FeMnO_{5.5}$ (air) at 4 and 290 K showing the development of a (1/2 1/2 1/2) magnetic peak at 4 K. The inset shows a Gaussian fit of the magnetic peak.

Summary and Conclusions

There is clearly a rather dramatic effect of the A-site cation on both the structure and magnetic properties between Ca_2FeMnO_{5+y} and Sr_2FeMnO_{5+y}. For the case of ideal oxygen stoichiometry with both materials prepared in argon, substitution of Sr for Ca induces a change from the vacancy-ordered brownmillerite structure (*Pnma*) to the disordered cubic structure (*Pm-3m*). Nonetheless, the local structure for $Sr_2FeMnO_{5.0}$ resembles strongly that of a brownmillerite to at least 5 Å. Remarkably, this phase oxidizes spontaneously at room temperature due primarily to the conversion of Mn^{3+} to Mn^{4+}.

An equally dramatic effect is seen in the magnetic properties, as brownmillerite Ca_2FeMnO_5[14] exhibits long-range antiferromagnetic ordering below ~407 K with a G-type magnetic structure whereas the cubic perovskite $Sr_2FeMnO_{5.0}$(Ar) shows only a ZFC/FC divergence below ~50 K in the bulk susceptibility, although Mössbauer spectroscopic data indicate that short-range magnetic correlations persist to much higher temperatures. Neutron diffraction reveals that the magnetic ground state consists at least in part of finite-size domains, $\xi = 50(1)$ Å, with local G-type order. Uncompensated spins associated with these domains give rise to a superparamagnetic behavior. It is remarkable that the effect of the substitution of Sr^{2+} for Ca^{2+} is to destroy the long-range AF G-type order in favor of finite-size domains. $Sr_2FeMnO_{5.5}$(air) behaves differently, showing mainly a very small G-type ordered volume fraction of ~4% at 4 K from neutron data. This is supported by the Mössbauer results that suggest a large fraction of still fluctuating spins at 4 K, indicative of an inhomogeneous magnetic ground state.

Acknowledgement

J.E.G. and D.H.R acknowledge the support of the Natural Sciences and Engineering Research Council (NSERC) of Canada through Discovery Grants, and D.H.R. is supported by grants from Fonds Québécois de la Recherche sur la Nature et les Technologies. The authors thank J.M. Cadogan for useful discussions. This work has benefited from the use of NPDF at the Lujan Center at Los Alamos Neutron Science Center, funded by the U.S. Department of Energy (DOE) Office of Basic Energy Sciences. Los Alamos National Laboratory is operated by Los Alamos National Security LLC under DOE Contract DE-AC52-06NA25396. The upgrade of NPDF has been funded by National Science Foundation (NSF) through grant DMR 00-76488. The Canadian Neutron Beam Centre is funded jointly by NSERC and the National Research Council (NRC) of Canada. Mr. Thomas Regier and Mr. David Chevrier are thanked for help in carrying out XANES measurements using the SGM beamline (11ID-1) located at the Canadian Light Source (CLS). The CLS is supported by NSERC, the National Research Council Canada, the Canadian Institutes of Health Research, the Province of Saskatchewan, Western Economic Diversification Canada, and the University of Saskatchewan.

References

[1] Berggren, J. *Acta Chem. Scand.* **1971,** 25, 3616.

[2] D'Hondt, H.; Abakumov, A. M.; Hadermann, J.; Kalyuzhnaya, A. S.; Rozova, M. G.; Antipov, E. V.; Tendeloo, G. V. *Chem. Mater*. **2008,** 20, 7188.

[3] Greaves, C; Jacobson, A. J. ; Tofield, B. C.; Fender, B. E. F. *Acta Cryst.* **1975,** B31, 641.
[4] Schmidt, M.; Campbell, S. J. *J. Solid State Chem.* **2001,** 156, 292.

[5] Hirone, T. *J. Appl. Phys.* **1965,** *36*, 988.

[6] Takeda, T.; Yamaguchi, Y.; Tomiyoshi, S.; Fukase, M.; Sugimoto, M.; Watanabe, H. *J. phys. Soc. Japan* **1968,** 24, 446.

[7] Berastegui1, P.; Eriksson, S. G.; Hull, S. *Mater. Res. Bull.* **1999,** 34, 303.

[8] Schmidt, M.; Campbell, S. J. *J. Phys. Chem. Solids* **2002,** 63, 2085.

[9] Hodges, J. P.; Short, S.; Jorgensen, J. D.; Xiong, X.; Dabrowski, B.; Mini, S. M.; Kimball, C. W. *J. Solid State Chem.* **2000,** 151, 190.

[10] Schmidt, M. *J. Phys. Chem. Solids* **2000,** 61, 1363.

[11] Poeppelmeier. K. R.; Leonowicz, M. E.; Scanlon, J. C.; Longo, J. M.; Yelon, W. B., *J. Solid State Chem.* **1982,** 45, 71.

[12] Matar, S.F. *Solid State Sci.* **2002,** 4, 1265.

[13] Suescun, L.; Chmaissem, O.; Mais, J.; Dabrowski, B.; Jorgensen, J. D. *J. Solid State Chem.* **2007,** 180, 1698.

[14] Ramezanipour, F.; Cowie, B.; Derakhshan, S.; Greedan, J. E.; Cranswick, L. M. D. *J. Solid State Chem.* **2009,** 182, 153.

[15] Nakahara, Y.; Kato, S.; Sugai, M.; Ohshima, Y.; Makino, K. *Mater. Lett.* **1997,** *30*, 163.

[16] Proffen, T.; Egami, T.; Billinge, S.J.L.; Cheetham, A.K.; Louca, D.; Parise, J.B. *Appl. Phys.* **2002,** A74, S163.

[17] Window, B. *J. Phys. E: Sci. Instrum.* **1971,** 4, 401.

[18] Regier, T.; Krochak, J.; Sham, T. K.; Hu, Y. F.; Thompson, J.; Blyth, R. I. R. *Nucl. Instrum. Methods Phys. Res., Sect. A* **2007**, *582*, 93.

[19] Thompson, A.; Attwood, D.; Gullikson, E.; Howells, M.; Kim, K.-J.; Kirz, J.; Kortright, J.; Lindau, I.; Pianetta, P.; Robinson, A.; Scofield, J.; Underwood, J.; Vaughan, D.; Williams, G.; Winick, H. *X-ray Data Booklet*: Lawrence Berkeley National Laboratory: Berkeley, CA, 2009.

[20] Ravel, B.; Newville, M. *J. Synchrotron Radiat.* **2005**, *12*, 537.

[21] Larson A.C.; Von Dreele, R.B. *General Structure Analysis System (GSAS)*; Los Alamos National Laboratory Report LAUR 86-748; Los Alamos National Laboratory: Los Alamos, NM, 1994.

[22] Toby, B. H. *J. Appl. Cryst.* **2001,** *34*, 210.

[23] Abakumov, A. M.; Rozova, M. G.; Pavlyuk, B. Ph.; Lobanov, M. V.; Antipov, E. V.; Lebedev, O. I.; Van Tendeloo, G.; Sheptyakov, D. V.; Balagurov, A. M.; Bourée, F. *J. Solid State Chem.* **2001**, 158, 100.

[24] Wright, A. J.; Palmer, H. M.; Anderson, P. A.; Greaves, C. *J. Mater. Chem.* **2002**, 12, 978.

[25] Abakumov, A. M.; Rozova, M. G.; Antipov, E. V. *Russ. Chem. Rev.* **2004**, 73, 847.

[26] Lambert, S.; Leligny, H.; Grebille, D.; Pelloquin, D.; Raveau, B. *Chem. Mater.* **2002,** *14*, 1818.

[27] Farrow, C. L.; Juhás, P.; Liu, J. W.; Bryndin, D.; Božin, E. S.; Bloch, J.; Proffen, Th.; Billinge, S. J. L. *J. Phys.: Condens. Matter* **2007,** 19, 335219.

[28] Ravidran, P.; Vidya, R.; Fjellvåg, H.; Kjekshus, A. *Phys. Rev. B* **2008,** 77, 134448.

[29] Dyar, M.D.; Agresti, D.G.; Schaefer, M.W.; Grant, C.A.; Sklute, E.C. *Annu. Rev. Earth Planet. Sci.* **2006,** 34, 83.

[30] Grosvenor, A.P.; Greedan, J. E. *J. Phys. Chem. C,* **2009,** 113, 11366.

[31] Grosvenor, A. P.; Ramezanipour, F.; Derakhshan, S.; Maunders, C.; Botton, G. A.; Greedan, J. E. *J. Mater. Chem.* **2009**, *19*, 9213.

[32] Stanley, H.E. *Introduction to Phase Transitions and Critical Phenomen*; Oxford University Press: Oxford, UK., 1971; p 104.

Chapter 7

The effect of B site cation on crystal and magnetic structures of $Sr_2Fe_{1.9}M_{0.1}O_{5+y}$ (M=Mn, Cr, Co; y= 0, 0.5)

This chapter includes the synthesis, local and average structure and magnetic properties of six oxygen deficient perovskites: two vacancy-disordered and four vacancy-ordered materials.

The candidate performed the syntheses of these materials, magnetization studies, local and average crystal structure determination, and magnetic structure studies.

Introduction

The unique physical properties of perovskites make them attractive for a variety of practical applications. Therefore, gaining an understanding of the parameters that can be used to manipulate these properties is essential. The general formula for perovskites is ABO_3, where A is a large cation, usually from the alkali earth or rare earth groups, residing in the interstitial spaces between corner sharing BO_6 octahedra that form a three dimensional network. It is possible to synthesize compounds that have lower oxygen content, i.e., with oxygen vacancies but which retain the perovskite structure. These oxygen vacancies may be distributed randomly throughout the structure, or they may order. One of the commonly observed ordered systems is called brownmillerite in which the vacancies order to form alternating layers of octahedra and tetrahedra. Figure 7.1 compares the perovskite and brownmillerite structures.

The properties of oxygen deficient perovskites can change depending on the B site cation type. For example it has been shown that the oxygen permeation properties will be affected by Bi doping on the B-site of $BaSc_{0.1}Co_{0.9}O_{3-\delta}$. This also affects the structural stability of this compound [1]. Such effects have also been observed for $BaFeO_{3-\delta}$, where Cu or Ni doping on the B-site stabilizes the high temperature cubic phase even at room temperature [2]. Also, for $La_xSr_{1-x}Co_yFe_{1-y}O_{3-\delta}$, substitution of Cr^{6+} and Mg^{2+} on the B-site improves chemical and thermal stability of the system [3]. B-site cation doping is also used to explore possible cathodes for solid-oxide fuel cells [4, 5].

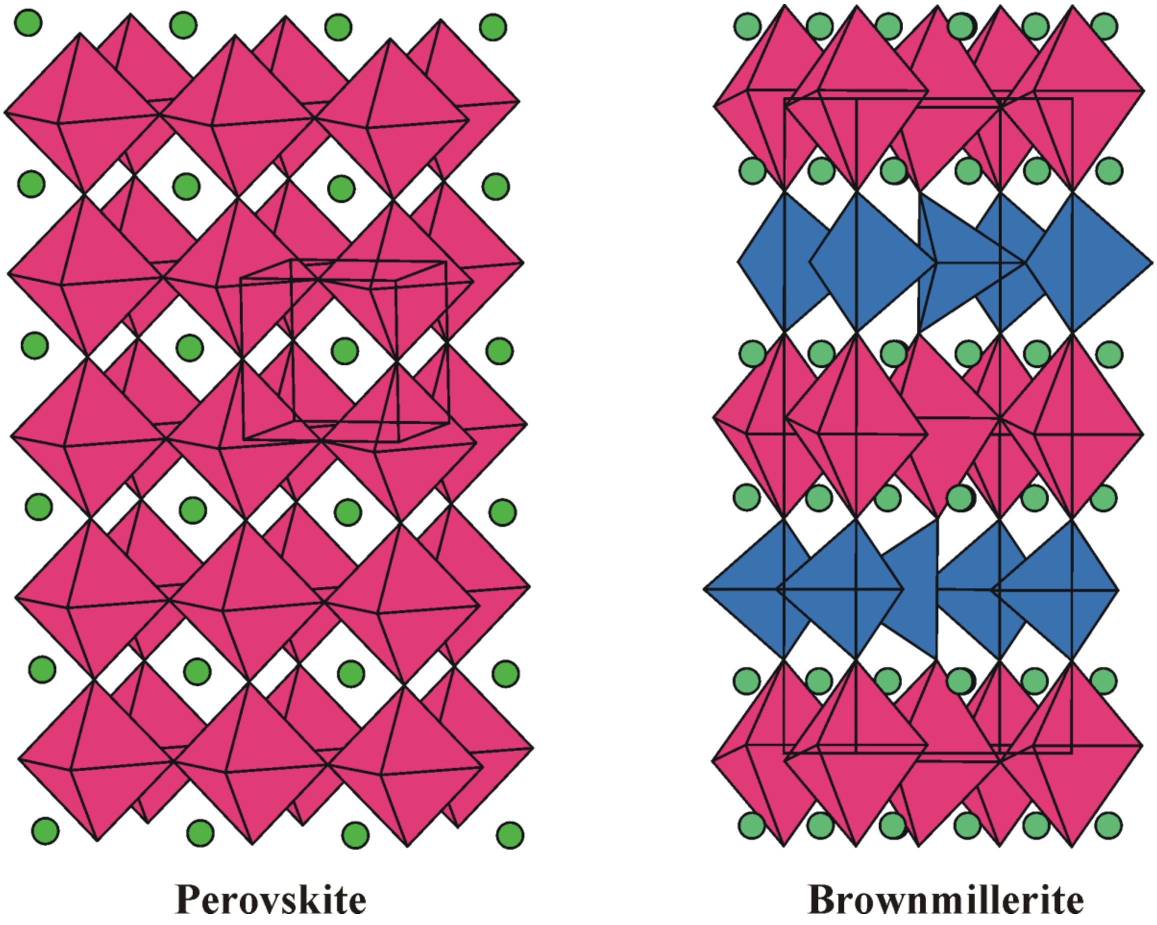

Figure 7.1. A comparison between perovskite and brownmillerite structure. The oxygen vacancies order to form alternating layers of octahedra and tetrahedra. Note the difference between the unit cell sizes. The relationship between the two is: $a_b \approx \sqrt{2}a_p$, $b_b \approx 4a_p$, $c_b \approx \sqrt{2}a_p$.

The oxygen deficient perovskite, $Sr_2Fe_2O_{5+y}$, can adopt *Icmm*, *Cmmm*, or *I*4/*mmm* structures depending on the value of y [6]. When y~0 a brownmillerite structure, described in *Icmm* with intact but disordered tetrahedral chains is found. For higher values, y~0.5 and y~0.75, structures described in *Cmmm* and *I*4/*mmm* are obtained, respectively, which involve ordered oxygen vacancies resulting in local square pyramidal and octahedral coordination of the iron atoms. The compositions of these oxidized phases are often written $Sr_4Fe_4O_{11}$(y ~ 0.5) and $Sr_8Fe_8O_{23}$ (y ~ 0.75). The oxygen deficiency can be completely removed by annealing in pure oxygen, which results in a cubic perovskite structure, *Pm-3m* [6].

In this chapter, the remarkable changes in properties of $Sr_2Fe_2O_{5+y}$ upon substitution of only 5% Fe by Cr, Mn, and Co are investigated. Six compounds, with formula $Sr_2Fe_{1.9}M_{0.1}O_{5+y}$ (M=Mn, Cr, Co) were synthesized in both argon and air and studied by powder x-ray, constant wavelength and time of flight neutron diffraction, as well as SQUID magnetometry. Neutron Pair Distribution function analyses were also used to study the local structures of these materials.

Experimental

Synthesis. Three $Sr_2Fe_{1.9}M_{0.1}O_{5+y}$ compounds, with M= Cr, Mn and Co, were synthesized in air using stoichiometric amounts of $SrCO_3$ (99.9% Sigma Aldrich), Fe_2O_3 (99.998% Alfa Aesar), Mn_2O_3 (99.9 % Cerac), Cr_2O_3 (99.97 % Alfa Aesar), and Co_3O_4 (99.3% Fisher Scientific), ground and pressed into pellets. In all cases the syntheses were performed at 1250 ºC, with both heating and cooling rates of 100 ºC/hour. Several intermediate regrinding and refiring steps were performed until pure phases were obtained. The syntheses were also performed in argon atmosphere, under the same conditions for all three compounds.

X-ray and Neutron diffraction

Powder x-ray diffraction data were obtained on a PANalytical X'Pert Pro MPD diffractometer with a linear X'Celerator detector. In all cases CuKα_1 radiation (λ = 1.54056 Å) with 2θ step interval 0.0084° was used for data collection.

Constant wavelength powder neutron diffraction data were obtained on the C2 diffractometer at the Canadian Neutron Beam Centre at Chalk River, Ontario and the HB2A diffractometer, at the High Flux Isotope Reactor at the Oak Ridge National Lab. The C2 data were collected at a variety of temperatures from 4K to 700K. A wavelength of 2.373 Å was used to collect data within the 2θ range of 4.4° to 84.5° at all temperatures. A wavelength of 1.331 Å was also used at 4K and 300K to obtain data from 34.9° to 115.0°. In both cases the 2θ step size was 0.10°.

HB2A measurements were performed using an incident neutron wavelength of 2.41 Å, selected from the (113) plane of a vertically focusing Ge monochromator. A pyrolytic graphite (PG) filter was used to remove the higher order contamination of the beam. A 12' Soller slit collimator was used in front of the monochromator and 21' in front of the sample. The scattered neutrons were detected by an array of 44 equally spaced (~ 2.7°) ^{3}He detectors; each proceeded by a 6' mylar foil collimator. For the data collection, the detector array was scanned to cover the total 2θ range of 10.5º to 131.9º, in steps of 0.1°. More details about the HB2A instrument and data collection strategies can be found in reference [7]. Powder samples weighting about 3 g were placed in vanadium cans (8 mm i.d. by 5 cm) and loaded in a Janis top-loading CCR capable of achieving temperatures up to 700 K.

Time of flight neutron powder diffraction data were collected on the instrument NPDF at the M. Lujan Jr. Center for Neutron Scattering at the Los Alamos Neutron Science Center [8]. Four data banks were collected at detector angle of 46º (bank 1), 90º (bank 2), 119º (bank 3) and 148º (bank 4).

Magnetic property measurements. Bulk magnetization measurements were performed using a Quantum Design MPMS SQUID Magnetometer. The zero-field cooled and field cooled (ZFC/FC) magnetic susceptibility measurements from 5 K to 300 K were performed on powder samples in gelatin capsules. Quartz sample-holders were used for the susceptibility measurements from 300 K to 700 K.

Thermal Gravimetric Analysis (TGA). The TGA experiments were performed on a Netzsch STA-409 TGA-DTA instrument (Thermal Gravimetric Analyzer- Differential Thermal analyzer), by heating the argon synthesized samples in air at the rate of 5 °C/min, up to 1250°C, and measuring the weight gains.

Results and discussion

Crystal Structures of compounds synthesized in argon

The argon synthesized compounds are all brownmillerites with long range ordering of oxygen vacancies (Figure 7.1). There are four major space groups reported for brownmillerites, depending on the relative orientations of tetrahedral chains [9, 10]. If they are all orientated similarly, the space group will be *I2mb* (*Ibm2*). If the orientation is the same within each tetrahedral layer but alternates from one layer to the next, *Pnma* occurs. A structure with long range disorder of tetrahedral chain orientation is described by *Imma*

(*Icmm*). Finally, there is a much less common space group *Pcmb* (*Pbcm*) that describes an alternating orientation of tetrahedral chains within each layer and between adjacent tetrahedral layers [9, 10]. Different settings of these space groups have been used by different authors, but the above notations refer to a cell with $b > c > a$, and the ones in brackets are the other commonly used settings. The *Pcmb* systems can be easily recognized by the presence of supercell reflections due to a doubling of one axis. In addition, the primitive cells can be readily identified by the occurrence of (1 5 1) and (1 3 1) reflections that are not allowed in the body centered *Ibm*2. These reflections are absent for all $Sr_2Fe_{1.9}M_{0.1}O_5$ (M=Cr, Mn,Co) compounds. The *Ibm*2 and *Icmm* models were therefore refined. The refinements yield good fits for both models using x-ray data, as well as constant wavelength and time of flight neutron diffraction. This is generally expected, as it is usually difficult to distinguish these two space groups using powder data. However, the *Icmm* model results in better agreement factors and more uniform thermal displacement parameters throughout the structure. It should be noted that there are actually fewer degrees of freedom for atomic positions in *Icmm*, and therefore, fewer parameters to be refined. In addition, the TOF data in all cases resulted in better fits due to the significantly larger Q range obtained from TOF experiments. Tables 7.1-7.3 show the refinement results for both *Icmm* and *Ibm*2 models using constant wavelength and TOF neutron data. Figure 7.2 shows the refinement profiles for the Cr-compound.

Table 7.1. The powder neutron refinement results at 300K, for $Sr_2Fe_{1.9}Cr_{0.1}O_5$ synthesized in argon.

λ =1.331 and λ =2.373, simultaneous refinement

*Ibm*2 *a* =5.6556(4)Å, *b* = 15.623(1)Å, *c* = 5.5320(4)Å, R_p= 0.0576, R_{wp}= 0.0771

	x	*y*	*z*	Occupancy	U_{iso} (Å^2)
Sr1	0.512(1)	0.1099(3)	-0.006(3)	1	0.017(1)
Fe1	0.063(1)	0.25	0.010(4)	1	0.035(2)
Fe2	*0*	*0*	*0*	0.9	0.018(1)
Cr1	*0*	*0*	*0*	0.1	0.018(1)
O1	0.242(2)	0.0074(4)	0.249(5)	1	0.013(1)
O2	-0.047(1)	0.1395(4)	-0.011(4)	1	0.024(2)
O3	0.354(2)	0.25	0.860(4)	1	0.031(3)

Icmm *a*=5.6555(4)Å, *b*=15.623(1)Å, *c*= 5.5317(3)Å, R_p= 0.0507, R_{wp}= 0.0684

	x	*y*	*z*	Occupancy	U_{iso} (Å^2)
Sr1	0.5111(8)	0.6098(2)	*0*	1	0.0178(9)
Fe1	0.5632(8)	0.25	0.4580(13)	0.5	0.016(1)
Fe2	*0*	*0*	*0*	0.9	0.016(1)
Cr1	*0*	*0*	*0*	0.1	0.016(1)
O1	0.25	0.9925(3)	0.25	1	0.015(1)
O2	0.0480(9)	0.1398(3)	*0*	1	0.026(1)
O3	0.643(2)	0.25	0.134(2)	0.5	0.023(2)

Time of flight neutron diffraction

*Ibm*2 *a*=5.6591(2)Å, *b*=15.6028(4)Å, *c*=5.5272(1)Å, R_p=0.0314, R_{wp}= 0.0446

	x	*y*	*z*	Occupancy	U_{iso} (Å^2)
Sr1	0.5118(3)	0.10959(7)	-0.0014(7)	1	0.0084(2)
Fe1	0.0656(3)	0.25	0.0328(6)	1	0.0165(4)
Fe2	*0*	*0*	*0*	0.93(1)	0.0109(4)
Cr1	*0*	*0*	*0*	0.07(1)	0.0109(4)
O1	0.2504(9)	0.0079(1)	0.248(1)	1	0.0072(2)
O2	-0.0483(3)	0.1401(1)	-0.0019(9)	1	0.0159(3)
O3	0.3556(6)	0.25	0.8715(9)	1	0.0168(6)

Icmm *a*=5.6590(1)Å, *b*=15.6024(4)Å, *c*=5.5271(1)Å, R_p=0.0303, R_{wp}= 0.0420

	x	*y*	*z*	Occupancy	U_{iso} (Å^2)
Sr1	0.5109(2)	0.60957(6)	*0*	1	0.0114(2)
Fe1	0.5668(3)	0.25	0.4596(3)	0.5	0.0107(3)
Fe2	*0*	*0*	*0*	0.934(9)	0.0124(4)
Cr1	*0*	*0*	*0*	0.066(9)	0.0124(4)
O1	0.25	0.9927(1)	0.25	1	0.0112(3)
O2	0.0487(3)	0.1403(1)	*0*	1	0.0188(3)
O3	0.6423(5)	0.25	0.1280(6)	0.5	0.0127(5)

Table 7.2. The powder neutron refinement results at 300K, for $Sr_2Fe_{1.9}Mn_{0.1}O_5$ synthesized in argon.

λ =1.331 and λ =2.373, simultaneous refinement

*Ibm*2 *a* = 5.6560(4)Å, *b* = 15.632(1)Å, *c* = 5.5198(4)Å, R_p= 0.0536, R_{wp}= 0.0705

	x	*y*	*z*	Occupancy	U_{iso} (Å^2)
Sr1	0.512(1)	0.1108(3)	-0.005(3)	1	0.020(1)
Fe1	0.068(1)	0.25	0.015(4)	1	0.033(2)
Fe2	*0*	*0*	*0*	0.9	0.020(1)
Mn1	*0*	*0*	*0*	0.1	0.020(1)
O1	0.241(2)	0.0070(4)	0.246(5)	1	0.016(1)
O2	-0.049(1)	0.1394(3)	-0.007(4)	1	0.024(2)
O3	0.359(2)	0.25	0.865(4)	1	0.031(3)

Icmm *a* = 5.6558(4)Å, *b* = 15.6313(9)Å, *c* =5.5197(3)Å, R_p=0.0479, R_{wp}= 0.0641

	x	*y*	*z*	Occupancy	U_{iso} (Å^2)
Sr1	0.5107(8)	0.61049(19)	*0*	1	0.020(1)
Fe1	0.5685(8)	0.25	0.4574(12)	0.5	0.013(2)
Fe2	*0*	*0*	*0*	0.9	0.018(1)
Mn1	*0*	*0*	*0*	0.1	0.018(1)
O1	0.25	0.9931(3)	0.25	1	0.018(1)
O2	0.0498(9)	0.1398(3)	*0*	1	0.025(1)
O3	0.640(2)	0.25	0.129(2)	0.5	0.025(3)

Time of flight neutron diffraction

*Ibm*2 *a* =5.6522(2)Å, *b* =15.6313(6)Å, *c* =5.5165(2)Å, R_p= 0.0357, R_{wp}= 0.0473

	x	*y*	*z*	Occupancy	U_{iso} (Å^2)
Sr1	0.5119(4)	0.1102(1)	-0.004(1)	1	0.0110(3)
Fe1	0.0674(4)	0.25	0.027(1)	1	0.0233(6)
Fe2	*0*	*0*	*0*	0.931(6)	0.0153(6)
Mn1	*0*	*0*	*0*	0.069(6)	0.0153(6)
O1	0.250(1)	0.0072(2)	0.248(2)	1	0.0110(4)
O2	-0.0483(4)	0.1397(2)	-0.002(2)	1	0.0186(5)
O3	0.3575(8)	0.25	0.873(1)	1	0.0184(9)

Icmm *a* =5.6522(2)Å, *b* =15.6305(5)Å, *c* =5.5165(2)Å, R_p= 0.0319, R_{wp}= 0.0425

	x	*y*	*z*	Occupancy	U_{iso} (Å^2)
Sr1	0.5117(3)	0.60996(7)	*0*	1	0.0124(3)
Fe1	0.5690(3)	0.25	0.4586(4)	0.5	0.0100(4)
Fe2	*0*	*0*	*0*	0.924(5)	0.0138(5)
Mn1	*0*	*0*	*0*	0.076(5)	0.0138(5)
O1	0.25	0.9930(1)	0.25	1	0.0124(3)
O2	0.0480(3)	0.1401(1)	*0*	1	0.0195(4)
O3	0.6398(6)	0.25	0.1253(7)	0.5	0.0110(6)

Table 7.3. The powder neutron refinement results at 300K, for $Sr_2Fe_{1.9}Co_{0.1}O_5$ synthesized in argon.

λ =1.331 and λ =2.373, simultaneous refinement

*Ibm*2 a = 5.6859(4)Å, b = 15.660(1)Å, c = 5.5410(4)Å, R_p= 0.0603, R_{wp}= 0.0788

	x	y	z	Occupancy	U_{iso} (Å^2)
Sr1	0.5154(9)	0.10946(31)	-0.0007(31)	1	0.008(2)
Fe1	0.067(1)	0.25	0.0242050(0)	1	0.017(2)
Fe2	0	0	0	0.9	0.009(2)
Co1	0	0	0	0.1	0.009(2)
O1	0.236(2)	0.0081(4)	0.239(3)	1	-0.002(2)
O2	-0.048(1)	0.1410(5)	-0.011(3)	1	0.012(2)
O3	0.361(2)	0.25	0.875(3)	1	0.019(3)

Icmm a =5.6816(3)Å, b =15.6489(9)Å, c = 5.5369(3)Å, R_p= 0.0547, R_{wp}= 0.0723

	x	y	z	Occupancy	U_{iso} (Å^2)
Sr1	0.5142(8)	0.6094(2)	0	1	0.008(1)
Fe1	0.5685(8)	0.25	0.456(1)	0.5	0.003(0)
Fe2	0	0	0	0.9	0.006(1)
Co1	0	0	0	0.1	0.006(1)
O1	0.25	0.9919(4)	0.25	1	0.006(1)
O2	0.0489(9)	0.1411(4)	0	1	0.015(2)
O3	0.640(2)	0.25	0.125(2)	0.5	0.009(2)

Time of flight neutron diffraction

*Ibm*2 a =5.6615(2)Å, b =15.5960(5)Å, c =5.5175(2)Å, R_p= 0.0318, R_{wp}= 0.0441

	x	y	z	Occupancy	U_{iso} (Å^2)
Sr1	0.5131(3)	0.10946(9)	-0.0035(7)	1	0.0099(2)
Fe1	0.0684(3)	0.25	0.0345(7)	1	0.0172(4)
Fe2	0	0	0	0.9	0.0089(3)
Co1	0	0	0	0.1	0.0089(3)
O1	0.2509(9)	0.0072(1)	0.248(1)	1	0.0090(3)
O2	-0.0483(3)	0.1412(1)	-0.005(1)	1	0.0154(4)
O3	0.3563(6)	0.25	0.8769(9)	1	0.0146(6)

Icmm a =5.6616(2)Å, b =15.5963(4)Å, c =5.5177(2)Å, R_p= 0.0274, R_{wp}= 0.0388

	x	y	z	Occupancy	U_{iso} (Å^2)
Sr1	0.5127(2)	0.60915(7)	0	1	0.0116(2)
Fe1	0.5689(2)	0.25	0.4565(3)	0.5	0.0075(3)
Fe2	0	0	0	0.9	0.0086(2)
Co1	0	0	0	0.1	0.0086(2)
O1	0.25	0.9926(1)	0.25	1	0.0103(2)
O2	0.0484(2)	0.1408(1)	0	1	0.0168(3)
O3	0.6401(5)	0.25	0.1237(5)	0.5	0.0096(4)

Table 7.4. Selected bond distances (Å) and angles (°) for brownmillerite compounds, *Icmm*, from Time-of-Flight neutron diffraction refinements.

$Sr_2Fe_{1.9}Cr_{0.1}O_5$	
Fe1–O2	1.848(2) × 2
Fe1–O3	1.882(4)
Fe1–O3	1.891(3)
Fe2–O1	1.9809(1) × 4
Fe2–O2	2.207(2) × 2
O2–Fe1–O2	136.0(1)
O2–Fe1–O3	101.45(6)
O2–Fe1–O3	104.40(7)
O3–Fe1–O3	106.4(1)
O1– Fe2–O1	88.462(6)
O1– Fe2–O1	91.538(6)
O1– Fe2–O2	88.17(5)
O1– Fe2–O2	91.83(5)
$Sr_2Fe_{1.9}Mn_{0.1}O_5$	
Fe1–O2	1.855(2) × 2
Fe1–O3	1.882(4)
Fe1–O3	1.885(4)
Fe2–O1	1.9775(1) × 4
Fe2–O2	2.206(2) × 2
O2–Fe1–O2	135.7(2)
O2–Fe1–O3	101.30(7)
O2–Fe1–O3	104.56(8)
O3–Fe1–O3	106.9(1)
O1–Fe2–O1	88.438(7)
O1–Fe2–O1	91.562(7)
O1–Fe2–O2	88.09 (7)
O1– Fe2–O2	91.91 (7)
$Sr_2Fe_{1.9}Co_{0.1}O_5$	
Fe1–O2	1.843(2) × 2
Fe1–O3	1.881(3)
Fe1–O3	1.888(3)
Fe2–O1	1.9798(1) × 4
Fe2–O2	2.213(2) × 2
O2–Fe1–O2	135.0(1)
O2–Fe1–O3	101.79(5)
O2–Fe1–O3	104.53(6)
O3–Fe1–O3	106.9(1)
O1–Fe2–O1	88.334(6)
O1–Fe2–O1	91.666(6)
O1–Fe2–O2	88.25(6)
O1– Fe2–O2	91.75(6)

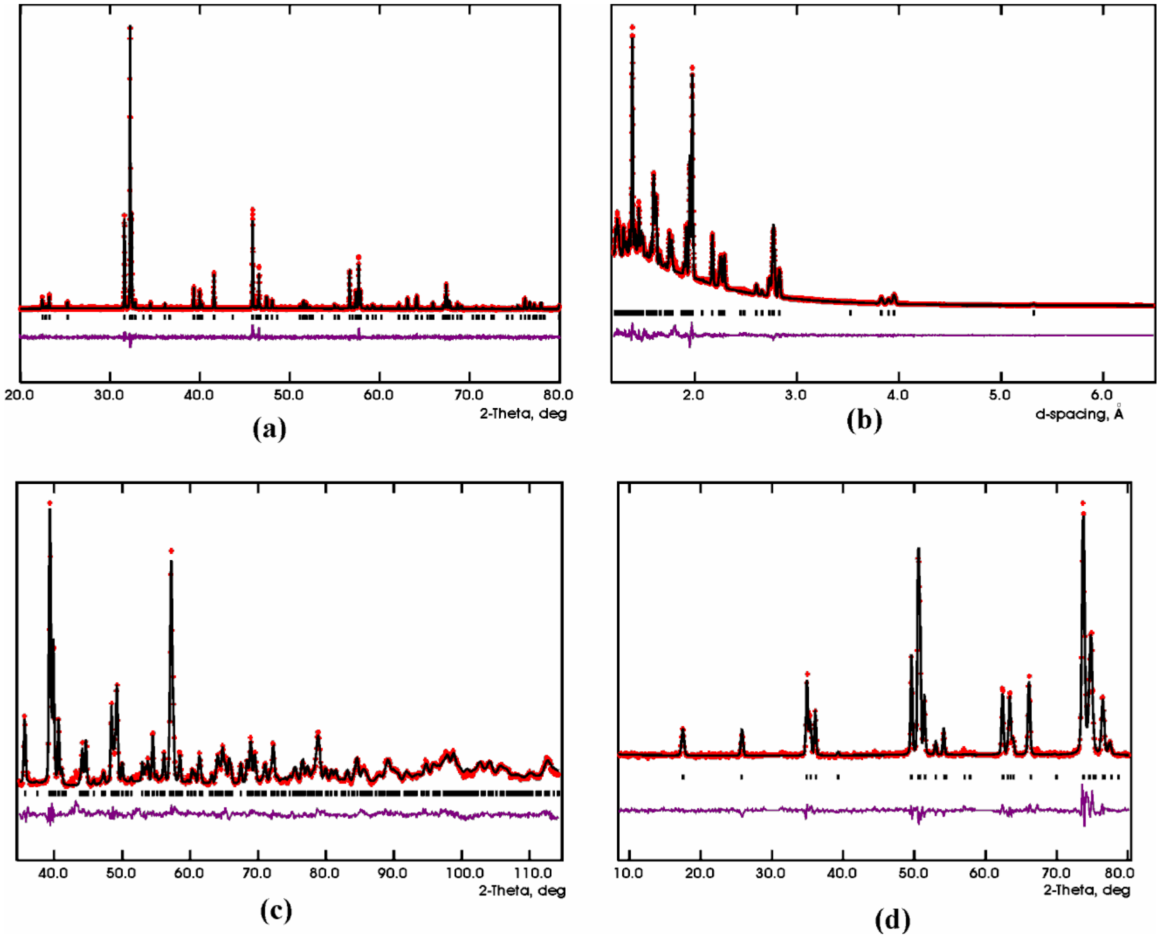

Figure 7.2. Rietveld refinement profiles for $Sr_2Fe_{1.9}Cr_{0.1}O_5$ (*Icmm*) synthesized in argon. Very similar refinement profiles were also obtained for the Mn and Co compounds. **(a)** Powder x– ray diffraction with λ = 1.54056 Å. **(b)** Time-of-Flight neutron diffraction. Only one of the four banks is shown. The detector angle for this bank was 46º. **(c)** and **(d)** Constant wavelength powder neutron diffraction, λ = 1.3307Å and λ = 2.3730Å, respectively. The stars indicate the experimental data, the solid line shows the model, the vertical tic marks locate Bragg peak positions and the lower solid line is the difference plot.

In all three brownmillerite compounds, elongation of octahedra is observed (Table 7.4). The two Fe–O2 bonds are longer than the other four bonds. O2 is the oxygen that links octahedral and tetrahedral layers. For the tetrahedra, the Fe–O2 bonds are shorter than the other two bonds. Therefore, O2 forms longer bonds with the octahedral Fe and shorter bonds with tetrahedral Fe. There is a strong distortion in the tetrahedral layer, where some tetrahedral bonds deviate from the ideal, 109.5°, by more than 26.5°. There is a smaller degree of distortion in the octahedral layer, where the deviations from ideal angles are less than 2° (Table 7.4).

Crystal Structures of compounds synthesized in air

Powder x-ray and neutron diffraction data were used for structural characterizations. The GSAS program [11], using the EXPGUI interface [12] was employed for the Rietveld refinements (Figure 7.3). The air synthesized Co-compound, $Sr_2Fe_{1.9}Co_{0.1}O_{5+y}$, has an orthorhombic *Cmmm* symmetry, as confirmed by x-ray, TOF and constant wavelength neutron diffraction refinements (Table 7.5). The refinement of oxygen occupancies resulted in very small deviations from full occupancy. Therefore, they were fixed at 1, consistent with y = 0.5.

The air synthesized Co-compound exhibits vacancy ordering, (Figure 7.4) which results in dimeric units of square pyramids and chains of octahedrally coordinated Fe atoms. This is the same structure found for $Sr_4Fe_4O_{11}$ ($Sr_2Fe_2O_{5.5}$) which is not surprising. Each pyramid shares the four corners of its base with four octahedra so that the dimeric units are isolated from each other and there is no corner sharing between them. The chains of octahedra are also isolated from each other by square pyramidal dimers (Figure 7.4). Looking at individual pyramids along the *a*-axis, it is evident that they have alternating up and down orientations. Also, taking the square pyramidal sub-lattice alone in Figure 7.4a, it can be seen that oxygen atoms and vacancies alternate along both *a* and *b*-axes, forming isolated dimers that are shifted parallel to *b* relative to the dimers on their right and left.

In sharp contrast, for air synthesized $Sr_2Fe_{1.9}M_{0.1}O_{5+y}$ (M=Cr, Mn), a cubic cell was readily identified from the x-ray diffraction pattern. A *Pm*-3*m* model (Table 7.6) was found to be in excellent agreement with both x-ray and neutron diffraction results. Figure 7.5 shows the Rietveld refinement profiles for the Cr-compound. Neutron diffraction refinements of oxygen occupancies give y ~ 0.568(8) and 0.514(6), for the Cr and Mn compounds, respectively (Table 7.6). However, it should be noted that the cell constant of the Mn-compound is slightly smaller than that of the Cr material (Table 7.6), indicating that the former is slightly more oxidized. This can also be observed from the bond distances, where the Fe(Mn)–O distance is 1.93319(2) Å, while the Fe(Cr)–O distance is 1.94448(4) Å.

All three air-synthesized compounds can be converted to brownmillerites, by firing in argon that results in the loss of oxygen. The reverse process, i.e. oxidation of the brownmillerite materials in air, is also possible.

Table 7.5. The time of flight neutron powder refinement results for $Sr_2Fe_{1.9}Co_{0.1}O_{5+y}$ synthesized in air.

Cmmm *a*=10.9619(2)Å,*b*=7.6942(1)Å,*c*=5.4676(1)Å,R_p=0.0370,R_{wp}=0.0486

	x	*y*	*z*	Occupancy	U_{iso} (Å^2)
Sr1	0.5	0	0.5	1	0.004(1)
Sr2	0	0	0.5	1	0.006(1)
Sr3	0.2567(3)	0	0	1	0.007(1)
Fe1	0.5	0.2485(3)	0	1	0.0046(4)
Fe2	0.25	0.25	0.5	0.9	0.0037(5)
Co1	0.25	0.25	0.5	0.1	0.0037(5)
O1	0.5	0	0	1	0.008(1)
O2	0.2647(4)	0	0.5	1	0.0078(8)
O3	0.3793(2)	0.2715(1)	0.2495(7)	1	0.0127(2)

Bond distances (Å)	
Fe1 – O1	1.912(2)
Fe1 – O3	1.909(3) × 4
Fe2 – O2	1.9303(3) × 2
Fe2 – O3	1.978(3) × 4
Sr1 – O1	2.73382(5) × 2
Sr1– O2	2.580(4) × 2
Sr1 – O3	2.826(3) × 8
Sr2 – O2	2.901(4) × 2
Sr2 – O3	2.592(3) × 8
Sr3 – O1	2.667(4)
Sr3 – O2	2.7352(2) × 2
Sr3 – O3	2.834(3) × 4
Sr3 – O3	2.679(4) × 4

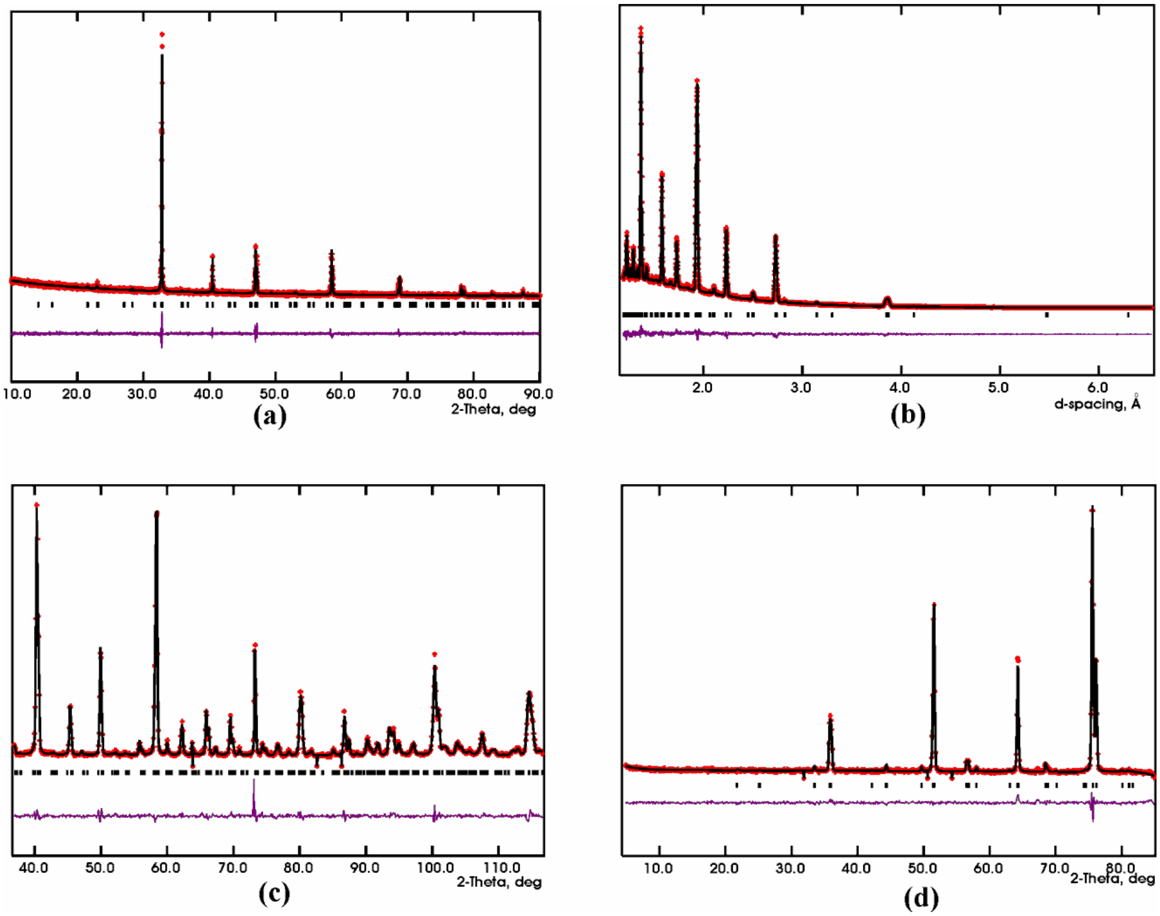

Figure 7.3. Rietveld refinement profiles for $Sr_2Fe_{1.9}Co_{0.1}O_{5+y}$ (*Cmmm*) synthesized in air. **(a)** Powder x– ray diffraction with λ = 1.54056 Å. (b) Time-of-Flight neutron diffraction. Only one of the four banks is shown. The detector angle for this bank was 46º. **(c)** and **(d)** Constant wavelength powder neutron diffraction λ = 1.3307Å and λ = 2.3730Å, respectively. The stars indicate the experimental data, the solid line shows the model, the vertical tic marks locate Bragg peak positions and the lower solid line is the difference plot.

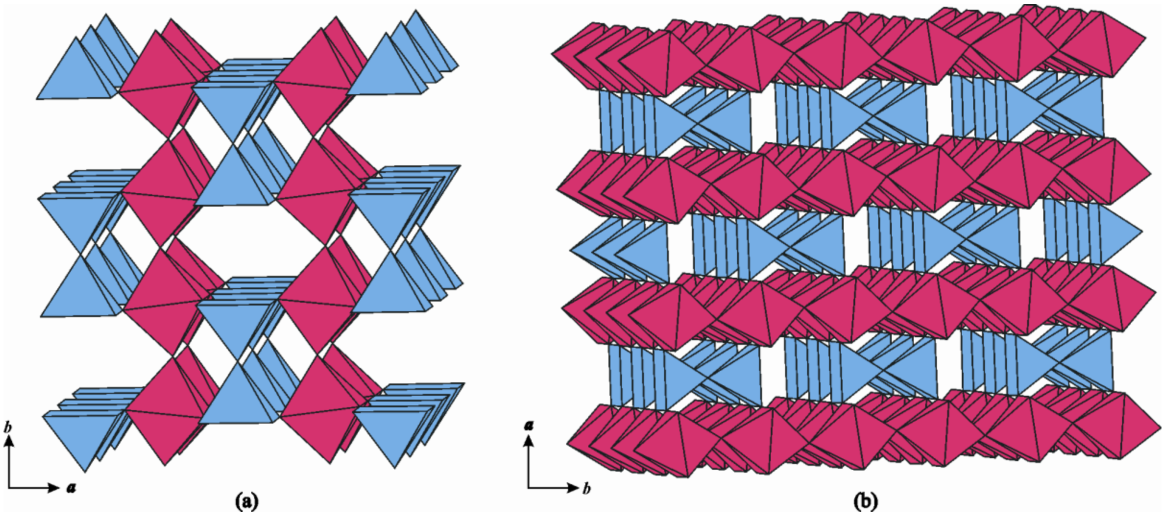

Figure 7.4. Crystal structure of $Sr_2Fe_{1.9}Co_{0.1}O_{5+y}$ (*Cmmm*) synthesized in air, with ordering of oxygen vacancies resulting in chains of octahedra, separated by dimeric units of square pyramids.

Table 7.6. The powder refinement results, for $Sr_2Fe_{1.9}B_{0.1}O_{5+y}$ (B=Cr, Mn) synthesized in air. The results are from simultaneous refinements with powder x-ray (λ=1.54056 Å) and neutron diffraction data (λ=1.331 Å and λ=2.373 Å), at 300K.

$Sr_2Fe_{1.9}Cr_{0.1}O_{5+y}$					
Pm-3*m*	a = 3.88896(8)Å, R_p= 0.0489, R_{wp}= 0.0680				
	x	y	z	Occupancy	U_{iso} (Å^2)
Sr1	0.5	0.5	0.5	1	0.0184(4)
Fe1	0	0	0	0.95	0.0101(3)
Cr1	0	0	0	0.05	0.0101(3)
O1	0.5	0	0	0.928(4)	0.0228(4)
$Sr_2Fe_{1.9}Mn_{0.1}O_{5+y}$					
Pm-3*m*	a = 3.86638(5)Å, R_p= 0.0507, R_{wp}= 0.0718				
	x	y	z	Occupancy	U_{iso} (Å^2)
Sr1	0.5	0.5	0.5	1	0.0167(4)
Fe1	0	0	0	0.95	0.0103(4)
Mn1	0	0	0	0.05	0.0103(4)
O1	0.5	0	0	0.919(3)	0.0211(5)
Bond distances (Å)					
	$Sr_2Fe_{1.9}Cr_{0.1}O_{5+y}$	$Sr_2Fe_{1.9}Mn_{0.1}O_{5+y}$			
Fe – O	1.94448(4) × 6	1.93319(2) × 6			
Sr – O	2.74991(4) × 12	2.73394(2) × 12			
Sr – Sr	3.88896(8) × 6	3.86638(5) × 6			
Sr – Fe	3.36794(5) × 8	3.34838(3) × 8			

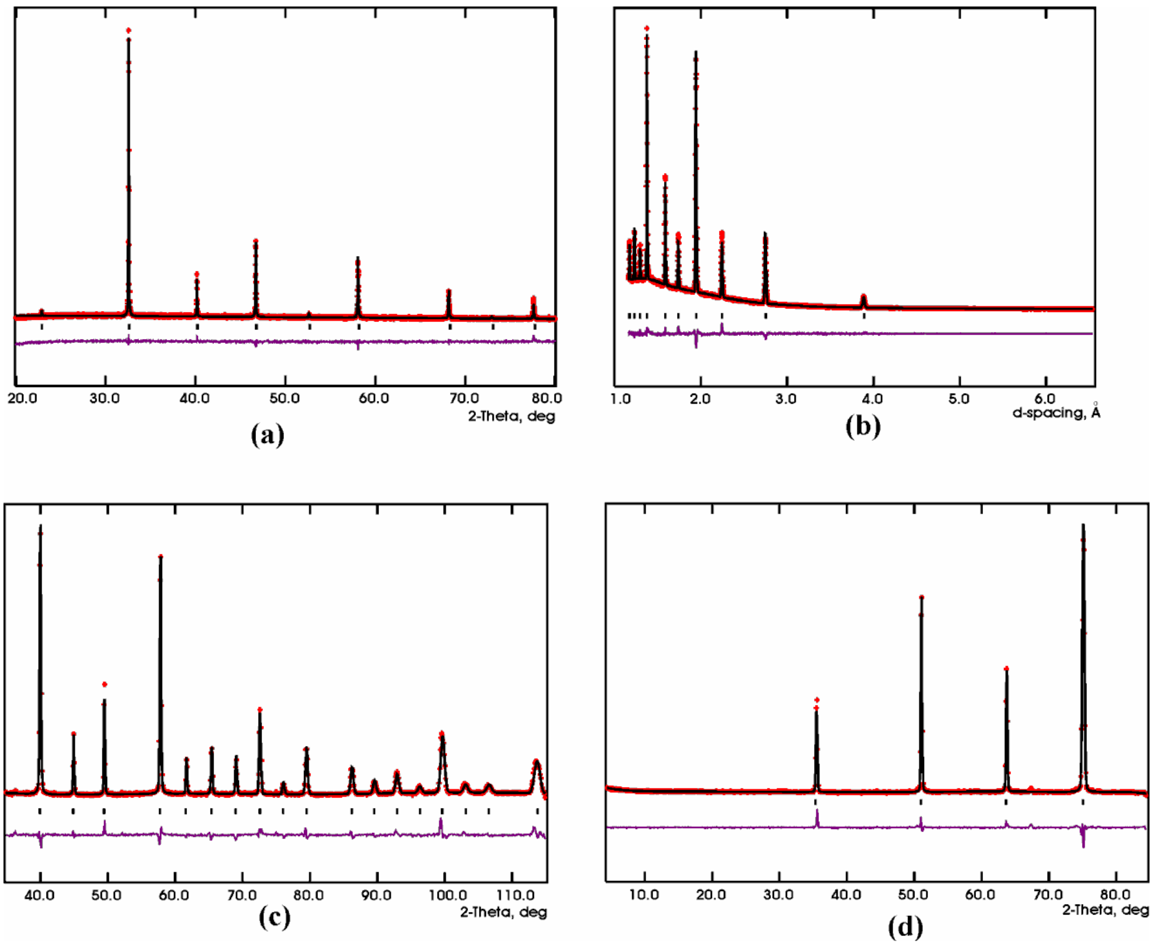

Figure 7.5. Rietveld refinement profiles for $Sr_2Fe_{1.9}Cr_{0.1}O_{5+y}$ (*Pm-3m*) synthesized in air. A very similar refinement profile was also obtained for the Mn compounds. **(a)** Powder x– ray diffraction with λ = 1.54056 Å. (b) Time-of-Flight neutron diffraction. Only one of the four banks is shown. The detector angle for this bank was 46º. **(c)** and **(d)** Constant wavelength powder neutron diffraction λ = 1.3307Å and λ = 2.3730Å, respectively. The stars indicate the experimental data, the solid line shows the model, the vertical tic marks locate Bragg peak positions and the lower solid line is the difference plot.

As mentioned before, the cubic, *Pm-3m*, and orthorhombic, *Cmmm*, structures occur for $Sr_2Fe_2O_{5+y}$. The *Pm-3m* structure corresponds to y ~ 1 and is obtained by firing the sample in pure oxygen [6], while *Cmmm* is obtained for y=0.5 by adjusting the oxygen content using proper mixture of gases [6]. At this point, it is not clear how substitution of 5% Cr and Mn destroys the ordering of vacancies leading to the disordered cubic, *Pm-3m*, structure. However, as discussed below, the local structures of these materials seem to be different from their average structures.

Local Structures

To explore the local structures of these materials, Neutron-Pair-Distribution-Function (NPDF) analysis was performed. This method analyzes the total-scattering by taking into account both Bragg peaks and diffuse scattering equally. Powder data are obtained to very large momentum transfer, Q, corrected for a number of parameters including the sample can scattering, normalized, and then a sine Fourier transform is carried out. The result is the real space atomic pair distribution, G(r). The intensity associated with each peak depends on the number of inter-atomic interactions at a particular distance, r, and the product of the neutron scattering lengths of the atoms involved in that interaction. This can be compared against the inter-atomic distances expected from the crystal structure obtained from conventional Rietveld refinement, to evaluate the local structure. The G(r) data can also be fitted to particular crystallographic models and defect models within a chosen length scale using the PDFGUI program [13].

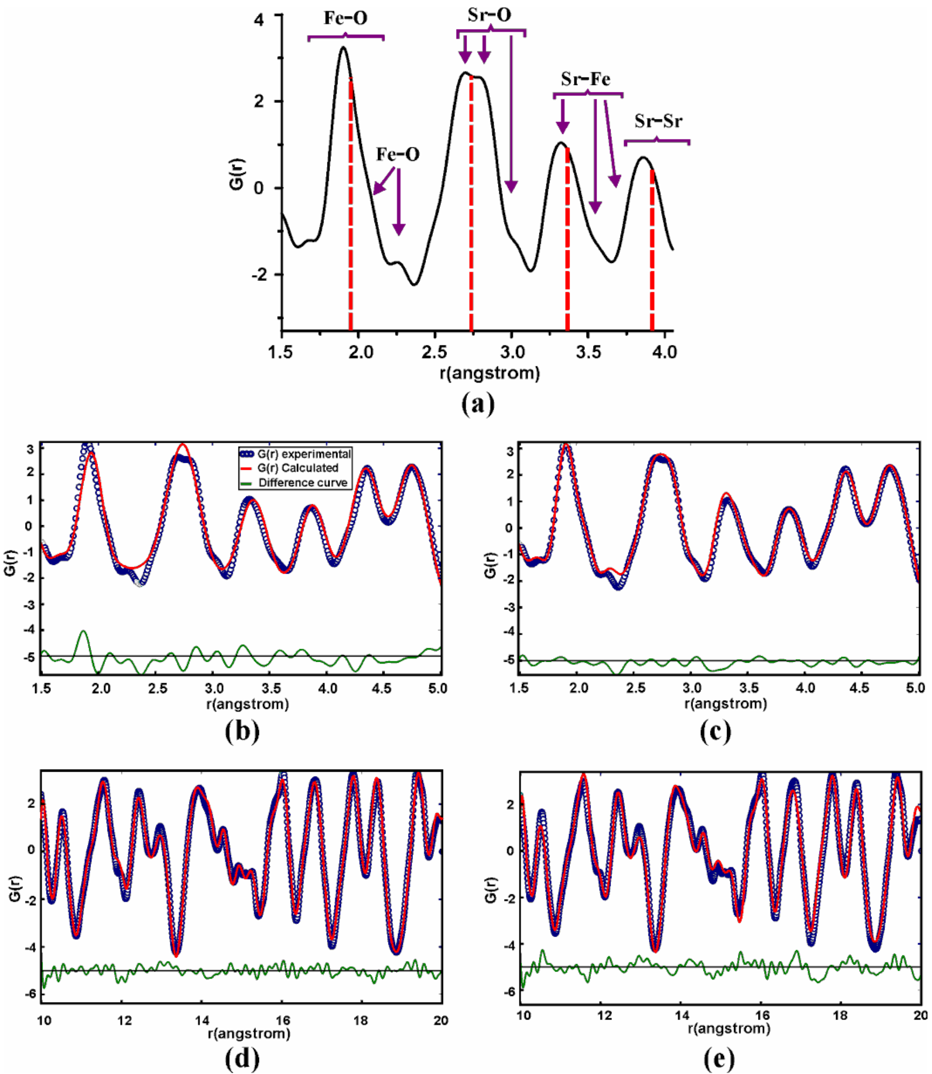

Figure 7.6. NPDF data truncated at Q_{max}=35Å^{-1} for $Sr_2Fe_{1.9}Cr_{0.1}O_{5+y}$, synthesized in air, that has a cubic average structure,*Pm-3m*. **(a)** The match between G(r) and inter-atomic distances of a vacancy-ordered brownmillerites system is shown by arrows and brackets. The dashed vertical lines locate the inter-atomic distances for a vacancy-disordered *Pm-3m* model. The local ordering of oxygen vacancies, i.e. brownmillerite local structure, is evident. **(b)** The PDFGUI refinement profile from r=1.5Å to 5Å with a cubic *Pm-3m* model, R_w=20.4%. **(c)** The PDFGUI refinement profile from r=1.5Å to 5Å with a brownmillerite *Ibm*2 model, R_w=10.7%. **(d)** The PDFGUI refinement profile from r=10Å to 20Å with a cubic *Pm-3m* model, R_w=10.5%. **(e)** The PDFGUI refinement profile from r=10Å to 20Å with a brownmillerite *Ibm*2 model, R_w=14.6%, and unreasonable atomic displacement factors.

Local structures of the air synthesized phases.

NPDF data are available for the M = Cr and Co materials. Air synthesized $Sr_2Fe_{1.9}Cr_{0.1}O_{5+y}$ with a *Pm-3m* average structure, is expected to show only one inter-atomic distance for each of the following atom pairs: Sr-O, Fe-O, Sr-Fe, and Sr-Sr. However, examining the G(r) data at short r reveals that there are more bond distances associated with each of these inter-atomic interactions (Figure 7.6a). A careful inspection of the data shows that these distances are nicely consistent with those expected from a brownmillerite structure, with ordering of oxygen vacancies. This indicates that there is a local ordering of oxygen vacancies and the local structure is brownmillerite- like. This was confirmed further by performing local structure refinements using PDFGUI. A vacancy-disordered cubic model, *Pm-3m*, for the range of r=1.5Å to 5Å, gives a poor fit with R_w=20.4%, while a vacancy-ordered brownmillerite model, *Ibm*2, results in a significantly better agreement factor, R_w=10.7% (Figure 7.6). However, for longer distances as the structure begins to resemble the average structure, the cubic model is a better match. For example refinements within the range of r=10Å to 20Å (Figure 7.6) with cubic *Pm-3m* model give R_w=10.5%, while a brownmillerite model results in R_w=14.6% with some very large displacement factors indicating further that this model is not suitable for longer distances.

The NPDF data for $Sr_2Fe_{1.9}Co_{0.1}O_{5+y}$ synthesized in air are shown in Figure 7.7. Recall that the average structure, *Cmmm*, incorporates ordering of oxygen vacancies, so that chains of corner-sharing octahedra are separated by square-pyramidal dimers. One might, therefore, expect that this model would describe the local structure fairly well.

However, the fit to the *Cmmm* model is markedly poor over the r range 1.5 Å to 5 Å, giving R_w = 35.5 %. On the other hand, a brownmillerite local model gives a significantly better fit, R_w = 14.9% within the same r range, revealing that, while oxygen vacancy ordering occurs in both the average and local structures, the brownmillerite ordering model better describes the short range local order.

Local structures of the argon synthesized phases.

For the three vacancy-ordered brownmillerite compounds synthesized in argon, $Sr_2Fe_{1.9}M_{0.1}O_5$ (M=Cr, Mn, Co), the NPDF data suggest that the ordering of oxygen vacancies is present at the local level, and the local structure is brownmillerite-like as well. The G(r) patterns of all three compounds can be described by the inter-atomic distances expected from a brownmillerite system. The NPDF patterns for these three compounds are shown in Figure 7.8. PDFGUI refinements were also performed with the brownmillerite structure, but fitting of the peaks was unsatisfactory. While the peaks and shoulders match the inter-atomic distances from a brownmillerite, the peak-shapes and relative intensities seem to be affected by magnetic scattering that causes some peak splittings and intensities to be exaggerated. A comparison between Figure 7.7c, where a reasonable fit to the brownmillerite model is obtained, and Figure 7.8 shows this effect. These discrepancies are possibly due to contributions from rather intense magnetic scattering which is present in the S(Q) data from which the G(r) is derived. Studies are currently underway to test this hypothesis.

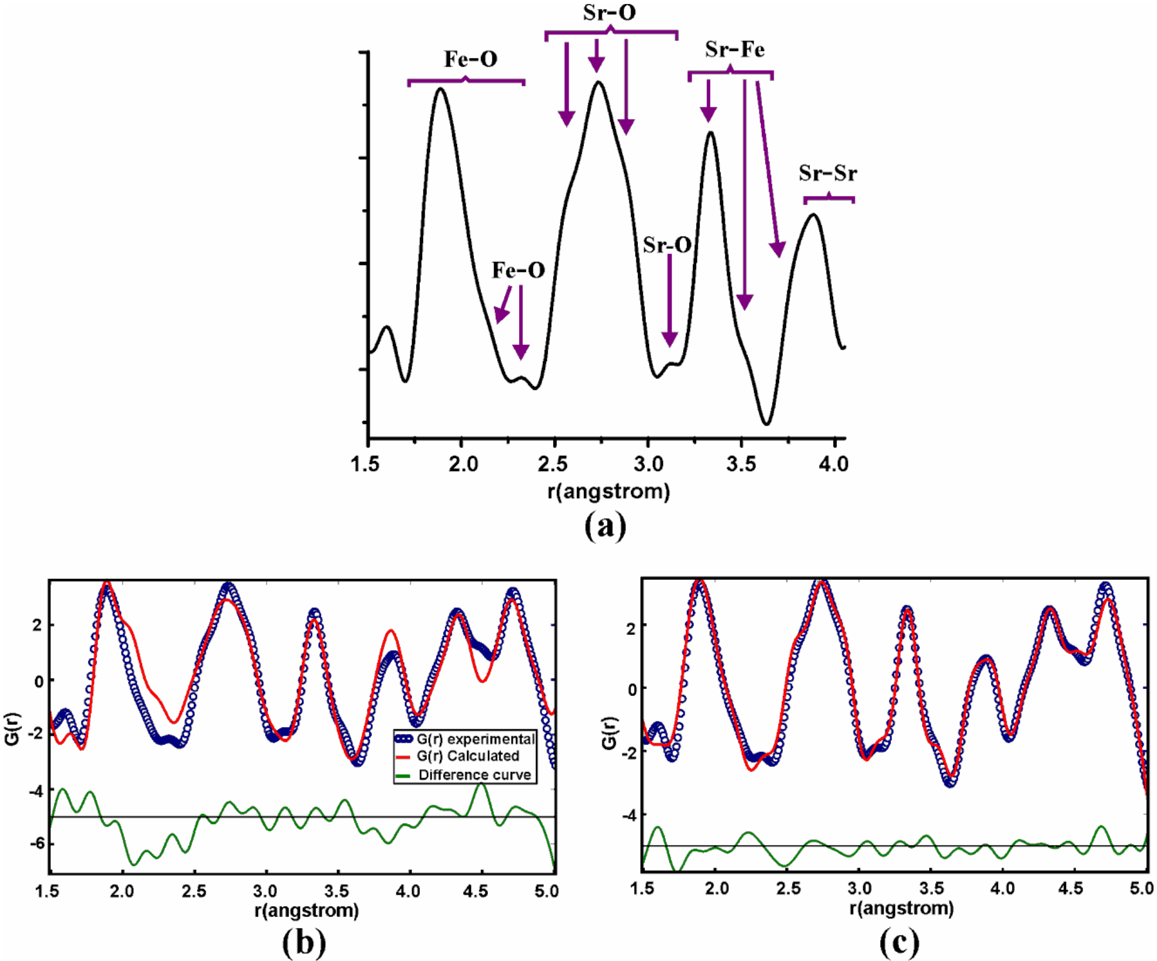

(a)

(b)

(c)

Figure 7.7. NPDF data truncated at Q_{max}=35Å^{-1} for $Sr_2Fe_{1.9}Co_{0.1}O_{5+y}$, synthesized in air, that has a *Cmmm* average structure. **(a)** The match between G(r) and inter-atomic distances of a vacancy-ordered brownmillerites model is shown by arrows and brackets. **(b)** The PDFGUI refinement profile from r=1.5Å to 5Å with a *Cmmm* model, R_w=35.5%. **(c)** The PDFGUI refinement profile from r=1.5Å to 5Å with a brownmillerite *Ibm*2 model, R_w= 14.9%.

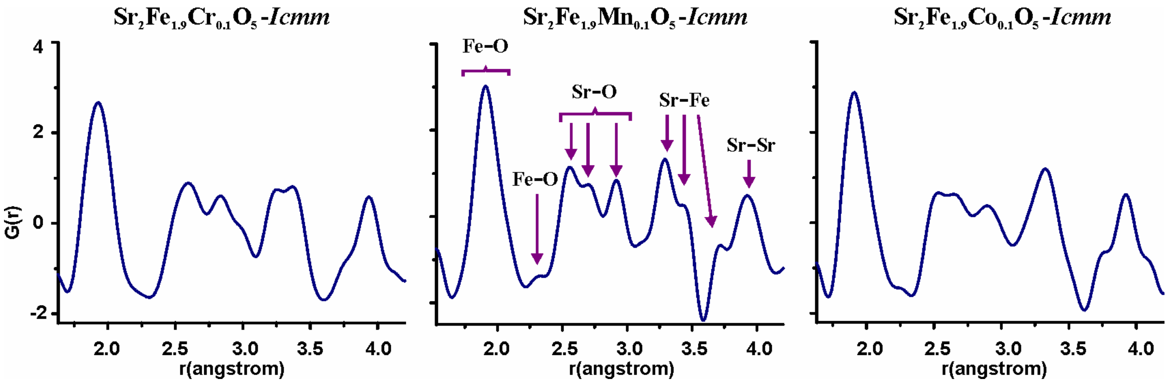

Figure 7.8. The NPDF data truncated at Q_{max}=35Å^{-1} for brownmillerite $Sr_2Fe_{1.9}M_{0.1}O_5$ (M=Cr, Mn, Co) synthesized in argon. As seen here, the patterns for all three materials are very similar. The arrows and brackets show the match between G(r) and inter-atomic distances of a vacancy-ordered brownmillerites model, indicating that the average structure model can describe the local structure as well.

Magnetic properties of the argon synthesized compounds.

For all three brownmillerite compounds, neutron diffraction results show the presence of long range magnetic ordering at 4K, evident from the magnetic Bragg peaks. Neutron diffraction experiments at temperatures up to 700K were then performed to determine the magnetic structure and magnetic moments as function of temperature and to determine the magnetic transition temperatures. (Figures 7.9 and 7.10). For all three materials, the familiar G-type structure is found in which all nearest neighbor spins are aligned antiferromagnetically. As this nomenclature was originally applied to perovskite materials, some confusion can arise in the case of brownmillerites. Recall that brownmillerites have alternating layers of octahedra and tetrahedra. If the octahedral sublattice is examined independently in Figure 7.10, it is clear that the moment on each site is aligned opposite to the nearest neighbors within the same layer, but parallel to the nearest neighbors in the adjacent layers. This is a C-type antiferromagnetic arrangement, which is also found for the tetrahedral sublattice. If both octahedral and tetrahedral sublattices are taken together, then overall magnetic structure can be called G-type antiferromagnetic, where the magnetic moment on each cation is oriented antiparallel to all nearest neighbor moments.

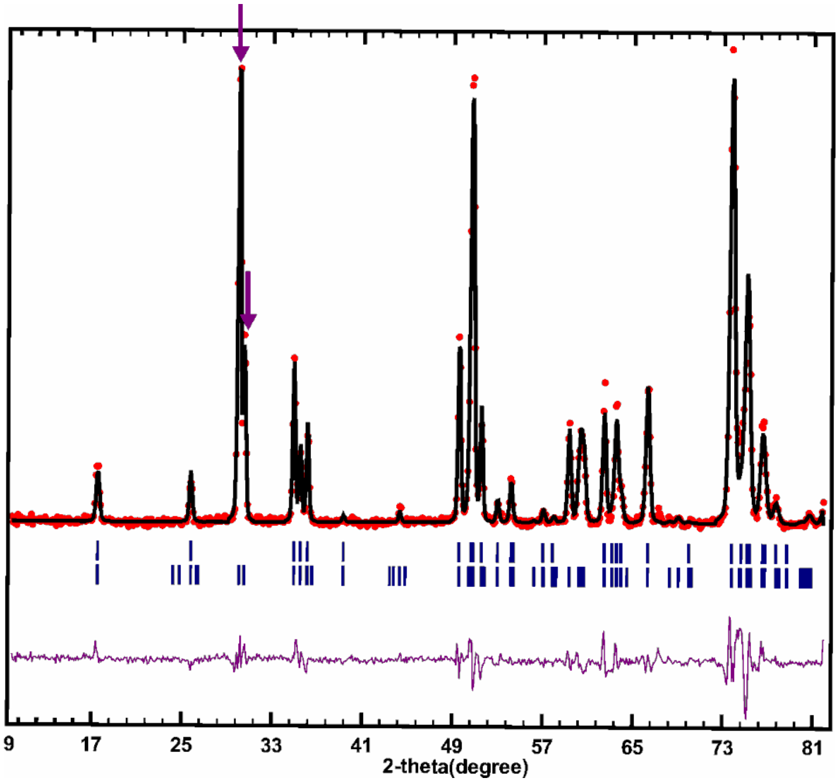

Figure 7.9. The refinement profile for crystal and magnetic structures of $Sr_2Fe_{1.9}Cr_{0.1}O_5$, *Icmm*, synthesized in argon. Very similar refinement profiles were also obtained for the Mn and Co compounds. The two major magnetic peaks are shown by arrows. The magnetic structure is a G-type antiferromagnetic (Figure 7.10), with magnetic moments oriented along the shortest axis, *c*. In the figure above, the circles represent the experimental data and the solid black line the model. Vertical tick marks show the positions of the peaks corresponding to the crystal (upper tick marks) and magnetic structures (lower tick marks). The purple solid line at the bottom is the difference plot.

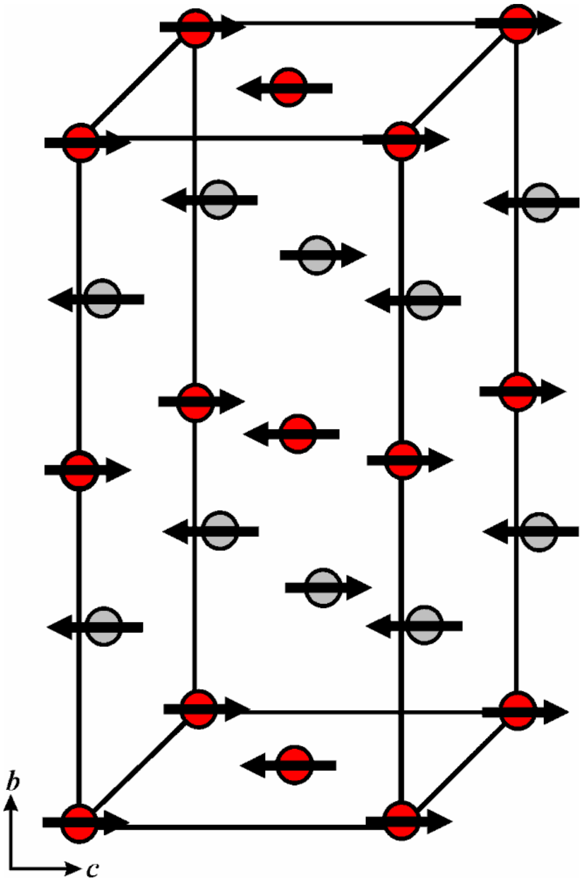

Figure 7.10. The magnetic structure of $Sr_2Fe_{1.9}M_{0.1}O_5$ (M=Cr, Mn, Co), *Icmm*, synthesized in argon, at 4K. The magnetic moment on each site is oriented anti-parallel to all nearest neighbors; a G-type antiferromagnetic structure with moments oriented along the shortest axis, *c*.

The preferred orientation of moments is along the shortest unit cell axis, *c*. This is immediately evident from the neutron diffraction patterns, as the intensity ratio of the two major magnetic peaks, marked by arrows in Figure 7.9, is indicative of the magnetic moment orientation [9]. If this ratio is close to 1.2, then the moments are aligned along the longest axis, and if the ratio is close to 2.9, the moments are oriented parallel to the shortest axis. In this case, the ratios of the two major magnetic peaks at 4K are 2.76, 2.41 and 2.61 for Cr, Mn and Co compounds, respectively.

Using neutron diffraction data, magnetic moments on tetrahedral and octahedral sites were determined and refined at different temperatures by the FullProf program suite [14, 15], using WinPLOTR [15, 16]. The variations of magnetic moments with temperature are shown in Figures 7.11, 7.12 and 7.13. As seen in these figures, the magnetic transition temperatures, T_N, are 652(2)K, 633(2)K, and 663(2)K for the Cr, Mn and Co compounds, respectively. Néel temperatures were estimated by comparing data near the transition to the equation $I(T)^{1/2} = I(4K)^{1/2}((T_N - T)/T_N)^{0.36}$ calculated for several temperatures near the assumed T_N. This of course is valid in the so-called critical regime and the exponent is that for the three dimensional Heisenberg model. For all cases there were at least two data points within the critical range and various T_N values were tried and those giving best agreement with the data were chosen. The estimated uncertainties in this procedure are indicated above.

To analyze these results the assumption was made that $T_N \sim \langle S \rangle^2$ where $\langle S \rangle^2$ is the average spin quantum number for the B-site ion combination. The S value for Fe^{3+} is 5/2, Co^{3+} and Mn^{3+} are both S = 2, assuming the high spin state for Co, while Cr^{3+} is an S = 3/2 ion. The parent phase, $Sr_2Fe_2O_5$ has T_N = 693K [17]. Thus, T_N/693K should vary as $\langle S \rangle^2/6.25$ for each B-site composition giving expected ratios of 0.98, 0.98 and 0.96 for M = Co, Mn and Cr, respectively. The actual values are 0.96, 0.91 and 0.94 for the same three ions. While the ratios for M = Co and Cr are in reasonable agreement with expectation, the M = Mn value is clearly too low. Among the possible explanations is that

Mn^{3+} – O – Fe^{3+} superexchange contributes ferromagnetic interactions which would weaken the overall antiferromagnetic exchange in disproportion to the Mn^{3+} concentration. This is in crude accord with the Goodenough-Kanamori rules for the 180° σ superechange pathway [18, 19]. It is also not impossible that a local Jahn-Teller distortion occurs at Mn sites which could weaken the superexchange.

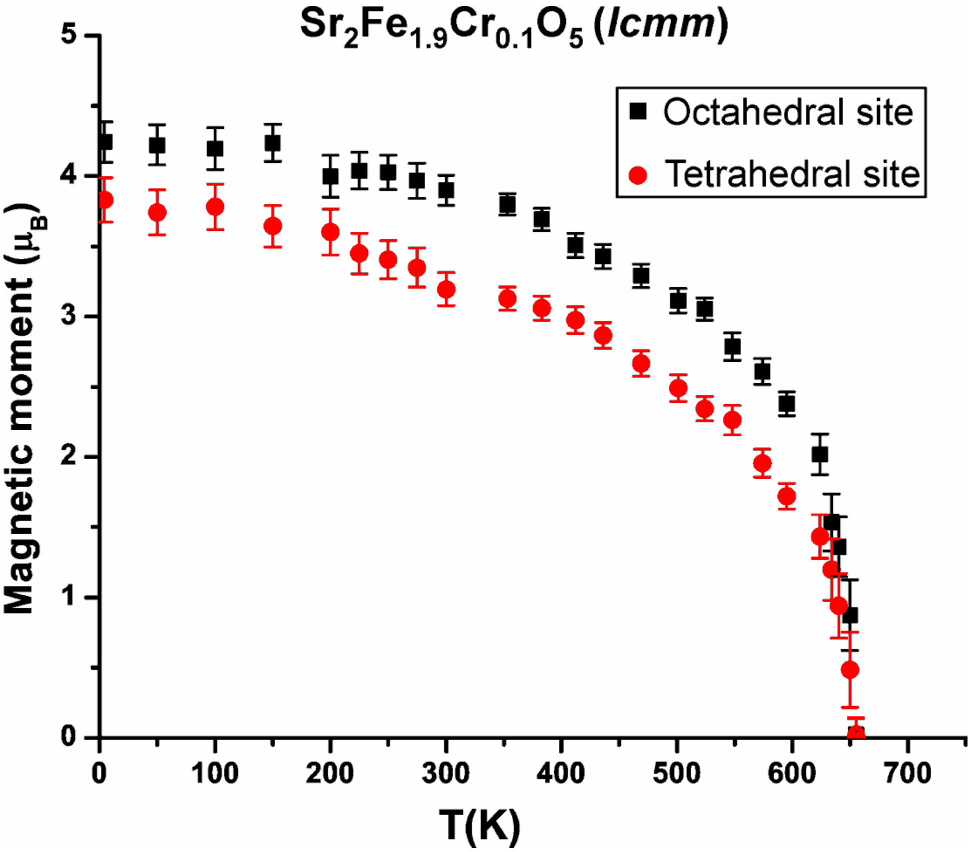

Figure 7.11. The magnetic moments of $Sr_2Fe_{1.9}Cr_{0.1}O_5$, *Icmm*, synthesized in argon, as function of temperature. The magnetic transition temperature is ~652

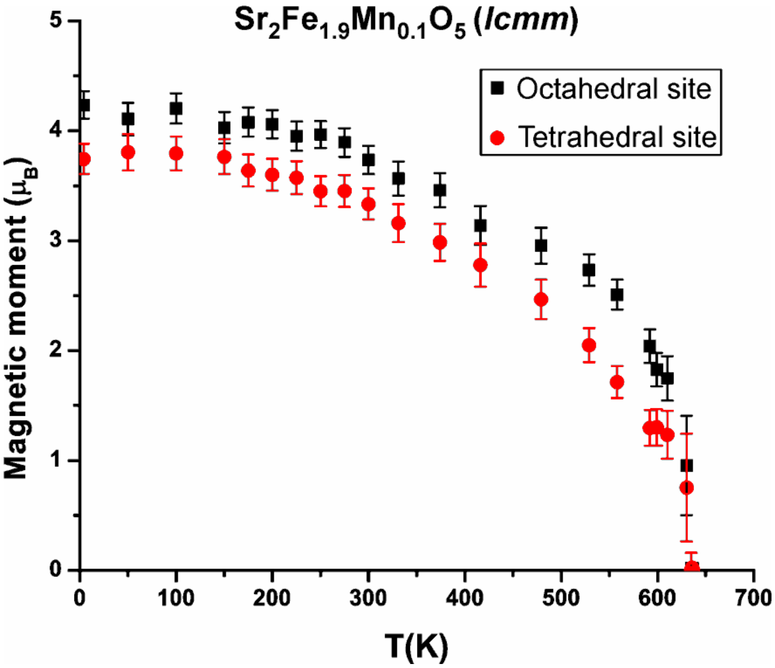

Figure 7.12. The magnetic moments of $Sr_2Fe_{1.9}Mn_{0.1}O_5$, *Icmm*, synthesized in argon, as function of temperature. The magnetic transition temperature is ~633K.

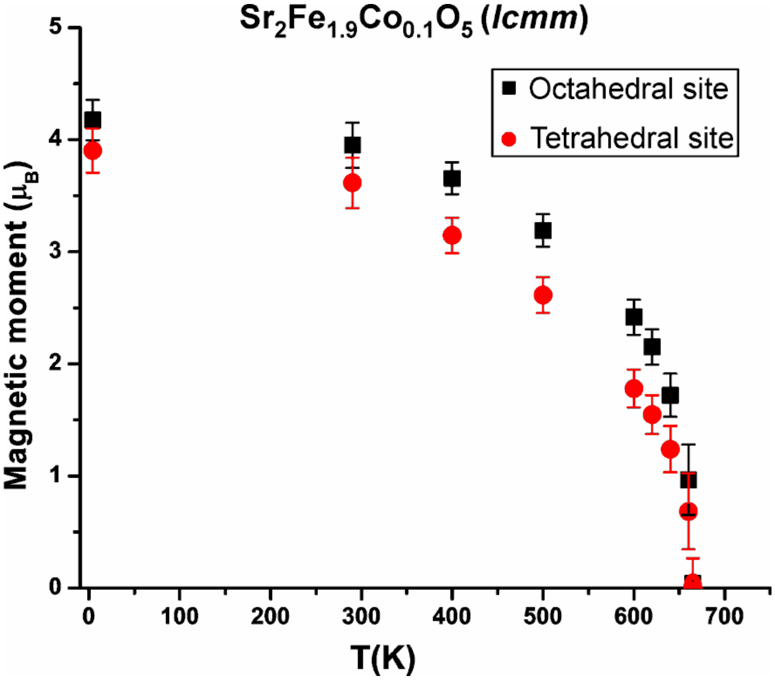

Figure 7.13. The magnetic moments of $Sr_2Fe_{1.9}Co_{0.1}O_5$, *Icmm*, synthesized in argon, as function of temperature. The magnetic transition temperature is ~663K.

Magnetic properties of air synthesized compounds

The Co-compound, $Sr_2Fe_{1.9}Co_{0.1}O_{5.5}$, is isostructural with $Sr_4Fe_4O_{11}$ ($Sr_2Fe_2O_{5.5}$) [6]. There is only a 5% substitution of Co for Fe and, thus, one might expect similar magnetic behavior. Magnetic susceptibility data for $Sr_2Fe_{1.9}Co_{0.1}O_{5.5}$ are shown in Figure 7.14b-c. A FC/ZFC divergence occurs near ~230K which can be taken as magnetic transition temperature, T_N, which is very near the value for un-doped $Sr_4Fe_4O_{11}$ of 232K [20]. The susceptibility above room temperature up to 700K is shown in Figure7.14c,d. The inverse susceptibility, Fig. 7.14d, clearly shows that the paramagnetic regime is not attained up to 700K. While $Sr_4Fe_4O_{11}$ also shows a FC/ZFC divergence at ~230K and a similar behavior of the FC data, the ZFC data is completely different showing an increase in susceptibility with increasing temperature [20]. A Curie-Weiss behavior is also reported for $Sr_4Fe_4O_{11}$ above 232K [20], while for $Sr_2Fe_{1.9}Co_{0.1}O_{5.5}$, the Curie-Weiss regime does not occur up to 700K, as shown in Figure 7.14d. Although, for $Sr_4Fe_4O_{11}$, the susceptibility data is reported only up to 300 K. In addition, the FC susceptibility is suggested to saturate at 5K for $Sr_4Fe_4O_{11}$, while for $Sr_2Fe_{1.9}Co_{0.1}O_{5.5}$, saturation does not occur down to 5K. The isothermal magnetization data for $Sr_2Fe_{1.9}Co_{0.1}O_{5.5}$, show clear hystereses at 5K and 100K. This may indicate spin canting.

Neutron diffraction experiments on $Sr_2Fe_{1.9}Co_{0.1}O_{5.5}$ were carried out at 4K and 290K. The difference plot, Fig. 7.15, shows the presence of many magnetic reflections, confirming long-range magnetic ordering, which can be indexed on the chemical cell as indicated. Comparing with data for $Sr_4Fe_4O_{11}$ [20] the magnetic diffraction patterns appear to be nearly identical.

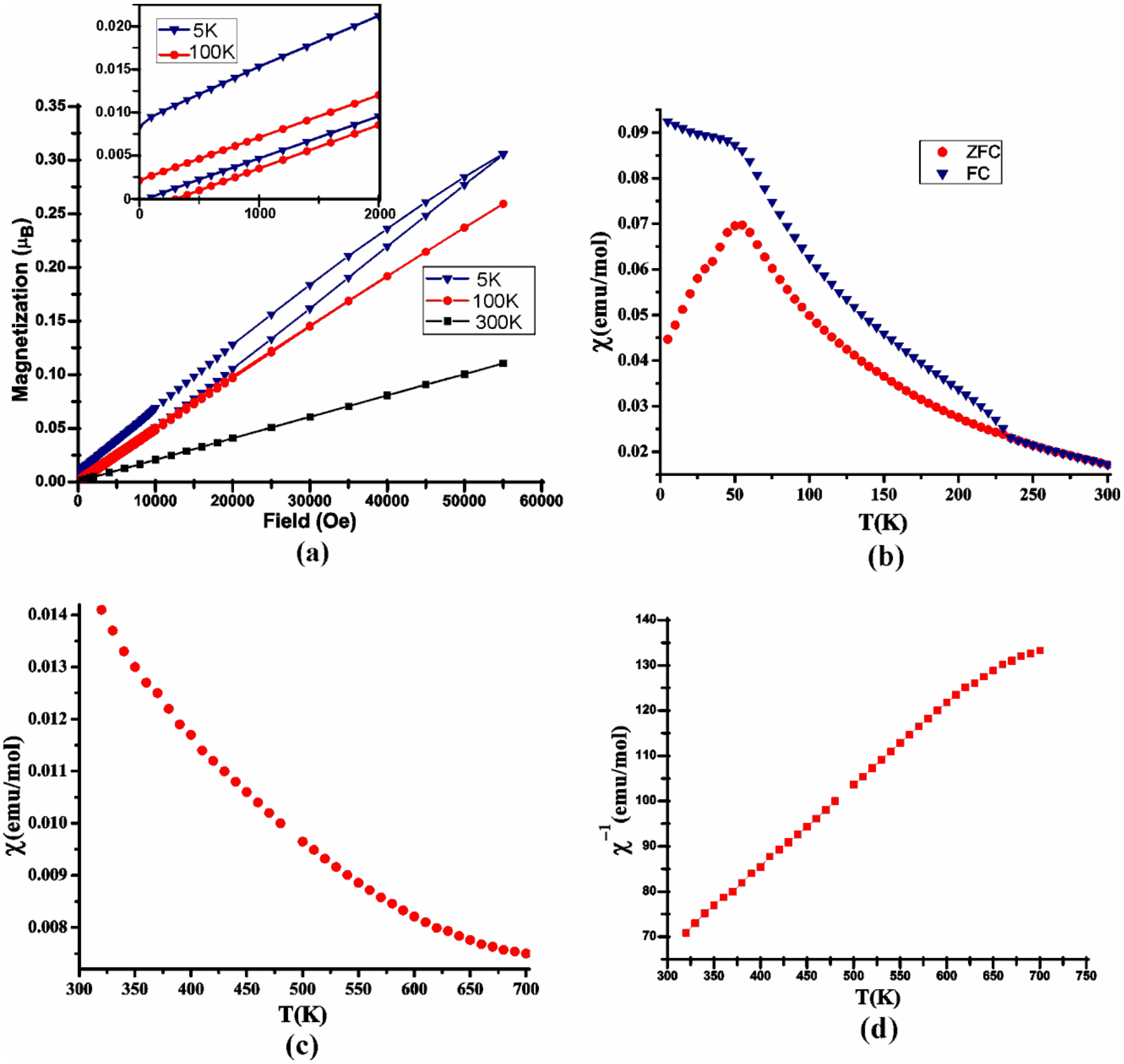

Figure 7.14. Bulk magnetic data for $Sr_2Fe_{1.9}Co_{0.1}O_{5.5}$, *Cmmm*, synthesized in air.**(a)** Isothermal magnetization data. A hysteresis, magnified in the inset, occurs at 5K, with a remnant magnetization of $0.0084\mu_B$. A smaller hysteresis is also present at 100K. **(b)** Zero field cooled-field cooled (ZFC-FC) data from 5K to 300K. The FC data begins diverging from ZFC above ~230K, which may indicate the transition to long range magnetic order. **(c)** Susceptibility data obtained while heating the sample from 300K to 700K. **(d)** Inverse susceptibility data from 300K to 700K. The graph shows clearly that Currie-Weiss regime does not occur up to 700K.

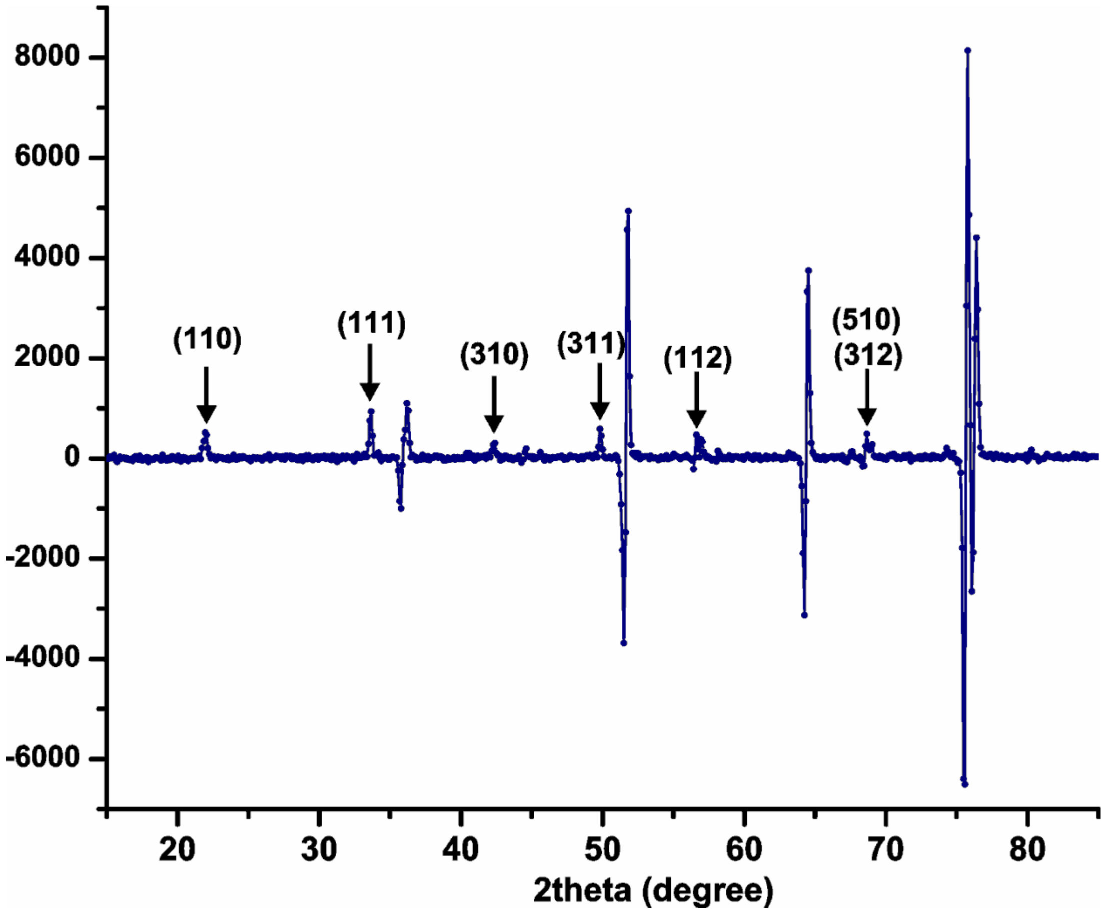

Figure 7.15. The difference plot for $Sr_2Fe_{1.9}Co_{0.1}O_{5.5}$, *Cmmm*, obtained by subtraction of neutron data at 290K from the data at 4K. The indexes for the main magnetic peaks are shown. The valleys and their adjacent peaks are due to the small shift of structural peak positions in the 290K data relative to the 4K data.

To summarize the situation for $Sr_4Fe_4O_{11}$, there are actually two proposed structural and magnetic structural models [6, 20]. In both, the Fe^{3+} and Fe^{4+} ions site order on the square pyramidal and octahedral sites, but the site preferences are opposite. Several arguments have been presented for each site order preference but the issue appears to be still unresolved [21-23]. In any case the magnetic structure is C-type antiferromagnetic order on only one of the sites – the other remains non-magnetic to 4K, due to local frustration. For example cations on the octahedral sites couple to four nearest square pyramidal neighbors and given AF order on these near neighbor sites, the frustration emerges. For $Sr_2Fe_{1.9}Co_{0.1}O_{5.5}$ several magnetic structure simulations and refinements were performed by the FullProf program suite [14, 15], using WinPLOTR [15, 16]. As anticipated, an antiferromagnetic C-type model fits the data very well. The refinement profile and the magnetic structure are shown in Figures 7.16 and 7.17. As seen in Figure 7.17, the magnetic moments are oriented along the *b*-axis. As mentioned, only one of the two Fe sites is ordered, and Rietveld refinements give equally good results for both site preference choices, as observed for $Sr_4Fe_4O_{11}$ [20]. The saturation magnetic moment obtained for $Sr_4Fe_4O_{11}$ at 1.5 K is 3.55(5) μ_B, unusually small for Fe^{3+} (S = 5/2), and was rationalized in terms of limited delocalization of d-electrons [20]. However, the refined moment for $Sr_2Fe_{1.9}Co_{0.1}O_{5.5}$ at 4K is even smaller μ= 2.99 (5) μ_B, which is a considerable difference, given the small degree of substitution.

For cubic $Sr_2Fe_{1.9}Cr_{0.1}O_{5+y}$ and $Sr_2Fe_{1.9}Mn_{0.1}O_{5+y}$ synthesized in air, bulk magnetic data are shown in Figures 7.18 and 7.19. Both show FC/ZFC divergences below ~ 60K and 45K for the Cr and Mn materials, respectively. High temperature data indicate that a true Curie-Weiss paramagnetic regime is not seen up to 700K. Both also show hysteresis at 5K with a remnant magnetization of 0.0018μ_B for the Cr-compound and of 0.0042μ_B for the Mn-material.

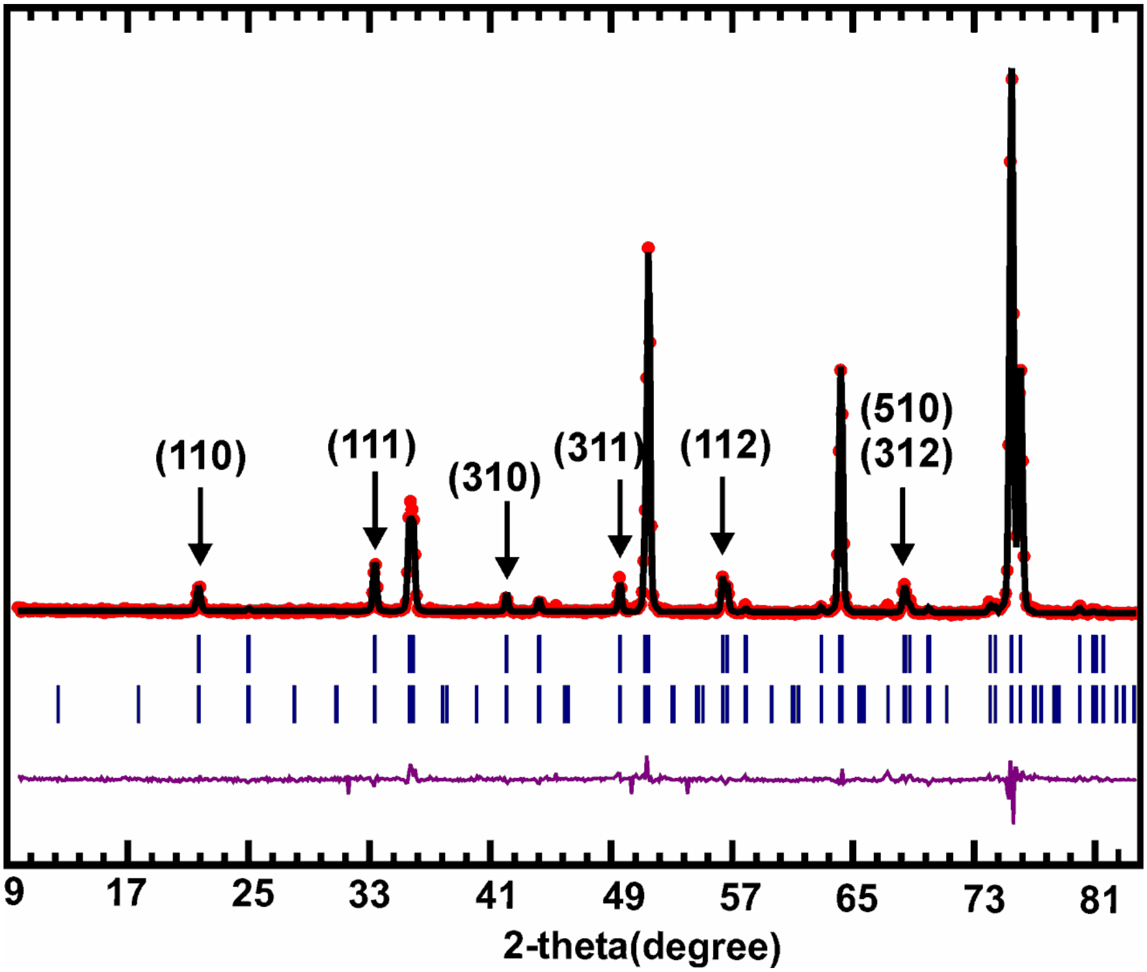

Figure 7.16. The refinement profile for crystal and magnetic structures of $Sr_2Fe_{1.9}Co_{0.1}O_{5.5}$, *Cmmm*, synthesized in air. Only one of the two sites, square-pyramidal or octahedral sites, contributes to the C-type magnetic structure (Figure 7.17). The Rietveld refinement gives equally good fits for both. Vertical tick marks show the positions of the peaks corresponding to the crystal (upper tick marks) and magnetic structures (lower tick marks). The purple solid line at the bottom is the difference plot.

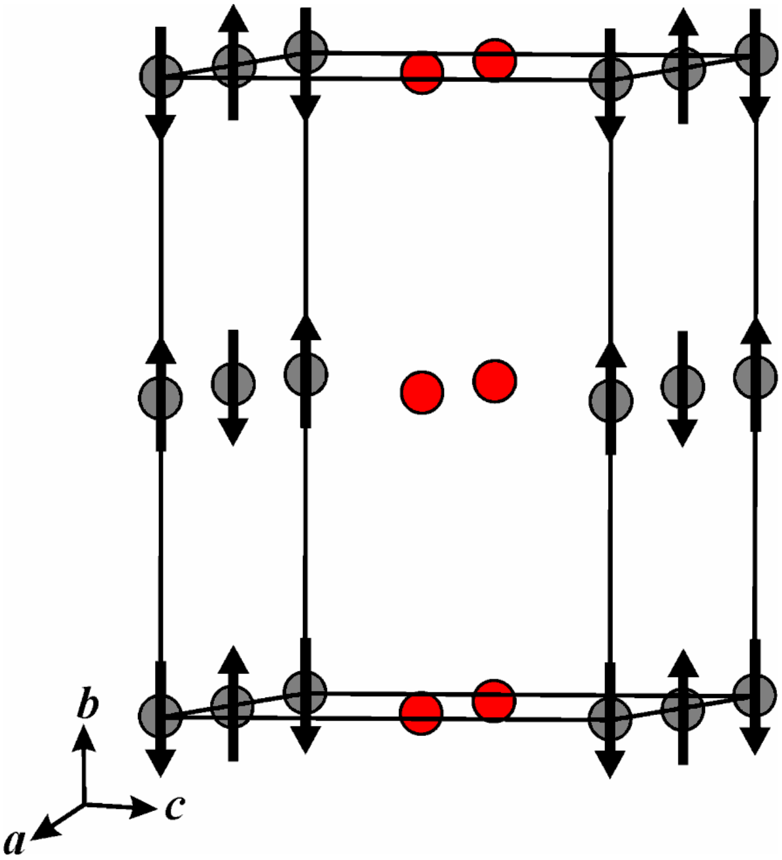

Figure 7.17. The magnetic structure of $Sr_2Fe_{1.9}Co_{0.1}O_{5.5}$, *Cmmm*, synthesized in air, at 4K. It is a C-type antiferromagnetic, and there are two competing models (1) Contribution to the magnetic structure from the octahedral sites only. (2) Contribution from the square-pyramidal sites only. The Rietveld refinement results are equally good for both models. The figure shows model number (2) with grey and red spheres representing square-pyramidal and octahedral sites, respectively.

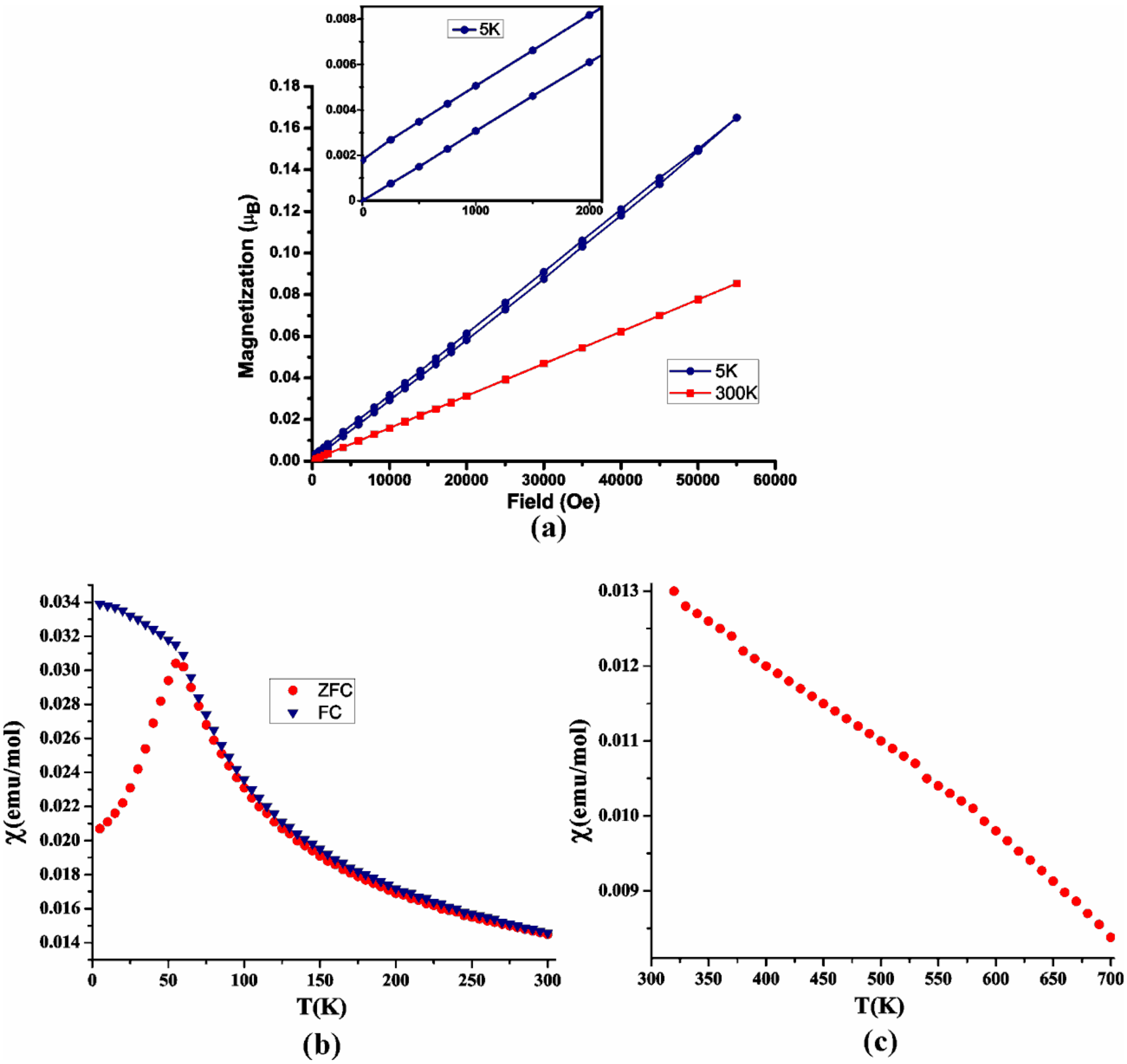

(a)

(b)

(c)

Figure 7.18. Bulk magnetic data for $Sr_2Fe_{1.9}Cr_{0.1}O_{5+y}$, *Pm-3m,* synthesized in air. **(a)** Isothermal magnetization data at 5K and 300K. A hysteresis, magnified in the inset, occurs at 5K, with a remnant magnetization of 0.0018μ_B. **(b)** Zero field cooled-field cooled (ZFC-FC) data from 5K to 300K. Note the divergence between ZFC and FC data below ~60K, indicative of a possible spin-glass transition. **(c)** Susceptibility data obtained while heating the sample from 300K to 700K. As seen here the paramagnetic behavior does not occur up to 700K.

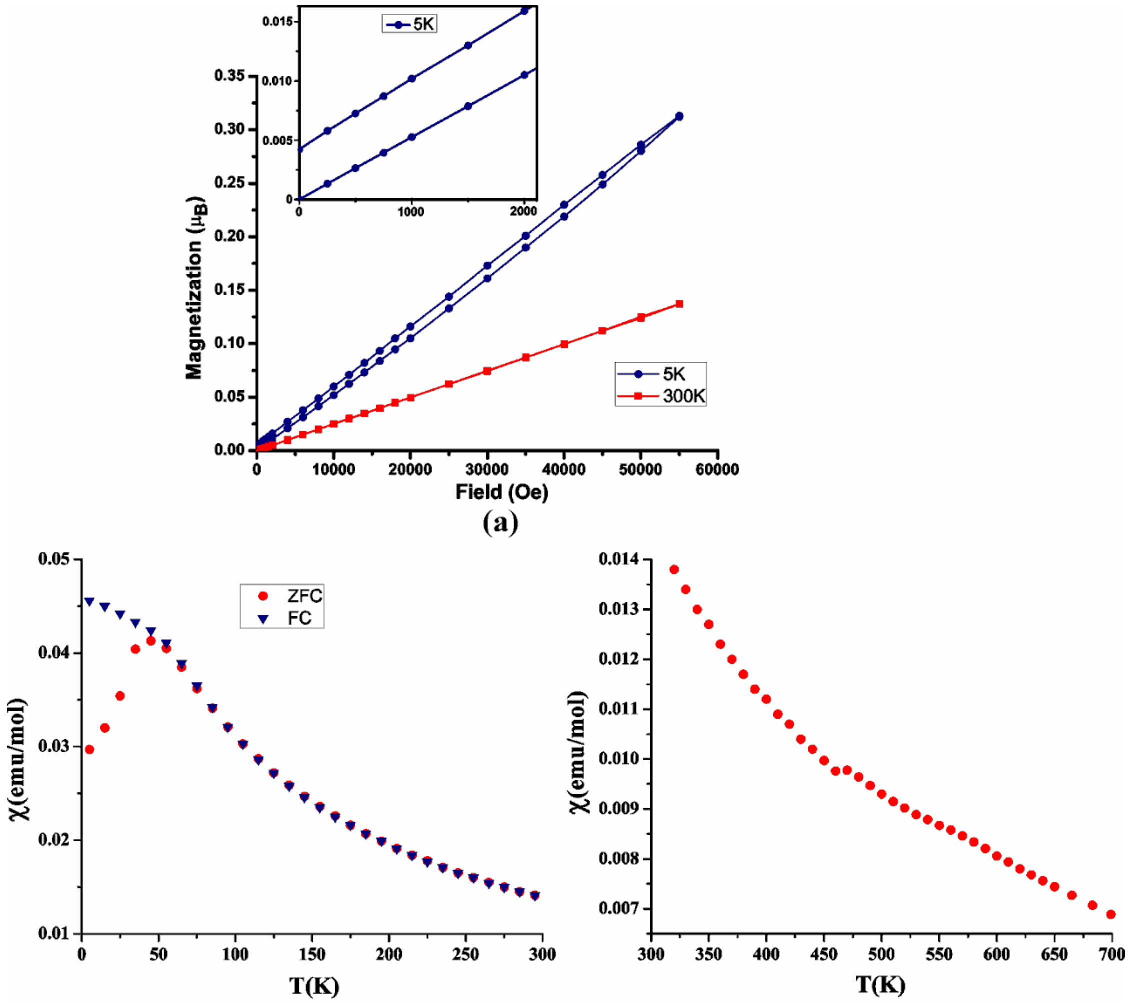

(a)

(b) **(c)**

Figure 7.19. Bulk magnetic data for $Sr_2Fe_{1.9}Mn_{0.1}O_{5+y}$, *Pm-3m,* synthesized in air. **(a)** Isothermal magnetization data. A hysteresis, magnified in the inset, occurs at 5K, with a remnant magnetization of $0.0042\mu_B$. **(b)** Zero field cooled-field cooled (ZFC-FC) data from 5K to 300K. The divergence between ZFC and FC data happens below ~45K. **(c)** Susceptibility data obtained while heating the sample from 300K to 700K. The paramagnetic regime is not achieved up to 700K.

Neutron diffraction data were obtained at 4K and 300K shown in Figures 7.20 and 7.21 for both Cr and Mn compounds. The apparent absence of any intense magnetic Bragg peaks suggests that there is no long range magnetic ordering in these two compounds down to 4K. However, in both materials there exist complex features at 4K that disappear at 300K. The temperature dependence of these peaks indicates they are magnetic peaks, diagnostic of mostly short range magnetic interactions. The insets of Figures 7.20 and 7.21 show these features. For the M = Mn phase there are two peaks at ~22 deg and ~33 deg which consist of a weak but sharp Bragg component superimposed on a broad diffuse peak. Fitting of the Bragg components gives precise positions of 21.83(3) deg and 33.45(3) deg which are apparently incommensurate with the *Pm-3m* unit cell but in fact index as (110) and (111) on the magnetic *Cmmm* unit cell found for $Sr_2Fe_{1.9}Co_{0.1}O_{5.5}$. This strongly suggests that the local chemical structure for the M = Mn phase is *Cmmm*-like. Underlying the Bragg peaks are very broad, diffuse peaks centered at the same positions, within error. Analysis of these peaks using the Ornstein-Zernike model [24], Figure 7.22, yields correlation lengths of 10(1) Å and 12(5) Å for the two peaks which agree within error. The fraction of the Bragg component to the total intensity is estimated as 0.08(2).

For the M = Cr material, only one such feature is seen, but now with the Bragg position at 30.69(3) deg indexes as (1/2 1/2 1/2) on the *Pm-3m* cell, i.e., indicative of a G-type magnetic order. However, this position is very near those found for the pair of magnetic reflections, (101) and (011) observed for the *Icmm* $Sr_2Fe_{1.9}Cr_{0.1}O_{5.0}$ phase. Thus, it is more difficult to infer the local chemical structure from the magnetic scattering in this case. The diffuse component, analyzed in the same manner as described for M = Mn gives a correlation length of 7(1) Å. As this is a much weaker feature, the Bragg/diffuse ratio is somewhat poorly defined. Thus, while the argon synthesized $Sr_2Fe_{1.9}M_{0.1}O_{5.0}$ phases show the expected magnetic structures, the three air synthesized materials are all different. Such a variation is remarkable given the low doping level of 5%.

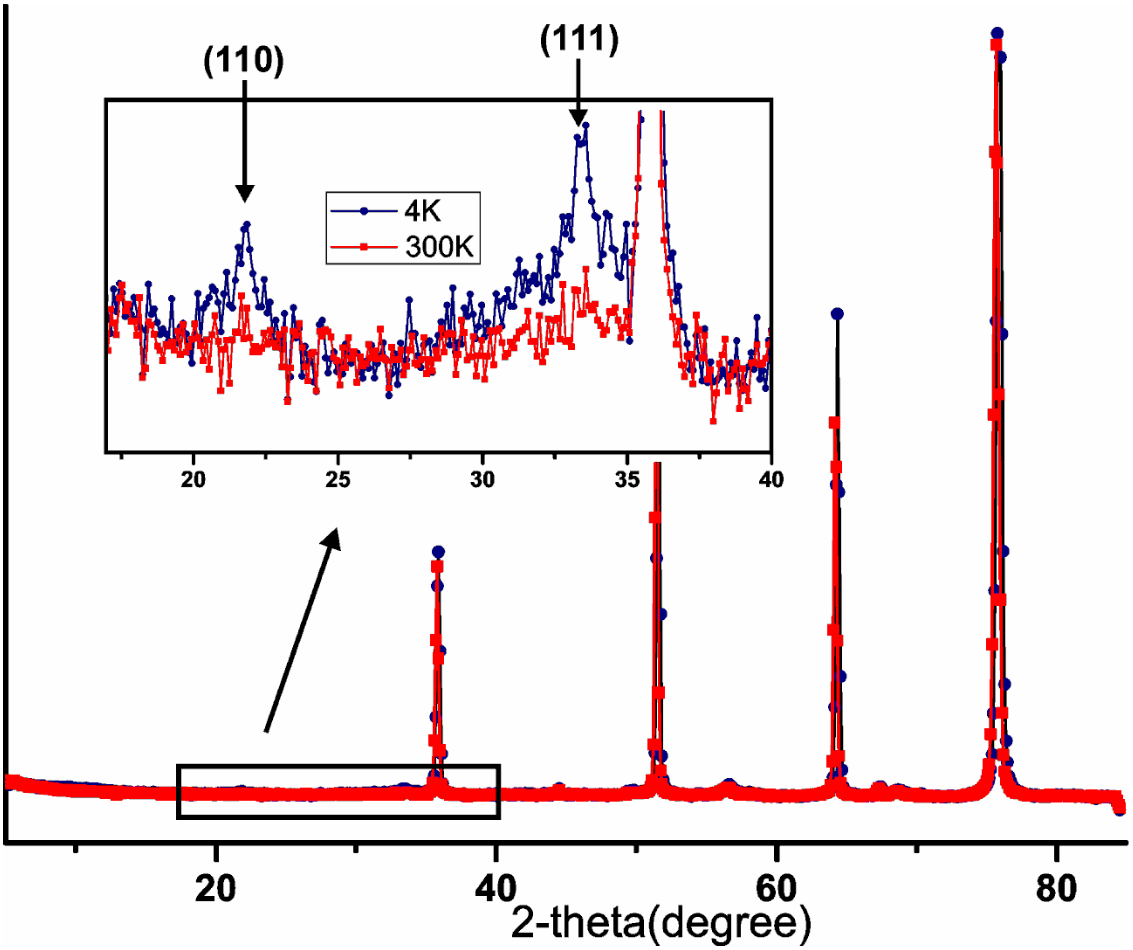

Figure 7.20. The neutron diffraction data for $Sr_2Fe_{1.9}Mn_{0.1}O_{5+y}$, synthesized in air, at 4K and 300K. The diffuse temperature dependent peaks at 21.83(3)° and 33.45(3)°, highlighted in the inset, indicate the presence of short range magnetic interactions at low temperature. The peak positions can be indexed on the magnetic *Cmmm* unit cell (Figure 7.16). The upper blue and the lower red patterns are the data at 4K and 300K, respectively.

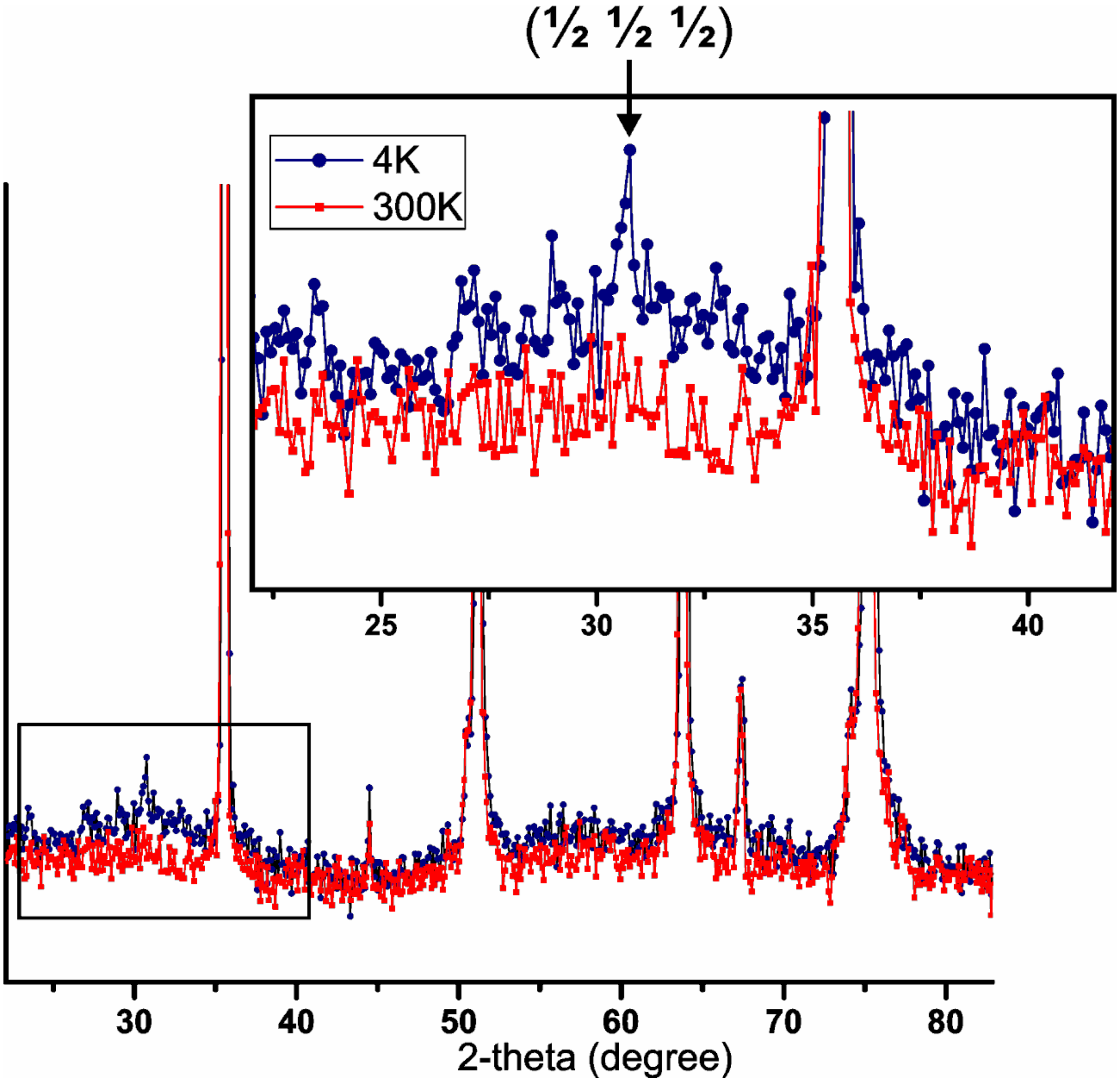

Figure 7.21. The neutron diffraction data for $Sr_2Fe_{1.9}Cr_{0.1}O_{5+y}$, synthesized in air, at 4K and 300K. The diffuse temperature dependent peak at 30.69(3)°, highlighted in the inset, indicates the presence of short range G-type magnetic interactions at low temperature. The peak can be indexed on the *Pm-3m* cell. The upper blue and the lower red patterns are the data at 4K and 300K, respectively.

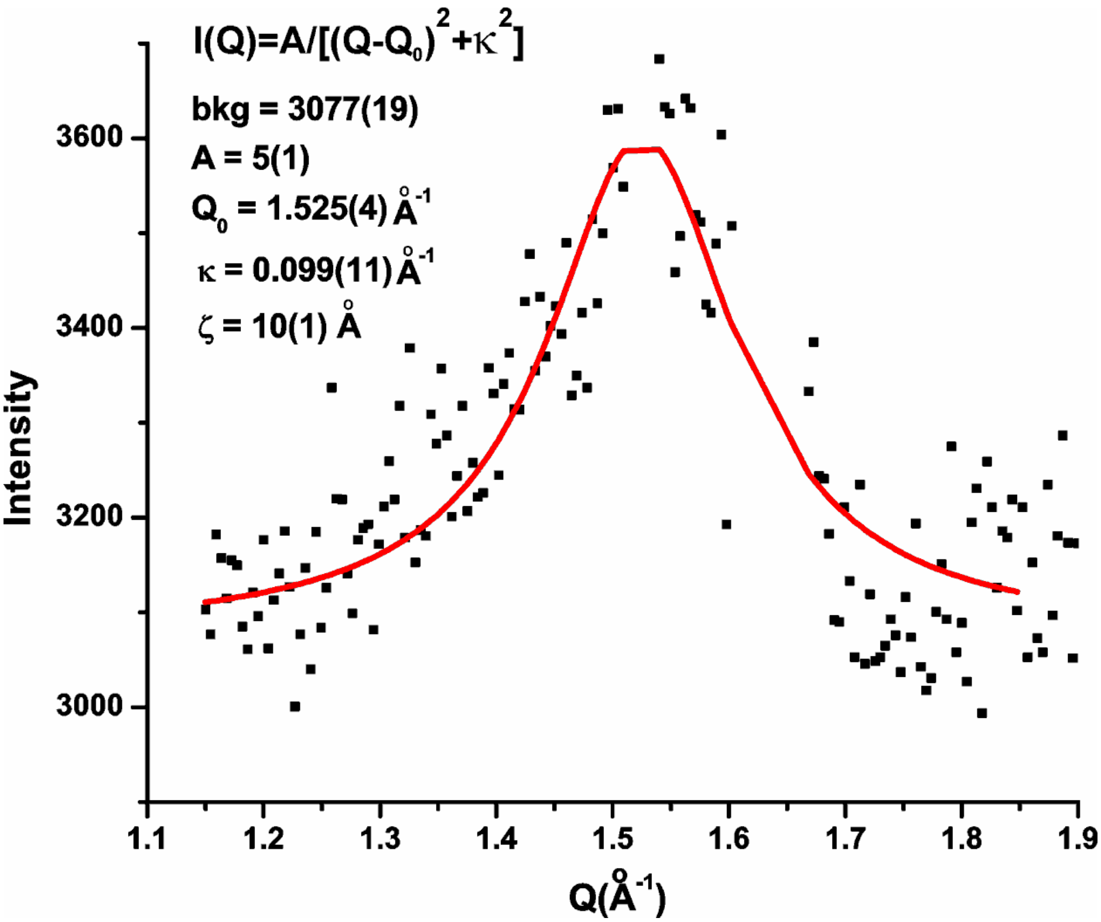

Figure 7.22. The fit of the diffuse magnetic peak underlying the (111) magnetic Bragg peak (which has been removed) of $Sr_2Fe_{1.9}Mn_{0.1}O_{5+y}$ to the Ornstein-Zernike model, $I(Q) = A/[(Q-Q_0)^2 + \kappa^2]$ where $Q = 4\pi\sin\theta/\lambda$, A is an amplitude, Q_0 is the peak centre and $\kappa = 1/\xi$ with ξ being the correlation length.

Conclusion

$Sr_2Fe_{1.9}M_{0.1}O_{5+y}$ (M=Mn, Cr, Co; y= 0, 0.5) were synthesized in air, y~0.5, and argon, y~0. The Ar-synthesized materials have long range brownmillerite-type ordering of vacancies with long range G-type magnetic ordering, and T_N = 652(2)K, 633(2)K, and 663(2)K, for the Cr, Mn and Co compounds, respectively. The low T_N for the Mn-compound can be due to the competing ferromagnetic interactions. NPDF analyses show the local structures of these compounds can also be described by the average structure models.

The air-synthesized Co-material has long range vacancy ordering that results in chains of corner-sharing octahedra separated by dimers of square-pyramids. It also has a long range C-type antiferromagnetic ordering with T_N~230K. The air-synthesized Cr and Mn-materials have vacancy-disordered cubic structures with no long range magnetic ordering. However, short range interactions are evident from the weak temperature-dependent peaks in the neutron diffraction data at 4K. For the Mn-compound these peaks can be indexed as (110) and (111) on the magnetic *Cmmm* unit cell indicating the presence of C-type domains with correlation lengths of ~10(1) Å. For the Cr-compound there is one temperature dependent peak indexed as (1/2 1/2 1/2) on the *Pm-3m* cell indicative of short range G-type ordering with the correlation length 7(1) Å. The air synthesized Cr and Mn-compounds both show FC/ZFC divergences at ~60K and 45K, respectively. The NPDF local structure studies on the Cr and Co-compounds show that a model with a brownmillerite-type ordering of vacancies can describe the local structures better than their average structure models.

References

(1) Sunarso, J.; Motuzas, J.; Liu, S.; Costa, J. C. D. d. Bi-doping effects on the structure and oxygen permeation properties of BaSc0.1Co0.9O3−δ perovskite membranes. *J. Membr. Sci.* **2010**, *361*, 120-125.

(2) Kida, T.; Yamasaki, A.; Watanabe, K.; Yamazoe, N.; Shimanoe, K. Oxygen-permeable membranes based on partially B-site substituted BaFe1−yMyO3−δ (M=Cu or Ni). *J. Solid State Chem.* **2010**, *183*, 2426-2431.

(3) Gong, Z.; Yin, X.; Hong, L. Modification of B-site doping of perovskite LaxSr1 − xFe1 − y−zCoyCrzO3 − δ oxide by Mg2+ ion. *Solid State Ionics* **2009**, *180*, 1471-1477.

(4) Zhang, G.; Dong, X.; Liu, Z.; Zhou, W.; Shao, Z.; Jin, W. Cobalt-site cerium doped SmxSr1−xCoO3−δ oxides as potential cathode materials for solid-oxide fuel cells. *J. Power Sources* **2010**, *195*, 3386-3393.

(5) Richter, J.; Holtappels, P.; Graule, T.; Nakamura, T.; Gauckler, L. Materials design for perovskite SOFC cathodes. *Monatsh. Chem. (Chem. Monthly)* **2009**, *140*, 985-999.

(6) Hodges, J. P.; Short, S.; Jorgensen, J. D.; Xiong, X.; Dabrowski, B.; Mini, S. M.; Kimball, C. W. Evolution of Oxygen-Vacancy Ordered Crystal Structures in the Perovskite Series SrnFenO3n−1 (n=2, 4, 8, and ∞), and the Relationship to Electronic and Magnetic Properties. *J. Solid State Chem.* **2000**, *151*, 190-209.

(7) Garlea, V.; Chakoumakos, B.; Moore, S.; Taylor, G.; Chae, T.; Maples, R.; Riedel, R.; Lynn, G.; Selby, D. The high-resolution powder diffractometer at the high flux isotope reactor. *Appl. Phys. A* **2010**, *99*, 531-535.

(8) Proffen, T.; Egami, T.; Billinge, S. J. L.; Cheetham, A. K.; Louca, D.; Parise, J. B. Building a high resolution total scattering powder diffractometer - upgrade of NPD at MLNSC. *Appl. Phys. A* **2002**, *74*, s163-s165.

(9) Ramezanipour, F.; Greedan, J. E.; Grosvenor, A. P.; Britten, J. F.; Cranswick, L. M. D.; Garlea, V. O. Intralayer Cation Ordering in a Brownmillerite Superstructure: Synthesis, Crystal, and Magnetic Structures of Ca_2FeCoO_5. *Chem. Mater.* **2010**, *22*, 6008-6020.

(10) Parsons, T. G.; D'Hondt, H.; Hadermann, J.; Hayward, M. A. Synthesis andStructural Characterization of $La_{1-x}A_xMnO_{2.5}$ (A=Ba,Sr,Ca) Phases:Mapping the Variants of the Brownmillerite Structure. *Chem. Mater.* **2009**, *21*, 5527-5538.

(11) Larson, A. C.; Von Dreele, R. B. General Structure Analysis System (GSAS). *Los Alamos National Laboratory Report LAUR* **1994**, 86-748.

(12) Toby, B. H. EXPGUI, a graphical user interface for GSAS. *J. Appl. Cryst.* **2001**, *34*, 210-213.

(13) Farrow, C. L.; Juhás, P.; Liu, J. W.; Bryndin, D.; Božin, E. S.; Bloch, J.; Proffen, T.; Billinge, S. J. L. *J. Phys. : Condens. Matter* **2007**, *19*, 335219.

(14) Rodríguez-Carvajal, J. Recent advances in magnetic structure determination by neutron powder diffraction. *Physica B: Condensed Matter* **1993**, *192*, 55-69.

(15) Rodriguez-Carvajal, J.; Roisnel, T. FullProf.98 and WinPLOTR: New Windows 95/NT Applications for Diffraction. *Commission For Powder Diffraction, International Union for Crystallography, Newletter N°20 (May-August) Summer* **1998**.

(16) Roisnel, T.; Rodriguez-Carvajal, J. In *In WinPLOTR: a Windows tool for powder diffraction patterns analysis;* Delhez, R., Mittenmeijer, E. J., Eds.; Proceedings of the Seventh European Powder Diffraction Conference (EPDIC 7), Materials Science Forum; 2000; , pp 118-123.

(17) Schmidt, M.; Campbell, S. J. Crystal and Magnetic Structures of Sr2Fe2O5 at Elevated Temperature. *J. Solid State Chem.* **2001**, *156*, 292-304.

(18) Martin, R. L. In Ebsworth, E. A. V., Maddock, A. G. and Sharpe, A. G., Eds.; New Pathways in Inorganic Chemistry; Cambridge University Press: New York, 1968; .

(19) Goodenough, J. B. *Magnetism and the Chemical Bond;* Interscience: New York, 1963; .

(20) Schmidt, M.; Hofmann, M.; Campbell, S. J. *J. Phys. : Condensed Matter* **2003**, *15*, 8691-8701.

(21) Ravindran, P.; Vidya, R.; Fjellvåg, H.; Kjekshus, A. Validity of bond-length and Mössbauer parameters to assign oxidation statesin multicomponent oxides: Case study of Sr4Fe4O11. *Phys. Rev. B* **2008**, *77*, 134448.

(22) Adler, P. Comment on “Spin- and charge-ordering in oxygen-vacancy-ordered mixed-valence Sr4Fe4O11”. *Phys. Rev. B* **2008**, *77*, 136401.

(23) Ravindran, P.; Vidya, R.; Fjellvåg, H.; Kjekshus, A. Reply to "Comment on 'Spin- and charge-ordering in oxygen-vacancy-orderedmixed-valence Sr4Fe4O11' ". *Phys. Rev. B* **2008**, *77*, 136402.

(24) Stanley, H. E. In *Introduction to Phase Transitions and Critical Phenomena;* Oxford Univ. Press: New York, 1971.

Chapter 8

A Vacancy-Disorder Oxygen-Deficient Perovskite with Long Range Magnetic Ordering: Local and Average Structures and Magnetic Properties of $Sr_2Fe_{1.5}Cr_{0.5}O_5$

This chapter describes the case of an unusual oxygen-deficient perovskite that unlike other vacancy-disordered phases displays a long-range magnetic ordering. The candidate performed the synthesis, the crystal and magnetic structure studies and the NPDF analyses of the local structure.

Introduction

The iron-based oxygen-deficient perovskites, $Ca_2Fe_2O_5$ and $Sr_2Fe_2O_5$ [1-3] both have brownmillerite-type structures with a long-range ordering of oxygen vacancies and a long-range antiferromagnetic ordering. The brownmillerite structure is preserved upon partial substitution of Fe by Co to form Ca_2FeCoO_5 [4] and Sr_2FeCoO_5 [5]. Both $Sr_2Fe_2O_5$ and Sr_2FeCoO_5 have the *Imma* (*Icmm*) space group because of the disorder of tetrahedral chain orientations that occurs due to the presence of strontium. For the Ca compounds, the ordering of chains occurs in both materials, but the transition from $Ca_2Fe_2O_5$, *Pnma*, to Ca_2FeCoO_5, *Pcmb*, changes the type of chain ordering and therefore yields different space groups, and unit cell sizes [4].

Partial substitution of Fe by Mn results in a brownmillerite compound, Ca_2FeMnO_5 [6], and a vacancy-disordered cubic material, Sr_2FeMnO_5 [7]. Again, the presence of Sr encourages disorder, but in this case it has a much greater impact by preventing the ordering of oxygen vacancies altogether.

The Cr-substituted phases are also known. $Ca_2Fe_{1.5}Cr_{0.5}O_5$ has a brownmillerite structure, *Pnma* [8,9], and a long-range antiferromagnetic ordering of the G-type. The authors of [8] also identified a phase with composition $Sr_2Fe_{1.5}Cr_{0.5}O_{5.540}$, as a vacancy-disordered cubic phase that shows evidence of local ordering in its Mössbauer data [10]. However, no further details about this material are known.

We synthesized $Sr_2Fe_{1.5}Cr_{0.5}O_{5+y}$ and studied its average and local structures, and magnetic structure. It has a *Pm-3m* structure with long-range disorder of oxygen vacancies. However, NPDF results show that local brownmillerite-type ordering of oxygen vacancies is present. An interesting finding is that while our previously studied vacancy disordered materials, discussed in the previous chapters, generally lack a long-range magnetic ordering, this material exhibits long-range G-type antiferromagnetism, with T_N~565K.

Experimental.

Synthesis. $Sr_2Fe_{1.5}Cr_{0.5}O_5$ was synthesized using stoichiometric amounts of $SrCO_3$ (99.9% Sigma Aldrich), Fe_2O_3 (99.998% Alfa Aesar), and Cr_2O_3 (99.97 % Alfa Aesar). The powders were thoroughly ground, mixed and pressed into a pellet that was fired at 1280 ºC in air, for 36h followed by quenching in liquid nitrogen, to give the cubic structure.

A Synthesis was also attempted by firing a pellet at 1200 ºC in air, followed by slow cooling, that resulted in many unusually wide peaks in the x-ray diffraction data, indicating the presence of multiple overlapping phases.

If the reaction is performed in Ar atmosphere at 1200 ºC followed by slow cooling, a cubic phase seems to form with a smaller unit cell, along with a significant amount of impurities.

X-ray and Neutron diffraction

A PANalytical X'Pert Pro MPD diffractometer with a linear X'Celerator detector was used to collect the x-ray data, with the $CuK\alpha_1$ radiation ($\lambda = 1.54056$ Å) and 2θ step interval of 0.0084°.

Time-of-flight neutron diffraction data at room temperature were obtained on the instrument NPDF at the M. J. Lujan Jr. Center for Neutron Scattering at the Los Alamos Neutron Science Center [11].

Constant wavelength neutron data were collected at the Canadian Neutron Beam Centre on the C2 diffractometer at 14 different temperatures with wavelength 2.3704 Å. Data with λ =1.32829 Å were also collected at room temperature and 4K.

Results and discussion

Crystal structure of $Sr_2Fe_{1.5}Cr_{0.5}O_5$

A cubic structure was readily identified form the powder x-ray diffraction data, and was refined in a vacancy-disordered *Pm-3m* model. The Rietveld refinements were performed by the GSAS program suite [12] using the EXPGUI interface [13]. The refinement profiles for the x-ray, TOF and constant wavelength neutron diffraction data are shown in Figure 8.1. Considering the large difference between the neutron scattering lengths of Fe (9.45 fm) and Cr (3.63 fm), neutron diffraction data were used to determine Fe and Cr occupancies. The occupancy of oxygen was also refined using the neutron data. The powder refinement results are shown in Tables 8.1 and 8.2.

The neutron refinements show that the compositional formula can be written as $Sr_2Fe_{1.60(3)}Cr_{0.40(3)}O_{5.05(2)}$, where the oxygen content is very close to the ideal value, 5, and the Fe/Cr ratio is slightly different but within 3σ of the expected ratio, 1.5/0.5.

Table 8.1. The refinement results from x–ray (300K), TOF (300K) and constant wavelength neutron diffraction data (290K) for $Sr_2Fe_{1.5}Cr_{0.5}O_5$

Space group	*Pm-3m*
Lattice parameter	a = 3.94491(14) Å V = 61.392(7) $Å^3$
Agreement factors	R_p (X–ray, λ=1.54056 Å) = 0.0263 R_{wp} (X–ray, λ=1.54056 Å) = 0.0409 R_p (TOF, four banks) = 0.0321 R_{wp} (TOF, four banks) = 0.0534 R_p (Neutron, λ= 1.32829Å) = 0.0345 R_{wp} (Neutron, λ= 1.32829 Å) = 0.0450 R_p (Neutron, λ= 2.3704Å) = 0.0425 R_{wp} (Neutron, λ= 2.3704Å) = 0.0532

Table 8.2. The atomic positions, occupancies and thermal displacement parameters for $Sr_2Fe_{1.5}Cr_{0.5}O_5$ obtained from powder neutron diffraction data, λ= 1.32829Å and λ= 2.3704Å at 290K.

	x	*y*	*z*	Occupancy	U_{iso} ($Å^2$)
Sr	0.5	0.5	0.5	1.0	0.0289(8)
Fe	0	0	0	0.80(1)	0.0229(6)
Cr	0	0	0	0.20(1)	0.0229(6)
O	0.5	0	0	0.842(8)	0.0337(6)
Bond distances (Å)					
Fe – O	1.97245(7)				
Sr – O	2.78947(7)				
Sr – Sr	3.9449(1)				
Sr – Fe	3.41639(9)				

The Fe–O and Sr–O bond distances in $Sr_2Fe_{1.5}Cr_{0.5}O_5$ are longer than the average distances observed for $Sr_2Fe_2O_5$ [2,3]. They are also slightly longer than the corresponding bond lengths in Sr_2FeMnO_5 [7]. Considering that the ionic radii for Mn^{3+} and Cr^{3+} are almost the same, these results confirm the refined occupancy of oxygen and show that the average oxidation states of Fe and Cr cannot be significantly greater than 3+, as further oxidation would result in noticeable shortening of bonds.

A comparison with the Ca-analogue, $Ca_2Fe_{1.5}Cr_{0.5}O_5$, is noteworthy, where the ordering of vacancies and the brownmillerite structure occur [8,9]. A similar effect has been previously observed for the Fe/Mn compounds, where a transition from Ca_2FeMnO_5 to Sr_2FeMnO_5 results in destruction of vacancy ordering [6,7]. However, as shown later, the case of Fe/Cr is unique due to the fact that the long-range magnetic ordering is not suppressed even when vacancy ordering is removed.

Local structure of $Sr_2Fe_{1.5}Cr_{0.5}O_5$

Neutron-Pair-Distribution-Function (NPDF) analysis was used to study the local structure. Based on the cubic model of the average structure, the inter-atomic distances that should appear in G(r) up to 4Å are those shown as dashed lines in Figure 8.2a. It is clear that the cubic model cannot describe the local structure properly. There are several shoulders and peaks, highlighted by arrows in Fig. 8.2a, that do not match the cubic model. PDFGUI [14] refinement from 1.5 Å to 5 Å with a *Pm-3m* model, shown in Fig. 8.2b, results in a poor fit with $R_w = 0.268$. The peaks and shoulders observed in the G(r) seem to match the inter-atomic distances expected from a brownmillerite model between

1.5 and 5 Å. The PDFGUI fit with a brownmillerite model, Fig. 8.2c, yields significantly better results with R_w= 0.127. Therefore, the local structure appears to be brownmillerite, which implies a local ordering of oxygen vacancies as previously suggested by the Mössbauer data [10].

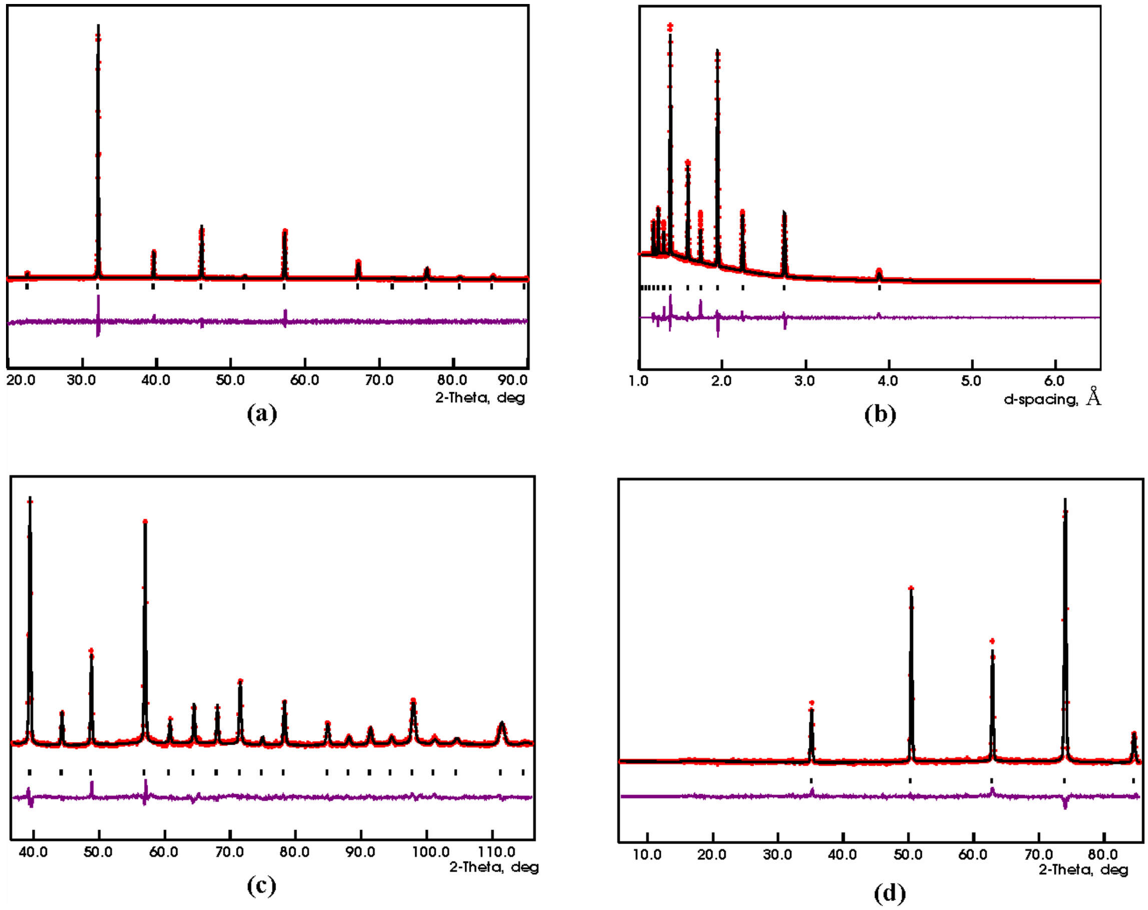

Figure 8.1. Rietveld refinement profiles for $Sr_2Fe_{1.5}Cr_{0.5}O_5$ **(a)** x-ray powder diffraction (λ=1.54056 Å) at 300K. **(b)** Time-of-Flight neutron diffraction at 300K. One of the four data banks is shown. The detector angle for this bank was 46°. **(c)** Constant wavelength neutron diffraction, λ= 1.32829 Å, at 290K. **(d)** Neutron diffraction, λ= 2.3704 Å, at 290K.

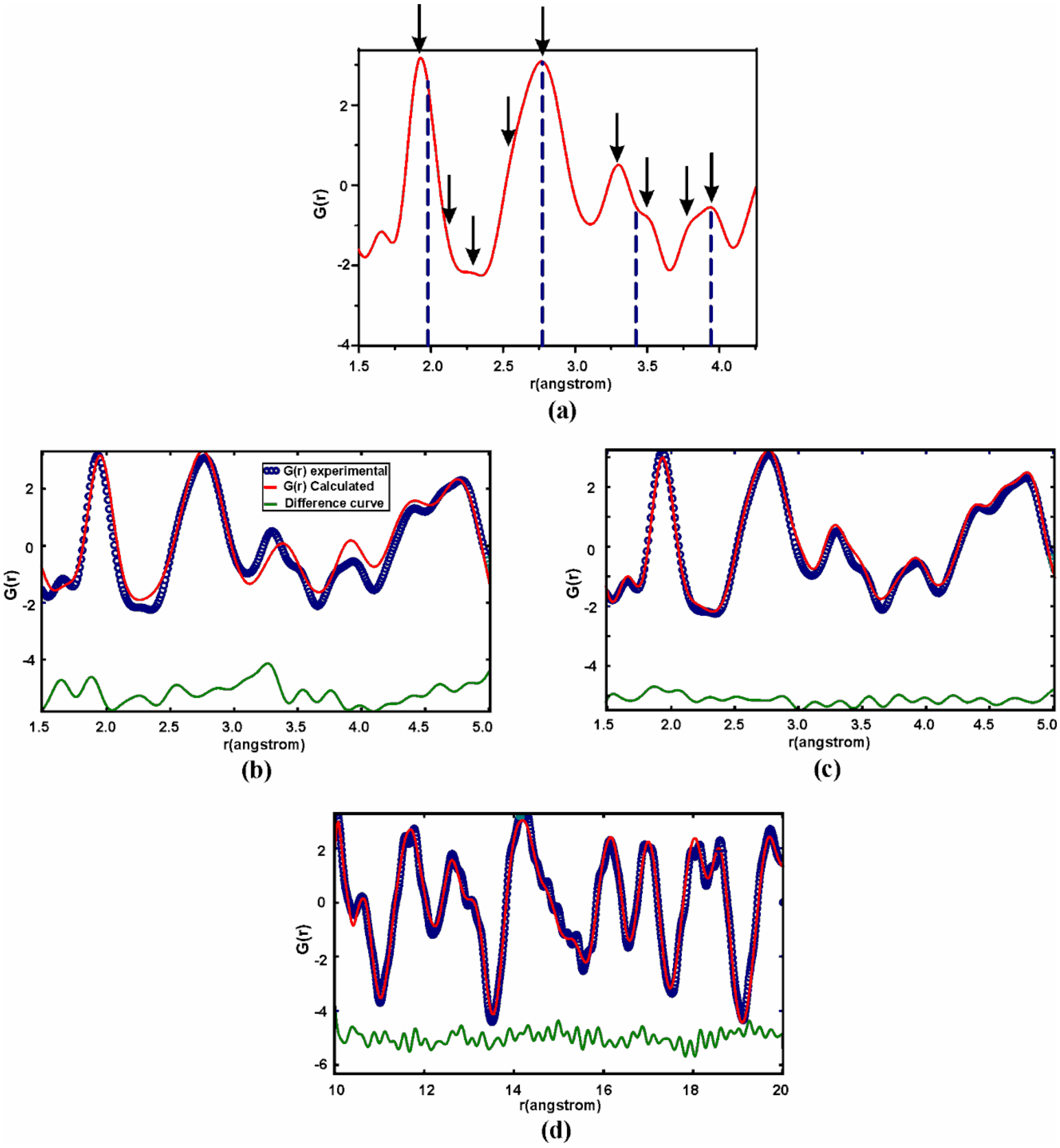

(a)

(b)

(c)

(d)

Figure 8.2. (a) The G(r) pattern for $Sr_2Fe_{1.5}Cr_{0.5}O_5$ from 1.5 to 4 Å. The purple dashed lines show the expected peak positions for the average structure model, *Pm-3m*. The arrows show the peaks and shoulders that match a brownmillerite model. **(b)** The G(r) fit using a *Pm-3m* model from 1.5 to 5 Å, R_w= 0.268. **(c)** The G(r) fit using a brownmillerite *Ibm*2 model from 1.5 to 5 Å, R_w= 0.127. **(d)** The G(r) fit using a *Pm-3m* model from 10 to 20 Å, R_w=0.135.

At longer distances, 10 to 20 Å, the local structure is expected to have more similarities to the average structure, a fact confirmed by the PDFGUI refinement, Fig. 8.2d, that shows a reasonable match with the cubic model, R_w=0.135.

Therefore, NPDF results indicate that while the oxygen vacancies are disordered in the long range, there is a short-range brownmillerite-type vacancy ordering in $Sr_2Fe_{1.5}Cr_{0.5}O_5$, a property that has been observed for Sr_2FeMnO_5 as well [7].

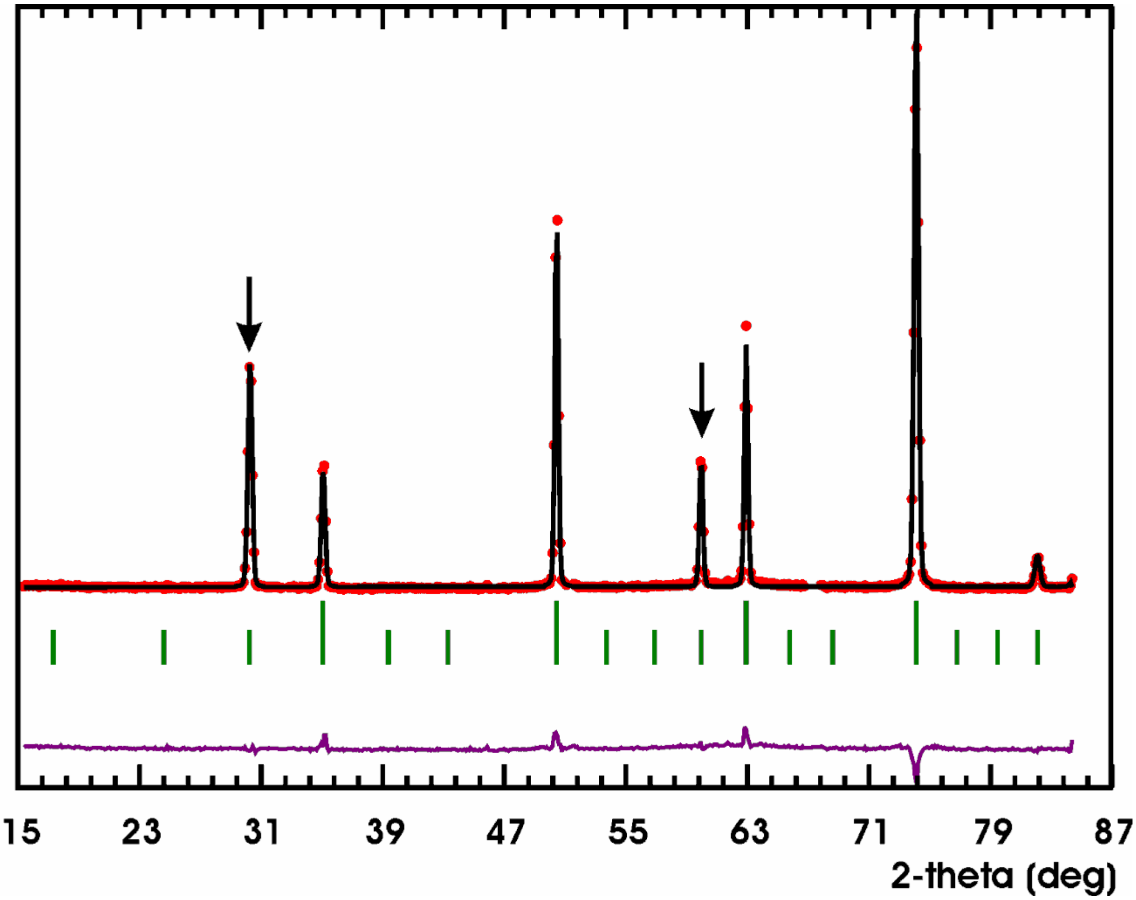

Figure 8.3. The refinement profile for crystal and magnetic structures of $Sr_2Fe_{1.5}Cr_{0.5}O_5$. The major magnetic peaks shown by arrows appear at 30.396(1)° and 60.076 (1)° and are indexed as (1/2 1/2 1/2) and (3/2 1/2 1/2), respectively, on the chemical cell. Red circles show the experimental data, black solid line the model and upper and lower vertical tick marks represent the crystal and magnetic structure peak positions, respectively. The lower solid line is the difference plot.

Magnetic structure of $Sr_2Fe_{1.5}Cr_{0.5}O_5$

The neutron diffraction data at 4K show magnetic Bragg peaks, indicating the presence of a long-range magnetic ordering. The two major magnetic peaks indexed as (1/2 1/2 1/2) and (3/2 1/2 1/2) on the structural cell are shown in Figure 8.3 by arrows.

The full-width-half-maxima (FWHM) for the magnetic peaks increase markedly above ~550K, as shown for (1/2 1/2 1/2) in Figure 8.4. As seen here, the FWHM nearly triples between 550K and 575K, while it remains constant for the structural peak (1 0 0). The magnetic structure was found to be G-type antiferromagnetic, with magnetic moments on each site pointing anti-parallel to all nearest neighbors. As a result the magnetic cell is 8 times larger than the structural cell, as the cell dimensions are doubled to accommodate antiferromagnetic ordering. While, the apparent transition temperature is ~583K, Figure 8.5, the true T_N is better determined by the sharp increase in FWHM that occurs at ~565K.

The magnetic moment obtained by the FullProf program [15], employing WinPLOTR [16] at 4K is 3.4(7)μ_B, significantly smaller than the spin only value expected from 25% Cr^{3+} and 75% Fe^{3+}, 4.5 μ_B.

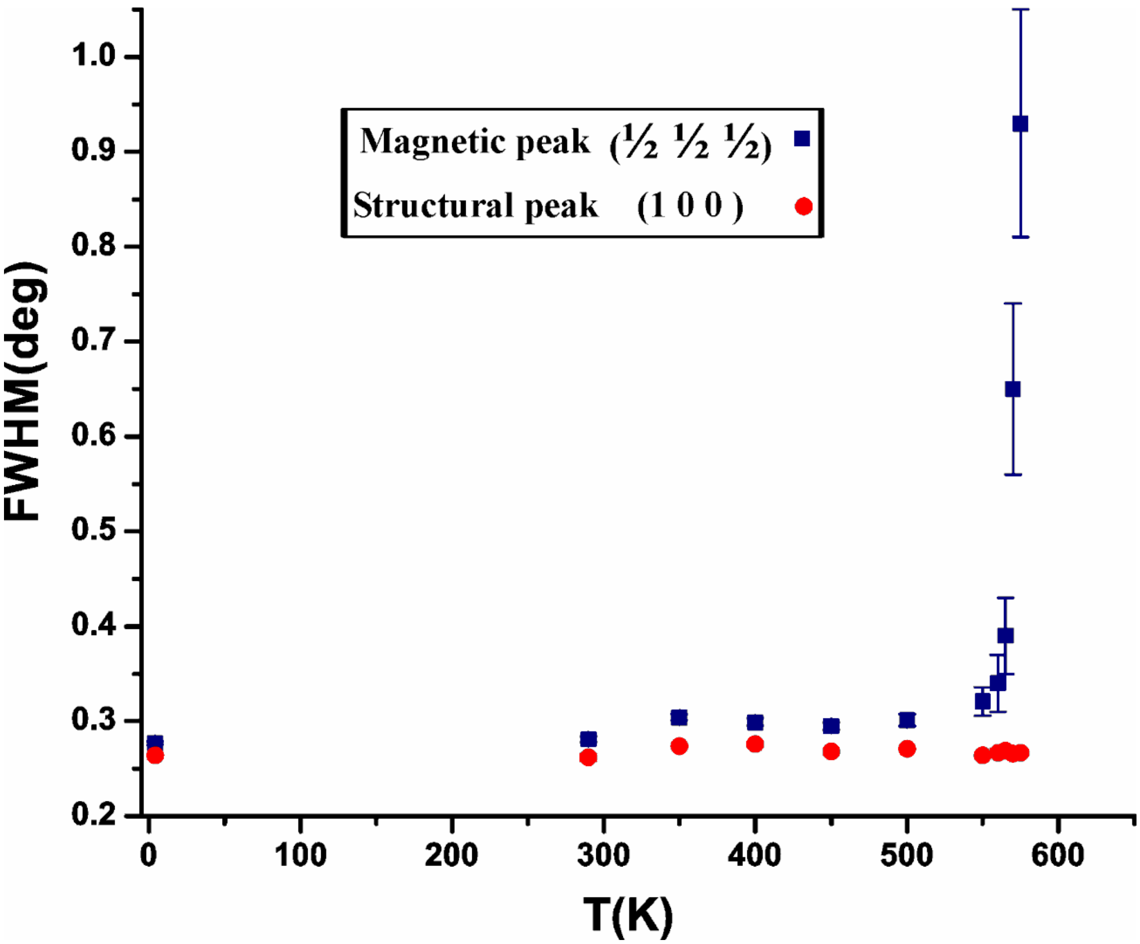

Figure 8.4. FWHM for a magnetic and a structural peak as function of temperature. Note the sharp increase in FWHM of the magnetic peak (1/2 1/2 1/2) at ~565K.

In summary, oxygen deficient perovskite, $Sr_2Fe_{1.5}Cr_{0.5}O_5$, was synthesized and its average structure was found to be a vacancy-disordered *Pm-3m,* while its local structure involves a short-range ordering of oxygen vacancies. $Sr_2Fe_{1.5}Cr_{0.5}O_5$ has a long-range magnetic ordering, with T_N~565K, apparent from a sharp increase in the FWHM of the magnetic reflections.

Note that in most oxygen deficient perovskites, the long-range ordering of vacancies is accompanied by a long-range magnetic ordering. On the contrary, the disorder of the vacancies usually destroys the long-range magnetic ordering, as discussed in the previous chapters. Therefore, the presence of long-range antiferromagnetism in $Sr_2Fe_{1.5}Cr_{0.5}O_5$ is unprecedented in cubic, disordered perovskites.

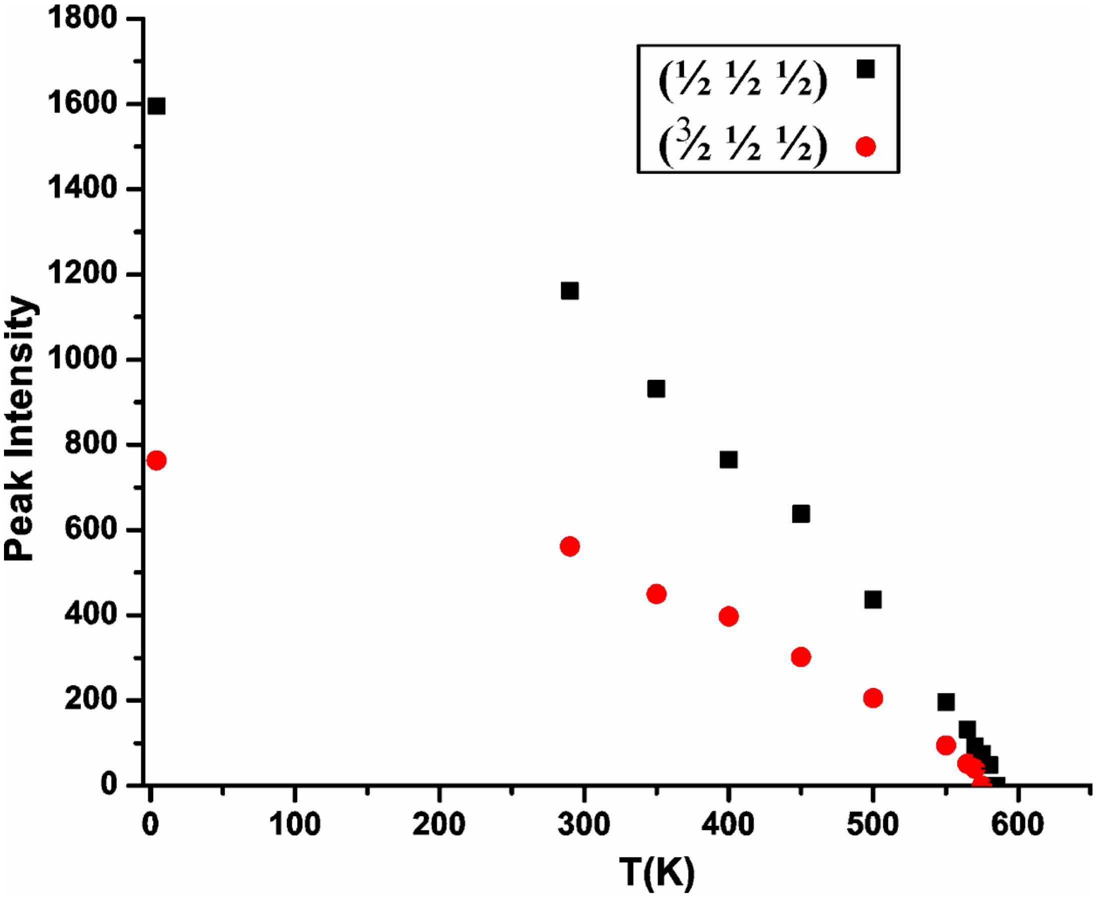

Figure 8.5. The intensities of magnetic peaks as function of temperature for $Sr_2Fe_{1.5}Cr_{0.5}O_5$. Note that the magnetic peaks disappear below ~583K.

References

[1] Berggren, J. *Acta Chem. Scand.* **1971,** 25, 3616.

[2] D'Hondt, H.; Abakumov, A. M.; Hadermann, J.; Kalyuzhnaya, A. S.; Rozova, M. G.; Antipov, E. V.; Tendeloo, G. V. *Chem. Mater*. **2008,** 20, 7188.

[3] Greaves, C; Jacobson, A. J. ; Tofield, B. C.; Fender, B. E. F. *Acta Cryst.* **1975,** B31, 641.

[4] Ramezanipour, F.; Greedan, J. E.; Grosvenor, A.P.; Britten, J.F.; Cranswick, L.M.D.; Garlea, V.O. *Chem. Mater*. **2010**, 22, 6008.

[5] Battle, P. D.; Gibb, T. C.; Lightfoot, P. *J. Solid. State Chem.* **1988,** 76, 334.

[6] Ramezanipour, F.; Cowie, B.; Derakhshan, S.; Greedan, J. E.; Cranswick, L. M. D. *J. Solid State Chem.* **2009,** 182, 153.

[7] Ramezanipour, F.; Greedan, J. E.; Siewenie, J.; Proffen, Th.;Ryan, D. H.; Grosvenor, A.P.; Donaberger, R. *Inorg. Chem.* 2011, In press.

[8] Gibb, T. C.; Matsuo, M. *J. Solid. State Chem.* **1990,** 88, 485.

[9] Battle, P.D.; Bollen, S.K.; Gibb, T. C.; Matsuo, M. *J. Solid. State Chem.* **1991,** 90, 42.

[10] Gibb, T. C.; Matsuo, M. *J. Solid. State Chem.* **1990,** 86, 164.

[11] Proffen, T.; Egami, T.; Billinge, S.J.L.; Cheetham, A.K.; Louca, D.; Parise, J.B. *Appl. Phys.* **2002,** A74, S163.

[12] Larson A.C.; Von Dreele, R.B. General Structure Analysis System (GSAS); Los Alamos National Laboratory Report LAUR, **1994**, pp. 86–748.

[13] Toby, B. H. *J. Appl. Cryst.* **2001,** *34*, 210.

[14] Farrow, C. L.; Juhás, P.; Liu, J. W.; Bryndin, D.; Božin, E. S.; Bloch, J.; Proffen, Th.; Billinge, S. J. L. *J. Phys.: Condens. Matter* **2007,** 19, 335219.

[15] Roisnel, T.; Rodriguez-Carvajal, J. FULLPROF ver 1.9c: Rietveld, Profile Matching & Integrated Intensity Refinement of X-ray and/or Neutron Data, Laboratoire Léon Brillouin, Saclay, France, **2001**.

[16] Roisnel, T.; Rodríguez-Carvajal, J. WinPLOTR: a Windows tool for powder diffraction patterns analysis, in: R. Delhez, E.J. Mittenmeijer (Eds.), Proceedings of the Seventh European Powder Diffraction Conference (EPDIC 7), Materials Science Forum, **2000**, pp. 118–123.

Chapter 9

Conclusion

The materials studied have crystal structures derived from the perovskite structure. The focus is on the layered materials that incorporate perovskite-type layers separated by edge-sharing octahedra or corner-sharing tetrahedra, the pillared perovskite and brownmillerite families. The application of a variety of techniques, including x-ray diffraction, SQUID magnetometry, TOF and constant wavelength neutron diffraction, neutron-pair-distribution-function analysis, Mössbauer and XANES helped to study different aspects and properties of these compounds. The first material that was studied had a pillared perovskite structure containing perovskite-type layers isolated from each other by dimeric units of edge-sharing octahedra. The work on layered perovskite-based systems then continued by synthesizing and studying several materials with the brownmillerite structure in which the perovskite-type layers are separated by chains of tetrahedra. Different aspects of these layered compounds were studied including the changes in the crystal structure and magnetic properties as a function of synthesis conditions and cation substitution at different crystallographic sites. The results of these studied can help in predicting the properties of new materials based on their compositions and synthetic procedures.

$La_5Mo_3VO_{16}$ [1] is the first molybdenum-based pillared perovskite whose properties were investigated by neutron diffraction. This study was possible because of the large quantity of product that could be obtained from the solid-state synthesis. The importance of the successful synthesis of this material is that pure phases of Mo-based systems are usually obtained in small quantities using electrolysis from molten salts [2-4]. A solid-state experiment was designed to take advantage of the low melting point of

V_2O_5 to facilitate the reaction, and for the redox couple, $Mo^{4+}/V^{5+} = Mo^{5+}/V^{4+}$ to give the desired oxidation states of cations. After several modifications to the synthesis procedure, the experiment was finally successful and a nearly single phase material with formula $La_5Mo_{2.76(4)}V_{1.25(4)}O_{16}$ was synthesized [1]. Considering that there are only a few materials known with the pillared perovskite structure, addition of a new compound to this family is a significant step. Furthermore, the determination of the magnetic structure using neutron diffraction was done for the first time for a Mo-based system, even though the original members of this family were Mo-compounds.

The next layered perovskite-based compound that was studied was the brownmillerite Ca_2FeMnO_5 [5]. This material contains a large degree of ordering between Fe and Mn with ~90% of the octahedral sites being occupied by Mn and ~90% of the tetrahedral sites by Fe. The site preference could be determined due to the strong contrast in neutron scattering lengths of Fe and Mn. The G_y-type antiferromagnetic ordering persists well above room temperature, up to 407K. Substitutions of cations on the B/B' sites in the brownmillerite formula, $AA'BB'O_5$ (B = octahedral site cation, B'= tetrahedral site cation, A,A'= large cations located at the interstitial spaces between polyhedra), were attempted next.

The brownmillerite compound, Ca_2FeCoO_5 [6] was therefore synthesized next. Surprisingly, it was found to display a rare type of tetrahedral chain ordering resulting in the space group *Pbcm,* (with a doubling of the unit cell volume) as opposed to *Pnma* in Ca_2FeMnO_5. This observation is not consistent with the latest attempt to systematize the known brownmillerite space group symmetries. In addition, this material is the first brownmillerite to contain an intra-layer cation ordering and a NaCl-type ordering between the octahedral and tetrahedral layers. There is also a G_z to G_x spin re-orientation occurring as a function of temperature, another property unique to this compound. Spin canting also takes place in Ca_2FeCoO_5, while there is no evidence to suggest any significant canting in Ca_2FeMnO_5.

Pursuing further this theme the series $Sr_2Fe_{1.9}M_{0.1}O_{5+y}$ (M=Mn, Cr, Co; y= 0, 0.5) was investigated to determine the degree of sensitivity of the material properties to low doping levels of 5%. Surprising changes in the crystal structures and magnetic properties were observed depending on the dopant ion and the synthesis procedure. Syntheses in argon in all cases result in a brownmillerite-type ordering of the oxygen vacancies, while the synthesis in air gives rise to a different type of vacancy ordering for the Co-compound, resulting in alternating octahedral and square pyramidal coordinations for the B/B'-sites, one already known for $Sr_2Fe_2O_{5.5}$. For the Mn and Cr-materials, syntheses in air result in complete destruction of the long range vacancy ordering, although the NPDF analyses show a local brownmillerite type ordering. The brownmillerite phases have a long-range magnetic ordering, but the T_N's are notably different for the three materials: 652K, 633K and 663K for the Cr, Mn and Co compounds, respectively. The low value for M = Mn is suggested to arise from competing ferromagnetic interactions on the octahedral sites. Concerning the air-synthesized phases, the Co compound contains a long-range antiferromagnetic ordering of the C-type at 4K, also seen for $Sr_2Fe_2O_{5.5}$, while the Mn and Cr materials do not have a long-range magnetic ordering but show evidence for complex magnetic ground states. In both cases features are seen in the neutron diffraction which appear to consist of a minor Bragg component superimposed on a broad Lorenztian. For M = Mn, the Bragg components index on a C-type cell found for M = Co while for M = Cr, the Bragg peak indexes as G-type. In both cases the correlation length for the short range order component is in the range 6 – 10 Å.

The next step was to look at the effect of the A-site cation by substituting Sr for Ca in Ca_2FeMnO_5. Therefore, two materials with formula Sr_2FeMnO_{5+y} (y=0, 0.5) were synthesized [7]. For these Sr-containing phases, syntheses in both air (y~0.5) and argon (y~0) result in long-range vacancy-disordered structures, while for the Ca-analogues, ordering of vacancies and a brownmillerite structure are obtained through both air and argon syntheses. The magnetic properties also change dramatically. $Sr_2FeMnO_{5.0}$ has no long-range magnetic ordering and undergoes a transition to a superparamagnetic state below ~50K, while Ca_2FeMnO_5 has a long-range magnetic ordering.

While disorder of oxygen vacancies comes with the suppression of the long-range magnetic ordering in $Sr_2FeMnO_{5.0}$ and $Sr_2Fe_{1.9}M_{0.1}O_{5.5}$ (M=Mn, Cr), this is not necessarily true for all vacancy-ordered systems. A neutron diffraction study on the *Pm-3m* $Sr_2Fe_{1.5}Cr_{0.5}O_5$ showed G-type antiferromagnetic ordering with T_N~565K.

Overall, the following conclusions can be drawn from the results of these studies: The crystal structure and magnetic properties of oxygen-deficient perovskites are strongly dependent on the oxygen content and the cation types on different sites. The effect of varying the B/B'-site cations depends largely on the A-site cation type. For vacancy-ordered systems with Ca on the A-site, altering the B/B'-site cations seems to preserve the ordering of oxygen vacancies, while changes to the tetrahedral chain ordering may occur, giving rise to different space groups. An example of such effect is observed upon transition from Ca_2FeMnO_5 [5] to Ca_2FeCoO_5 [6], as seen in Table 9.1.

Table 9.1. Variations of crystal structures upon varying the A-site and B/B'-site cations.

	Vacancy ordering	*Orientation of tetrahedral chains*
Ca_2FeMnO_5	•long-range ordering •brownmillerite	•same within layers; opposite between layers •*Pnma* space group
Ca_2FeCoO_5	•long-range ordering •brownmillerite	• alternating within layers and between layers •*Pcmb* space group
Sr_2FeMnO_5	•only short range ordering •disordered-perovskite	•no long range chains are present •*Pm-3m* space group
$Sr_2FeMnO_{5.5}$	•only short range ordering •disordered-perovskite	•no long range chains are present •*Pm-3m* space group
$Sr_2Fe_{1.9}Cr_{0.1}O_5$	•long-range ordering •brownmillerite	•chains are long-range disordered •*Icmm* space group
$Sr_2Fe_{1.9}Mn_{0.1}O_5$	•long-range ordering •brownmillerite	•chains are long-range disordered •*Icmm* space group
$Sr_2Fe_{1.9}Co_{0.1}O_5$	•long-range ordering •brownmillerite	•chains are long-range disordered •*Icmm* space group
$Sr_2Fe_{1.9}Cr_{0.1}O_{5.5}$	•only short range ordering •disordered-perovskite	•no long range chains are present •*Pm-3m* space group
$Sr_2Fe_{1.9}Mn_{0.1}O_{5.5}$	•only short range ordering •disordered-perovskite	•no long range chains are present •*Pm-3m* space group
$Sr_2Fe_{1.9}Co_{0.1}O_{5.5}$	•long-range ordering • alternating square-pyramids and octahedra	•Instead of tetrahedral chains, dimeric units of square-pyramids are present •*Cmmm* space group
$Sr_2Fe_{1.5}Cr_{0.5}O_5$	•only short range ordering •disordered-perovskite	•no long range chains are present •*Pm-3m* space group

Table 9.2. Variations of magnetic properties upon varying the A-site and B/B'-site cations.

	Magnetic ground state
Ca_2FeMnO_5	•long range G-type ordering •magnetic moments along the longest axis •T_N=407K
Ca_2FeCoO_5	•long range G-type ordering •magnetic moments along the longest axis between 4K and 100K • magnetic moments along the shortest axis between 225K and 595K •T_N=595K
Sr_2FeMnO_5	•no long range magnetic ordering •short range G-type domains of ~50Å •superparamagnetic below ~50K
$Sr_2FeMnO_{5.5}$	•long range G-type ordering in a small fraction of the sample (~4%) •ZFC/FC divergence at ~25K •Fluctuating spins at 5K
$Sr_2Fe_{1.9}Cr_{0.1}O_5$	•long range G-type ordering •magnetic moments along the shortest axis •T_N=652K
$Sr_2Fe_{1.9}Mn_{0.1}O_5$	•long range G-type ordering • magnetic moments along the shortest axis •T_N= 633K
$Sr_2Fe_{1.9}Co_{0.1}O_5$	•long range G-type ordering •magnetic moments along the shortest axis •T_N= 663K
$Sr_2Fe_{1.9}Cr_{0.1}O_{5.5}$	•no long range magnetic ordering •short range G-type domains of ~7Å •ZFC/FC divergence at ~60K
$Sr_2Fe_{1.9}Mn_{0.1}O_{5.5}$	•no long range magnetic ordering •short range G-type domains of ~10Å •ZFC/FC divergence at ~45K
$Sr_2Fe_{1.9}Co_{0.1}O_{5.5}$	•long range C-type ordering •magnetic moments along the intermediate axis at 4K • T_N=230K
$Sr_2Fe_{1.5}Cr_{0.5}O_5$	•long range G-type ordering •T_N=565K

For vacancy-ordered systems with Sr on the A-site, there is usually a lesser degree of ordering, manifested in the tetrahedral chain disorder. For these compounds substitution on the B/B'-site can increase the degree of disorder even further to prevent the ordering of oxygen vacancies altogether. However, in some cases it is possible to preserve the vacancy ordering by modifying the synthesis procedure to lower the oxygen content. Generally, the brownmillerite-type ordering of vacancies is associated with a lower oxygen content. Therefore, reduction experiments can be one of the ways to obtain vacancy-ordered structures. However, caution should be taken, as exceptional cases may exist where even a low oxygen content cannot promote ordering. An example is Sr_2FeMnO_5 [7] as discussed above.

The absence of a long-range vacancy ordering is usually accompanied by the lack of a long-range magnetic ordering, as explained before. While this is true for many oxygen-deficient perovskites, special cases may exist that incorporate disorder of vacancies and a long-range ordering of magnetic moments, as observed in $Sr_2Fe_{1.5}Cr_{0.5}O_5$.

The results of these studies can help to provide a better picture of the parameters that determine the properties of oxygen-deficient perovskites, and can be used as a guide in further investigation of this family of compounds. One of the issues to be addressed in the future studies is determination of the minimum excess of oxygen that triggers the transition from an ordered to a disordered structure. Also, considering the significance of the A-site cation size, substitution of varying amounts of a larger cation on this site can be performed to determine the optimum average size that preserves the ordering of vacancies. Furthermore, the discovery of the intra-layer cation ordering in Ca_2FeCoO_5, as well as the intra and inter-layer ordering of the tetrahedral chains that results in a *Pcmb* superstructure, demands a fresh review of the parameters that govern the structural variations of brownmillerites. The occurrence of this particular structure type in this material cannot be explained by the existing studies in this area.

References

[1] Ramezanipour, F., Derakhshan, S., Greedan, J. E., Cranswick, L.M.D. *J. Solid State Chem*. **2008**, 181, 3366.

[2] McCarroll, W. H.; Darling, C.; Jakubicki, G. *J. Solid State Chem.* **1983**, 48, 189.

[3] Ledesert, M.; Labbe, Ph.; McCarroll, W. H.; Leligny, H.; Raveau, B. *J. Solid State Chem.* **1993,** 105, 143.

[4] Ramanujachary, K.V.; Lofland, S.E.; McCarroll, W.H.; Emge, T.J.; Greenblatt, M. *J. Solid State Chem.* **2002**, 164, 70.

[5] Ramezanipour, F.; Cowie, B.; Derakhshan, S.; Greedan, J. E.; Cranswick, L. M. D. *J. Solid State Chem.* **2009,** 182, 153.

[6] Ramezanipour, F.; Greedan, J. E.; Grosvenor, A.P.; Britten, J.F.; Cranswick, L.M.D.; Garlea, V.O. *Chem. Mater*. **2010**, 22, 6008.

[7] Ramezanipour, F.; Greedan, J. E.; Siewenie, J.; Proffen, Th.;Ryan, D. H.; Grosvenor, A.P.; Donaberger, R. *Inorg. Chem.* 2011, In press.